

NASA Technical Memorandum 106383  
ICOMP-93-44; CMOTT-93-16

111-34  
000-61  
249 P

## Center for Modeling of Turbulence and Transition: Research Briefs—1993

(NASA-TM-106383) CENTER FOR  
MODELING OF TURBULENCE AND  
TRANSITION: RESEARCH BRIEFS, 1993  
Annual Report, Jun. 1992 - Jul.  
1993 (NASA) 249 p

N94-24336

Unclass

G3/34 0206661

January 1994





## Table of Contents

<b>Preface</b> . . . . .	<u>Page</u> iv
<b>Research Activities at the Center for Modeling of Turbulence and Transition</b> Tsan-Hsing Shih . . . . .	1
<b>Eddy Viscosity Models for Turbulent and Transitional Flows</b> Zhigang Yang . . . . .	23
<b>Testing New Two-Equation Turbulence Models for Complex Flows</b> Jiang Zhu . . . . .	47
<b>Low <math>Re_t</math> <math>k - \epsilon</math> Models and the Backward-Facing Step Flow</b> Christopher J. Steffen, Jr. . . . .	63
<b>Modeling of Homogeneous Scalar Turbulence</b> Aamir Shabbir . . . . .	67
<b>A Multiple-Scale Turbulence Model for Incompressible Flow</b> Beverly Duncan . . . . .	81
<b>Modeling of Turbulent Shear Flows</b> William W. Liou . . . . .	101
<b>PDF Models for Compressible Reactive Flows and DNS</b> Andrew T. Hsu . . . . .	109
<b>Modeling of Turbulent, Reacting Flows by PDF Methods</b> Andrew T. Norris . . . . .	141
<b>A Time Dependent Generalization of the Nonlinear Eddy Viscosity Representation of Turbulence</b> Robert Rubinstein . . . . .	147
<b>High-Order Accurate Osher Schemes with Application to Compressible Boundary Layer Stability</b> Jacobus J. Van der Vegt . . . . .	157
<b>Calculation of Waves in Fluids Using A High-Order Compact Difference Scheme</b> Sheng-Tao Yu . . . . .	183

**Visitors' Research Activities**

J.-Y. Chen ( University of California at Berkeley ) . . . . .	215
P. G. Huang ( Elore Institute ) . . . . .	216
Arne V. Johansson ( Royal Institute of Technology, Sweden) . . . . .	216
Chaoqun Liu ( University of Colorado ) . . . . .	216
<b>Appendix A : Organization - 1993</b> . . . . .	219
<b>Appendix B : CMOTT Biweekly Seminars</b> . . . . .	223
<b>Appendix C : List of Member's Publications</b> . . . . .	251



## Preface

This research brief contains the progress reports of the research staff of the Center for Modeling of Turbulence and Transition (CMOTT) from June 1992 to July 1993. It is also an annual report to the Institute for Computational Mechanics in Propulsion located at Ohio Aerospace Institute and NASA Lewis Research Center.

The main objectives of the research activities at CMOTT are to develop, validate and implement turbulence and transition models for flows of interest in propulsion systems. Currently, our research covers eddy viscosity one- and two-equation models, Reynolds-stress algebraic equation models, Reynolds-stress transport equation models, non-equilibrium multiple-scale models, bypass transition models, joint scalar probability density function models and Renormalization Group Theory and Direct Interaction Approximation methods. Some numerical simulations (LES and DNS) have also been carried out to support the development of turbulence modeling. Last year was CMOTT's third year in operation. During this period, in addition to the above mentioned research, CMOTT has also hosted the following programs: an eighteen-hour short course on "Turbulence — Fundamentals and Computational Modeling (Part I)" given by CMOTT at the NASA Lewis Research Center; a productive summer visitor research program that has generated many encouraging results; collaborative programs with industry customers (e.g. P. & W. and RocketDyne) to help improve their turbulent flow calculations for propulsion system designs; a biweekly CMOTT seminar series with speakers from within and without the NASA Lewis Research Center, including foreign speakers. In addition, CMOTT members have been actively involved in the national and international turbulence research activities.

The current CMOTT roster and organization are listed in Appendix A. Listed in Appendix B are the abstracts of the biweekly CMOTT seminars. Appendix C lists the papers contributed by CMOTT members.

Tsan-Hsing Shih

ORIGINAL PAGE  
BLACK AND WHITE PHOTOGRAPH



# Research Activities at the Center for Modeling of Turbulence and Transition

Tsan-Hsing Shih

1. Introduction
2. General developments
  - 2.1 Turbulent constitutive relations
  - 2.2 Mechanical and scalar dissipation equations
  - 2.3 Eddy viscosity transport equation
3. One-point closure schemes
  - 3.1 One-equation eddy viscosity transport equation model
  - 3.2 Galilean and tensorial invariant realizable  $k$ - $\epsilon$  model
  - 3.3 Reynolds stress algebraic equation model
  - 3.4 Scalar flux algebraic equation model
  - 3.5 Reynolds stress transport equation model
  - 3.6 Non-equilibrium multiple-scale model
  - 3.7 Bypass transition model
  - 3.8 Joint scalar PDF model
4. RNG and DIA
5. Numerical simulation

## Abstract

The main research activities at the Center for Modeling of Turbulence and Transition (CMOTT) are described. The research objective of CMOTT is to improve and/or develop turbulence and transition models for propulsion systems. The flows of interest in propulsion systems can be both compressible and incompressible, three dimensional, bounded by complex wall geometries, chemically reacting, and involve "bypass" transition. The most relevant turbulence and transition models for the above flows are one- and two-equation eddy viscosity models, Reynolds stress algebraic- and transport-equation models, pdf models, and multiple-scale models. All these models are classified as one-point closure schemes since only one-point (in time and space) turbulent correlations, such as second moments (Reynolds stresses and turbulent heat fluxes) and third moments ( $\overline{u_i u_j u_k}$ ,  $\overline{u_i \theta^2}$ ), are involved. In computational fluid dynamics, all turbulent quantities are one-point correlations. Therefore, the study of one-point turbulent closure schemes is the focus of our turbulence research. However, other research, such as the renormalization group theory, the direct interaction approximation method and numerical simulations are also pursued to support the development of turbulence modeling.

## 1. Introduction

The center for modeling of turbulence and transition was established as a special focus group within the Institute for Computational Mechanics in Propulsion at NASA Lewis Research Center in 1990. Its objective is to improve and/or develop turbulence and transition models for computational fluid dynamics (CFD) applied in propulsion systems. With the advance of computer technology and algorithms, accurate turbulence and transition modeling becomes the pacing item for improving flow calculations used in propulsion system design in all its key elements. The flows of interest in propulsion systems are, in general, very complex since there are wall-bounded three-dimensional complex geometries, chemical reactions, compressibility and transition, etc. In order to accurately predict these flows one must correctly model the turbulent stresses and scalar fluxes which are one-point (in time and space) turbulent correlations. For flows with finite rate chemical reactions, accurate modeling of the production rate of species is crucial for turbulent flow calculations. Based on the above considerations, turbulence modeling activities at CMOTT are focused on one-point closure schemes, that is, using the moment closure schemes for the turbulent velocity field and the joint scalar pdf method for the reacting scalar field.

There are various moment closure schemes which have been developed for various engineering applications. However, in practice, one often finds that the existing models need to be improved and/or re-developed in order to reasonably simulate complex flow structures appearing in propulsion systems. For this purpose, CMOTT devotes itself to improving and/or re-developing these moment closure schemes which include eddy viscosity (one- and two-equation) models, second moment algebraic- and transport-equation models, non-equilibrium multiple-scale models, and bypass transition models. In addition, other studies supporting the development of one-point closure schemes have been also carried out (for example, studies on renormalization group theory (RNG), direct interaction approximation (DIA), direct numerical simulation (DNS) and large eddy simulation (LES)).

In this report, we first describe the general development of turbulent constitutive relations, turbulent mechanical and thermal dissipation and a new eddy viscosity equation. Second, we describe the detailed developments on each moment closure scheme and the pdf method. Then the RNG and DIA methods and finally, the numerical simulation of particular turbulence phenomena, such as rotation and bypass transition, etc., are considered.

Each research subject is the joint project of several CMOTT researchers and visitors. In describing research activities, the names of involved researchers will be mentioned for reference.

## 2. General Developments

### 2.1 Turbulent Constitutive Relations

#### Reynolds stress

Using the invariant theory in continuum mechanics and Generalized Cayley-Hamilton formulas for tensor products, a turbulent constitutive relation (or a general turbulence model) for any turbulent correlations can be obtained, in principle. Therefore, this theory provides an avenue to develop better turbulence models than those existing. For example, a commonly used constitutive relation for Reynolds stresses  $\overline{u_i u_j}$  (in terms of the mean deformation rate tensor  $U_{i,j}$  and the turbulent velocity and length scales characterized by the turbulent kinetic energy  $k$  and its dissipation rate  $\varepsilon$ ) is

$$-\overline{u_i u_j} = C_\mu \frac{k^2}{\varepsilon} (U_{i,j} + U_{j,i}) - \frac{2}{3} k \delta_{ij} \quad (2.1.1)$$

The effective eddy viscosity  $\nu_T$  defined as

$$\nu_T = \frac{-\overline{u_i u_j}}{U_{i,j} + U_{j,i}} = C_\mu \frac{k^2}{\varepsilon} \quad \text{for } i \neq j \quad (2.1.2)$$

is isotropic since  $\nu_T$  is a scalar quantity. However, the invariant theory enables us to formulate the following general model (Shih and Lumley<sup>1</sup>, Johansson<sup>2</sup>):

$$\begin{aligned} \overline{u_i u_j} = & \frac{2}{3} k \delta_{ij} + 2a_2 \frac{K^2}{\varepsilon} (U_{i,j} + U_{j,i} - \frac{2}{3} U_{i,i} \delta_{ij}) \\ & + 2a_4 \frac{K^3}{\varepsilon^2} (U_{i,j}^2 + U_{j,i}^2 - \frac{2}{3} \Pi_1 \delta_{ij}) \\ & + 2a_6 \frac{K^3}{\varepsilon^2} (U_{i,k} U_{j,k} - \frac{1}{3} \Pi_2 \delta_{ij}) \\ & + 2a_7 \frac{K^3}{\varepsilon^2} (U_{k,i} U_{k,j} - \frac{1}{3} \Pi_2 \delta_{ij}) \\ & + 2a_8 \frac{K^4}{\varepsilon^3} (U_{i,k} U_{j,k}^2 + U_{i,k}^2 U_{j,k} - \frac{2}{3} \Pi_3 \delta_{ij}) \\ & + 2a_{10} \frac{K^4}{\varepsilon^3} (U_{k,i} U_{k,j}^2 + U_{k,j}^2 U_{k,i} - \frac{2}{3} \Pi_3 \delta_{ij}) \\ & + 2a_{12} \frac{K^5}{\varepsilon^4} (U_{i,k}^2 U_{j,k}^2 - \frac{1}{3} \Pi_4 \delta_{ij}) \\ & + 2a_{13} \frac{K^5}{\varepsilon^4} (U_{k,i}^2 U_{k,j}^2 - \frac{1}{3} \Pi_4 \delta_{ij}) \\ & + 2a_{14} \frac{K^5}{\varepsilon^4} (U_{i,k} U_{l,k} U_{l,j}^2 + U_{j,k} U_{l,k} U_{l,i}^2 - \frac{2}{3} \Pi_5 \delta_{ij}) \\ & + 2a_{16} \frac{K^6}{\varepsilon^5} (U_{i,k} U_{l,k}^2 U_{l,j}^2 + U_{j,k} U_{l,k}^2 U_{l,i}^2 - \frac{2}{3} \Pi_6 \delta_{ij}) \\ & + 2a_{18} \frac{K^7}{\varepsilon^6} (U_{i,k} U_{l,k} U_{l,m}^2 U_{j,m}^2 + U_{j,k} U_{l,k} U_{l,m}^2 U_{i,m}^2 - \frac{2}{3} \Pi_7 \delta_{ij}) \end{aligned} \quad (2.1.3)$$

where

$$\begin{aligned}\Pi_1 &= U_{i,k} U_{k,i}, & \Pi_2 &= U_{i,k} U_{i,k}, & \Pi_3 &= U_{i,k} U_{i,k}^2, & \Pi_4 &= U_{i,k}^2 U_{i,k}^2, \\ \Pi_5 &= U_{i,k} U_{l,k} U_{l,i}^2, & \Pi_6 &= U_{i,k} U_{l,k}^2 U_{l,i}^2, & \Pi_7 &= U_{i,k} U_{l,k} U_{l,m}^2 U_{i,m}^2\end{aligned}\quad (2.1.4)$$

From Eq.(2.1.3), the effective eddy viscosity

$$(\nu_T)_{ij} = \frac{-\overline{u_i u_j}}{U_{i,j} + U_{j,i}} \quad (2.1.5)$$

is no longer a scalar and, hence, is an anisotropic eddy viscosity. It is noticed that the first two terms on the right hand side of Eq.(2.1.3) represent the standard  $k$ - $\varepsilon$  eddy viscosity model (2.1.1) and that the first five terms of Eq.(2.1.3) are of the same form as the models derived from both the two-scale DIA approach (Yoshizawa<sup>3</sup>) and the RNG method (Rubinstein and Barton<sup>4</sup>).

Eq.(2.1.3) is a general model for  $\overline{u_i u_j}$ . It contains 11 undetermined coefficients which are, in general, scalar functions of various invariants of the tensors in question, such as  $S_{ij} S_{ij}$  (strain rate) and  $\Omega_{ij} \Omega_{ij}$  (rotation rate) which are  $(\Pi_2 + \Pi_1)/2$  and  $(\Pi_2 - \Pi_1)/2$  respectively. The detailed forms of these scalar functions must be determined by other model constraints, for example, realizability, and by experimental data. Eq.(2.1.3) contains 12 terms; however, its quadratic tensorial form may be sufficient for practical applications. We will see later in section 3.3 that the constitutive relation (2.1.3) has a significant impact on the development of Reynolds stress algebraic equation models.

### Turbulent scalar flux $\overline{\theta u_i}$

We assume the following functional form:

$$\overline{\theta u_i} = F_i(U_{i,j}, T_{i,j}, k, \varepsilon, \overline{\theta^2}, \varepsilon_\theta) \quad (2.1.6)$$

where  $\overline{\theta^2}$  is the variance of a fluctuating scalar and  $\varepsilon_\theta$  is its dissipation rate. Eq.(2.1.6) indicates that the scalar flux depends on not only the mean scalar gradient  $T_{i,j}$ , but also the mean velocity gradient  $U_{i,j}$  and the scales of both velocity and scalar fluctuations characterized by  $k$ ,  $\varepsilon$ ,  $\overline{\theta^2}$ ,  $\varepsilon_\theta$ .

Applying the invariant theory, we may obtain the following general constitutive

relation for  $\overline{\theta u_i}$ :

$$\begin{aligned}
\overline{\theta u_i} = & a_1 k \left( \frac{k}{\varepsilon} \frac{\overline{\theta^2}}{\varepsilon_\theta} \right)^{1/2} T_{,i} + \frac{k^2}{\varepsilon} \left( \frac{k}{\varepsilon} \frac{\overline{\theta^2}}{\varepsilon_\theta} \right)^{1/2} (a_2 U_{i,j} + a_3 U_{j,i}) T_{,j} \\
& + \frac{k^3}{\varepsilon^2} \left( \frac{k}{\varepsilon} \frac{\overline{\theta^2}}{\varepsilon_\theta} \right)^{1/2} (a_4 U_{i,k} U_{k,j} + a_5 U_{j,k} U_{k,i} + a_6 U_{i,k} U_{j,k} + a_7 U_{k,i} U_{k,j}) T_{,j} \\
& + \frac{k^4}{\varepsilon^3} \left( \frac{k}{\varepsilon} \frac{\overline{\theta^2}}{\varepsilon_\theta} \right)^{1/2} (a_8 U_{i,k} U_{j,k}^2 + a_9 U_{i,k}^2 U_{j,k} + a_{10} U_{k,i} U_{k,j}^2 + a_{11} U_{k,i}^2 U_{k,j}) T_{,j} \\
& + \frac{k^5}{\varepsilon^4} \left( \frac{k}{\varepsilon} \frac{\overline{\theta^2}}{\varepsilon_\theta} \right)^{1/2} (a_{12} U_{i,k}^2 U_{j,k}^2 + a_{13} U_{k,i}^2 U_{k,j}^2 \\
& \quad + a_{14} U_{i,k} U_{l,k} U_{l,j}^2 + a_{15} U_{j,k} U_{l,k} U_{l,i}^2) T_{,j} \\
& + \frac{k^6}{\varepsilon^5} \left( \frac{k}{\varepsilon} \frac{\overline{\theta^2}}{\varepsilon_\theta} \right)^{1/2} (a_{16} U_{i,k} U_{l,k}^2 U_{l,j}^2 + a_{17} U_{j,k} U_{l,k}^2 U_{l,i}^2) \\
& + \frac{k^7}{\varepsilon^6} \left( \frac{k}{\varepsilon} \frac{\overline{\theta^2}}{\varepsilon_\theta} \right)^{1/2} a_{18} U_{i,k} U_{l,k} U_{l,m}^2 U_{j,m}^2 T_{,j}
\end{aligned} \tag{2.1.7}$$

The coefficients  $a_1 - a_{18}$  are, in general, functions of the time scale ratio  $\frac{k}{\varepsilon} / \frac{\overline{\theta^2}}{\varepsilon_\theta}$  and the other invariants formed by the tensors in question, for example,  $T_{,k} T_{,k}$ ,  $T_{,i} U_{i,j} T_{,j}$ , etc.. Again, Eq.(2.1.7) implies that the effective eddy diffusivity

$$(\gamma_T)_i = \frac{-\overline{\theta u_i}}{T_{,i}}$$

is not isotropic. It is noticed that the first term on the right hand side of Eq.(2.1.7) is the standard eddy diffusion model, and the models derived from the two-scale DIA (Yoshizawa<sup>5</sup>) and the RNG method (Rubinstein and Barton<sup>6</sup>) are similar to the first two terms of Eq.(2.1.7). In practice, a form containing the first two terms on the right hand side of Eq.(2.1.7) may suffice. Further development of this model for turbulent heat transfer is described in Section 3.4.

The Researchers involved with the subject in this section are T.-H. Shih, J. Zhu, A. Shabbir, J.L. Lumley<sup>†</sup> and A. Johansson.<sup>‡</sup>

## 2.2 Mechanical and Scalar Dissipation Equation

### Mechanical dissipation $\varepsilon$

In turbulence modeling, we often need turbulent characteristic velocity and length scales. While the turbulent kinetic energy  $k$  is used to characterize the velocity scale, the mechanical dissipation rate  $\varepsilon$  and the scalar dissipation rate  $\varepsilon_\theta$  are used to characterize the length scales for mechanical and scalar fields, respectively. Comparing with the turbulent kinetic energy equation, the exact dissipation rate equation is

<sup>†</sup> Professor, Cornell University, Ithaca, NY

<sup>‡</sup> Professor, Royal Institute of Technology, Stockholm, Sweden

very complicated. In this equation, all the terms which represent important turbulence physics (for example, turbulent diffusion, generation and destruction) are unknown and are of complex forms that are all related to small scales of turbulence. Therefore, in the literature, the exact dissipation equation is not considered as a useful equation to work with. Instead, one creates a model equation by assuming an analogy to the turbulent kinetic energy equation, i.e., one assumes that the model dissipation rate equation also has generation and destruction terms which are assumed to be proportional respectively to the production and dissipation terms in the turbulent kinetic energy equation over the period of large eddy turn-over time characterized by  $k/\epsilon$ . The resulting model dissipation rate equation is written as

$$\begin{aligned} \epsilon_{,t} + U_i \epsilon_{,i} = & \nu \epsilon_{,ii} - (\overline{\epsilon u_i})_{,i} \\ & - C_{\epsilon 1} \frac{\epsilon}{k} \overline{u_i u_j} U_{i,j} - C_{\epsilon 2} \frac{\epsilon^2}{k} \end{aligned} \quad (2.2.1)$$

Recently, Lumley<sup>7</sup> proposed a dissipation rate equation based on the concept of spectral energy transfer caused by interactions between eddies of different sizes. This model equation mimics the physics of statistical energy transfer from large eddies to small eddies and is of a different form than equation (2.2.1).

In this study, we explore another rational way to obtain the model dissipation rate equation which contains certain important physics and hope it will work better than the existing one. The idea is that first, there is a relationship between the dissipation rate  $\epsilon$  and the mean-square vorticity fluctuation  $\overline{\omega_i \omega_i}$  at high Reynolds numbers or in homogeneous turbulence:

$$\epsilon = \nu \overline{\omega_i \omega_i}$$

and second, all the terms appearing in the  $\overline{\omega_i \omega_i}$  equation have more clear physical meanings than that in the  $\epsilon$  equation so that the  $\overline{\omega_i \omega_i}$  equation is easier to model. Once the  $\overline{\omega_i \omega_i}$  equation is modeled, a model dissipation rate equation will be readily obtained.

The exact equation for  $\overline{\omega_i \omega_i}$  is

$$\begin{aligned} \left( \frac{\overline{\omega_i \omega_i}}{2} \right)_{,t} + U_j \left( \frac{\overline{\omega_i \omega_i}}{2} \right)_{,j} = & \nu \left( \frac{\overline{\omega_i \omega_i}}{2} \right)_{,jj} - \frac{1}{2} (\overline{u_j \omega_i \omega_i})_{,j} + \overline{\omega_i u_{i,j}} \Omega_j \\ & - \overline{u_j \omega_i} \Omega_{i,j} + \overline{\omega_i \omega_j} U_{i,j} + \overline{\omega_i \omega_j u_{i,j}} - \nu \overline{\omega_{i,j} \omega_{i,j}} \end{aligned} \quad (2.2.2)$$

where  $u_i$  and  $U_i$  are the fluctuating and mean velocities, and  $\omega_i$  and  $\Omega_i$  are the fluctuating and mean vorticity which are defined by

$$\omega_i = \epsilon_{ijk} u_{k,j} \quad \Omega_i = \epsilon_{ijk} U_{k,j} \quad (2.2.3)$$

Tennekes and Lumley<sup>8</sup> clearly described the physical meaning of each term in equation (2.2.2). Order of magnitude analysis shows that the first, third, fourth and fifth terms on the right hand side of Eq.(2.2.2) become small compared with all other



terms in the equation as the turbulent Reynolds number increases. The sixth and seventh terms are the production due to fluctuating vortex stretching and the dissipation due to the viscosity of the fluid. As the turbulent Reynolds number increases these last two terms become dominant and the balance between them determines the evolution of vorticity fluctuations. Neglecting terms  $\overline{\omega_i u_{i,j}} \Omega_j$ ,  $-\overline{u_j \omega_i} \Omega_{i,j}$ ,  $\overline{\omega_i \omega_j} U_{i,j}$  and  $\nu(\frac{\overline{\omega_i \omega_i}}{2})_{,jj}$ , the evolution of  $\overline{\omega_i \omega_i}$  at large Reynolds number will be described by the following equation,

$$(\frac{\overline{\omega_i \omega_i}}{2})_{,t} + U_j (\frac{\overline{\omega_i \omega_i}}{2})_{,j} = -\frac{1}{2}(\overline{u_j \omega_i \omega_i})_{,j} + \overline{\omega_i \omega_j u_{i,j}} - \nu \overline{\omega_{i,j} \omega_{i,j}} \quad (2.2.4)$$

To model  $\overline{\omega_i \omega_j u_{i,j}} - \nu \overline{\omega_{i,j} \omega_{i,j}}$ , let us first estimate  $\overline{\omega_i \omega_j u_{i,j}}$ . we define an anisotropic tensor  $b_{ij}^\omega$ :

$$b_{ij}^\omega = \frac{\omega_i \omega_j}{\omega_k^2} - \frac{1}{3} \delta_{ij} \quad (2.2.5)$$

then  $\overline{\omega_i \omega_j u_{i,j}}$  can be written as

$$\overline{\omega_i \omega_j u_{i,j}} = \overline{b_{ij}^\omega \omega_k^2 u_{i,j}} \quad (2.2.6)$$

We expect that the vortex stretching tends to align vortex lines with the strain rate so that the anisotropy  $b_{ij}^\omega$  would be proportional to the strain rate  $s_{ij}$ , i. e.,

$$b_{ij}^\omega \propto \frac{s_{ij}}{s}, \quad \text{where } s = (2s_{ij}s_{ij})^{1/2}, \quad s_{ij} = (u_{i,j} + u_{j,i})/2 \quad (2.2.7)$$

This leads to the following model:

$$\overline{\omega_i \omega_j u_{i,j}} \propto \overline{\omega_k^2 (2s_{ij}s_{ij})^{1/2}} \propto \overline{\omega_k^2} \sqrt{2s_{ij}s_{ij}} \quad (2.2.8)$$

where we have assumed that  $\omega_k^2$  and  $(2s_{ij}s_{ij})^{1/2}$  are well correlated.

Using the relation,  $\omega_i = \epsilon_{ijk} u_{k,j}$ , it is not difficult to show that at large turbulent Reynolds number,

$$\overline{\omega_i \omega_i} \approx 2\overline{s_{ij}s_{ij}} \quad (2.2.9)$$

and Eq.(2.2.8) can be also written as

$$\overline{\omega_i \omega_j u_{i,j}} \propto \overline{\omega_k^2} \sqrt{\overline{\omega_i^2}} = \frac{\overline{\omega_k^2} \overline{\omega_i^2}}{\sqrt{\overline{\omega_i^2}}} \quad (2.2.10)$$

Equation (2.2.10) indicates that this term is of the order  $(u^3/l^3)R_t^{3/2}$  as it should be. On the other hand, from eq.(2.2.4) the term  $\overline{\omega_i \omega_j u_{i,j}} - \nu \overline{\omega_{i,j} \omega_{i,j}}$  must be of the order  $(u^3/l^3)R_t$  which is the order of magnitude of all the other terms in Eq.(2.2.4), therefore the term  $-\nu \overline{\omega_{i,j} \omega_{i,j}}$  must cancel the term (2.2.10) or (2.2.8) such that the difference of these two terms is smaller than the term (2.2.10) or (2.2.8) by an order

of  $R_t^{1/2}$ . This suggests that the combination  $\overline{\omega_i \omega_j u_{i,j}} - \nu \overline{\omega_{i,j} \omega_{i,j}}$  can be modeled by the following two terms:

$$\frac{\overline{\omega_k^2 \omega_i^2}}{\frac{k}{\nu} + \sqrt{\omega_i^2}}, \quad \overline{\omega_k^2} S \quad (2.2.11)$$

because the ratio of  $k/\nu$  to  $\sqrt{\omega_i^2}$  and the ratio of  $s$  to  $S$  are of order  $R_t^{1/2}$ , where  $k \approx u^2$  is the turbulent kinetic energy and  $S$  is the mean strain rate  $(2S_{ij}S_{ij})^{1/2}$ . Equation (2.2.11) does give the right order of magnitude for  $\overline{\omega_i \omega_j u_{i,j}} - \nu \overline{\omega_{i,j} \omega_{i,j}}$ . Therefore, the dynamical equation for fluctuating vorticity (2.2.4) at large Reynolds number can be modeled as

$$\left(\frac{\overline{\omega_i \omega_i}}{2}\right)_{,t} + U_j \left(\frac{\overline{\omega_i \omega_i}}{2}\right)_{,j} = -\frac{1}{2}(\overline{u_j \omega_i \omega_i})_{,j} + C_{\omega 1} \overline{\omega_k^2} S - C_{\omega 2} \frac{\overline{\omega_k^2 \omega_i^2}}{\frac{k}{\nu} + \sqrt{\omega_i^2}} \quad (2.2.12)$$

Using  $\varepsilon = \nu \overline{\omega_i \omega_i}$ , we readily obtain the following model dissipation rate equation,

$$\varepsilon_{,t} + U_j \varepsilon_{,j} = -(\overline{u_j \varepsilon})_{,j} + C_{\omega 1} S \varepsilon - C_{\omega 2} \frac{\varepsilon^2}{k + \sqrt{\nu \varepsilon}} \quad (2.2.13)$$

where  $C_{\omega 1}$  and  $C_{\omega 2}$  are the model coefficients which are expected to be constant at large Reynolds number.

It should be noticed that Eq.(2.2.13) is different from the standard  $\varepsilon$  equation (2.2.1) by both the generation and destruction terms. First, the Reynolds stresses do not appear in the generation term and the new form of the generation term is similar to that proposed by Lumley<sup>7</sup> which is based on the concept of spectral energy transfer. Second, the destruction term is well behaved so that equation (2.2.13) will not have a singularity anywhere in the flow field. We expect that equation (2.2.13) will be numerically much more robust than equation (2.2.1).

Equation (2.2.13) can be applied to any level of turbulence modeling including second order closure models; however the turbulent transport term  $(\overline{\varepsilon u_i})_{,i}$  needs to be modeled differently at different levels of turbulence modeling. In an eddy viscosity model, the term  $(\overline{\varepsilon u_i})_{,i}$  will be modeled as

$$(\overline{\varepsilon u_i})_{,i} = -\left(\frac{\nu_T}{\sigma_\varepsilon} \varepsilon_{,i}\right)_{,i} \quad (2.2.14)$$

The coefficients  $C_{\omega 1}$ ,  $C_{\omega 2}$ ,  $\sigma_\varepsilon$  and the eddy viscosity  $\nu_T$  must be calibrated using experimental data (Shih *et al.*<sup>9</sup>)

### Scalar dissipation $\varepsilon_\theta$

A similar analysis leads to the following model scalar dissipation rate equation:

$$\varepsilon_{\theta,t} + U_j \varepsilon_{\theta,j} = -(\overline{u_j \varepsilon'_\theta})_{,j} + C_{\theta 1} S \varepsilon_\theta + C_{\theta 2} Pr^{-1/2} \Phi \sqrt{\varepsilon \varepsilon_\theta} - C_{\theta 3} \frac{\varepsilon \varepsilon_\theta}{k + \sqrt{\nu \varepsilon}} \quad (2.2.15)$$

where  $\Phi = \sqrt{T_{,i} T_{,i}}$  and  $T$  is the mean scalar quantity, such as, the mean temperature. Further development of heat transfer model is described in Section 3.4.

The Researchers involved with the subject in this section are T.-H. Shih, W. Liou, A. Shabbir and Z. Yang.

### 2.3 Eddy Viscosity Transport Equation

In eddy viscosity models, one accepts the following simple constitutive relation

$$\overline{u_i u_j} = -2\nu_T S_{ij} + \frac{2}{3}k\delta_{ij} \quad (2.3.1)$$

and assumes that the eddy viscosity is characterized by some kind of velocity and length scales  $u'$  and  $\ell$ :

$$\nu_T \propto u' \ell \quad (2.3.2)$$

In two-equation  $k$ - $\varepsilon$  eddy viscosity models, for example, one specifies that

$$u' \propto k^{\frac{1}{2}}, \quad \ell \propto \frac{k^{\frac{3}{2}}}{\varepsilon} \quad (2.3.3)$$

and, hence, the eddy viscosity is assumed as

$$\nu_T = C_\mu \frac{k^2}{\varepsilon} \quad (2.3.4)$$

The eddy viscosity assumption (2.3.4) is commonly adopted in two-equation models. Eqs.(2.3.1) and (2.3.4) together with appropriate  $k$  and  $\varepsilon$  equations have been widely used in engineering calculations. However, for cases where the mean flow changes quickly or has a strong mean stream-line curvature or rotation, etc., this kind of model does not work very well, since the assumption (2.3.4) is too simple to account for the effect of the above mean flow structure on eddy viscosity.

The main purpose of this study is to drop the assumption (2.3.4) and to derive an exact equation for  $\nu_T$  based on Eq.(2.3.1) and other exact turbulence equations (i.e. first principles). In this way, we hope that some important turbulent physics can be brought into the eddy viscosity and that a physically sound turbulence eddy viscosity can be calculated.

Using Eq.(2.3.1), we may write for incompressible flows

$$\overline{u_i u_j} \overline{u_i u_j} = 2\nu_T^2 S^2 + \frac{4}{3}k^2, \quad \text{where } S^2 = 2S_{ij}S_{ij} \quad (2.3.5)$$

Differentiating both sides, we obtain

$$\frac{D}{Dt} \nu_T = -\frac{S_{ij}}{S^2} \frac{D}{Dt} \overline{u_i u_j} - \frac{\nu_T}{2S^2} \frac{D}{Dt} S^2 \quad (2.3.6)$$

The equation for  $\overline{u_i u_j}$  can be written as

$$\frac{D}{Dt} \overline{u_i u_j} = D_{ij} + P_{ij} + \Pi_{ij} - \varepsilon_{ij} + Co_{ij} \quad (2.3.7)$$

where

$$\begin{aligned}
 D_{ij} &= [\nu \overline{u_i u_j} - \overline{u_i u_j u_k}]_{,k} \\
 P_{ij} &= -\overline{u_i u_k} U_{j,k} - \overline{u_j u_k} U_{i,k} \\
 \Pi_{ij} &= -\frac{1}{\rho} \overline{p_{,i} u_j + p_{,j} u_i} \\
 \varepsilon_{ij} &= 2\nu \overline{u_{i,k} u_{j,k}} \\
 Co_{ij} &= -2\varepsilon_{imk} \Omega_m \overline{u_k u_j} - 2\varepsilon_{jmk} \Omega_m \overline{u_k u_i}
 \end{aligned}$$

Inserting Eq.(2.3.7) into Eq.(2.3.6), we obtain an exact transport equation for eddy viscosity

$$\frac{D}{Dt} \nu_T = -\frac{S_{ij}}{S^2} (D_{ij} + P_{ij} + \Pi_{ij} - \varepsilon_{ij} + Co_{ij}) - \frac{\nu_T}{2S^2} \frac{D}{Dt} S^2 \quad (2.3.8)$$

In this equation, all the important turbulence physics in the Reynolds stress equation, such as Reynolds stress diffusion term  $D_{ij}$ , production term  $P_{ij}$ , pressure-velocity gradient correlation term  $\Pi_{ij}$  and dissipation tensor  $\varepsilon_{ij}$ , are involved. Comparing with the standard eddy viscosity assumption (2.3.4), this exact eddy viscosity equation (2.3.8) contains very rich turbulence physics. This equation also implies that a second order closure model will naturally lead to a corresponding eddy viscosity model.

Now, as an example, we use Launder Reece and Rodi's<sup>10</sup> model and a gradient transport model for the triple velocity correlation ( $-\overline{u_i u_j u_k} = \frac{\nu_T}{\sigma} \overline{u_i u_{j,k}}$ ) to derive a model equation for  $\nu_T$ . The resulting equation is

$$\begin{aligned}
 \frac{D}{Dt} \nu_T &= [(\nu + \frac{\nu_T}{\sigma}) \nu_{T,k}]_{,k} + (\nu + \frac{3}{2} \frac{\nu_T}{\sigma}) \frac{\nu_{T,k} S_{,k}^2}{S^2} + (\nu + \frac{\nu_T}{\sigma}) \frac{2\nu_T S_{ij} S_{ij,kk}}{S^2} \\
 &+ \frac{4}{15} k - C_1 \frac{\varepsilon}{k} \nu_T + 2(C_2 - 2) \nu_T \frac{S_{ik} S_{kj} S_{ji}}{S^2} - \frac{\nu_T}{2S^2} \frac{D}{Dt} S^2
 \end{aligned} \quad (2.3.9)$$

Note that the Coriolis terms do not explicitly appear in this equation; however the rotation effect on  $\nu_T$  could be carried over through the mean flow field. In addition, we also note that there are no extra model coefficients introduced in Eq.(2.3.9). All model coefficients ( $\sigma$ ,  $C_1$  and  $C_2$ ) are brought in from the second order closure model. The values of these model coefficients may need adjustment in model applications. Note that Eq.(2.3.9) is not a self-consistent equation since the turbulent kinetic energy  $k$  and its dissipation rate  $\varepsilon$  are also involved. Eq.(2.3.9) together with  $k$ - $\varepsilon$  transport equations will provide a new three-equation model which may better represent the effect of mean flow structure as well as mean flow history on the eddy viscosity.

The Researchers involved with the subject in this section are T.-H. Shih, Z Yang, and W. Liou.

### 3. One-Point Closure Schemes

In this section, we describe the developments on each of the moment closure scheme and the pdf method which are of concern at CMOTT. The first two sections

3.1 and 3.2 describe the one- and two-equation isotropic eddy viscosity models. Sections 3.3 and 3.4 describe the new developments on Reynolds stress and scalar flux algebraic equation models. Section 3.5 assesses Reynolds stress transport equation models. Section 3.6 describes a multiple-scale model for non-equilibrium turbulence. Section 3.7 is about transition models. Finally, in Section 3.8 the pdf method for turbulent chemical reaction is described.

### 3.1 One-equation eddy viscosity model

Recently developed one-equation eddy viscosity models are either based on the assumption (Baldwin and Barth<sup>11</sup>):

$$\nu_T = C_\mu \frac{k^2}{\varepsilon} \quad (3.1.1)$$

or created according to computational experience (Spalart and Allmaras<sup>12</sup>). Both of them are successful in some flow calculations. This scheme is quite attractive in CFD because one only needs to solve one scalar  $\nu_T$  equation without bothering about other turbulence quantities. However, comparing with  $k$ - $\varepsilon$  two equation models, the above mentioned one-equation  $\nu_T$  models do not contain any more turbulent physics. In fact, Baldwin and Barth's model is, basically, a change of dependent variable based on Eq.(3.1.1) plus some extra approximations. Therefore, in principle, we should not expect any superior performance over two-equation models. However, if we do not use the assumption (3.1.1), there is the possibility to improve and extend the capability of one-equation eddy viscosity models.

The objective of this study at CMOTT is to derive a physically sound eddy viscosity equation which contains rich turbulent physics and accounts for various effects from mean flow structures.

Note that in Section 2.3 we have already derived an exact equation for the eddy viscosity (2.3.8) and also a model equation (2.3.9) which is based on the Reynolds stress transport equation model of Launder, Reece and Rodi (LRR). All turbulent physics contained in the Reynolds stress equation can be brought into the eddy viscosity equation. Therefore, in principle, the transport equation (2.3.9) should be better than existing one-equation models based on Eq.(3.1.1). However, Eq.(2.3.9) is not self-consistent because  $k$  and  $\varepsilon$  are also involved. To make Eq.(2.3.9) self-consistent, we must model  $k$  and  $k/\varepsilon$  in terms of  $\nu_T$  and  $S$ . In most shear flows, the energy-containing eddy turn-over time  $k/\varepsilon$  is of the same order as the mean flow time scale  $S^{-1}$ , so that  $\varepsilon/k \propto S$  is a reasonable model. In addition, a crude dimensional analysis gives  $k \propto \nu_T S$  and this is, of course, reasonable only for shear flows. After the above considerations, the resulting self-consistent one-equation model is:

$$\begin{aligned} \frac{D}{Dt} \nu_T = & \left[ \left( \nu + \frac{\nu_T}{\sigma} \right) (\nu_T)_{,k} \right]_{,k} - \frac{C_{\nu 0}}{\sigma} (\nu_T)_{,k} (\nu_T)_{,k} + C_{\nu 1} S \nu_T \\ & + 2(C_{\nu 2} - 2) \nu_T \frac{S_{ik} S_{kj} S_{ji}}{S^2} - \frac{\nu_T}{2S^2} \frac{D}{Dt} S^2 \end{aligned} \quad (3.1.2)$$

where the diffusion terms from the Reynolds stress equation (2.3.7) have been manipulated and approximated. Eq.(3.1.2) clearly exhibits the various effects of the mean flow on the eddy viscosity.

The model coefficients  $C_{\nu 1}$ ,  $C_{\nu 2}$  and  $\sigma$  can be determined by using the experimental data of homogeneous shear flows, free shear flows and boundary layer flows as well as the relations in the inertial sublayer. Extensive tests of this model in various flows are carrying out at the CMOTT.

The Researchers involved with the subject in this section are T.-H. Shih, W. Liou, Z. Yang and J. Zhu.

### 3.2 Galilean and tensorial invariant realizable $k$ - $\epsilon$ model

The two-equation  $k$ - $\epsilon$  eddy viscosity model is one of the most widely used turbulence models in engineering calculations. The  $k$ - $\epsilon$  model has versions for high Reynolds numbers and for low Reynolds numbers. For wall bounded turbulent flows, the high Reynolds number  $k$ - $\epsilon$  model (for example, Launder and Spalding<sup>13</sup>) must be applied together with a wall function as its boundary condition, while the low Reynolds number  $k$ - $\epsilon$  model (for example, Jones and Launder<sup>14</sup>) can be integrated to the wall. The high Reynolds number  $k$ - $\epsilon$  model of Launder and Spalding is considered as a standard  $k$ - $\epsilon$  model. We notice that even though the model dissipation rate equation is created by assuming an analogy with the turbulent kinetic energy, there was not much modification until Lumley<sup>7</sup> and Shih *et al.*<sup>9</sup> For near wall turbulence, in addition to Jones and Launder's model, there are many other versions of low Reynolds number  $k$ - $\epsilon$  models (such as Chien<sup>15</sup>, Shih and Lumley<sup>16</sup>, Yang and Shih<sup>17</sup>) which have made better performance over Jones and Launder's model.

There are, probably, four or five issues worth mentioning about existing low Reynolds number  $k$ - $\epsilon$  models: the model constants are not consistent with those in the high Reynolds number  $k$ - $\epsilon$  model; the wall correction terms and damping functions are related to the wall distance so that models are not tensorial invariant; a nonrealistic dissipation rate near the wall is introduced; they are not always realizable since normal stress could become negative; and finally, they do not work very well for boundary layer flows with various pressure gradients.

The objective of this study at CMOTT is to overcome the above mentioned problems. First, we propose a vorticity dynamics based dissipation rate equation as a part of high Reynolds number  $k$ - $\epsilon$  base model.<sup>9</sup> Second, based on the invariant theory, inhomogeneous terms for the dissipation rate equation are proposed which enable the model to better respond to the change of pressure gradients (Yang and Shih<sup>18</sup>). Third, the wall distance parameter is removed from the damping function so that the model is tensorially invariant (Yang and Shih<sup>19</sup>). The model constants are consistent with those in the high Reynolds number  $k$ - $\epsilon$  model. Finally, the non-negativity of normal Reynolds stresses, the realizability condition, is imposed.

The Researchers involved with the subject in this section are Z. Yang, T.-H. Shih and C. Steffen.

### 3.3 Reynolds stress algebraic equation model

All eddy viscosity models including one- and two-equation models are isotropic. For the flows where anisotropy is important, for example, the secondary flows driven by turbulent normal stresses in a square duct or curved duct, eddy viscosity models do not produce correct flow structures. To overcome this intrinsic deficiency of isotropic eddy viscosity models, one proposes a Reynolds stress algebraic equation model which will provide an effective anisotropic eddy viscosity. The first such a model was proposed by Rodi<sup>20</sup> and it achieved some success in the prediction of anisotropic related flow structure. However, Rodi's formulation is a set of algebraic non-linear system equations for Reynolds stresses and it often creates numerical difficulty in obtaining a converged solution. Recently, Taulbee<sup>21</sup> obtained an explicit algebraic expression for the Reynolds stress using Pope's<sup>22</sup> tensor expansion formulation and solved this numerical difficulty. However, in general, Rodi's formulation assumes that the ratio  $\overline{u_i u_j}/k$  is constant and, of course, this is not really true for most turbulent flows of interest. Therefore, sometimes, this Reynolds stress algebraic equation model produces even worse results than the isotropic eddy viscosity models for cases where eddy viscosity models are appropriate.

Alternative ways for obtaining effective anisotropic eddy viscosity models have been tried by a few researchers, for example, the DIA method by Yoshizawa<sup>3</sup>, the RNG method by Rubinstein and Barton<sup>4</sup> and invariant theory by Shih and Lumley.<sup>1</sup> It is interesting to point out that the RNG and DIA methods result in the same formulation and that this formulation is the first five terms of a general constitutive relation Eq.(2.1.3) except that the model coefficients are different.

One of our goals at CMOTT is to search for an effective anisotropic eddy viscosity model for complex turbulent flows where the nonequilibrium of turbulence is not very severe so that the constitutive relation (2.1.3) is more or less valid. We have explored the potential capability of Eq.(2.1.3) and found that a truncation of Eq.(2.1.3) up to the quadratic terms of the mean velocity gradients is sufficient for various flows of interest. The model coefficients are determined such that realizability for the normal stresses is ensured. The detailed analysis is described by Shih *et al.*<sup>23</sup>

The quadratic version of Eq.(2.1.3) together with the standard  $k$ - $\epsilon$  transport equations, successfully predicts many complex flows as well as simple flows which include backward-facing step flows; confined coflowing jets; confined swirling coaxial jets; flows in 180° curved duct; flows in a diffuser and a nozzle; boundary layer flows with pressure gradient and turbulent free shear flows. See references<sup>23-25</sup> for detailed results.

The Researchers involved with the subject in this section are J. Zhu and T.-H. Shih.

### 3.4 Scalar flux algebraic equation model

In parallel with Reynolds stress algebraic equation model, we have also tried to develop an effective anisotropic scalar eddy diffusivity model for scalar (heat) fluxes based on the new constitutive relation (2.1.7) and the new thermal dissipation rate

equation (2.2.16). We have determined that it seems sufficient to truncate Eq.(2.1.7) up to linear terms of the mean velocity gradient, i.e.,

$$\overline{\theta u_i} = a_1 k \left( \frac{k}{\varepsilon} \frac{\overline{\theta^2}}{\varepsilon_\theta} \right)^{1/2} T_{,i} + \frac{k^2}{\varepsilon} \left( \frac{k}{\varepsilon} \frac{\overline{\theta^2}}{\varepsilon_\theta} \right)^{1/2} (a_2 U_{i,j} + a_3 U_{j,i}) T_{,j} \quad (3.4.1)$$

This equation indicates that the heat flux and the mean temperature gradient are not necessarily in alignment due to the distortion of the flow field. This means that the effective scalar eddy diffusivity is anisotropic.

Eq.(3.4.1) together with the  $\overline{\theta^2}$  and  $\varepsilon_\theta$  equations will be a closed set of model equations for turbulent heat fluxes. The model coefficients are calibrated from homogeneous flows. Detailed analysis and a few model tests are described in this research briefs by A. Shabbir.

The Researchers involved with the subject in this section are A. Shabbir and T.-H. Shih.

### 3.5 Reynolds stress transport equation model

The Reynolds stress transport equation model is considered as a next generation of advanced turbulence modeling for engineering applications. In principle, the second moment equations describe various effects of the mean flow and external agencies on the evolution of turbulence, hence, are the most attractive way (also the simplest correct way) to study turbulent flows.

Various closure models for second moment equations have been developed. The success of these closures are marginal and vary with each flow. To identify the sources of their deficiencies, one often uses simple flows where the specific model term in the second moment equations can be isolated, hence, the corresponding model can be checked against experimental data or direct numerical simulation (DNS). For example, using pre-distorted anisotropic homogeneous relaxation flows, we may check the return-to-isotropy models with experimental data or DNS. However, for other flows, several model terms, such as, triple velocity correlations, rapid and slow pressure-strain correlations, etc., simultaneously exist and can not be isolated in the experiments. In these cases (for example, in a homogeneous shear flow or a channel flow) only DNS can provide all the information for simultaneously checking various models.

We have examined various existing closure models using experimental data as well as DNS data (Shih *et al.*<sup>26</sup> and Shih and Lumley<sup>27</sup>). Conclusive statements are difficult to draw at this time. However, the following remarks can be made about various closures for the second moment equations, i.e., the triple velocity correlation  $T_{ijk}$ , the rapid and slow pressure related correlations  $\Pi_{ij}^{rp}$ ,  $\Pi_{ij}^{sl}$ , and the dissipation rate tensor  $\varepsilon_{ij}$ :

a)  $T_{ijk}$ . All the existing models, such as Daly and Harlow<sup>28</sup>, LRR<sup>10</sup>, Lumley<sup>29</sup>, etc., are not very satisfactory for highly inhomogeneous flows, such as flow near the wall. However, for flows where the inhomogeneity is not very high, the above closure models become close to each other and also closer to the DNS data. In addition, the triple velocity correlations in these situations are usually small comparing with



other terms in the equation, so that modeling of this term is not as critical as other terms for the results of turbulent flow calculations, except for the flow near the wall. b)  $\Pi_{ij}^{rp}$ . It is very clear from all the available DNS data that nonlinear models, such as, Shih and Lumley<sup>30</sup> are much better than linear models, such as SSG<sup>31</sup>. It seems also that the following constitutive relation

$$\Pi_{ij}^{rp} = F(\overline{u_i u_j}, U_{i,j})$$

is quite appropriate, i.e., its dependence on turbulent Reynolds number and other parameters is quite weak and can be neglected. However, one deficiency of this form observed by Reynolds<sup>32</sup> is that it can not take the rotation effect into account.

c)  $\Pi_{ij}^{sl}$ . This term is usually modeled together with the dissipation tensor  $\epsilon_{ij}$  and the combination of the two is called the return-to-isotropy term. All existing models are unsatisfactory at the present time. They are far from "universal", i.e., their performance varies from flow to flow. It is noticed that some strange behavior of return-to-isotropy (for example, for some pre-distorted flow relaxation, turbulence evolves toward anisotropy before it returns to isotropy) occurs and cannot be possibly modeled with the following constitutive relation:

$$\Pi_{ij}^{sl} = F(\overline{u_i u_j}, k, \epsilon)$$

In addition, the behavior of return-to-isotropy was found to depend not only on the Reynolds stresses at the present time but also on their history according to DNS data (Lee<sup>33</sup>). It may be also necessary to include triple velocity correlations into the above constitutive relations from the definition of  $\Pi_{ij}^{sl}$ . The term  $\Pi_{ij}^{sl}$  seems highly dependent on the turbulent Reynolds number and slowly approaches to its asymptote as Reynolds number goes to infinity, so that, in general, one should not exclude its dependence on turbulent Reynolds number even for moderate Reynolds numbers. In addition,  $\Pi_{ij}^{sl}$  is also noticeably affected by the mean strain rate according to the DNS data<sup>34</sup>, so that, in general, the mean strain rate should be also considered in the constitutive relation. In short, much more research is needed for developing a better model of  $\Pi_{ij}^{sl}$ .

The Researchers involved with the subject in this section are T.-H. Shih and A. Shabbir.

### 3.6 Non-equilibrium multiple-scale model

To consider the effect of the nonequilibrium of energy spectrum on turbulent quantities, such as  $k$ ,  $\epsilon$  and  $\overline{u_i u_j}$ , etc., Hanjelic et al.<sup>35</sup> are the first to propose a partition in the turbulent energy spectrum. Because of the nonequilibrium, the rate that energy enters the low wave number region,  $\epsilon_p$ , does not equal to the energy transfer rate from low wave numbers to high wave numbers,  $\epsilon_t$ . Therefore it is reasonable to describe the evolution of the energy contained in low wave number region,  $k_p$ , and high wave number region  $k_t$ , separately. As a result, the time scale or the length scale defined by different energy transfer rates will be different and this multiple-scale concept reflects the nonequilibrium effect of turbulence.

We think that this concept would be more appropriate for compressible flows because the compressibility often creates nonequilibrium interactions between large and small eddies. We first modify Hanjelic et al.'s model, test it in various free shear flows and boundary layer flows and then extend it to compressible flows by consideration of the effects of compressibility on the equations for  $k_p$  and  $\epsilon_p$ . The proposed model is tested in both compressible free shear flows and boundary layer flows. For detailed analysis and flow calculations see the report by Duncan *et al.*<sup>36</sup> and Liou and Shih<sup>37</sup>.

The Researchers involved with the subject in this section are W. Liou, T.-H. Shih and B. Duncan.

### 3.7 Bypass transition model

The onset of turbulence transition in the propulsion system is often highly influenced by the free stream turbulence. This transition process does not go through the linear instability but is mainly controlled by nonlinear processes. Therefore, it is sometimes called "bypass" transition. Because of this highly nonlinear process of transition, turbulence models may be used to predict it. In fact, many two-equation models, for example,  $k$ - $\epsilon$  eddy viscosity models of Launder and Sharma<sup>38</sup>, Chien<sup>15</sup>, etc., do mimic bypass transition on a flat plate when the free stream has a certain amount of turbulent intensity. However, to obtain an accurate prediction of bypass transition, the study of the bypass transition process and physics is needed. The conventional turbulence models must be modified to take into account the intermittent phenomena of transitional flows.

We have proposed transition models based on a two-equation turbulence model using an intermittency factor to modify either the eddy viscosity or modeled  $k$ - $\epsilon$  equations. Successful results for a flat plate boundary layer under various free-stream turbulence intensities are obtained. For details see the report by Yang and Shih<sup>39</sup>.

The Researchers involved with the subject in this section are Z. Yang and T.-H. Shih.

### 3.8 Joint scalar PDF model

One of the critical problems in turbulent combustion is how to treat the interaction between the chemical reaction on the turbulence. The estimation of the production rate of compositions based on the mean flow temperature would be in a very large error for flows with finite rate chemical reactions. The reason is that the production rate of compositions depends not only on the mean values of temperature  $T$  and compositions  $C_i$ , but also very much depends on the detailed fluctuations of temperature  $\theta$  and compositions  $c_i$ . The moment closure scheme of modeling the production rate of compositions in terms of the mean flow temperature, the mean compositions and various correlations consisting of the fluctuating temperature and composition, such as  $\overline{\theta^2}$ ,  $\overline{\theta c_i}$ ,  $\overline{c_i c_j}$ , ..., has not been successful. However, the PDF method allows us to treat chemical reaction exactly without modeling (Pope<sup>40</sup>). Therefore, for the study of turbulent combustion problems, we use the joint scalar PDF transport equation for the scalar field and the moment closure schemes for

the velocity field and develop a hybrid solver consisting of a Monte Carlo scheme and a conventional CFD method. For detailed description of this procedure and its applications see Hsu<sup>41</sup> and Hsu *et al.*<sup>42</sup>

The Researchers involved with the subject in this section are A. Hsu, A.T. Norris and J.Y. Chen<sup>†</sup>

#### 4. RNG and DIA

In developing one point turbulence models, conventional modeling methods can be supplemented by “non-conventional” methods such as renormalization group theory (RNG) and the direct interaction approximation (DIA). These are two point theories formulated in wavevector or fourier space; one point models are derived by integration over wavevectors. This approach provides theoretical support for conventionally derived models and sometimes suggests theoretically derived forms for the empirical elements, whether constants or functions, which appear in these models.

We have applied RNG methods to both the eddy viscosity and Reynolds stress transport equation models. In addition to the  $k - \epsilon$  model proposed by Yakhot and Orszag<sup>43</sup>, it is possible to obtain constitutive relations for Reynolds stress and heat fluxes (Rubinstein and Barton<sup>4,6</sup> which are special cases of the general results Eqs.(2.1.3) and (2.1.7). By applying the perturbation theories of Yakhot and Orszag<sup>43</sup> to the relevant correlations, expansions in powers of the mean velocity gradient are obtained for the stresses and heat fluxes; quadratic truncation of the series leads to a stress model Eq.(2.1.3) with constant  $a_4, a_6, a_7$  and a heat flux model Eq.(2.1.7) with constant  $a_2, a_3$  in which the constants are in good agreement with empirically selected values. The forms derived are also consistent with the DIA analysis of Yoshizawa<sup>3,5</sup>.

The RNG method also provides a formulation for closing the Reynolds stress transport equation (Rubinstein and Barton<sup>44</sup>). Perturbative evaluation of the correlations  $\Pi_{ij}^{r,p}$  and  $\Pi_{ij}^{s,l}$  leads to series expansions in powers of the mean velocity gradient. These series can be consolidated, or “resumed” using the known perturbation series for the Reynolds stresses by methods analogous to Pade approximation. Systematic lowest order summation leads to a Reynolds stress transport equation with a form identical to the LRR model equation and with constants in reasonable agreement with empirically chosen values. Higher order resummation leading to nonlinear models of the type described in Sec. 3.5 remains an open possibility. The possibility of such resummation in the context of DIA has been discussed by Yoshizawa<sup>45,46</sup>.

Recent work has focussed on nonequilibrium time dependent relations between the Reynolds stress and the mean flow derived from a simplification of the DIA theory of shear turbulence. In this theory, shear turbulence is modeled by a non-Markovian eddy damping acting against the mean shear. The RNG and DIA Reynolds stress transport models and the LRR model all assume Markovian damping; as in the

<sup>†</sup> Professor, University of California, Berkeley, CA

molecular theory of transport coefficients, Markovian damping describes long time behavior and is incorrect at short times. The most important consequence of non-Markovian damping is a *strong suppression of eddy damping at short times*. This leads to closer agreement between the present theory and rapid distortion theory at short time. this is important in modeling oscillating shear flows: recent work of Mankbadi<sup>47</sup> shows that RDT based models best predict such flows. In transient homogeneous shear flow at high strain rates, the LRR model predicts rapid onset of eddy damping leading to excessive growth of turbulence kinetic energy at short times. The suppression of eddy damping at short times in the present model should lead to improved predictions for this flow as well.

Another consequence of this theory is a stress model Eq.(2.1.3) in which the coefficients  $a_2, \dots$  are functions of the mean strain rate. This theory can be described as RDT with a modified total strain determined by the response function of the DIA theory of isotropic turbulence. The introduction of a phenomenological modified total strain has often been advocated in the RDT literature to improve the agreement between RDT and shear flow data; here the modified total strain is deduced as a consequence of the theory. In the special but important case of simple shear flow in which  $\partial U_i / \partial x_j = S \delta_{i1} \delta_{j2}$ , the result can be formulated in terms of Eq.(2.1.3) in which, for example,  $a_2 = a_2(Sk/\varepsilon)$  and the function  $a_3$  is found exactly from RDT. There are analogous results for the coefficients  $a_4, a_6, a_7$ ; in simple shear flow, the remaining terms in Eq.(2.1.3) identically vanish. Extension of this theory to other mean shear tensors depends on the tabulation of the corresponding RDT solution.

The researchers involved with the subject in this section are R. Rubinstein and A. Yoshizawa.<sup>†</sup>

## 5. Numerical Simulation

To obtain a better understanding of the effect of compressibility and rotation on turbulence, numerical simulations of compressible homogeneous shear flows and rotational flows are carried out. The effects of compressibility and rotation on the energy spectrum and energy cascade between turbulent eddies has been analyzed (Hsu and Shih<sup>48</sup>). These simulations support the idea of the multiple-scale model for nonequilibrium compressible turbulent flows (W. Liou and Shih<sup>37</sup>).

Another numerical simulation is the transition subjected to the free stream large disturbances. The objective of this simulation is to obtain some insight into the transition physics and to provide data base for bypass transition modeling. Based on the assumption that the transition process is mainly controlled by large scale motions, we use a high accuracy finite difference Navier-Stokes solver with course grids to simulate the large scale motions of transition. A preliminary calculation of bypass transition was carried out. Various statistics of the calculated flow field are under examination.

The Researchers involved with the subject in this section are A. Hsu, C. Liou<sup>‡</sup>, Z. Yang, A. Shabbir, T.-H. Shih.

<sup>†</sup> Professor, Tokyo University, Japan

<sup>‡</sup> Professor, University of Colorado, Denver, CO

## References

- <sup>1</sup> Shih, T.-H. and Lumley, J., "Remarks on turbulent constitutive relations," NASA TM 106116 (1993).
- <sup>2</sup> Johansson, A., Private communication.
- <sup>3</sup> Yoshizawa, A., *Phys. Fluids*, **27**, 1377-1387 (1984).
- <sup>4</sup> Rubinstein R. and Barton, J. M., "Nonlinear Reynolds stress models and the renormalization group," *Phys. Fluids* **2**, 1472-1476 (1990).
- <sup>5</sup> A. Yoshizawa, *J. Fluid Mech.* **195**, 541 (1988).
- <sup>6</sup> Rubinstein, R. and Barton, J. M., "Renormalization group analysis of anisotropic diffusion in turbulent shear flows," *Phys. Fluids* **3**, 415-421 (1991).
- <sup>7</sup> Lumley, J. L., "Some comments on turbulence," *Phys. Fluids*, **4** (1992).
- <sup>8</sup> Tennekes, H. and Lumley, J. L., *A First Course in Turbulence* Massachusetts Institute of Technology, 1972.
- <sup>9</sup> Shih, T.-H., Liou, W. W., Shabbir, A., Yang, Z., and Zhu, J., "A vorticity dynamics based model for the turbulent dissipation," NASA TM 107177 (1993).
- <sup>10</sup> Launder, B.E., Reece, G.J., and Rodi, W. , " Progress in the development of a Reynolds-stress turbulence closure," *J. Fluid Mech.* **68**, 537-566 (1975).
- <sup>11</sup> Baldwin B. S. and Barth, J. T., "A one-equation turbulence transport model for high Reynolds number wall-bounded flows," NASA TM 102847 (1990).
- <sup>12</sup> Spalart, P. R. and Allmaras, S. R., "A one-equation turbulence model for aerodynamic flows," AIAA-92-0439 (1992).
- <sup>13</sup> Launder, B. E. and Spalding, D. B., "The numerical computation of turbulent flow," *Computer Methods in Applied Mechanics and Engineering* **3**, 269-289 (1974).
- <sup>14</sup> Jones, W. P. and Launder, B. E., "The calculation of low-Reynolds Number phenomena with a two-equation model of turbulence," *International Journal of Heat and Mass Transfer*, **16**, 1119-1130 (1973).
- <sup>15</sup> Chien, K.-Y., "Predictions of channel and boundary-layer flows with a low-Reynolds-number turbulence model," *AIAA Journal*, **20**, 33-38, (1982).
- <sup>16</sup> Shih, T.-H. and Lumley, J. L., "Kolmogorov behavior of near-wall turbulence and its application in turbulence modeling," NASA TM 105663 (1992).
- <sup>17</sup> Yang, Z. and Shih, T. -H., "A new time scale based  $k - \epsilon$  Model for Near Wall Turbulence," *AIAA J.* **31**, 1191-1198 (1993).
- <sup>18</sup> Yang, Z. and Shih, T. -H., NASA TM to appear.
- <sup>19</sup> Yang, Z. and Shih, T. -H., "A Galliean and tensorial invariant  $k - \epsilon$  model for near wall turbulence," AIAA 24th Fluid Dynamics Conference 93-3105, July 6-9 1993/Orlando, FL.

- <sup>20</sup> Rodi, W., "Turbulence models and their application in hydraulics — A state of the art review," Book Publication of the International Association for Hydraulics Research, Delft, Netherlands (1980).
- <sup>21</sup> Taulbee, D. B., "An improved algebraic Reynolds stress model and corresponding nonlinear stress model," *Phys. Fluids* **4**, 2555 (1992).
- <sup>22</sup> S.B. Pope, "A more general effective-viscosity hypothesis," *J. Fluid Mech.*, **72**, 331 (1975)
- <sup>23</sup> Shih, T.-H., Zhu, J., and Lumley, J. L., "A realizable Reynolds stress algebraic equation model," NASA TM 105993 (1992).
- <sup>24</sup> Zhu, J. and Shih, T.-H., "Computations of confined coflowing jets with three turbulence models," AIAA paper 93-3120 (1993).
- <sup>25</sup> Zhu, J. and Shih, T.-H., "A numerical study of confined turbulent jets," NASA TM 106197 (1993).
- <sup>26</sup> Shih, T.-H., Shabbir, A., and Lumley, J. L., "Advances in modeling the pressure correlation term in the second moment equations," NASA TM 104413 (1991).
- <sup>27</sup> Shih, T.-H. and Lumley, J.L., "Critical comparison of second order closures with direct numerical simulation of homogeneous turbulence," *AIAA J.*, **31**, 663-671 (1993)
- <sup>28</sup> Daly, B.J. and Harlow, F.H., "Transport equations of turbulence," *Phys. Fluid*, **13**, 2634 (1970).
- <sup>29</sup> Lumley, J.L., "Computational modeling of turbulent flows," *Adv. Appl. Mech.*, **18**, 123 (1978).
- <sup>30</sup> Shih, T.-H. and Lumley, J. L., "Second-order modeling of boundary-free turbulent shear flows," *AIAA Journal*, **30**, 1553-1561 (1992).
- <sup>31</sup> Speziale, C.G., Sarkar, S. and Gatski, T.B., "Modeling the pressure-strain correlation of turbulence: an invariant dynamical systems approach," *J. Fluid Mech.*, **227**, 245-272 (1991).
- <sup>32</sup> Reynolds, W. C., "Effect of rotation on homogeneous turbulence," Tenth Australian Fluid Mechanics Conference, December 11-15, 1989.
- <sup>33</sup> Lee, M.J. and Reynolds, W.C., "Numerical experiments on structure of homogeneous turbulence," Dept. Mech. Engng. Rep. TF-24, Stanford University: Stanford California (1985).
- <sup>34</sup> Hallback, M., "Development of Reynolds stress closures of homogeneous turbulence through physical and numerical experiments," Doctoral Thesis, Royal Institute of Technology, Stockholm, 1993.
- <sup>35</sup> Hanjalic, K., Launder, B.E. and Schiestel, R., "Multiple-time-scale concepts in turbulent transport equation," *Turbulent Shear Flow 2* (1980).
- <sup>36</sup> Duncan, B., Liou, W. W. and Shih, T.-H., "A multiple-scale turbulent model for incompressible flow," AIAA 93-0086 (1993).

- <sup>37</sup> Liou, W. W. and Shih, T. H., "A multiple-scale model for compressible turbulent flows," NASA TM 106072 (1993).
- <sup>38</sup> Launder, B. E. and Sharma, B. I., "Application of the energy-dissipation model of turbulence to the calculation of a flow near a spinning disk," *Letters in Heat and Mass Transfer*, **1**, 131-138 (1974).
- <sup>39</sup> Yang, Z. and Shih, T.-H., "A  $k-\epsilon$  model for turbulent and transitional boundary layer," *Near Wall Turbulent Flows*, Elsevier, 165-175 (1993).
- <sup>40</sup> S.B. Pope, "PDF methods for turbulent Reactive Flows," *Prog. Energy Combust. Sci.*, **11**, 119-192 (1985).
- <sup>41</sup> Hsu, A. T., "Study of hydrogen diffusion flames using pdf turbulence model," AIAA paper 91-1780 (1991).
- <sup>42</sup> Hsu, A. T., Tsai, Y. L. T., and Raju, M. S., "A PDF approach for compressible turbulent reacting flows," AIAA-93-0087 (1993).
- <sup>43</sup> V. Yakhot and S.A. Orszag, *J. Sci. Comput.* **1**, 3 (1986).
- <sup>44</sup> Rubinstein, R. and Barton, J. M., "Renormalization group analysis of the Reynolds stress transport equation," *Phys. Fluids*, **4**, 1759-1766 (1992).
- <sup>45</sup> Yoshizawa, A., "Derivation of a model Reynolds stress transport equation using the renormalization of the eddy-viscosity type representation," *Phys. Fluids*, **5**, 707-715 (1993).
- <sup>46</sup> Yoshizawa, A., "Bridging between eddy-viscosity type and second order models using a two-scale DIA," 9th Symposium Turbulent Shear Flows Kyoto Japan, 1993.
- <sup>47</sup> Mankbadi, R. R. and Liu, J. T. C., "Near-wall response in turbulent shear flows subjected to imposed unsteadiness," *J. Fluid Mech.*, **238**, 55-71 (1992).
- <sup>48</sup> Hsu, A. T. and Shih, T.-H., "Effect of the coriolis force on compressible turbulence," 9th Symposium on Turbulent Shear Flows, Kyoto, Japan, 1993.





# Eddy Viscosity Models for Turbulent and Transitional Flows

Z. Yang

## 1. Motivation and Objective

The purpose of this research is to develop eddy viscosity models for the complex flows of engineering interest. The models are required to be able to handle the complex flow situations and the model calculations are to be computationally robust.

## 2. Work Accomplished

In the past year, a number of projects have been conducted in the area of eddy viscosity modeling. In addition, the linear marginal stability of the trailing line vortex has been investigated. In the following, each project will be reported briefly.

### 2.1 A Galilean and Tensorial Invariant $k-\epsilon$ Model for Near Wall Turbulence

In turbulence modeling, the  $k-\epsilon$  model is the most widely used model in engineering calculations. The standard  $k-\epsilon$  model<sup>1,2</sup> was devised for high Reynolds number turbulent flows and is traditionally used in conjunction with wall functions when applied to wall bounded turbulent flows. However, universal wall functions do not exist in complex flows and it is thus necessary to develop a form of  $k-\epsilon$  model equations which can be integrated down to the wall.

Jones and Launder<sup>3</sup> were the first to propose a low Reynolds number  $k-\epsilon$  model for near wall turbulence, which was then followed by a number of similar  $k-\epsilon$  models. A critical evaluation of the pre-1985 models was made by Patel et al.<sup>4</sup>. More recently proposed models are found in Lang and Shih<sup>5</sup>. Three major deficiencies can be pointed out about existing  $k-\epsilon$  models. (Some of the models may have only one or two of the three deficiencies.) First, a near wall pseudo-dissipation rate was introduced to remove the singularity in the dissipation rate equation at the wall. The definition of the near wall pseudo-dissipation rate was quite arbitrary. Second, the model constants were different from those of the standard  $k-\epsilon$  model, making the near wall models less capable of handling flows containing both high Reynolds number turbulence and near wall turbulence, which is often the case for a real flow situation. Patel et al.<sup>4</sup> put as the first criterion the ability of the near wall models to be able to predict turbulent free shear flows. Third, the variable  $y^+$  was used in the damping function  $f_\mu$  of the eddy viscosity formula. Since the definition of  $y^+$  involves  $u_\tau$ , the friction velocity, any model containing  $y^+$  can not be used in flows with separation. In addition,  $y^+$  may not be well defined for flows with complex geometry.

In an earlier paper by the authors<sup>6</sup>, a time scale based  $k-\epsilon$  model for near wall turbulence was proposed. In this model,  $k^{1/2}$  was chosen as the turbulent

velocity scale. The time scale was bounded from below by the Kolmogorov time scale. When this time scale is used to reformulate the dissipation rate equation, there is no singularity at the wall and the introduction of a pseudo-dissipation rate is avoided. The model constants were exactly the same as those in the standard  $k - \epsilon$  model, which ensures the correct performance of the model far from the wall. The damping function was proposed as a function of  $R_y = \frac{k^{1/2}y}{\nu}$  instead of  $y^+$ . Thus, the model can be used for flows with separation and reattachment.

However, the  $R_y$  dependence in the damping function makes the model coordinate dependent. It also creates some ambiguity when the model is used for complex geometries, for example, a corner flow. A similar problem also exists in most  $k - \epsilon$  models. In the present study, this deficiency is overcome by introducing a new parameter  $R$  in the damping function. The parameter is defined as

$$R = \frac{k}{S\nu} \quad (1)$$

where  $S$  is the modulus of the strain rate tensor of the mean velocity field.

The parameter  $R$ , defined above, is expressed in terms of the local variables of the field and is thus coordinate independent. The physical meaning of  $R$  can be explained as follows,

$$R = \frac{k}{S\nu} = \frac{k^2}{\epsilon\nu} / \frac{Sk}{\epsilon}; \quad (2)$$

$R$  is then the ratio of two important physical parameters: the turbulent Reynolds number and the time scale ratio of the turbulence to the mean flow. The variation of  $R$  with the wall distance  $y^+$  for the case of turbulent channel flow at  $Re_\tau = 180$  is shown in figure 1. The gradual and monotonic increase of  $R$  with  $y^+$  in the near wall region makes  $R$  an ideal candidate for constructing the damping function.

In the present study, the form of the damping function is chosen as

$$f_\mu = [1 - \exp(-a_1 R - a_2 R^2 - a_3 R^3)]^{1/2} \quad (3)$$

where  $a_1 = 3 \times 10^{-4}$ ,  $a_2 = 6 \times 10^{-5}$ ,  $a_3 = 2 \times 10^{-6}$ . These constants are obtained by calibrating the model prediction for the turbulent channel flow at  $Re_\tau = 180$  against the direct numerical simulation data of Kim et al.<sup>7</sup>

By introducing the parameter  $R$ , the  $y$  dependence is removed. Now, the model is free from the three deficiencies mentioned above, and is Galilean and tensorial invariant. This allows the model to be used in more complicated flow situations, i.e., flows with separation. Since all the quantities in the proposed model are given in the local variables, the model is very suitable for a general purposed CFD code with unstructured grid.

Turbulent channel flows at different Reynolds numbers and turbulent boundary layers with zero pressure gradient, favorable pressure gradient, and adverse pressure gradient were calculated using the present model. The model calculations were compared with the available data from the experiments and direct numerical simulations. At low Reynolds number, the comparison between the direct numerical

simulation data and the present model is found to be excellent. At higher Reynolds numbers, the velocity profiles are well predicted in all cases. However, the predicted skin friction does not respond adequately with the pressure gradient. All the other existing  $k - \epsilon$  models suffer from the same deficiency, as pointed out by Wilcox<sup>8</sup>. The results of the calculations and the details of the model can be found in Yang and Shih<sup>9</sup>.

## 2.2 On the Wall Functions for Two-Equation Turbulence Models

Near the wall, the turbulence quantities (especially the dissipation rate) change rapidly. Very fine grids are needed to resolve such a rapid variation. This would lead to a substantial increase in the overall number of grid points. For example, for two dimensional boundary layer flows, more than half of the total grid points are located in the near wall region. In addition to the increase in the number of grid points, the fine grid spacing near the wall means that the grids will be severely stretched, leading to what is commonly known as the numerical stiffness problem associated with the dissipation rate equation.

The use of the wall functions which provide the boundary conditions at the log layer rather than at the wall obviates all the difficulties mentioned above. However, existing wall functions were proposed based on the behavior of the turbulent boundary layer over a flat plate at zero pressure gradient and it is known that they are not universally valid.

In the present study, the validity of the wall functions is investigated for the case of turbulent boundary layers with pressure gradient. We will show that the standard wall functions presented in Ref. 1 and Ref. 2 do not give an adequate response to the pressure gradient. A new set of wall functions are derived. Rather than using the properties of the turbulence quantities in the equilibrium turbulent boundary at zero pressure gradient, the new wall functions are asymptotic solutions of the governing equations (Reynolds averaged Navier-Stokes equations, the equation for the turbulent kinetic energy, and the definition of the eddy viscosity in the framework of two-equation turbulence models) as the log layer is approached.

The assumptions involved in deriving such a new set of wall functions are: 1) the advection term is negligible compared with the turbulent transport term in both the mean momentum equation and the equation for turbulent kinetic energy, 2) turbulent eddy viscosity is much larger than the molecular viscosity, 3) the mean velocity profile follows the law of wall.

These assumptions are all met in the log layer in a high Reynolds number turbulent boundary layer with pressure gradient as long as the boundary layer remains attached. The direct numerical simulation data of Spalart<sup>10</sup> shows that the advection term is at least two orders of magnitude smaller than the turbulent transport term in the log layer. For high Reynolds number turbulent flows, the eddy viscosity is also much larger than the molecular viscosity in the log layer. Coles<sup>11</sup> found that the law of wall expression for the mean velocity remains valid for turbulent boundary layers with different pressure gradients.

Under these conditions, the new wall functions are

$$U = U_\tau \left[ \frac{1}{\kappa} \ln y^+ + C \right], \quad (4)$$

$$k = \frac{1}{C_\mu^{1/2}} \left[ \frac{1}{\rho} \frac{dP}{dx} y + U_\tau^2 \right], \quad (5)$$

$$\epsilon = \frac{U_\tau}{\kappa y} \left[ \frac{1}{\rho} \frac{dP}{dx} y + U_\tau^2 \right], \quad (6)$$

where  $\kappa = 0.41$  is the von Karman constant,  $C = 5.0$ , and  $C_\mu = 0.09$ . A body fitted coordinate system has been used in the above equations with  $x$  in the streamwise direction and  $y$  in the direction normal to the wall. It is worth noting that when the pressure gradient term is dropped, the new wall functions recover to the standard wall functions.

The performances of both the standard wall functions and the new wall functions were tested for the turbulent boundary layers with different pressure gradients. It is known that the  $k - \omega$  model of Wilcox<sup>12</sup> integrated down to the wall gives good skin friction coefficient predictions for turbulent boundary layers with different pressure gradients. The comparison of the results from the  $k - \omega$  model integrated to the wall and the results from the  $k - \omega$  model using the wall functions would then pin down the effect of the wall functions.

The results for the flat plate boundary layer at zero pressure gradient is shown in figure 2. (In this case, the new wall functions reduce to the standard wall functions.) It is seen that the results from the  $k - \omega$  model integrated to the wall and the results from the  $k - \omega$  model with wall functions are equally accurate when compared with the experiment data of Wieghardt and Willmann<sup>13</sup>. Thus, for the zero pressure gradient boundary layer, the standard wall functions give good results. However, the situation is quite different when the pressure gradient is not zero. Figure 3 shows the distribution of the skin friction coefficient for Herring and Norbury flow<sup>14</sup> which is a turbulent boundary layer under a favorable pressure gradient. Figure 4 shows the skin friction distribution for Samuel and Joubert flow<sup>15</sup> in which the turbulent boundary layer develops under an increasingly adverse pressure gradient. The standard wall functions fail to respond adequately to the pressure gradient, causing the predicted skin friction to be lower than the experiment in the favorable pressure gradient case and higher in the adverse pressure gradient case. In comparison, the new wall functions give results that are of the same order of accuracy as the  $k - \omega$  model integrated down to the wall. Thus, the capacity of the new wall functions to capture the effect of the pressure gradient is established.

The wall functions were then used in conjunction with the standard  $k - \epsilon$  model for Herring and Norbury flow and for Samuel and Joubert flow. It is known that the standard  $k - \epsilon$  model with the standard wall functions poorly predicts the effect of the pressure gradient. The comparison of the results from the standard  $k - \epsilon$  model with the standard wall functions and the results from the standard  $k - \epsilon$  model with the new wall functions, and the comparison of the model predictions with the

experiment would tell us whether the poor performance comes from the standard  $k - \epsilon$  model, or the wall function used, or both. The model calculations are shown in figure 5 and figure 6, respectively. The use of the new wall functions improves substantially the model prediction for both the favorable pressure gradient case and the adverse pressure gradient case. However, the errors are still quite pronounced. This indicates that the standard  $k - \epsilon$  model needs improvement in order to fully capture the effect of the pressure gradient. This is the topic of the following two projects.

The derivation of the wall functions and more extensive calculations using the wall functions can be found in Yang and Shih<sup>16</sup>.

### 2.3 A Vorticity Dynamics Based Model for the Dissipation Rate Equation

A new dissipation rate equation is proposed based on the dynamic equation for the vorticity fluctuation. This newly proposed model equation has the advantage over the standard  $\epsilon$  equation in that it is based on the first principle rather than an equation made-up in analogy with the equation for the turbulent kinetic energy. Since the production of the dissipation rate in the new equation is always positive, the model is expected to be more robust for complex flow calculations when used in conjunction with Reynolds stress models. When used in conjunction with the  $k$  equation, the overall performance is found to be better than that of the standard  $k - \epsilon$  equation. The model is given by Shih in this year's Research Brief. The details of model development and model performance can be found in Shih et al.<sup>17</sup>.

### 2.4 Flow Inhomogeneity and the Dissipation Rate Equation

The dissipation rate equation is the weakest link in both the  $k - \epsilon$  and the second order closure models. The standard  $\epsilon$  equation was made up in analogy with the equation for turbulent kinetic energy. Recently, Shih et al.<sup>17</sup> proposed a model equation for the dissipation rate based on the dynamic equation for the fluctuating vorticity. Both the standard  $\epsilon$  equation and the model equation of Shih et al. are homogeneous models in the sense that except for the transport term, the model form remains the same for both homogeneous flow and inhomogeneous flow. Since the dissipation rate represents the energy flux from the large eddies to the small eddies in the eddy cascade, and the energy containing large eddies are sensitive to the inhomogeneity, it can be expected that the flow inhomogeneity should enter the modeled dissipation rate equation.

The exact dissipation rate equation is

$$\begin{aligned} \epsilon_{,t} + U_j \epsilon_{,j} = & \nu \epsilon_{,jj} - \nu \langle u_{i,k} u_{i,k} u_{j,j} \rangle_{,j} - \frac{2\nu}{\rho} \langle p_{,k} u_{j,k} \rangle_{,j} \\ & - 2\nu (\langle u_{i,k} u_{j,k} \rangle + \langle u_{k,i} u_{k,j} \rangle) U_{i,j} - 2\nu \langle u_j u_{i,k} \rangle U_{i,kj} \\ & - 2\nu \langle u_{i,k} u_{j,k} u_{i,j} \rangle - 2\nu^2 \langle u_{i,kj} u_{i,kj} \rangle \end{aligned} \quad (7)$$

where  $u_i$ ,  $p$  represent the fluctuation field and  $U_i$  represents the mean field. It is seen that in addition to the transport terms, the flow inhomogeneity also contributes to the production and destruction in equation (7). However, the exact dissipation

rate equation is very complex, containing many new unknown terms, and is very difficult to model directly. Here, we use the invariant theory approach instead. The invariant theory is a powerful tool to find out the possible functional form once the independent physical variables are known. It has been widely used in continuum mechanics. It was also used for turbulent flows by Lumley<sup>18</sup>, Pope<sup>19</sup>, Shih and Lumley<sup>20</sup> to find the general constitutive relations for turbulent flows.

In the present analysis, we assume that the inhomogeneity will produce another term in the production/destruction of the modeled dissipation rate equation, which now reads

$$\frac{D\epsilon}{Dt} = \frac{\partial}{\partial x_i} \left[ \left( \nu + \frac{\nu_T}{\sigma_\epsilon} \right) \frac{\partial \epsilon}{\partial x_i} \right] + C_{1\epsilon} S \epsilon - C_{2\epsilon} \frac{\epsilon^2}{k} + \Phi_I \quad (8)$$

where the last term  $\Phi_I$  represents the contribution of the inhomogeneity. In the above equation, the inhomogeneity contribution was added to the homogeneous model of Shih et al.<sup>17</sup>.

We use  $\nabla S$  to measure the inhomogeneity of the mean field, where  $S$  is the size of the strain tensor of the mean field, and  $\nabla k$  and  $\nabla \epsilon$  to measure the inhomogeneity of the turbulent field. The general form for the contribution of the inhomogeneity to the production/destruction of the dissipation rate is

$$\Phi_I = \Phi_I(\nabla k, \nabla \epsilon, \nabla S; k, \epsilon, S). \quad (9)$$

The homogeneous quantities ( $k$ ,  $\epsilon$ , and  $S$ ) enter parametrically. Since equation (9) represents the contribution of the inhomogeneity effect, it would be zero if all the gradient quantities are zero.

We are studying the situations when the inhomogeneity is relatively weak and could be viewed as a perturbation about the homogeneous state. The three gradient quantities are then related and only two of them are needed to specify the inhomogeneity. In the present study, we choose  $\nabla k$  and  $\nabla S$ . Since  $\Phi_I$  is a scalar whereas  $\nabla k$  and  $\nabla S$  are vectors, we need to form scalar quantities out of the vectors. Further, the scalar parameters should be grouped in such a way that they would have the same dimension as other production/destruction terms in the dissipation rate equation. There are three parameter groups altogether and the general form for the inhomogeneity term is

$$\Phi_I = \Phi_I(\nabla k \cdot \nabla k, \nu_t \nabla S \cdot \nabla k, \nu_t^2 \nabla S \cdot \nabla S) \quad (10)$$

where  $\nu_t$  is the eddy viscosity used in the  $k - \epsilon$  equation and is given by

$$\nu_t = C_\mu \frac{k^2}{\epsilon}.$$

Since we are considering flows with relatively weak inhomogeneity, we can carry a Taylor series expansion for equation (10). To the leading order, the result is

$$\Phi_I = a_1 \nabla k \cdot \nabla k + a_2 \nu_t \nabla S \cdot \nabla k + a_3 \nu_t^2 \nabla S \cdot \nabla S \quad (11)$$

where  $a_1$ ,  $a_2$ , and  $a_3$  are the coefficients from the expansion. In general, they are functions of  $\eta = Sk/\epsilon$ , which is the only invariant that can be formed from the homogeneous quantities. In the present study, they are taken as constants.

With the inhomogeneity term given by equation (11), we have a model for the dissipation rate equation which takes into account the effect of the flow inhomogeneity. The model constants  $C_{1\epsilon}$  and  $C_{2\epsilon}$  are taken the same as in Shih et al.<sup>17</sup>, i.e.,  $C_{1\epsilon} = 0.42$  and  $C_{2\epsilon} = 1.90$ . The model constants in the inhomogeneity terms are taken as  $a_1 = 0.1$ ,  $a_2 = -0.65$ , and  $a_3 = 0.1$ . The value of  $\sigma_\epsilon$  is changed from 1.21 in Ref. 17 to 1.4 in the present model. In the homogeneous model, the turbulent diffusion is the only term that accounts for the effect of the inhomogeneity. Thus, it must account for both the transport and the production due to the inhomogeneity. In the present model, since the contribution of the inhomogeneity to the production of the dissipation rate is accounted for explicitly, it is expected that the value of  $\sigma_\epsilon$  be changed.

The model was then tested for turbulent boundary layer flows. Figures 7-9 show the predicted skin friction distributions for turbulent boundary layers with zero pressure gradient (Wieghardt and Willmann flow), favorable pressure gradient (Herring and Norbury flow), and adverse pressure gradient (Samuel and Joubert flow), respectively. The model predictions are in good agreement with the experiment in all cases. More details of the model development and more validating calculations are presented in a paper by Yang and Shih<sup>21</sup>.

In the works presented above, the inhomogeneity contribution was added to the homogeneous model of Shih et al.<sup>17</sup>. It should be mentioned that the same inhomogeneity contribution was also added to the standard  $\epsilon$  equation and results were found to be good too.

## 2.5 A Transport Equation for Eddy Viscosity

Algebraic turbulence models<sup>22,23</sup> have been used extensively in calculations of aerodynamic flows. These algebraic models are easy to implement numerically and give fairly accurate predictions for simple flows, such as that over an airfoil with an attached boundary layer; however, they are inadequate when used for more complex flows, such as that over an airfoil with separation. The failings of simple algebraic models have motivated recent research into dynamical equations for eddy viscosity.

The idea of formulating an eddy viscosity transport model, first suggested by Nee and Kovasznay<sup>24</sup>, was recently revived by Baldwin and Barth<sup>25</sup>, and Spalart and Allmaras<sup>26</sup>. Another motivation of working on the eddy viscosity transport model rather than higher level models, the  $k - \epsilon$  model for example, is the observation that near the wall the dissipation rate changes rapidly and the  $k - \epsilon$  model is numerically stiff; while the eddy viscosity varies much more gradually and it is expected that an equation for the eddy viscosity would be numerically better behaved.

In the models by Baldwin and Barth, and Spalart and Allmaras, wall effects were introduced using damping functions, in which the distance to the wall  $y$  enters as a parameter. This wall distance  $y$  is not a local property; its definition would be ambiguous for flows in complex geometry, i.e., corner flows. Also, the damping functions are assumed to be universal, which does not seem valid in flows with

strong adverse pressure gradients and separation.

In the present work, we propose a new transport model for the eddy viscosity. Far away from the wall, the model is based on the quasi-homogeneous approximation; near the solid surface, the wall effect is introduced via an elliptic relaxation equation first proposed by Durbin<sup>27</sup> in the context of the second order closure. This would completely eliminate the damping functions. In addition, the present model is formulated solely in terms of local variables and it is Galilean and tensorial invariant.

The model consists of a parabolic transport equation for the eddy viscosity:

$$\frac{D}{DT}\nu_T = \nabla(\nu + \nu_T)\nabla\nu_T + P_\nu - c_2|S|\nu_T - c_4\frac{\nu_T^2}{L_\nu^2} \quad (12)$$

where the production term  $P_\nu$  is subject to the following elliptic relaxation:

$$L_p^2\nabla^2 P_\nu - P_\nu = c_3|\nabla\nu_T|^2 - |S|\nu_T. \quad (13)$$

In these equations, the  $c$ 's are model constants, the  $L$ 's are length scales, and  $S$  is the size of the strain tensor of the mean field, which is used to characterize the gradients of the mean flow.

The length scales are given as

$$L_\nu^2 = \left(\frac{S}{|\nabla S|}\right)^2 + \left(\frac{|\nabla\nu_t|}{S}\right)^2 \quad (14)$$

$$L_p^2 = \min\left[L_\nu^2, c_p^2 \max\left(\frac{\nu_t}{S}, c_l^2 \frac{\nu}{S}\right)\right]. \quad (15)$$

The model constants used are

$$c_2 = 0.85, \quad c_4 = 0.2, \quad c_l = 3.2, \quad c_p = 1.21 \quad c_m = 2,$$

with  $c_3$  determined by

$$c_3 = \frac{1 - c_2}{\kappa^2} + 1 - \frac{c_4}{1 + \kappa^4 c_m} \quad (16)$$

which is obtained by using the log layer relation of the flat plate boundary layer at zero pressure gradient. These model constants were determined on the basis of a few points of reference: DNS of plane channel flow<sup>28</sup> give centerline velocities of  $U/U_\tau = 18.08$  at  $Re_\tau = 180$  and  $U/U_\tau = 19.96$  at  $Re_\tau = 395$ ; experiments<sup>29</sup> on zero pressure-gradient boundary layers give  $C_f = 3 \times 10^{-3}$  at  $Re_\theta = 5,000$ ; the spreading rate of a two-stream mixing layer based on  $\delta = y(0.95) - y(0.05)$  is<sup>30</sup>  $(1 + R)/2(1 - R)d\delta/dx = 0.1$  where  $R$  is the velocity ratio. These are points of reference in the sense that they were targets in the selection of model constants; they were met to varying degrees of accuracy.

A primary motivation for the present work is the current interest in turbulent transport models for computation of complex aerodynamic flows. To test the performance of the present model for aerodynamic flows, a *NACA 4412* airfoil at  $13.87^\circ$



angle of attack is simulated using the present model. This is the flow studied experimentally by Coles and Wadcock<sup>31</sup>. The experiment provides mean flow profiles at  $x/c = 0.62, 0.675, 0.731, 0.786, 0.842, 0.897$  and  $0.953$  on the upper surface of the airfoil. Figure 10 shows these data along with the model calculations.  $x/c$  increases from left to right in the sequence of profiles. The model shows a premature separation (experimentally it is near to 85% chord; the model has it at 71% chord). However, the experimental separation bubble grows quickly and by  $x/c = 0.89$  the experiment and the model show the same vertical extent of the separation bubble. The velocity profiles in figure 10 are in very much better agreement with data than those obtained by Rogers et al.<sup>32</sup> using the Baldwin-Lomax and Baldwin-Barth models. The predicted pressure coefficient on the airfoil is shown in figure 11 along with the experimental data.

In addition to this airfoil calculation, many flows of boundary layer type have been calculated using the present model. The results of these calculations and the details of the model development can be found in Durbin and Yang<sup>33</sup>, and Durbin, Mansour, and Yang<sup>34</sup>.

## 2.6 Modeling of Bypass Transition

In a quiescent environment, transition is preceded by the amplification of linear instability waves. These waves eventually break down, giving rise to turbulent spots, which can be viewed as the onset of transition. In an environment with high freestream turbulence, say the flow passing over a turbine blade, turbulent spots are formed due to the transport of turbulence from the freestream to the boundary layer rather than the amplification of the linear instability waves. This type of transition is called bypass transition. Accurate prediction of bypass transitional boundary layers is very important for internal fluid mechanics because a significant proportion of the turbine blade is in the transitional boundary layer region. Furthermore, the performance and the life span of a turbine are directly related to the peak values of the momentum and heat transfers both of which occur in the transitional boundary layer region.

Priddin<sup>35</sup> was the first to notice that the low Reynolds number two equation models have the potential to predict transitional flows under the influence of the freestream turbulence. This is probably due to the fact that the generation of turbulent spots in a boundary layer is a random process and the flow is almost fully developed turbulent within a turbulent spot. A detailed calculation procedure was given by Rodi and Scheuerer<sup>36</sup>, in which the Lam & Bremhorst low Reynolds number  $k - \epsilon$  model was used. More recently, a comparative study of the performance of existing low Reynolds number  $k - \epsilon$  models in predicting laminar-turbulent transition was made by Fujisawa<sup>37</sup>.

While the low Reynolds number  $k - \epsilon$  models could mimic transition, the quantitative predictions do not compare very well with the experimental data. This is due to the fact that all these low Reynolds number  $k - \epsilon$  models were originally proposed for fully developed turbulent flows and did not take into consideration the distinct feature of a transitional boundary layer — intermittency. The intermittency of a transitional boundary layer is measured by the intermittency factor which can be

viewed as the percentage time a transitional boundary layer is in the turbulent state due to the passing of turbulent spots.

We have proposed two eddy viscosity models for the calculation of transitional boundary layers, which take the effect of intermittency into consideration. Both models are based on a  $k - \epsilon$  model for near wall turbulence proposed by Yang and Shih<sup>6</sup>. In the first model, the effect of the intermittency is introduced in the eddy viscosity. In the second model, the effect of the intermittency is introduced in all the terms which are generated due to the turbulence. The modifications to the existing  $k - \epsilon$  appear in the introduction of the weighting factor in the eddy viscosity (in the first model) or in all the turbulent terms (in the second model). In order to close the above equations, an expression for the weighting factor is needed. We assume the weighting factor is related to both the freestream turbulent level and the intermittency factor of the boundary layer. The intermittency factor is assumed to be determined by the local state of the boundary layer. Further, the shape factor is used to characterize the local state of the boundary layer since both the intermittency factor and the shape factor change monotonically from the laminar boundary layer to the turbulent boundary layer. The details of the model form can be found in Yang and Shih<sup>38</sup>, and Yang and Shih<sup>39</sup>.

One of the issues in the calculation of transitional boundary layers using  $k - \epsilon$  models is the prescription of the initial profiles for the turbulent kinetic energy and its dissipation rate, the latter of which could not be found from the experiment directly. An expression for the initial profiles were given in Rodi and Scheuerer<sup>36</sup>. However, computations by Yang and Shih<sup>40</sup> which tested the effect of the initial conditions on the transition prediction found that the predicted onset of the transition is sensitive to the initial profiles. A similar conclusion was also reached by Patankar and Schmit<sup>41</sup>. This sensitivity of the results to the initial conditions suggests that the only place where the initial conditions could be specified unambiguously is at the leading edge. At the leading edge, the turbulent kinetic energy and its dissipation rate take constant profiles, the values of which are determined by the law for the decaying turbulence.

Flat plate boundary layers with free stream turbulence levels of 3% (Case T3A) and 6% (Case T3B) respectively were calculated using the present model. These are the benchmark cases in an ongoing project coordinated by Savill<sup>42</sup>, testing the capability of turbulence models in predicting transitional flows. The variations of skin friction coefficient  $c_f$  against  $Re_x$  in these two cases are shown in figure 12 and figure 13, respectively. Results from the experiment are shown for comparison. In addition, the prediction of the Launder-Sharma model is also shown in the figure because it was reported that among the lower Reynolds number  $k - \epsilon$  models, the Launder-Sharma model performs best for transitional boundary layers. It is clear that the present model gives a better prediction than the Launder-Sharma model. Other features in the transitional boundary layers and the calculations of the transitional boundary layers with other levels of freestream turbulence can be found in Ref. 39

## 2.7 Linear Marginal Stability of a Trailing Line Vortex

The stability of the trailing line vortex (Batchelor vortex) has attracted many researchers in the past thirty years. There are three reasons for such an interest. First, the trailing line vortex flow is of great practical importance. Second, the Batchelor vortex provides an archetype for swirling flows. Swirling flows are commonly found in nature and technology and their stability characteristics are of great interest. Third, the Batchelor vortex is also used as a model of a columnar vortex prior to its breakdown. Thus, it is hoped that the stability analysis of the Batchelor vortex would shed some light on the phenomenon of vortex breakdown, which plays an important role in a number of engineering flows.

The trailing line vortex is characterized by two parameters, the Reynolds number  $Re$  and the swirling parameter  $q$ . In the linear stability analysis, the perturbations are written in the normal mode form which is characterized by two wavenumbers, the axial wavenumber  $k$  and the azimuthal wavenumber  $n$ . For a given pair of the control parameters  $(Re, q)$ , the stability property will also depend on wavenumbers  $(k, n)$ . We assume that in a natural environment, all perturbations are possible. Thus, we will need to search over the  $(k, n)$  plane for a perturbation which gives the maximum growth rate because such a perturbation dominates the flow development. For a given trailing line vortex characterized by the pair of parameters  $(Re, q)$ , if the maximum growth flow rate is zero, the flow is said to be marginally stable. Combinations of such  $(Re, q)$  pairs giving rise to the marginal stability form a curve in the  $(Re, q)$  plane. This curve is called the marginal stability curve and this curve separates the stable domain from the unstable domain in the control parameter space. An extensive computation was carried out to generate such a curve. In the present study, the marginal stability curve was found for Reynolds numbers up to  $10^5$ . The resulting curve is shown in figure 14.

One of the features of the marginal stability curve is that the swirling rate needed to stabilize the flow increases with the Reynolds number and does not approach a constant value even for Reynolds number as high as  $10^5$ . For  $Re = 10^5$ , the value of  $q$  needed to render the flow stable is larger than 6. In contrast, the asymptotic analysis by Leibovich and Stewartson<sup>43</sup> for the inviscid perturbations of large azimuthal wavenumbers shows that flow becomes stable for  $q$  around 1.4. For inviscid perturbations with finite values of azimuthal wavenumber, the asymptotic analysis by Stewartson and Brown<sup>44</sup> show that the values of  $q$  for which the near neutral center mode exists could be around 2.3. The recent numerical calculations by Mayer and Powell<sup>45</sup> show that for the inviscid perturbations, the  $n = -1$  (in current notation) mode has the largest unstable domain and the largest value of  $q$  is about 1.5.

The comparison between the current viscous study and the inviscid analysis by previous researchers shows that the unstable domain of the flow (as measured by range of  $q$  for which the flow is unstable) is larger for viscous perturbations at large Reynolds numbers than that for the inviscid perturbations. For a value of  $q$  which is larger than the stability bound for the inviscid perturbations, the flow is predicted as being stable on the inviscid ground. However, the flow can be unstable to viscous perturbations at large Reynolds numbers. As the Reynolds number is increased,

the flow tends to be more unstable. Since the present calculations are carried out for Reynolds number as high as  $10^5$ , it is expected from figure 14 that the present viscous analysis will not approach to the inviscid results as the Reynolds number is further increased.

For  $Re$  greater than 200, it is found that the modes giving rise to the marginal stability have an azimuthal wavenumber of  $n = -1$ . Modes with azimuthal wavenumbers of  $|n| = 1$  are very important in that they are the only modes that move the fluid particles away from the axis of the vortex. It is for this reason that the  $|n| = 1$  modes are termed 'bending modes' by Leibovich, Brown, and Patel<sup>46</sup>. The deflection of fluid particles away from the vortex axis is one of the features of the vortex breakdown of the spiral type, as was pointed out in Leibovich<sup>47</sup>. Thus, our stability analysis would provide some ingredients as found in vortex breakdown.

To see the effect of the Reynolds number on the eigenfunction, the real part of the axial component of the eigenfunctions at  $Re = 10^4$  and  $Re = 10^5$  are shown in figure 15. The eigenfunctions are normalized such that the maximum value is 1. As the Reynolds number is increased, the modes giving rise to the marginal stability moves closer to the vortex axis. This suggests that these modes are similar to the 'viscous centers mode' found by Stewartson, Ng, and Brown<sup>48</sup> for the flow in a rotating pipe. The term 'viscous center mode' was used because viscosity plays an important role for these modes even for large Reynolds number and because the modes have nontrivial behaviors near the center of the vortex axis. The major difference between trailing line vortex flow in the present study and flow in the rotating pipe flow is that for the trailing line vortex flow, the present study suggests that viscous center modes are the dominating modes near the marginal stability curve while in the rotating pipe flow, the viscous center modes found by Stewartson, Ng, and Brown are dominated by perturbations of the wall mode type studied by Maslowe and Stewartson<sup>49</sup>, and Yang and Leibovich<sup>50</sup>.

More details of the linear marginal stability of the trailing line vortex could be found in Yang and Leibovich<sup>51</sup>.

### 3. Future Plans

#### 1) Turbulence modeling

The research on turbulence modeling will be carried on two fronts. The first one is to test the eddy viscosity models we have developed for more complex flows. The models will be eventually incorporated into an existing general purpose Navier-Stokes code if they pass the tests. The second direction will be the development of Reynolds stress models, in particular for near wall flows. The eddy viscosity models have some basic limitations which are expected to be overcome by the Reynolds stress models.

#### 2) Transition modeling

So far, the proposed transition models are only used for flat plate boundary layers with zero pressure gradient. We will apply the proposed models to transitional boundary layers with pressure gradient and curvature. We will also extend the model to thermal boundary layers. In the theoretical aspect, we will try to derive

a set of equations from the conditional averaging point of view rather than the Reynolds averaging point of view. This set of equations would at least serve as a point of reference when we modify the turbulence equations for the transitional flows.

### 3) Stability analysis of swirling flows

Stability analysis will be carried out for swirling flows observed in propulsion systems. Turbulence model calculations for these swirling flows are inadequate. We hope that the stability analysis would provide some insight on how to construct a better turbulence model. In addition, we will be studying the mixing properties of such flows.

## 4. References

- <sup>1</sup> Launder, B.E. and Spalding, D.B., "The numerical computation of turbulent flow," *Computer Methods in Applied Mechanics and Engineering* **3**, 269 (1974).
- <sup>2</sup> Rodi, W., *Turbulence Models and Their Application in Hydraulics*, Book Pub. of International Association for Hydraulic Research, Delft, the Netherlands, 1980.
- <sup>3</sup> Jones, W.P., and Launder, B.E., "The calculation of low-Reynolds number phenomena with a two-equation model of turbulence," *Intl. J. of Heat and Mass Transfer* **16**, 1119 (1973).
- <sup>4</sup> Patel, V.C., Rodi, W., and Scheuerer, G., "Turbulence models for near-wall and low-Reynolds number flows: a review," *AIAA J.* **23**, 1308 (1985).
- <sup>5</sup> Lang, N.J. and Shih, T.H., "A critical comparison of two equation turbulence models," NASA TM 105237 (1991).
- <sup>6</sup> Yang, Z. and Shih, T.H., "A new time scale based  $k - \epsilon$  model for near wall turbulence," *AIAA J.* **31**, 1191 (1993).
- <sup>7</sup> Kim, J., Moin, P., and Moser, R., "Turbulent statistics in fully developed channel flow at low Reynolds Number," *J. Fluid Mech.* **177**, 133 (1987).
- <sup>8</sup> Wilcox, D.C., "Application of low Reynolds number two-equation turbulence models to high Reynolds number flows," in *Near Wall Turbulent Flows*, Elsevier, 1993.
- <sup>9</sup> Yang, Z. and Shih, T.H., "A Galilean and tensorial invariant  $k - \epsilon$  model for near wall turbulence," AIAA Paper 93-3105 (1993).
- <sup>10</sup> Spalart, P.R., "Direct simulation of a turbulent boundary layer up to  $Re_\theta = 1410$ ," *J. Fluid Mech.* **187**, 61 (1988).
- <sup>11</sup> Coles, D. E., "The young person's guide to data," in *Computation of Turbulent Boundary Layers, V. II*, AFOSR-IFP-Stanford Conference, 1968.
- <sup>12</sup> Wilcox, D.C., "Reassessment of the scale-determining equation for advanced turbulence models," *AIAA J.* **26**, 1299 (1988).
- <sup>13</sup> Wieghardt, K. and Willmann, W., "On the turbulent friction layer for rising pressure," NACA TM-1314 (1951).
- <sup>14</sup> Herring, H.J., and Norbury, J.F., "Some experiments on equilibrium turbulent boundary layers in favorable pressure gradients," *J. Fluid Mech.* **27**, 541 (1967).

- 15 Samuel, A.E., and Joubert, P.N., "A boundary layer developing in an increasingly adverse pressure gradient," *J. Fluid Mech.* **66**, 481 (1974).
- 16 Yang, Z. and Shih, T.H., "On the wall functions for two equation turbulence models," prepared for publication.
- 17 Shih, T. H., Liou, W. W., Shabbir, A., Yang, Z., and Zhu, J., "Dynamics of vorticity fluctuations and the dissipation rate equation," NASA TM 105993 (1993).
- 18 Lumley, J. L., "Toward a turbulent constitutive relation," *J. Fluid Mech.*, **41**, 413 (1970).
- 19 Pope, S. B., "A more general effective-viscosity hypothesis," *J. Fluid Mech.*, **72**, 331 (1975).
- 20 Shih T. H. and Lumley, J. L., "Remarks on turbulent constitutive relations," NASA TM 106116 (1993).
- 21 Yang, Z. and Shih, T. H., "Flow inhomogeneity and the dissipation rate equation," In preparation.
- 22 Baldwin, B. S. and Lomax, H., "Thin layer approximation and algebraic model for separated turbulent flows," AIAA Paper 78-256 (1978).
- 23 Cebeci, T. and Smith, A. M. O., *Analysis of Turbulent Boundary Layers*, Academic Press, 1974.
- 24 Nee, V. W. and Kovasznay, L. S. G., "The calculation of incompressible turbulent boundary layers by a simple theory," in *Computation of Turbulent Boundary Layers, V. I*, AFOSR-IFP-Stanford Conference, 1968.
- 25 Baldwin, B. S. and Barth, T. J., "A one-equation turbulence transport model for high Reynolds number wall-bounded flows," NASA TM 102847 (1990).
- 26 Spalart, P. R. and Allmaras, S. R., "A one-equation turbulence model for aerodynamic flows," AIAA-92-0439 (1992).
- 27 Durbin, P., "Near-wall turbulence closure modeling with 'damping function'," *Theo. and Comp. Fluid Dynamics*, **3**, 1 (1991).
- 28 Kim, J., Private communication.
- 29 Purtell, L. P., Klebanoff, S., and Buckley, F. T., "Turbulent boundary layer at low Reynolds number," *Phys. Fluids* **24**, 802 (1981).
- 30 Mehta, R. D. and Westphal, R. V., "Near-field turbulence properties of single and two-stream plane mixing layers," *Experiments in Fluids* **4**, 257 (1986).
- 31 Coles, D. E. and Wadcock, A. J., "Flying hot wire study of flow past an NACA 4412 airfoil at maximum life," *AIAA J.*, **17**, 321 (1979).
- 32 Rogers, S. E., Wiltberger, N. L., and Kwak, D., "Efficient simulation of incompressible viscous flow over single and multi-element airfoils," AIAA Paper 92-0405 (1992).
- 33 Durbin, P. A. and Yang, Z., "A transport equation for eddy viscosity," in *Proc. of the 1992 Summer Program*, Center for Turbulence Research, Stanford (1992).
- 34 Durbin, P. A., Mansour, N. N., and Yang, Z., "Eddy viscosity transport model for turbulent flow," Submitted for publication.
- 35 Priddin, C.H., *The Behaviour of the Turbulent Boundary Layer on a Curved Porous Wall*, PhD Thesis, Imperial College, London, 1975.

- <sup>36</sup> Rodi, W. and Scheuerer, S., "Calculation of laminar-turbulence boundary layer transition on turbine blades," in *Proc. 65th AGARD-REP Symposium on Heat Transfer and Cooling in Gas Turbine*, Bergen, Norway, 1985.
- <sup>37</sup> Fujisawa, N., "Calculation of transitional boundary layers with a refined low Reynolds number version of a  $k - \epsilon$  model of turbulence," in *Engineering Turbulence Modeling and Experiment*, Elsevier, 1990.
- <sup>38</sup> Yang, Z. and Shih, T.H., "A  $k - \epsilon$  model for turbulent and transitional boundary layers," in *Near Wall Turbulent Flows*, Elsevier, 1993.
- <sup>39</sup> Yang, Z. and Shih, T.H., "Modeling of transitional boundary layers," prepared for publication.
- <sup>40</sup> Yang, Z. and Shih, T.H., "A  $k - \epsilon$  calculation of transitional boundary layers," in *Transition and Turbulence*, Springer-Verlag, 1992.
- <sup>41</sup> Schmidt, R.C. and Patankar, S.V., "Two-equation low-Reynolds number turbulence modeling of transitional boundary layer flows characteristic of gas turbine blades," NASA CR-4145 (1988).
- <sup>42</sup> Savill, A.M., "Turbulence model predictions for transition under free-stream turbulence," in *RAeS Transition and Boundary Layer Conference*, Cambridge, England, 1991.
- <sup>43</sup> Leibovich, S. and Stewartson, K., "A sufficient condition for the instability of columnar vortices," *J. Fluid Mech.*, **126**, 335 (1983).
- <sup>44</sup> Stewartson, K. and Brown, S. N., "Near-neutral center-modes as inviscid perturbations to a trailing line vortex," *J. Fluid Mech.*, **156**, 387 (1985).
- <sup>45</sup> Mayer, E. W. and Powell, K. G., "Viscous and inviscid instabilities of a trailing vortex," *J. Fluid Mech.*, **245**, 91 (1992).
- <sup>46</sup> Leibovich, S., Brown, S. N., and Patel, Y., "Bending waves on inviscid columnar vortices," *J. Fluid Mech.*, **173**, 595 (1986).
- <sup>47</sup> Leibovich, S., "Vortex stability and breakdown: Survey and extension," *AIAA J.*, **22**, 1192 (1984).
- <sup>48</sup> Stewartson, K., Ng, T. W., and Brown, S. N., "Viscous center modes in the stability of swirling Poiseuille flow," *Phil. Trans. Roy. A.*, **324**, 473 (1988).
- <sup>49</sup> Maslowe, S. A. and Stewartson, K., "On the linear inviscid stability of rotating Poiseuille flow," *Phys. Fluids*, **25**, 1517 (1982).
- <sup>50</sup> Yang, Z. and Leibovich S., "Unstable viscous wall modes in rotating pipe flow," *AIAA Paper 91-1801* (1991).
- <sup>51</sup> Yang, Z. and Leibovich S., "On the linear marginal stability of the trailing line vortex," Submitted for publication.

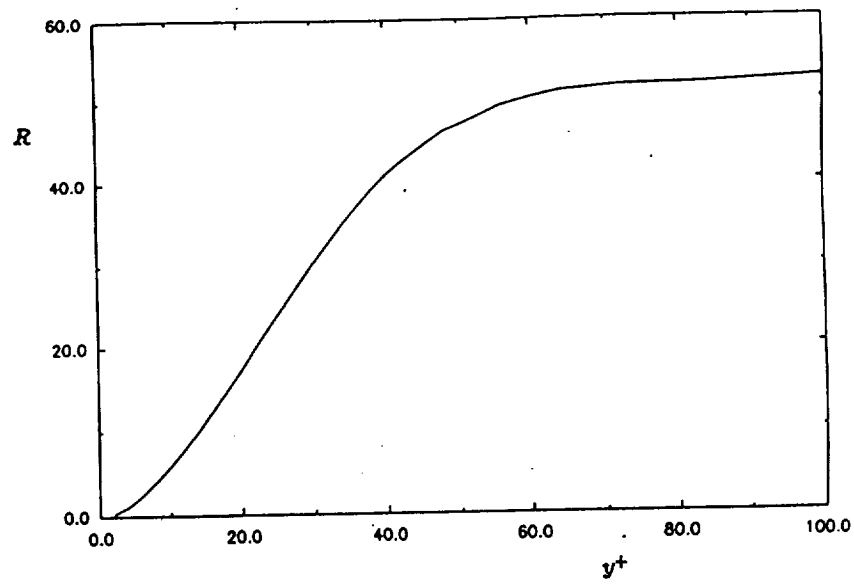


Figure 1: Variation of  $R$  for turbulent channel flow at  $Re_\tau = 180$ .

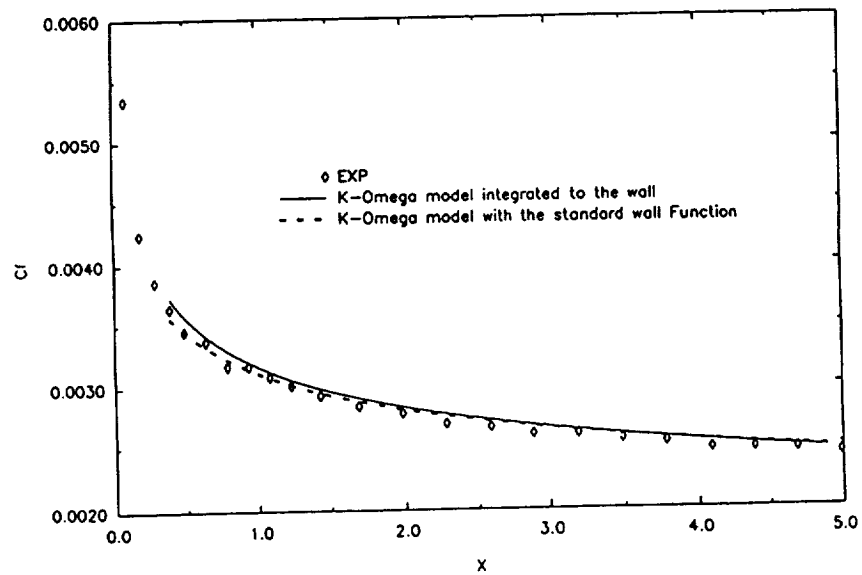


Figure 2:  $k - \omega$  prediction of the skin friction distribution for ZPG turbulent boundary layer.



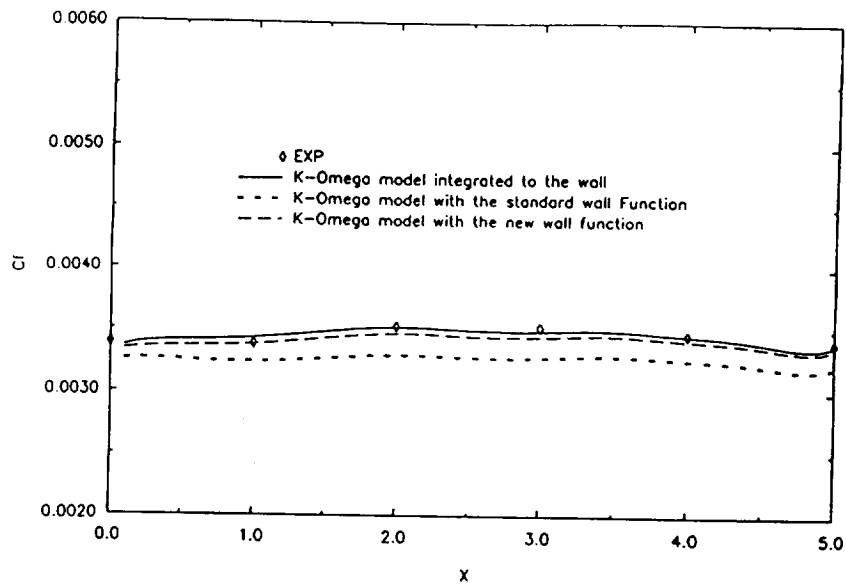


Figure 3:  $k-\omega$  prediction of the skin friction distribution for FPG turbulent boundary layer.

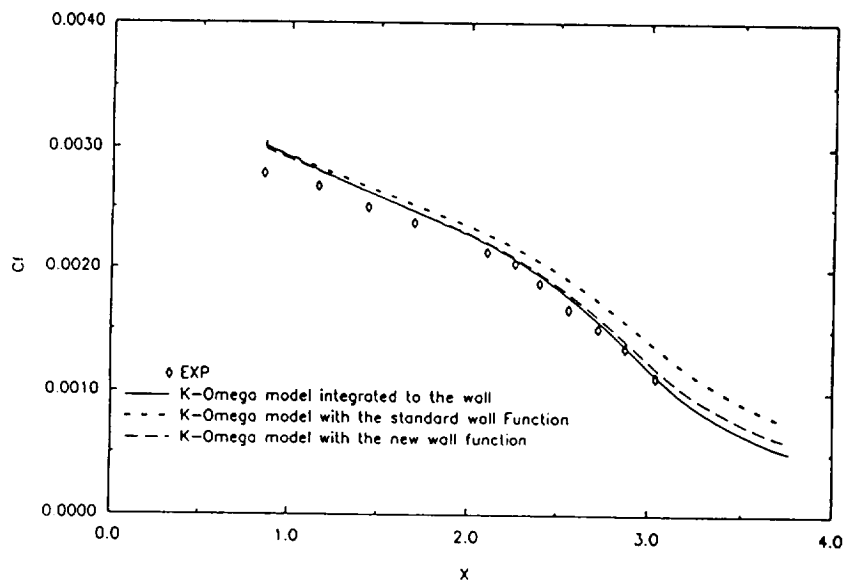


Figure 4:  $k-\omega$  prediction of the skin friction distribution for APG turbulent boundary layer.

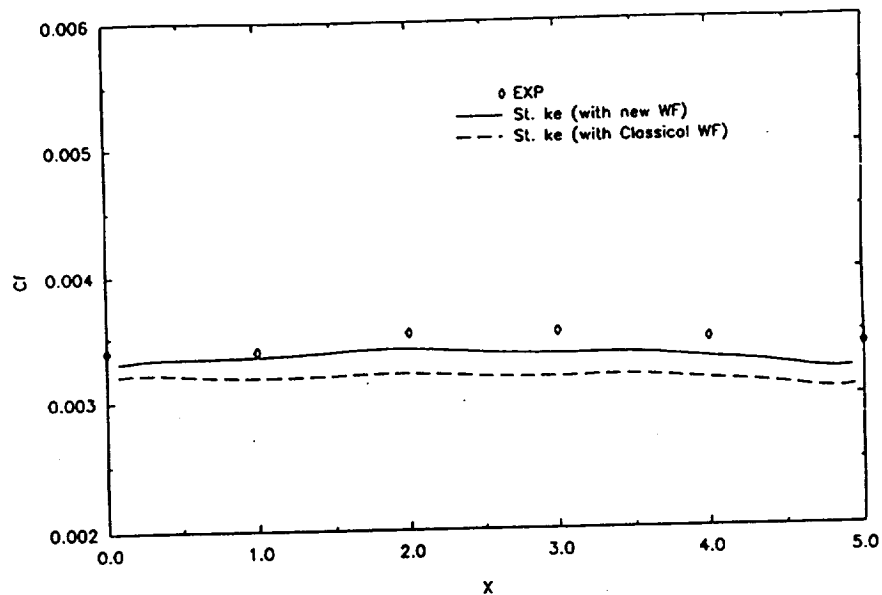


Figure 5: Prediction of the skin friction distribution for FPG turbulent boundary layer by standard  $k-\epsilon$  model with wall functions.

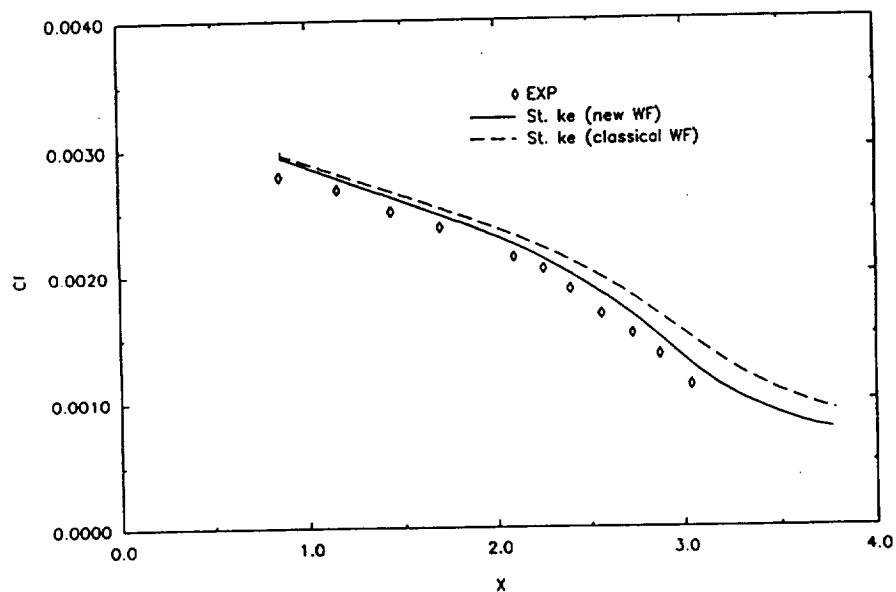


Figure 6: Prediction of the skin friction distribution for APG turbulent boundary layer by standard  $k-\epsilon$  model with wall functions.

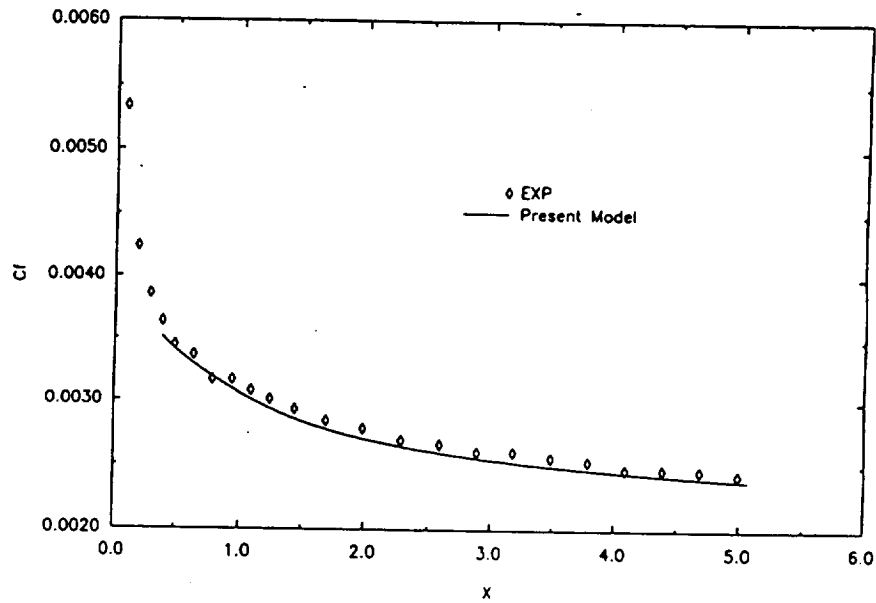


Figure 7: Prediction of the skin friction distribution for ZPG turbulent boundary layer by the new dissipation rate equation.

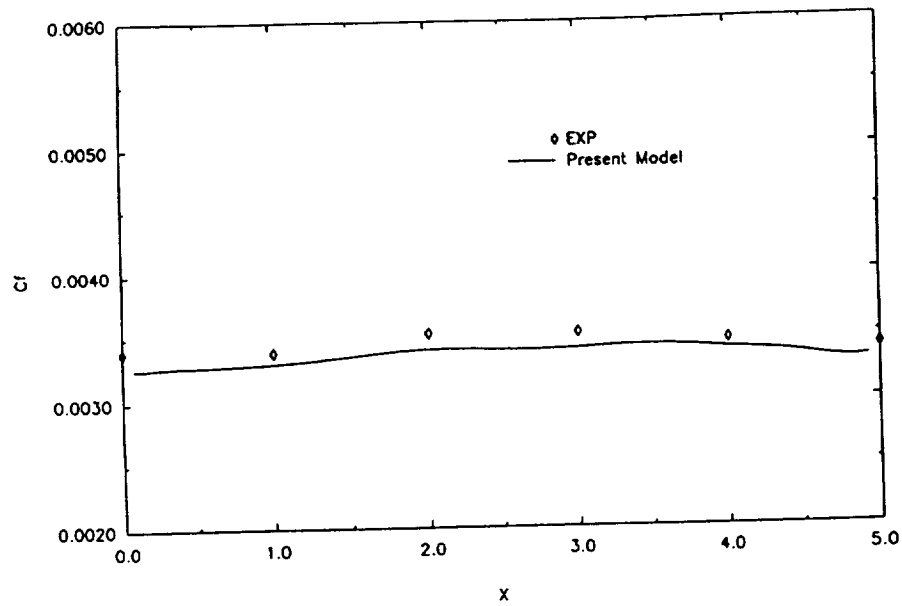


Figure 8: Prediction of the skin friction distribution for FPG turbulent boundary layer by the new dissipation rate equation.

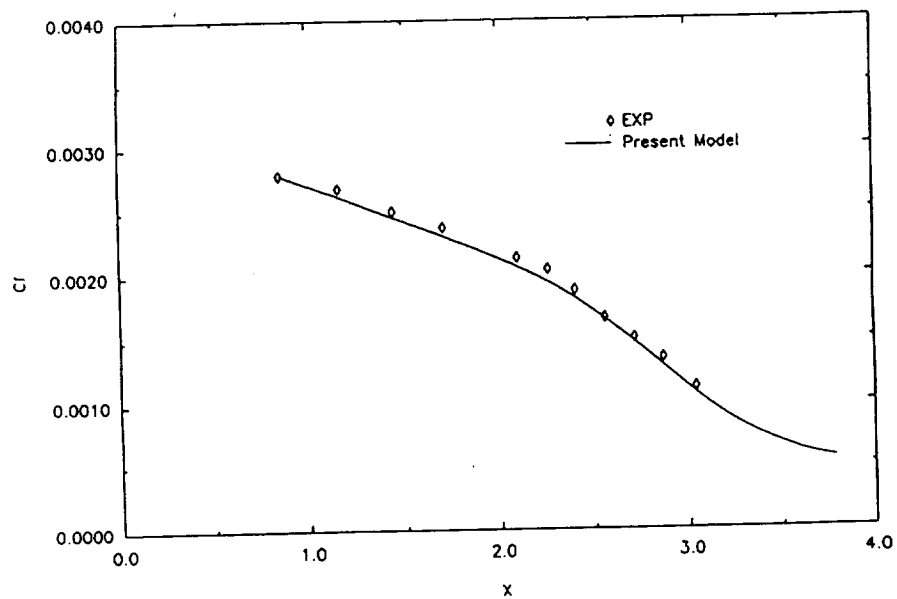


Figure 9: Prediction of the skin friction distribution for APG turbulent boundary layer by the new dissipation rate equation.

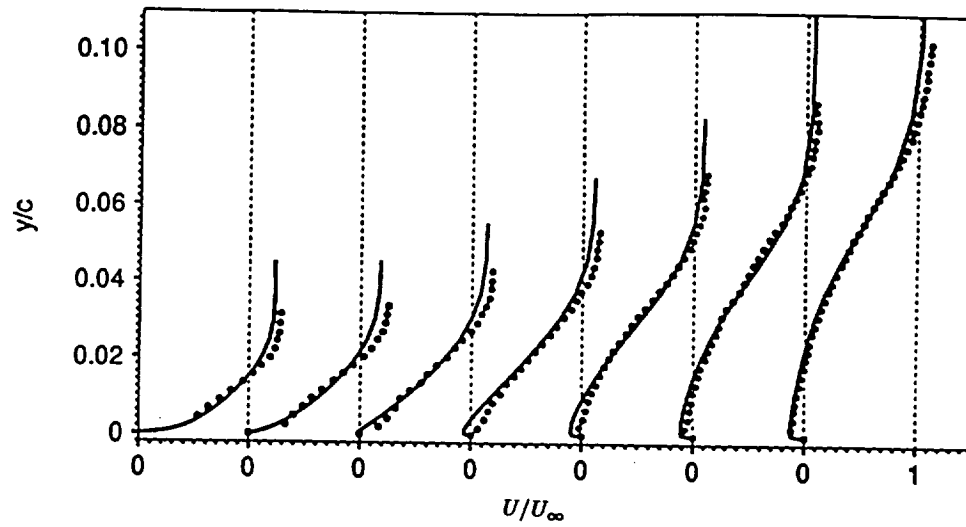


Figure 10: Mean velocity profiles on the suction surface.

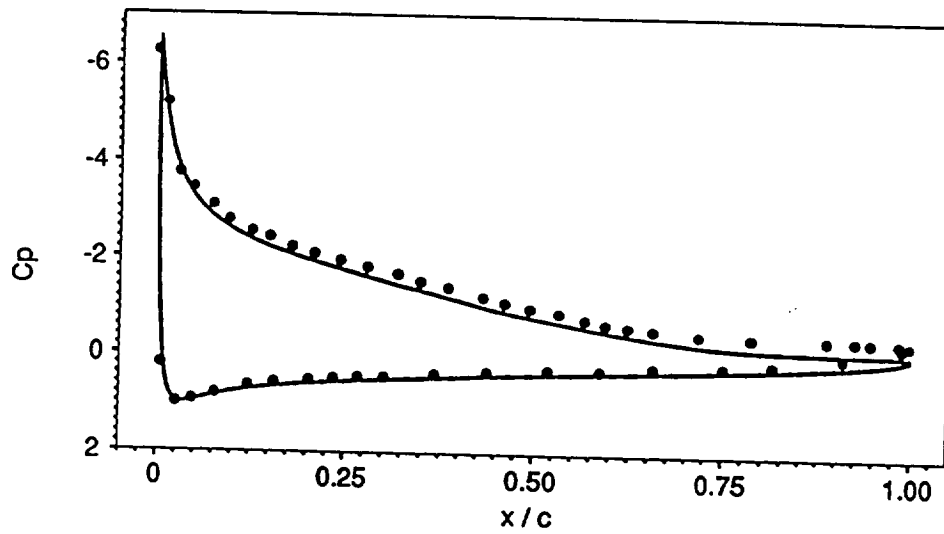


Figure 11: Pressure distribution around the airfoil surface.

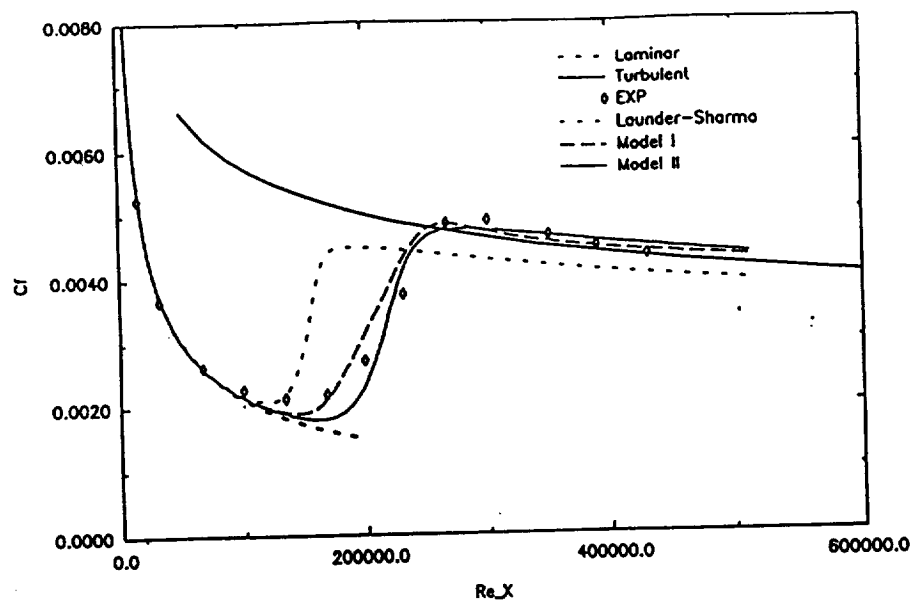


Figure 12: Skin friction coefficient for T3A.

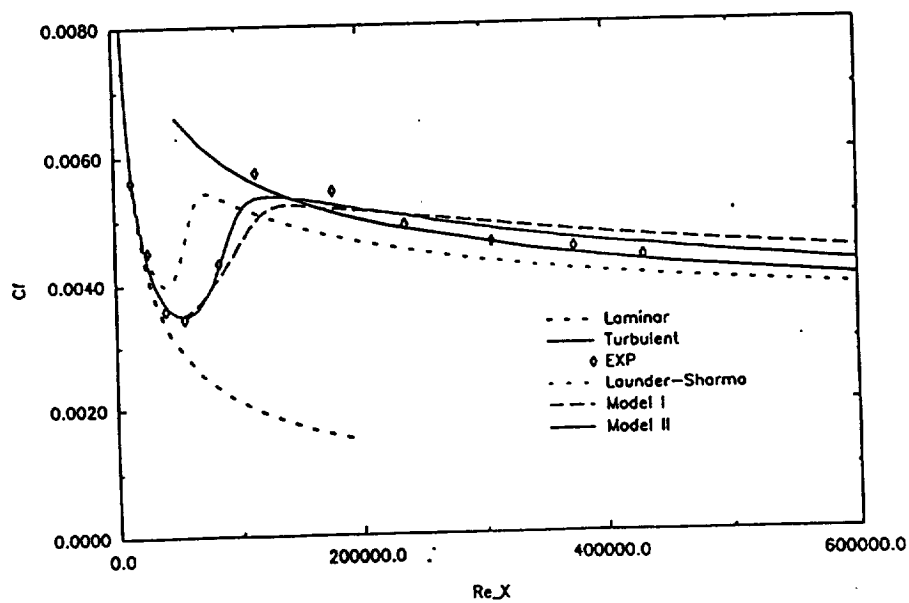


Figure 13: Skin friction coefficient for T3B.

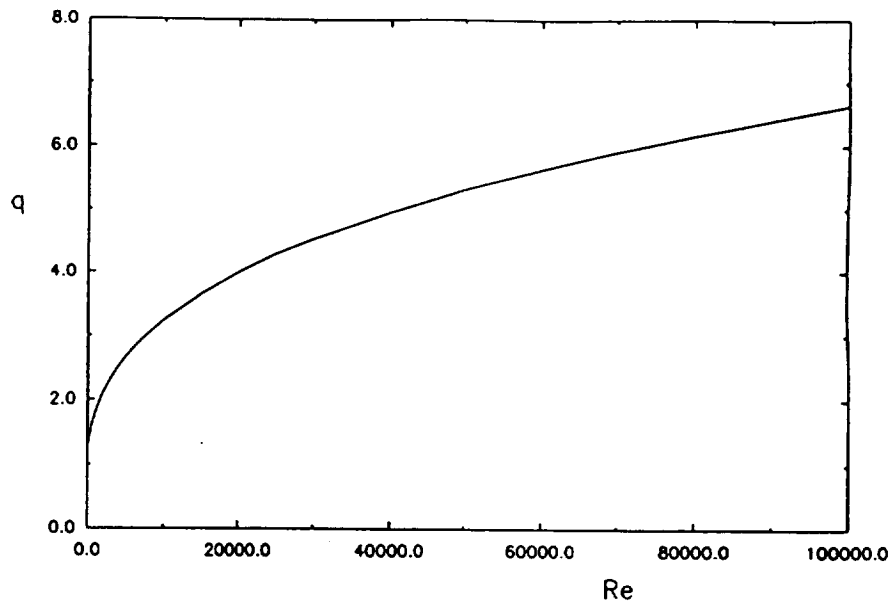


Figure 14: The marginal stability curve for the trailing line vortex.

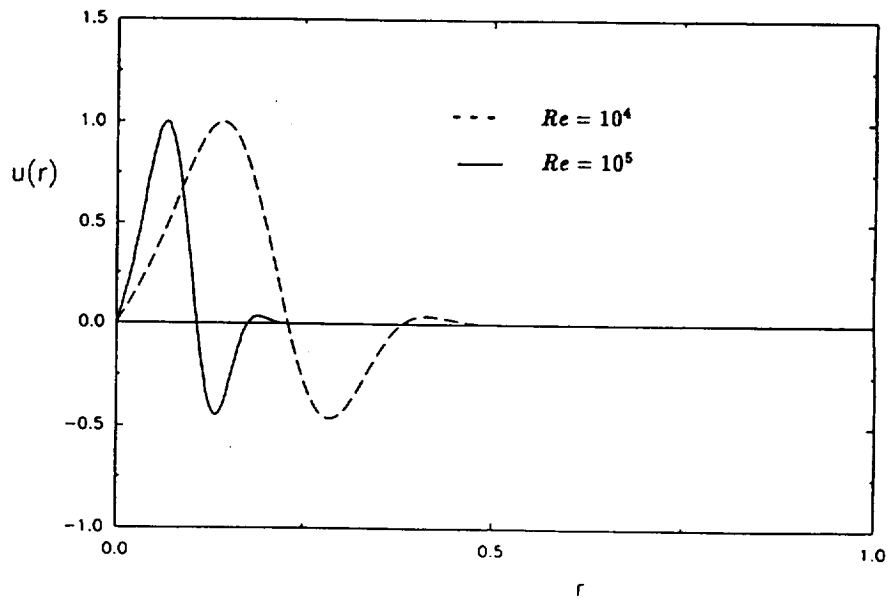


Figure 15: The eigenfunctions at different Reynolds numbers.





# Testing New Two-Equation Turbulence Models for Complex Flows

J. Zhu

## 1. Motivation and Objective

In the past year, several new proposals for the two-equation turbulence modeling have been made at CMOTT. These proposals include: a functional expression of  $C_\mu$ ; a vorticity dynamics based model for the turbulent dissipation equation; and a realizable Reynolds stress algebraic equation model. The objective of the present work is to assess these proposals in complex flows of engineering importance.

## 2. Work Accomplished

All the proposals tested have been implemented into a conservative finite-volume code designed for calculating incompressible elliptic flows with complex boundaries<sup>1</sup>. In order for the calculation to reflect the actual performance of the turbulence models, it is crucial that the numerical diffusion be reduced to the minimum. This is achieved via the use of second-order accurate differencing schemes and sufficiently fine grids. Test cases include two backward-facing step flows<sup>2,3</sup>, confined jets in a cylindrical duct<sup>4</sup> and in a conical duct with a 5° divergence<sup>5,6</sup>. These test cases have been chosen because they involve complicated flow features such as strong adverse pressure gradient, separation and reattachment, and also because reliable and well-documented experimental data are available, allowing the performance of the models to be examined in detail. For comparison, the standard  $k - \epsilon$  model<sup>7</sup> is considered in all the cases and an RNG-based  $k - \epsilon$  model<sup>8</sup> is also considered in some of the cases.

### 2.1 A New Formulation of $C_\mu$

In the standard  $k - \epsilon$  model, the eddy viscosity is given by

$$\nu_t = C_\mu \frac{k^2}{\epsilon}, \quad C_\mu = 0.09 \quad (1)$$

where the value of  $C_\mu = 0.09$  was chosen from a set of experiments for simple flows under the equilibrium condition. Several authors have found that using a non-constant  $C_\mu$  may significantly improve the  $k - \epsilon$  model's ability to predict certain flows in which the equilibrium condition is not satisfied. On the basis of correlated experimental data for thin shear layers, Rodi<sup>9</sup> related  $C_\mu$  to a function of the average value of  $P/\epsilon$  ( $P$  is the production of the turbulent kinetic energy). Ljuboja and Rodi<sup>10</sup> derived a  $C_\mu$  formula from the simplified algebraic stress model and successfully used it to predict wall jets. Leschziner and Rodi<sup>11</sup> proposed a function for  $C_\mu$  which takes into account the effect of streamline curvature and obtained improved results in the calculation of annular and twin parallel jets. However, these modifications to  $C_\mu$  are either of fully empirical or of preliminary nature.

In this work<sup>12</sup>, the realizability principle which requires the non-negativity of turbulent normal stresses is applied to analyze the  $k - \epsilon$  model. The analysis leads to

$$C_\mu = \frac{2/3}{A + \eta} \quad (2)$$

where  $A$  is a positive constant and  $\eta$  is the time scale ratio of the turbulence to the mean strain rate

$$\eta = SK/\epsilon, \quad S = (2S_{ij}S_{ij})^{1/2}, \quad S_{ij} = (U_{i,j} + U_{j,i})/2 \quad (3)$$

This  $C_\mu$  will ensure the positivity of each component of the turbulent kinetic energy – realizability that most existing eddy-viscosity models do not satisfy. The model validation is made on the basis of applications to the two backward-facing step flows experimentally studied by Driver and Seegmiller<sup>2</sup> (DS) and Kim, Kline and Johnston<sup>3</sup> (KKJ). The value of the model constant  $A$  is taken as

$$A = 5.5 \quad (4)$$

which has been found to work well for both the test cases. The present model has been compared with the standard  $k - \epsilon$  model and with the RNG  $k - \epsilon$  model<sup>8</sup>. The comparison shows that the present model effectively reduces the turbulent eddy-viscosity level, resulting in significant improvement over the standard  $K - \epsilon$  model. The RNG model generally gives very similar predictions to the present model, but overly reduces the turbulent eddy-viscosity level in the recirculation region near the step.

## 2.2 A New Dissipation Equation

Although one can write the exact  $\epsilon$  equation, it is of little use to serve as a starting point for deriving its model counterpart because of lack of knowledge about the various correlations in this equation. Therefore, one often ignores the exact equation and creates a model equation which has a structure similar to that of the turbulent kinetic energy equation. Due to its highly empirical nature, such a model equation is often considered as a weakness in existing turbulence models.

Table 1. Comparison of the reattachment point locations

Case	measurement	standard $k - \epsilon$ model	present model
DS	6.1	4.99	5.36
KKJ	$7 \pm 0.5$	6.35	6.8

Recently, Shih et al.<sup>13</sup> have proposed a new  $\epsilon$  equation based on the vorticity fluctuation equation. The proposed  $\epsilon$  equation can be applied to any level of turbulence modeling. In this work, it is applied, in conjunction with a realizable isotropic eddy-viscosity formulation, to calculate the two backward-facing step flows (DS case<sup>2</sup> and KKJ case<sup>3</sup>). Table 1 shows the comparison of the reattachment points. The detailed comparisons for both mean and turbulent quantities are given in Shih et al.<sup>13</sup>. The comparisons show that the overall performance of the present model is better than that of the standard  $k - \epsilon$  model.

### 2.3 A Realizable Reynolds Stress Algebraic Equation (RRSAE) Model

The standard  $k - \epsilon$  model, like many others in the algebraic equation modeling group, uses the Boussinesq's isotropic eddy-viscosity concept which assumes that the Reynolds stresses are proportional to the mean velocity gradients. The concept usually does well for the shear stresses in two-dimensional mean flows of the boundary-layer type, but not for the normal stresses due to the erroneous isotropic nature of the concept. This suggests that linear dependence on the mean velocity gradients is insufficient and that a more general relation is needed for more complex flows. In fact, by eliminating the convection and diffusion terms in the modeled transport equations for the Reynolds stresses, Rodi<sup>9</sup> developed an algebraic stress model (ASM) in which the Reynolds stresses are calculated by algebraic expressions. Owing to its anisotropic nature, the model does perform better than the isotropic  $k - \epsilon$  model for certain flows; a well known example is fully-developed flow in non-circular ducts where ASM is capable of generating turbulence-driven secondary motions while the isotropic eddy viscosity model is not. However, ASM does not appear in a tensorial invariant form, which may limit its generality. In addition, inappropriate modeling of higher order correlations, such as pressure-strain correlations, will also cause deficiencies of the second-order closure based ASM. Moreover, special care needs to be taken to prevent the turbulent normal stresses from becoming negative (Huang and Leschziner<sup>14</sup>), and the numerical implementation of ASM may even be more complicated than that of its parent second-order closure model, especially in general three dimensional flows.

There are other approaches to developing Reynolds stress algebraic equation models. For example, Yoshizawa<sup>15</sup> derived a relation for the turbulent stresses using a two-scale direct interaction approximation. It contains both linear and quadratic terms of the mean velocity gradients. A similar relation has been also derived recently by Rubinstein and Barton<sup>16</sup> using Yokhot and Orszag's RNG method. An interesting point in these two methods is that the values of the model coefficients can all be determined analytically. Speziale<sup>17</sup> proposed a different expression, based on the principle of material frame-indifference, which contains the Oldroyd derivative of the mean strain rates. However, the principle of material frame-indifference is valid only in the limit of two-dimensional incompressible turbulence, and hence it is not an appropriate constraint for general turbulent flows. In addition, these non-linear models are not fully realizable and have not been extensively tested.

Recently, Shih and Lumley<sup>18</sup> have shown that the Reynolds stress, being a second rank tensor, can be expressed as a fourth-order polynomial of the mean velocity gradients. This is the most general stress-strain relationship within the framework of algebraic turbulence modeling, with the linear stress-strain relation in the Boussinesq's eddy-viscosity concept being its first-order approximation. Based on this, Shih et al.<sup>19</sup> have recently proposed a quadratic stress-strain relation in conjunction with the two modeled equations of  $k$  and  $\epsilon$  for practical engineering calculations. Realizability constraints have been used to derive appropriate functional expressions for the model coefficients so that the resulting model will ensure the positivity of individual turbulent normal stresses, an important feature that is not

present in most existing turbulence models. Since the model appears promising as a competitive alternative in the turbulence modeling arsenal, it is of interest to test its performance under various complex flow situations. A few representative test results will be presented in the following and the detailed results can be found in the relevant reports.

### 2.3.1 Backward-facing step flows (Shih et al.<sup>19</sup>)

The empirical constants in the model have been fine-tuned in the calculation of the two backward-facing step flows (DS case<sup>2</sup> and KKJ case<sup>3</sup>). The computed and measured reattachment points are compared in Table 2. The reattachment point is a critical parameter which has often been used to assess the overall performance of turbulence models as well as numerical procedures. Figs. 1(a) and 1(b) show the comparison of computed and measured static pressure coefficient  $C_p$  along the bottom wall. In both cases, the standard  $k - \epsilon$  is seen to predict premature pressure rises, which is consistent with its underprediction of the reattachment lengths, while the RRSAE model captures these pressure rises quite well. The comparisons of predicted and measured turbulent stresses  $\overline{uu}$ ,  $\overline{vv}$  and  $\overline{uv}$  are shown in Figs. 2 and 3 at various  $x$ -locations. In the KKJ-case, no experimental data for the turbulent stresses are available in the recirculation region, and the reattachment point was found in the experiment to move forward and backward continuously around seven step heights downstream of the step, leaving an uncertainty of  $\pm 0.5$  step height for the reattachment length. This also points to some uncertainty in the measured turbulent quantities in the recovery region. On the other hand, the experimental data in the DS-case should be considered more reliable because of the smaller uncertainty of the reattachment location, indicating a smaller unsteadiness of the flow. As compared with the standard  $k - \epsilon$  model results in Figs. 2 and 3, it can be seen that the anisotropic terms increase  $\overline{uu}$  while decreasing  $\overline{vv}$ , leading to significant improvements in both  $\overline{uu}$  and  $\overline{vv}$  results. On the other hand, the anisotropic terms have little impact on the turbulent shear stress  $\overline{uv}$ . The improvement obtained by the RRSAE model in Fig. 2 for  $\overline{uv}$  is due to the reduction in  $C_\mu$ .

Table 2. Comparison of the reattachment point locations

Case	measurement	standard $k - \epsilon$ model	RRSAE model
DS	6.1	4.99	5.82
KKJ	$7 \pm 0.5$	6.35	7.35

### 2.3.2 Confined jets in a conical duct (Zhu and Shih<sup>20</sup>)

The general features of the flow considered are sketched in Fig. 4. At the entrance, two uniform flows, a jet of high velocity and an ambient stream of low velocity, are discharged into the duct. Due to turbulent entrainment, the jet increases its mass flux while spreading and this causes an equal decrease in the mass flux of the ambient stream. An adverse pressure gradient is thus set up by the decrease in the velocity of the ambient stream which can be considered as a potential flow. When the ratio of

jet to ambient velocities at the entrance is above a critical value, a recirculation zone occurs at the duct wall downstream of the inlet plane. This is because the jet has consumed the whole ambient flow before reaching the wall and further entrainment must create reverse flows in order to maintain the total mass flux conservation. The inlet flow conditions can be characterized by the Craya-Curtet number  $C_t$  and the experiment of Binder and Kian<sup>5,6</sup> shows that recirculation occurs when  $C_t < 1.1$  in the conical duct with a  $5^\circ$  divergence. For a given geometry, recirculation as well as adverse pressure gradients can be intensified by reducing the value of  $C_t$  at the entrance.

The separation and reattachment points are given in Table 3. For the reattachment point, only a range of  $3.4 \sim 3.8D_o$  was given experimentally due to the high unsteadiness of the recirculating bubbles. The experiment revealed that as  $C_t$  decreased, the separation points moved upstream while the reattachment points remained basically unchanged. The RRSAB model captures this feature well and predicts the locations of the recirculation bubbles better than the standard  $k - \epsilon$  model.

Table 3. Separation and reattachment points ( $x_s/D_o$ ,  $x_r/D_o$ )

$C_t$	experiment	$k - \epsilon$ model	RRSAE model
0.775	2.5, 3.4~3.8	1.82, 3.17	2.15, 3.79
0.59	1.5, 3.4~3.8	1.43, 3.22	1.45, 3.81

Fig. 5 shows the variation of pressure coefficient along the duct wall. The pressure gradient is governed by the jet entrainment, the contraction and expansion of the flow caused by recirculating eddies as well as the geometry of the duct. The entrainment and the divergence of the duct can only produce a maximum pressure difference equal to  $\rho U_a^2/2$ , while the pressure difference created by the divergence of streamlines in the downstream part of the recirculating bubble can be much larger than  $\rho U_a^2/2$ . Regarding the comparison between predictions and experiments, it can be seen that although both models predict practically the same total pressure rise, the RRSAB model captures the location where the pressure starts to shoot up much better than the standard  $k - \epsilon$  model at all the  $C_t$  values.

Detailed experimental data for the turbulent stresses  $\overline{u'u'}$ ,  $\overline{v'v'}$  and  $\overline{u'v'}$  are available only at  $C_t = 0.59$ . The computed and measured radial profiles of these quantities at four downstream locations are compared in Figs. 6(a)-6(c). With regard to the turbulent normal stresses, the experimental data are basically followed by the results of both the RRSAB model and the standard  $k - \epsilon$  model, with the former predicting more anisotropy than the latter. The experimental data at  $x/D_o = 2.5$  are seen to exhibit a different trend for both  $\overline{u'u'}$  and  $\overline{v'v'}$ , which may possibly be due to measurement errors. The flow visualization in the experiment indicated that the global flow pattern was highly unsteady in the presence of recirculation. With due regard to flow complexities and measurement difficulties, the agreement between the predictions and measurements seen in Figs. 6(a) and 6(b) should be considered

as reasonably good, but it is difficult to judge which model performs better for the turbulent normal stresses, overall. For the turbulent shear stress  $\overline{uv}$  shown in Fig. 6(c), the results obtained with the RRSAE model are clearly better than those with the  $k - \epsilon$  model for all the locations considered. The large discrepancy seen at  $x/D_o = 2.5$  is partially due to the underprediction of the width of the backflow region and partially due to the experimental uncertainty, as evidenced by the fact that in the experimental data, the change in sign of the shear stress profile occurs much further away from the duct wall than the velocity minimum.

### 2.3.3 Confined jets in a cylinder (Zhu and Shih<sup>21</sup>)

This case is taken from the experiment of Barchilon and Curtet<sup>4</sup>. The general flow features are similar to those in the preceding case. Recirculation occurs when  $C_t < 0.96$ . In this case, the calculation with the RNG  $k - \epsilon$  model<sup>8</sup> is also performed for comparison.

Figs. 7(a)-7(c) show the axial mean velocity profiles at three  $C_t$  numbers. All the three models are seen to predict very well the upstream evolution of the flow. As for the downstream development, the results obtained with the RRSAE model remained in good agreement with experiments, while those obtained with the other two models deteriorated with the RNG model producing the largest discrepancies.

The separation and reattachment points of the predicted recirculating bubbles are compared with the experimental data in Fig. 8. The experiment indicated that as  $C_t$  decreased, the separation point moved upstream while the reattachment point remained practically unchanged. The comparison shows that the RRSAE model gives the best predictions for both the separation and reattachment points.

Fig. 9 shows the variation of the recirculating flow rate with  $x$  at  $C_t=0.305$  and  $0.152$ . This is the integral of negative velocities at each cross-section. The experiment indicated that the recirculating flow rate at  $C_t=0.152$  is about 3 times larger than that at  $C_t=0.305$ . The results of the RRSAE model are in good agreement with the experiment while those of the standard  $k - \epsilon$  model and the RNG model show substantial deviations from experiment. As for the maximum recirculating flow rate which is a critical parameter to characterize the performance of combustion chambers, the RRSAE model gives the same result as the experimental data at  $C_t=0.305$  and a 9% overprediction at  $C_t=0.152$  while the other two models produce larger overpredictions. It should be pointed out that results from different measurements<sup>4</sup> for this quantity showed considerable scatter at small  $C_t$  numbers. The results of all the three models are within the experimental scatter.

The variation of the pressure coefficient  $C_p$  along the duct wall is shown in Fig. 10. In the cylindrical duct, the evolution of the pressure is governed by the jet entrainment as well as the contraction and expansion of the flow caused by the recirculating bubble. The decrease in the ambient velocity induced by the entrainment gives rise to an adverse pressure gradient, while the contraction of streamlines produces the opposite effect. These two mechanisms interact more intensely with each other as  $C_t$  decreases, causing the pressure to vary little in the region upstream of the center of the recirculating bubble. In the downstream part of the recirculating bubble, the deceleration of the flow sets up an adverse pressure gradient the

slope of which becomes steeper as  $C_t$  decreases. Therefore, the ability to capture the location of the recirculation center will have a direct impact on the prediction of the pressure. The three models capture the steep pressure gradients in the same way as they capture the ambient velocity minimums. However, for the total pressure rise, an important parameter to the designer of jet pump devices, all the three models are seen to give the same results which are in excellent agreement with the measurements.

#### 2.3.4 Concluding remarks

The extensive comparisons with the experiments clearly show the superiority of the RRSAE model over the standard  $k - \epsilon$  model in all the test cases considered, and the improvement is achieved at an insignificant penalty to the computational efficiency and algorithmic simplicity of the latter.

#### 3. Future Plans

- 1) Further assessment of these new proposals in flows with swirl, in diffusers, in U- and S-shaped ducts, and in a constricted tube;
- 2) Extension of the present code for accommodating second-order closure models.

#### 4. References

- <sup>1</sup> Zhu, J., "FAST-2D: A computer program for numerical simulation of two dimensional incompressible flows with complex boundaries," Rept. No.690, Institute for Hydromechanics, University of Karlsruhe, (1991).
- <sup>2</sup> Driver, D.M. and Seegmiller, H.L., "Features of a reattaching turbulent shear layer in divergent channel flow," AIAA Journal **23**, 63-171 (1985).
- <sup>3</sup> Kim, J., Kline, S.J. and Johnston, J.P., "Investigation of separation and reattachment of a turbulent shear layer: Flow over a backward-facing step," Rept. MD-37, Thermosciences Div., Dept. of Mech. Eng., Stanford University (1978).
- <sup>4</sup> Barchilon, M. and Curtet, R., "Some details of the structure of an axisymmetric confined jet with backflow," Journal of Basic Engineering **86**, 777-787 (1964).
- <sup>5</sup> Binder, G. and Kian, K., "Confined jets in a diverging duct," Proceedings, Turbulent Shear Flows 4, Karlsruhe, 7.18-7.23 (1983).
- <sup>6</sup> Kian, K., "Jets confinés dans un divergent," Doctoral dissertation, l'Université Scientifique et Médicale de Grenoble et l'Institut National Polytechnique de Grenoble, France (1981).
- <sup>7</sup> Launder, B.E. and Spalding, D.B., "The numerical computation of turbulent flow," Computer Methods in Applied Mechanics and Engineering **3**, 269-289 (1974).
- <sup>8</sup> Speziale, C.G. and Thangam, S., "Analysis of an RNG based turbulence model for separated flows," NASA CR-189600 (1992).
- <sup>9</sup> Rodi, W., "Turbulence models and their application in hydraulics - A state of the art review," Book Publication of the International Association for Hydraulic Research, Delft, the Netherlands (1980).

- <sup>10</sup> Ljuboja, M. and Rodi, W., "Calculation of turbulent wall jets with an algebraic Reynolds stress model," *Journal of Fluids Engineering* **102**, 350-356 (1980).
- <sup>11</sup> Leschziner, M.A. and Rodi, W., "Calculation of annular and twin parallel jets using various discretization schemes and turbulence model variations," *Journal of Fluids Engineering* **103**, 352-360 (1981).
- <sup>12</sup> Zhu, J. and Shih, T.-H., "Calculations of turbulent separated flows," NASA TM 106154 (1993).
- <sup>13</sup> Shih, T.-H., Liou, W.W., Shabbir, A., Yang, Z. and Zhu, J., "A vorticity dynamics based model for the turbulent dissipation," NASA TM 106177 (1993).
- <sup>14</sup> Huang, P.G. and Leschziner, M.A., "Stabilization of recirculating-flow computations performed with second moment closures and third order discretization," *Proceedings of the 5th Symposium on Turbulent Shear Flows*, Cornell University, 5.19-5.24 (1985).
- <sup>15</sup> Yoshizawa, A., "Statistical analysis of the derivation of the Reynolds stress from its eddy-viscosity representation," *Physics of Fluids* **27**, 1377-1387 (1984).
- <sup>16</sup> Rubinstein, R. and Barton, J.M., "Nonlinear Reynolds stress models and the renormalization group," *Physics of Fluids A* **2**, 1472-1476 (1990).
- <sup>17</sup> Speziale, C.G., "On nonlinear  $k-l$  and  $k-\epsilon$  models of turbulence," *Journal of Fluid Mechanics* **178**, 459-475 (1987).
- <sup>18</sup> Shih, T.-H. and Lumley, J.L., "Remarks on turbulent constitutive relations," NASA TM 106116 (1993).
- <sup>19</sup> Shih, T.-H., Zhu, J. and Lumley, J.L., "A realizable Reynolds stress algebraic equation model," NASA TM 105993 (1993).
- <sup>20</sup> Zhu, J. and Shih, T.-H., "A numerical study of confined turbulent jets," NASA TM 106197 (1993).
- <sup>21</sup> Zhu, J. and Shih, T.-H., "Computation of confined coflow jets with three turbulence models," AIAA Paper 93-3120.



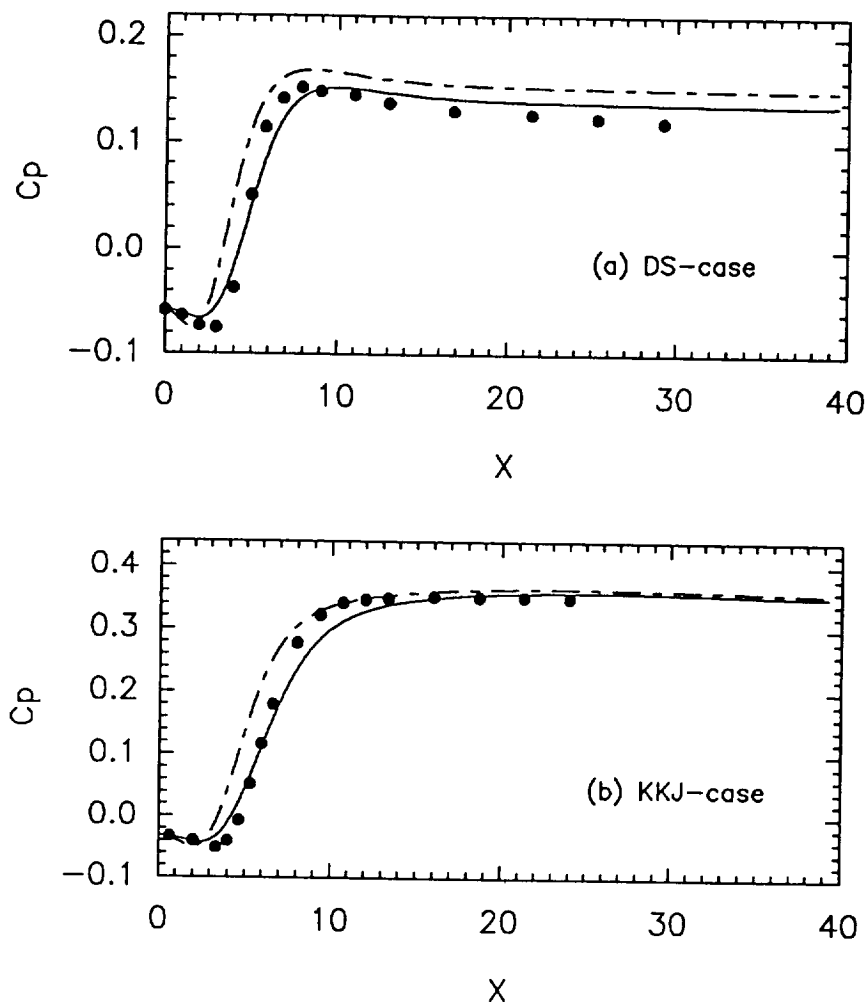


Figure 1. Static pressure coefficient  $C_p$  along the bottom wall.  
 - - -: Standard K- $\epsilon$ ; —: RRSAE model; •: experiment

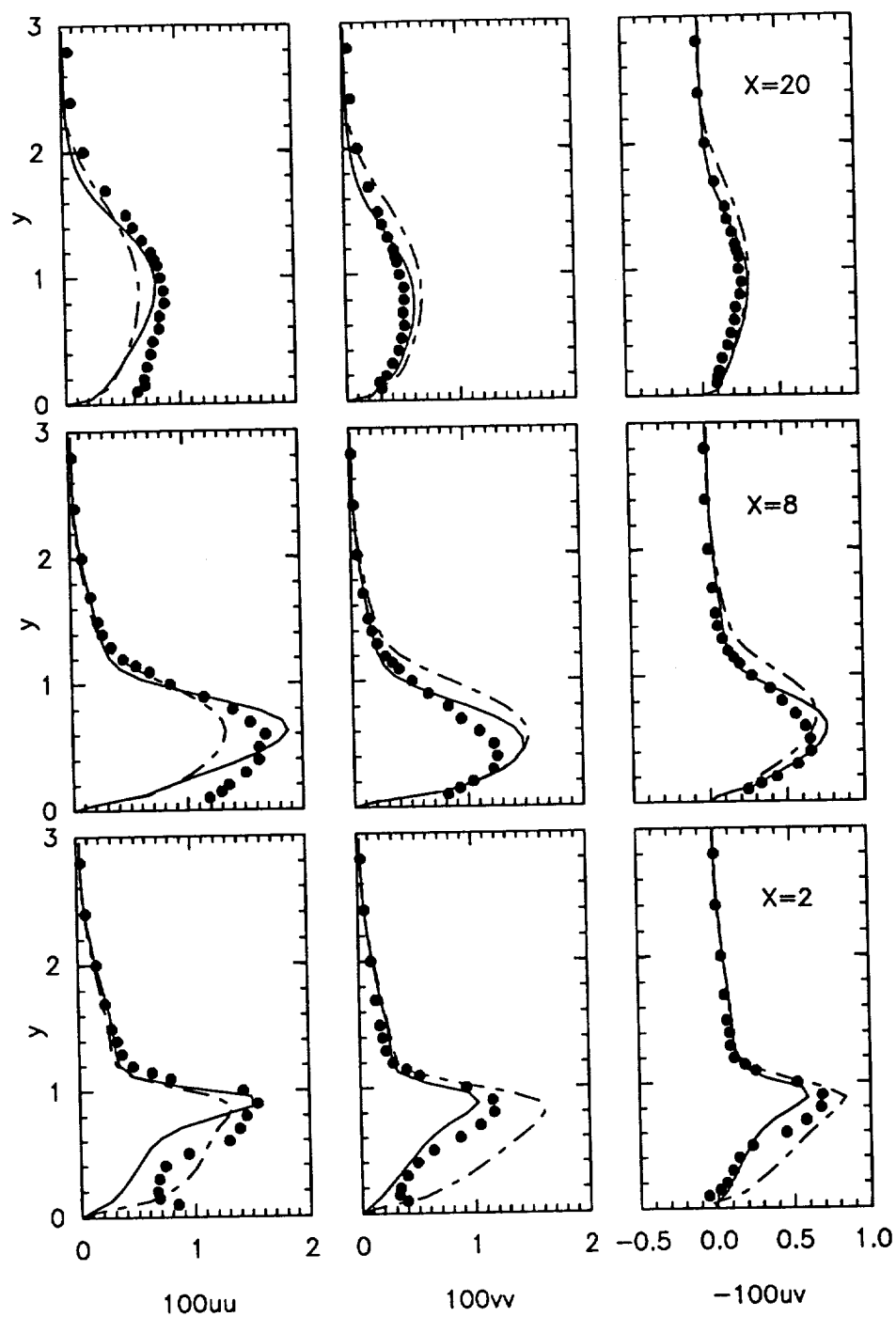


Figure 2. Turbulent stress profiles in DS-case.  
 - - -: Standard  $K-\epsilon$ ; —: RRSAB model; •: experiment

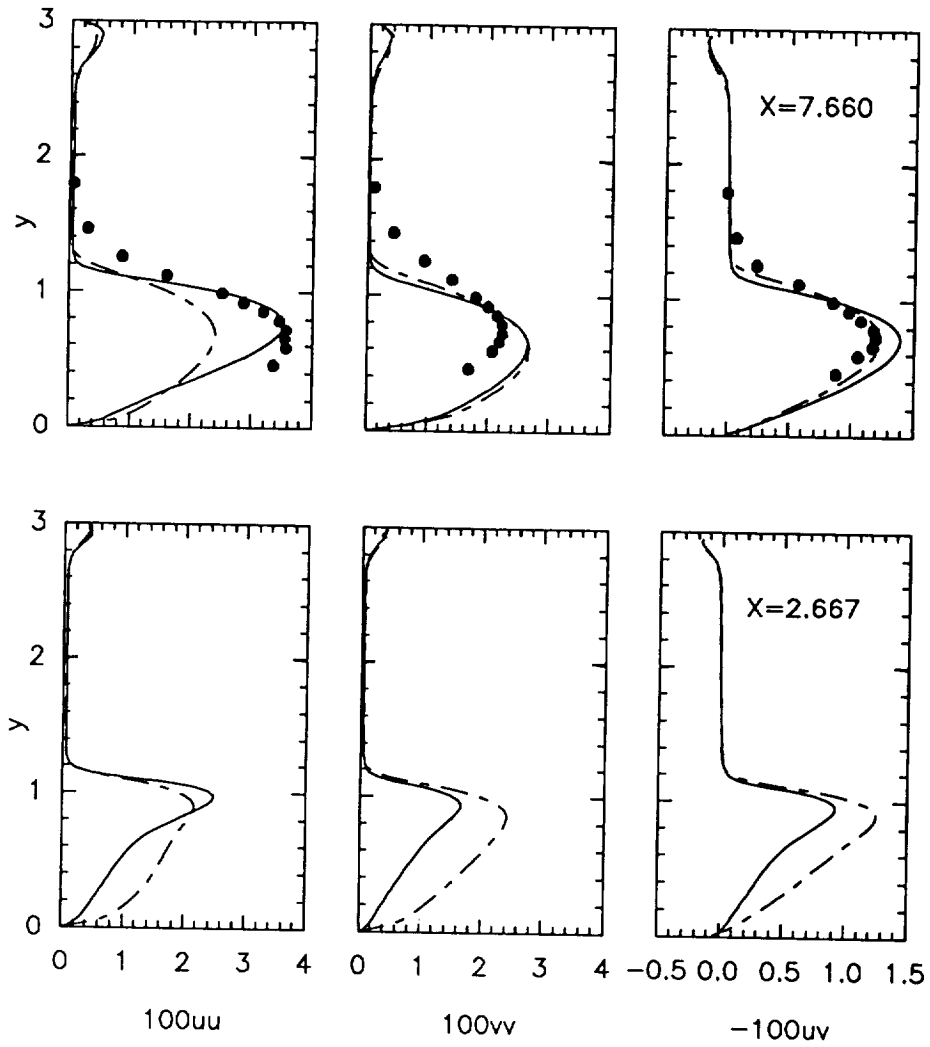


Figure 3. Turbulent stress profiles in KKJ-case.  
 - - -: Standard K- $\epsilon$ ; —: RRSAE model; •: experiment

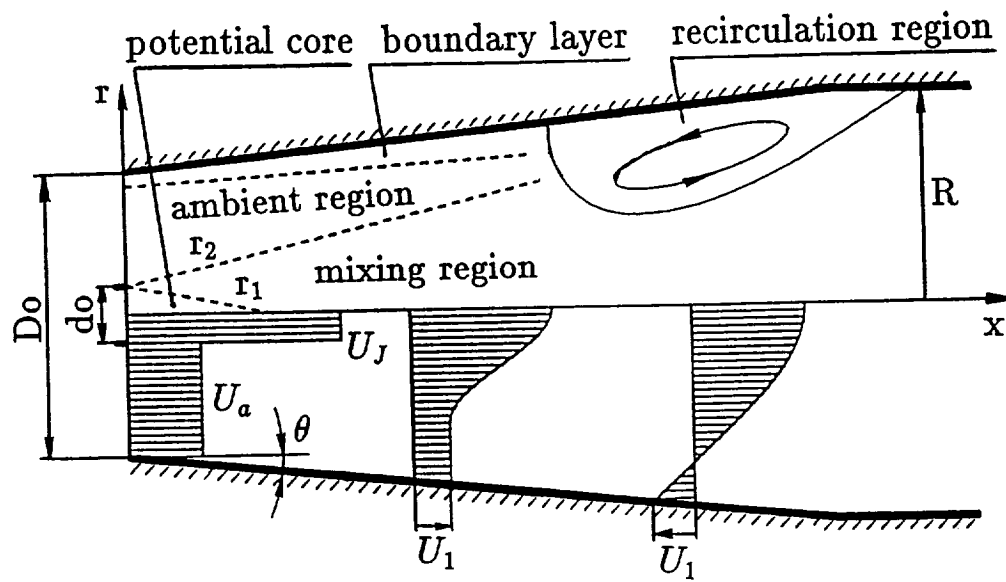


Figure 4. Flow configuration and notations

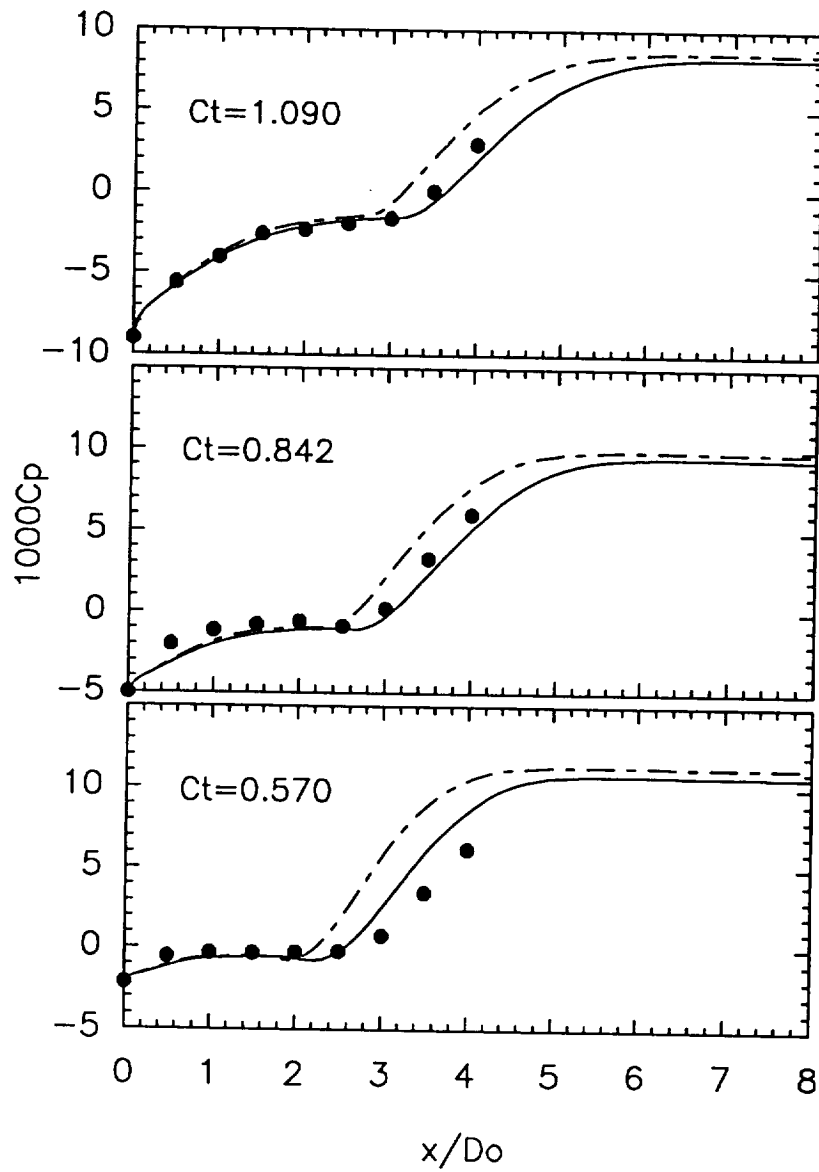


Figure 5. Pressure coefficient along the duct wall in the BK-case  
(Notation as in figure 1)

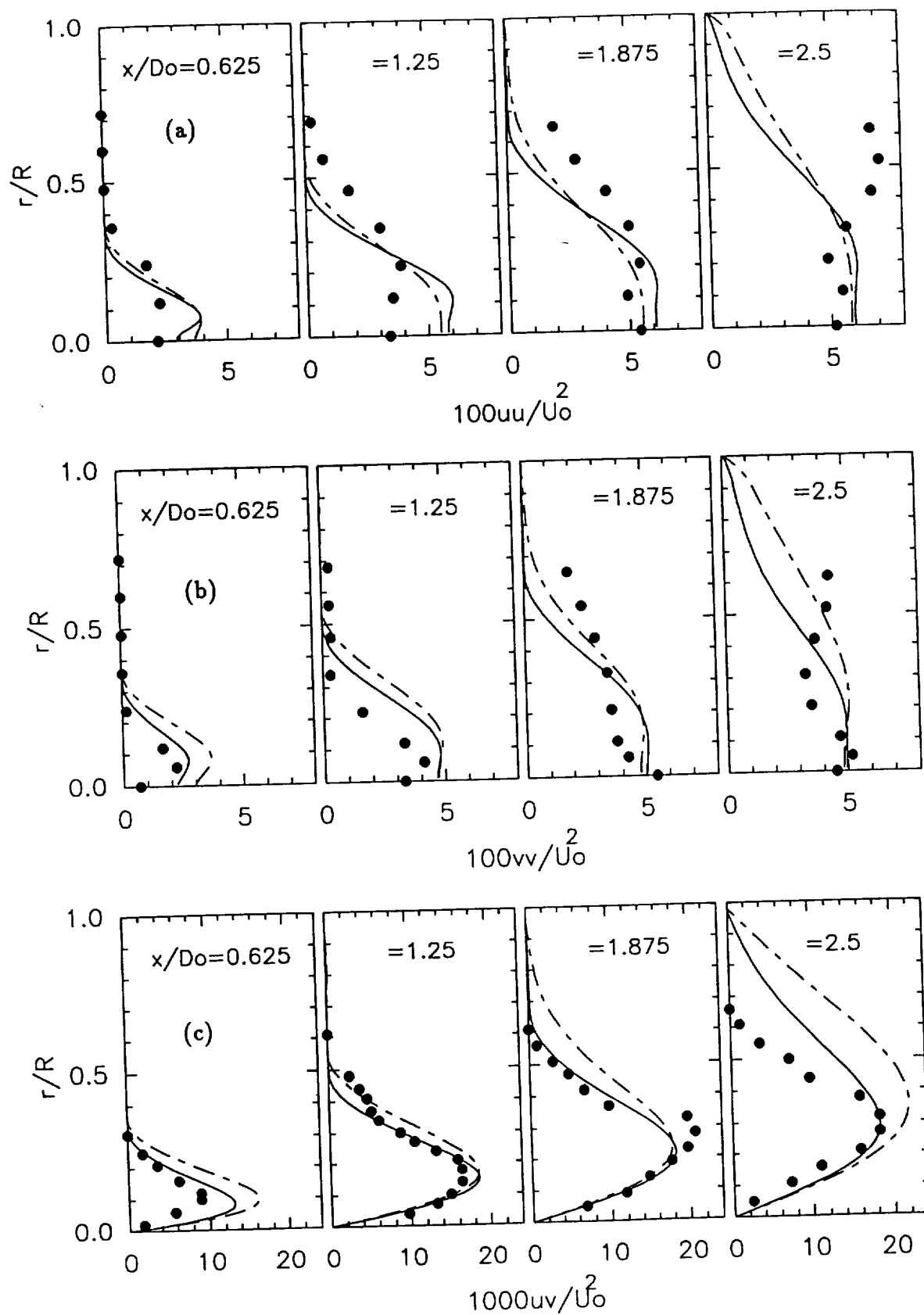


Figure 6. Turbulent stress profiles at  $C_t = 0.59$  in the BK-case  
(Notation as in figure 1)

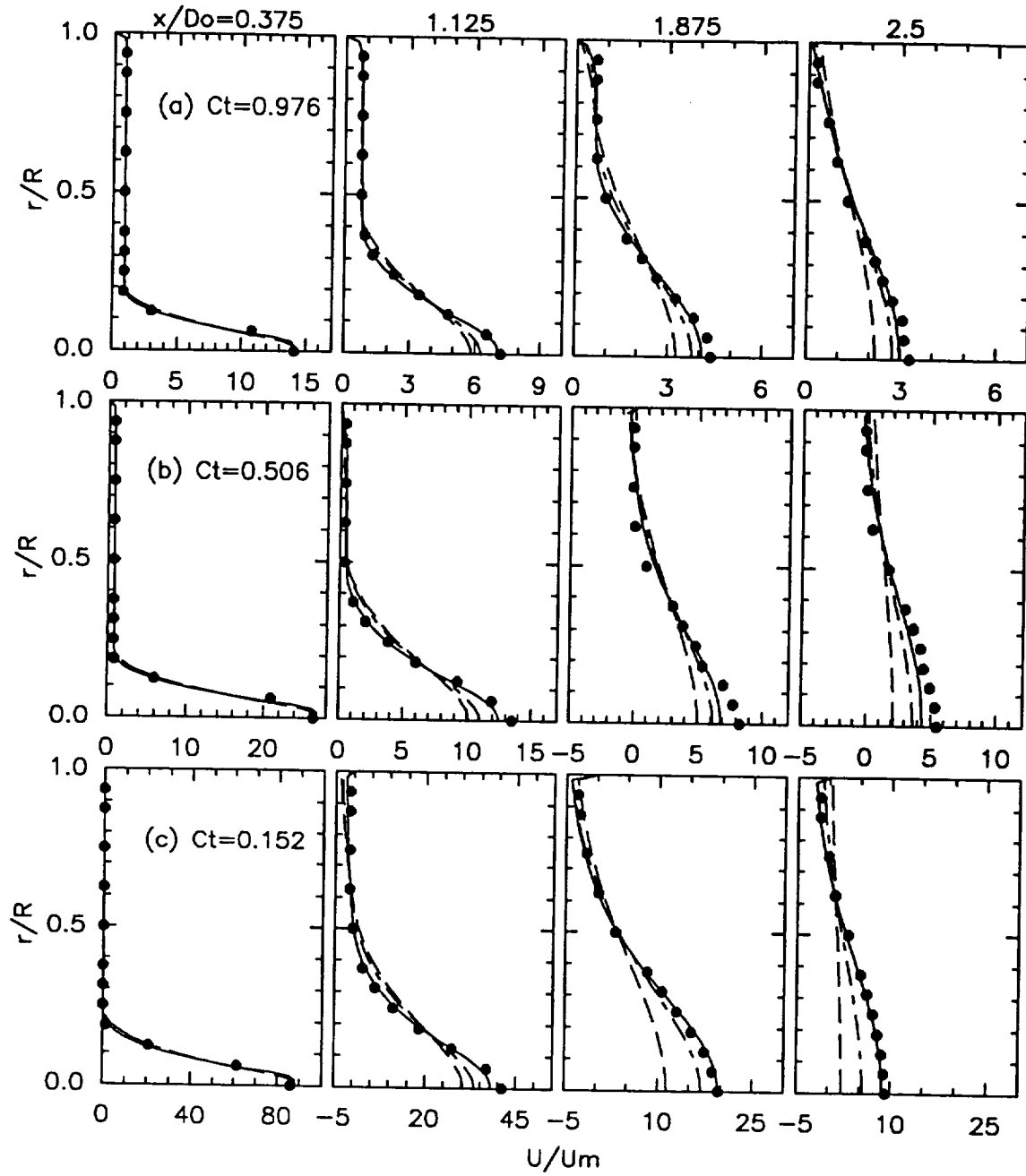


Figure 7 Axial mean velocity profiles. •: Experiment;  
 - - -: Standard  $K-\epsilon$ ; - - -: RNG  $K-\epsilon$ ; —: RRSAB.

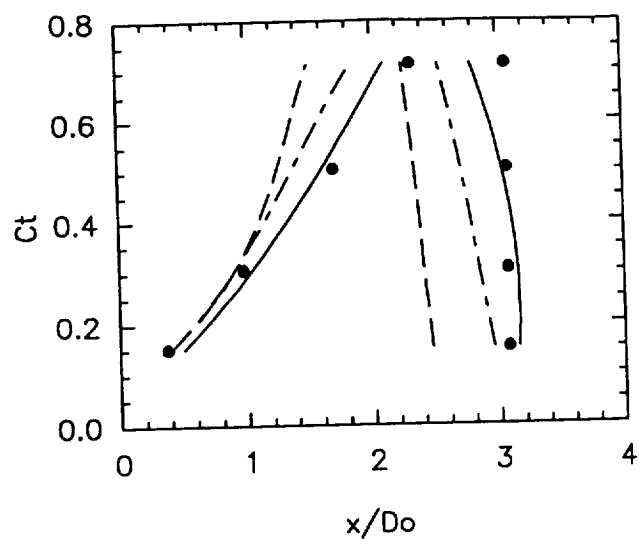


Figure 8 Separation and reattachment points  
(Notation as in Figure 7)

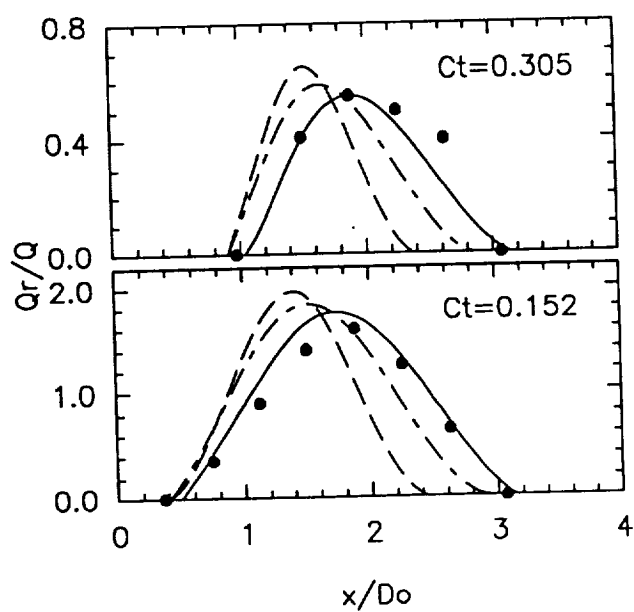


Figure 9 Recirculating flow rate  
(Notation as in Figure 7)

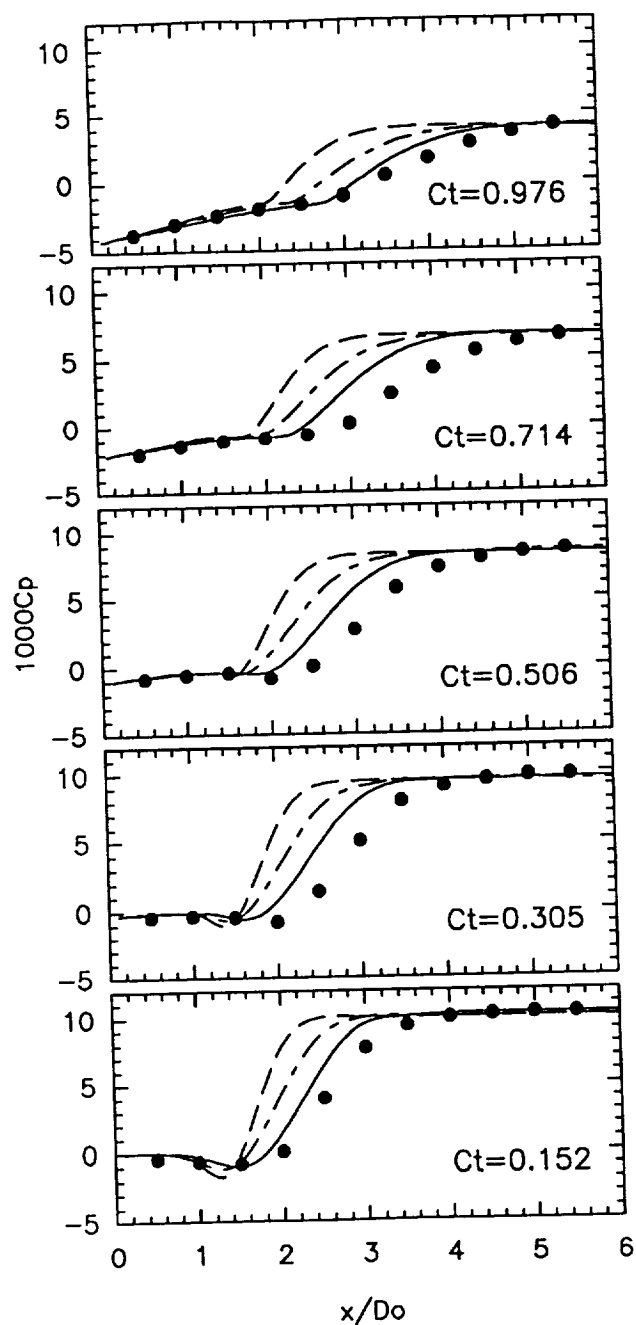


Figure 10 Pressure coefficient at wall  
(Notation as in Figure 7)



## Low $Re_t$ $k - \epsilon$ Models and the Backward-Facing Step Flow

C. J. Steffen, Jr.

### 1. Motivation and Objective

The primary objective of the Center for Modelling of Turbulence and Transition (CMOTT) is to further the understanding of turbulence modelling for engineering applications. One important foundation for this research is the establishment of a data base encompassing the multitude of existing models as well as newly proposed ideas. The research effort described in the next few pages involves a study of several two-equation turbulence models for separated flow over a backward-facing step.

Recently, several authors have examined the performance of two equation models in the context of the backward-facing step flow. Conflicting results, however, demand that further attention is necessary to properly understand the behavior and limitations of this popular technique, especially the low Reynolds number formulations. This is particularly relevant to the application of the near-wall modelling for separated flows. It is well known that the Chien  $k - \epsilon$  model does not accurately resolve skin friction measurements near the reattachment point of a separated shear layer. This is attributed to the behavior of the eddy viscosity damping function. The question remains, however, for other LR models which do not suffer from the same singularity in the damping function. The intention of this study is to investigate several low turbulent Reynolds number (LR) models and compare against the performance of the standard (HR) formulation.

### 2. Work Accomplished

The study of four LR  $k - \epsilon$  models and the standard HR form has been completed. This work is documented in reference<sup>1</sup>. The models investigated include the Chien<sup>2</sup>, Jones-Launder<sup>3</sup>, Launder-Sharma<sup>4</sup>, and Shih-Lumley<sup>5</sup> as well as standard form with a two layer wall function. The experimental reference of Driver and Seegmiller<sup>6</sup> was chosen because of the extensive data including LDV velocity and turbulence profiles throughout the tunnel as well as pressure and skin friction measurements along the tunnel wall. Below I will briefly discuss the numerical methods involved in this analysis. Next I will present a summary of the data and include a figure depicting the most intriguing result.

#### 2.1 Numerical Methods

The Reynolds averaged Navier-Stokes equations for incompressible flow are solved via the pseudo-compressibility technique of Chorin<sup>7</sup>. This permits the use of time marching schemes and the upwind-biased finite volume formulation. Details are given in <sup>1,8</sup>. The system is closed by modeling the Reynolds stress tensor with the mean velocity gradient tensor and a turbulent eddy viscosity. The eddy viscosity is

modeled with turbulent velocity and length scales,  $\sqrt{k}$  and  $\frac{\sqrt{k^3}}{\epsilon}$  respectively. The transport of  $k$  and  $\epsilon$  are modeled as shown below:

$$k_{,t} + U_j k_{,j} - \left[ \left( \nu + \frac{\nu_t}{\sigma_k} \right) k_{,j} \right]_{,j} = \mathcal{P} - \epsilon + D$$

$$\epsilon_{,t} + U_j \epsilon_{,j} - \left[ \left( \nu + \frac{\nu_t}{\sigma_\epsilon} \right) \epsilon_{,j} \right]_{,j} = C_1 f_1 \frac{\epsilon}{k} \mathcal{P} - C_2 f_2 \frac{\epsilon^2}{k} + E$$

where production of turbulent kinetic energy is defined as  $\mathcal{P}$ . The constants  $C_\mu$ ,  $C_1$ ,  $C_2$ ,  $\sigma_k$  and  $\sigma_\epsilon$  are defined a priori. The terms  $D$ ,  $E$ ,  $f_\mu$ ,  $f_1$  and  $f_2$  are damping functions and correction terms for the LR formulation and are necessary to give asymptotically correct behavior if the numerical domain is extended to the wall.

## 2.2 Low $Re_t$ $k - \epsilon$ models

The four low  $Re_t$   $k - \epsilon$  models examined include the Chien, Jones-Launder, Launder-Sharma, and Shih-Lumley. This set was chosen with two criterion in mind: to isolate the effect of the  $y^+$  based damping function of Chien, and to examine the effect of damping functions based solely upon the dependent variable set. As mentioned above, the former effect results in anomalous behavior due to the singularity associated with reattachment. The latter effect leads to a very general damping function which is advantageous for multidimensional flows. The Jones-Launder and Launder-Sharma models are of this latter type. Finally, the Shih-Lumley model was chosen because the damping function is based upon both dependent and independent variables but does not include the  $y^+$  dependence.

## 2.3 Results

The results for the five  $k - \epsilon$  models tested agree for velocity and pressure field data. The trends are also the same for the turbulent kinetic energy and turbulent shear stress data available<sup>1</sup>. The results I wish to call attention to are associated with the skin friction along the step side wall. Below in figure 1, the results are plotted for the normalized tunnel streamwise coordinate ( $x/H$ ) versus the skin friction coefficient ( $C_f$ ). Notice the particularly misleading results associated with the Chien model prediction. The effect of the  $y^+$  dependence can also be observed clearly in a contour plot of the turbulent eddy viscosity<sup>1</sup>. The only appropriate resolution given here results from the standard formulation with the two-layer wall function.

I believe two observations can be made about these results. First, the design of an eddy viscosity damping function ( $f_\mu$ ) appears to have an important effect upon the resolution of the wall shear stress. Secondly, the lack of a pressure gradient effect in the damping functions for this group of low  $Re_t$   $k - \epsilon$  models is causing a premature recovery of the near wall velocity gradient in the redeveloping channel flow. However, the value of the redeveloping channel velocity are underpredicted in this same region. Further investigation into the connection between adverse pressure gradients and the design of an eddy viscosity damping function is needed for this class of models.

### 3. Future Plans

Currently an effort is underway to examine the effect of various turbulence models upon the prediction of separated flow for multistage turbomachinery. This is being conducted within the framework of the average passage technique of Adamczyk<sup>9</sup>. Preliminary results indicate that a change from the Baldwin-Lomax<sup>10</sup> model to that of Johnston-King<sup>11</sup> may indeed improve the numerical prediction of internal passage aerodynamics dominated by secondary flow physics.

### 4. References

- <sup>1</sup> Steffen, C.J., Jr., "A Critical Comparison of Several Low Reynolds Number  $k$ -epsilon Turbulence Models for Flow over a Backward-Facing Step," NASA TM 106173 (1993).
- <sup>2</sup> Chien, K. -Y., "Predictions of Channel and Boundary Layer Flows with a Two Equation Model of Turbulence," AIAA Journal **20**, 33-38 (1982).
- <sup>3</sup> Jones, W.P., and Launder, B.E., "The Calculation of Low-Reynolds Number Phenomena with a Two-Equation Model of Turbulence," International Journal of Heat and Mass Transfer **16**, 1119-1130 (1973).
- <sup>4</sup> Launder, B.E., and Sharma, B.I., "Application of the Energy-Dissipation Model of Turbulence to the Calculation of Flow Near a Spinning Disc," Letters in Heat and Mass Transfer **1**, 131-138 (1974).
- <sup>5</sup> Shih, T.-H., and Lumley, J.L., "Kolmogorov Behavior of Near-Wall Turbulence and Its Application in Turbulence Modeling," NASA TM 105663 (1992).
- <sup>6</sup> Driver, D.M., and Seegmiller, H.L., "Features of a Reattaching Turbulent Shear Layer in Divergent Channel Flow," AIAA Journal **23**, 163-171 (1985).
- <sup>7</sup> Chorin, A.J., "A Numerical Method for Solving Incompressible Viscous Flow Problems," Journal of Computational Physics **2**, 12-26 (1967).
- <sup>8</sup> Steffen, C.J., Jr., "An Investigation of DTNS2D for Use as an Incompressible Turbulence Modelling Testbed," NASA TM 105593 (1993).
- <sup>9</sup> Adamczyk, J.J., "Model Equation for Simulating Flows in Multistage Turbomachinery," ASME Paper 85-GT-226, (1985).
- <sup>10</sup> Baldwin, B., and Lomax, H., "Thin Layer Approximation and Algebraic Model for Separated Turbulent Flow," AIAA Paper 78-0257, (1978).
- <sup>11</sup> Johnson, D.A., and King, L.S., "A Mathematically Simple turbulence Closure Model for Attached and Separated Turbulent Boundary Layers," AIAA Journal **23**, 1684-92 (1985).

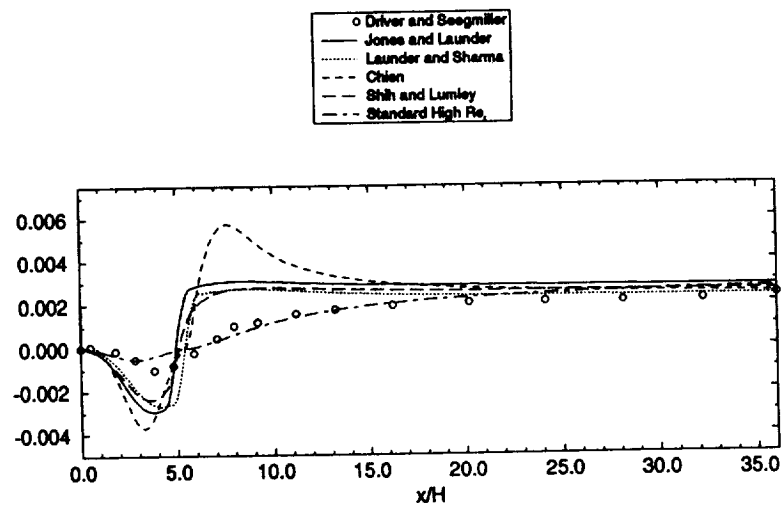


Figure 1 Friction coefficient for the stepside wall downstream of the step

# Modeling of Homogeneous Scalar Turbulence

Aamir Shabbir

## 1. Motivation and Objectives

Modeling of the scalar field of a turbulent flow has lagged the modeling of its velocity field. The most commonly used approaches employ a two equation model to calculate the turbulent eddy viscosity for the turbulent velocity field but assume a constant value of the turbulent Prandtl number to calculate the turbulent scalar diffusivity. Obviously this approach has limitations in situations where the turbulent Prandtl number is not constant.

To overcome this shortcoming, some recent studies have proposed new models in which transport equations for scalar variance and its dissipation rate are solved to calculate the thermal diffusivity. These include, for instance the work of Nagano and Kim<sup>1</sup> and Youssef, Nagano and Tagawa.<sup>2</sup> The later study presents an updated and refined version of Nagano and Kim model.

This study proposes a new two equation model for the scalar turbulence in which transport equations for the scalar variance and its dissipation rate are used to calculate the turbulent scalar flux. This study differs from the other work in the following two respects. (1) In the above cited works, the extension of the scalar dissipation rate is based upon the work of Newman *et al.*<sup>3</sup> who developed the production/destruction mechanisms of the thermal dissipation equation in an analogue fashion to those of the mechanical dissipation rate equation. The model equation proposed in the present study is based on the exact transport equation for scalar dissipation and, its production/destruction mechanisms differ from those proposed in the other studies. (2) The model coefficient in the the scalar flux constitutive relation used in the present study is not a constant but is a function of the local invariants.

Although the newly developed scalar dissipation equation is used in the present study at the two equation level, its use is not restricted to this level of models. It can be used at any level of modeling which requires an equation for this variable. Therefore, in future studies at CMOTT we will be using this new model equation at the second order level. Another ongoing effort at CMOTT is to propose models for bypass transitional flows. The  $k - \epsilon$  model modifications for the velocity field of such a flow have already been proposed and tested by Yang and Shih.<sup>4</sup> The models proposed here will form the basis for the scalar part of such bypass transitional flows.

## 2. Work Accomplished

### 2.1 Model for the Scalar Dissipation Rate Equation

The exact equation for the scalar dissipation,  $\epsilon_\theta = \overline{\gamma \theta_{,i} \theta_{,i}}$ , is

$$\epsilon_{\theta,t} + U_j \epsilon_{\theta,j} = \gamma \epsilon_{\theta,jj} - \gamma (\overline{\theta_{,i} \theta_{,i} u_j})_{,j} - 2 \gamma \overline{\theta_{,i} \theta_{,j}} U_{j,i} - 2 \gamma \overline{\theta_{,i} u_{j,i}} \Theta_{,j}$$

$$-2\gamma\overline{\theta_{,i}u_j}\Theta_{,ij}-2\gamma\overline{\theta_{,i}\theta_{,j}u_{i,j}}-2\gamma^2\overline{\theta_{,ij}\theta_{,ij}} \quad (1)$$

where  $\gamma$  is the molecular thermal diffusivity. The first term on the right hand side of (1) represents the molecular diffusion of scalar dissipation. The second term represents the diffusion by fluctuating velocity field. Third and fourth terms represent the production of scalar dissipation through the gradients of mean velocity and temperature fields. First term on the second line represents the production through mean scalar gradients. Second term on the second line is also a production term for the scalar dissipation rate; it represents the stretching of the scalar eddies through the fluctuating velocity gradients. The last term on the second line represents the destruction of the scalar dissipation rate.

We consider only wall-free flows so that the effects introduced by a wall can be avoided. First we want to do the order of magnitude analysis of (1), for a high Reynolds number flow, to find out which terms can be ignored. For this purpose we assume that:  $l$  is the length scale of the large eddies;  $\theta$  is the scale of the scalar fluctuations; and  $u$  is the scale for velocity fluctuations. Further we estimate that:  $U_{i,j} \sim u/l$ ;  $u_{i,j} \sim (u/l)R_t^{1/2}$ ;  $\Theta_{,i} \sim \theta/l$ ; and  $\gamma\overline{\theta_{,i}\theta_{,i}} \sim (\theta^2/l^2)R_tPr$ . With this scaling the order of magnitude of each term in (1) can be estimated. The result is

$$\epsilon_{\theta,i} + U_j\epsilon_{\theta,j} \sim \frac{\gamma\theta^2u}{l^3} R_tPr \quad (2.a)$$

$$\gamma\epsilon_{\theta,jj} \sim \frac{\gamma\theta^2u}{l^3} \quad (2.b)$$

$$\gamma(\overline{\theta_{,i}\theta_{,i}u_j})_{,j} \sim \frac{\gamma\theta^2u}{l^3} R_tPr \quad (2.c)$$

$$2\gamma\overline{\theta_{,i}\theta_{,j}U_{j,i}} \sim \frac{\gamma\theta^2u}{l^3} R_t^{1/2}Pr \quad (2.d)$$

$$2\gamma\overline{\theta_{,i}u_{j,i}}\Theta_{,j} \sim \frac{\gamma\theta^2u}{l^3} R_tPr^{1/2} \quad (2.e)$$

$$2\gamma\overline{\theta_{,i}u_j}\Theta_{,ij} \sim \frac{\gamma\theta^2u}{l^3} Pr^{1/2} \quad (2.f)$$

$$2\gamma\overline{\theta_{,i}\theta_{,j}u_{i,j}} \sim \frac{\gamma\theta^2u}{l^3} R_t^{3/2}Pr \quad (2.g)$$

$$2\gamma^2\overline{\theta_{,ij}\theta_{,ij}} \sim \frac{\gamma\theta^2u}{l^3} R_t^{3/2}Pr \quad (2.f)$$

Note that we have used the following relation to estimate  $2\gamma\overline{\theta_{,i}\theta_{,j}U_{j,i}}$

$$\overline{\theta_{,i}\theta_{,j}} \approx \frac{\theta^2}{l^2} R_t(a\delta_{ij} + c_{ij}R_t^{-1/2} + \dots) \quad (3)$$

where  $a$  and  $c_{ij}$  are coefficients of order one. (This is similar to the estimate of  $\overline{\omega_i\omega_j}$  made by Tennekes and Lumley<sup>5</sup>). It should also be noted that the estimate (2.e) above is more liberal than obtained by some of the other studies.

So to the leading order we find that

$$-2\gamma\overline{\theta_{,i}\theta_{,j}u_{i,j}} \sim 2\gamma^2\overline{\theta_{,ij}\theta_{,ij}} \quad (4)$$

Based on (2) and (4) we expect that  $-2\gamma\overline{\theta_{,i}\theta_{,j}u_{i,j}} - 2\gamma^2\overline{\theta_{,ij}\theta_{,ij}}$  should be of  $R_t$  order. From (2) we also conclude that, for a large Reynolds number flow,  $\gamma\epsilon_{\theta,jj}$ ,  $2\gamma\overline{\theta_{,i}\theta_{,j}U_{j,i}}$  and  $2\gamma\overline{\theta_{,i}u_j\Theta_{,ij}}$  are of relatively smaller magnitude and, therefore, can be neglected. Under these assumptions, therefore, (1) reduces to

$$\epsilon_{\theta,t} + U_j\epsilon_{\theta,j} = -\gamma(\overline{\theta_{,i}\theta_{,i}u_j})_{,j} - 2\gamma\overline{\theta_{,i}u_{j,i}\Theta_{,j}} - 2\gamma\overline{\theta_{,i}\theta_{,j}u_{i,j}} - 2\gamma^2\overline{\theta_{,ij}\theta_{,ij}} \quad (5)$$

**Modeling of  $2\gamma\overline{\theta_{,i}u_{j,i}\Theta_{,j}}$ :**

First we define a tensor  $\phi_j$  as

$$\phi_j = \frac{\overline{\theta_{,i}u_{j,i}}}{\sqrt{\overline{\theta_{,k}\theta_{,k}}\overline{u_{l,m}u_{l,m}}}} \quad (6)$$

Using this definition we can write

$$2\gamma\overline{\theta_{,i}u_{j,i}\Theta_{,j}} = 2\gamma\sqrt{\overline{\theta_{,k}\theta_{,k}}\overline{u_{l,m}u_{l,m}}} \phi_j \Theta_{,j} \quad (7)$$

Modeling  $\phi_j \propto \Theta_{,j}/\Phi$  (where  $\Phi = \sqrt{\overline{\Theta_{,k}\Theta_{,k}}}$ ), and after some manipulation of (7) we obtain the following result

$$2\gamma\overline{\theta_{,i}u_{j,i}\Theta_{,j}} = C_{\theta 2} \frac{\sqrt{\epsilon_{\theta}\epsilon}}{\sqrt{Pr}} \Phi \quad (8)$$

where  $Pr = \nu/\gamma$  and  $C_{\theta 2}$  is a model coefficient.

**Modeling of  $-2\gamma\overline{\theta_{,i}\theta_{,j}u_{i,j}} - 2\gamma^2\overline{\theta_{,ij}\theta_{,ij}}$ :**

We define a tensor  $b_{ij}^{\prime\theta}$  as

$$b_{ij}^{\prime\theta} = \frac{\overline{\theta_{,i}\theta_{,j}}}{\overline{\theta_{,k}\theta_{,k}}} - \frac{1}{3}\delta_{ij} \quad (9)$$

Using this definition  $2\gamma\overline{\theta_{,i}\theta_{,j}u_{i,j}}$  can be expressed in terms of  $b_{ij}^{\prime\theta}$  as

$$2\gamma\overline{\theta_{,i}\theta_{,j}u_{i,j}} = 2\gamma\overline{\theta_{,k}\theta_{,k}(b_{ij}^{\prime\theta} + \delta_{ij}/3)u_{i,j}} \quad (10)$$

Modeling  $b_{ij}^{\prime\theta} \propto s'_{ij}/s$  (where  $s'_{ij} = (u_{i,j} + u_{j,i})/2$ , and  $s = \sqrt{2s'_{ij}s'_{ij}}$ ) and substituting  $u_{i,j} = s'_{i,j} + w'_{i,j}$  (where  $w'_{i,j} = (u_{i,j} - u_{j,i})/2$ ) we have

$$2\gamma\overline{\theta_{,i}\theta_{,j}u_{i,j}} \propto \overline{2\gamma\theta_{,k}\theta_{,k}\frac{s'_{ij}}{s}s'_{ij}} \quad (11)$$

As was discussed earlier, each  $2\gamma\overline{\theta_{,i}\theta_{,j}u_{i,j}}$  and  $2\gamma^2\overline{\theta_{,ij}\theta_{,ij}}$  is of order  $R_t^{3/2}$  but their sum is of order  $R_t$ . This suggests that the sum of these two terms can be modeled by the following three terms

$$\frac{\sqrt{\epsilon_\theta\epsilon}}{\sqrt{Pr}}\Phi, \quad \epsilon_\theta S, \quad \frac{\epsilon_\theta\epsilon}{(k + \sqrt{\nu\epsilon})} \quad (12)$$

where  $S = \sqrt{S_{ij}S_{ij}}$  and  $S_{ij} = (U_{i,j} + U_{j,i})/2$ . Note that the first term is the same as the model for  $2\gamma\overline{\theta_{,i}u_{j,i}\Theta_{,j}}$  obtained above. So both of these terms can be combined together into one term.

Therefore, the final form of the modeled scalar dissipation equation becomes

$$\epsilon_{\theta,t} + U_j\epsilon_{\theta,j} = -(\overline{u_j\epsilon_\theta})_{,j} + C_{\theta 1}\epsilon_\theta S + C_{\theta 2}\frac{\sqrt{\epsilon_\theta\epsilon}}{\sqrt{Pr}}\Phi - C_{\theta 3}\frac{\epsilon_\theta\epsilon}{(k + \sqrt{\nu\epsilon})} \quad (13)$$

where  $C_{\theta 1}$ ,  $C_{\theta 2}$ , and  $C_{\theta 3}$  are the model coefficients.

## 2.2 Determination of Model Coefficients

There are three model coefficients in equation (13) and these are yet to be determined. These can be determined by considering a hierarchy of flows of increasing complexity so that each flow allows calibration of one coefficient at a time.

First we consider decaying homogeneous turbulence. Warhaft and Lumley<sup>6</sup> found that in such a flow the time scale ratio  $r = \frac{2k}{\epsilon} \frac{\epsilon_\theta}{\theta^2}$  remains unchanged. Substituting  $\frac{Dr}{Dt} = 0$  in equation (A12) we obtain the following relation

$$C_{\theta 3} = C_2 - 1 + r \quad (14)$$

where  $C_2$  is the constant appearing in the decay term of the mechanical dissipation equation and is 1.9 for the model used in the present study (see appendix A).

To determine the second constant  $C_{\theta 2}$  in (13), we use the same approach as used by Jones and Musonge<sup>7</sup> and Nagano and Kim<sup>1.1</sup> Both of these references used the fact that in experiments on homogenous turbulence with non-zero mean temperature gradients (Sirivat and Warhaft<sup>8</sup>) the time scale ratio approached a constant value toward the downstream end of the flow i.e.  $\frac{Dr}{Dt} \rightarrow 0$  for large  $t$ . We use this experimental finding to obtain a value for  $C_{\theta 2}$ . Therefore, by letting  $\frac{Dr}{Dt} = 0$  for this experiment we obtain

$$C_{\theta 2} = \frac{2}{Pr^{1/2}} \rho_{vt} \left(\frac{r}{3}\right)^{1/2} \quad (15)$$

where  $\rho_{vt}$  is the cross-stream heat flux correlation coefficient. Upon substituting the asymptotic values of quantities from the experiment of Sirivat and Warhaft in the above equation we obtain  $C_{\theta 2} = 1.28$ . (Experiment suggests a value of 1.4 but in computations a value of 1.28 gives a better overall agreement.) The last constant to be determined in the scalar dissipation equation is  $C_{\theta 1}$ . For this purpose the homogeneous shear flow experiment of Tavoularis and Corrsin<sup>9</sup> to obtain  $C_{\theta 1} = 0.1$ .



### 2.3 Modeling of the Heat Flux

In order to complete the model for the scalar turbulence, an expression is needed for the heat flux tensor  $\overline{u_i \theta}$ . We use the model proposed by Shih and Lumley<sup>10</sup>. We keep only those terms of their model which are linear in the mean temperature gradient. i.e.

$$\overline{u_i \theta} = a_1 \frac{k^2}{\epsilon} \left(\frac{2}{r}\right)^{1/2} \Theta_{,i} + \frac{k^3}{\epsilon^2} \left(\frac{2}{r}\right)^{1/2} (a_2 U_{i,j} + a_3 U_{j,i}) \Theta_{,j} \quad (16)$$

The above model expression is the same as obtained by Yoshizawa<sup>11</sup> and Rubenstein and Barton<sup>12</sup> using DIA and RNG approaches respectively. Our purpose now is to determine the model coefficients  $a_1$  and  $a_2$ . We point out that the term involving the coefficient  $a_3$  is zero for all the flows considered in this study and, therefore, this coefficient is left undetermined for now. In order to determine  $a_1$  we hypothesize a situation where

$$\frac{D}{Dt} \frac{\overline{u_i \theta}}{(k\theta^2)^{1/2}} = \alpha S$$

with  $\alpha$  is a constant. Of course one can make other assumptions which could be more general than this. However, this assumption seems to be adequate for the homogeneous flows considered in this study and, therefore, we will be using this as a **guide** in obtaining the formulation for  $a_1$ . After differentiating the above expression we obtain

$$\frac{D\overline{u_i \theta}}{Dt} - \frac{1}{2\theta^2} \frac{D\theta^2}{Dt} - \frac{1}{2k} \frac{Dk}{Dt} = \alpha S \sqrt{k\theta^2} \quad (17)$$

We restrict our attention to homogeneous flows and substitute the transport equations for  $k$ ,  $\theta^2$  and  $\overline{u_i \theta}$  in the above relation. We note that in order to do so we need a closed (modeled) equation for the heat flux. We employ the model equation of Shih and Lumley<sup>13</sup>. After substituting these transport equations in (17) and then replacing  $\overline{u_i u_j}$  and  $\overline{u_i \theta}$  with their constitutive relations (A3) and (A9) we obtain a quadratic equation for the constant  $a_2$ . The final solution of this quadratic equation is further simplified to obtain the following expression for  $a_1$ .

$$a_1 = -0.72 \frac{\epsilon \epsilon_\theta}{4k^2 \Phi^2 \sqrt{r}} (r^2 + 2r + 2) + \frac{\epsilon_\theta}{\theta^2 \epsilon \sqrt{r}} \frac{(2k/3 - .45S \sqrt{\theta^2 q^2 / \Phi})}{(r^2 + 2r + 2)} \quad (18)$$

The second constant  $a_2$  is calibrated from the experiment of Tavoularis and Corrsin<sup>9</sup> and is found to be about 0.024.

### 2.4 Application of Model to Homogeneous Flows

The present model for homogeneous flows is summarized in Appendix A. We compute some homogeneous flows using this model to see if it can reproduce them

reasonably. For these homogeneous flows the model represents four ordinary differential equations for  $k$ ,  $\epsilon$ ,  $\overline{\theta^2}$ , and  $\epsilon_\theta$  and constitutes an initial value problem. These equations were solved using a fourth order Runge-Kutta method. The assessment of the  $k - \epsilon$  model used with the present model has already been reported in Shih *et al.*<sup>14</sup>. Therefore, we will be showing results for only the scalar field. For comparison we will also be showing results obtained from Youssef, Nagano and Tagawa model<sup>2</sup> (hereafter referred to as YNT model). Figures 1-7 shows results for the homogeneous flow experiment<sup>6</sup> which has a constant cross-stream temperature gradient  $d\Theta/dy$  (but no velocity gradients). The agreement between the present model and experiment is reasonable for most of the cases, and better than the YNT model in all the cases. We do note, however, that the present model overpredicts the measured temperature variance for the case shown in figure 2 and underpredicts the same quantity for the case shown in figure 4. The model performs poorly for the case shown in figure 7. In this case the experiment shows that the temperature variance first decreases until about  $x/M = 70$  and then increases. Prediction of this kind of behavior is beyond the scope of the kind of algebraic models presented here for the heat flux (i.e. equation 18). The heat flux model given by equation (18) can not produce a decrease in its level. Thus the production term  $-u_i\theta\Theta_{,i}$  in the temperature variance equation also increases instead of decreasing. This leads to the continuous increase in the temperature variance level. The correct way to handle the kind of experimental behaviour shown in figure 7 is to use an evolution equation for the heat flux rather than the algebraic expressions like (18).

The results for the homogeneous shear flow which has constant cross-stream temperature and velocity gradients are shown in figure 8. Both the temperature variance and the thermal dissipation rate predicted by the current model are in reasonable agreement with the experiment of Tavoularis and Corrsin<sup>9</sup>. On the other hand YNT model overpredicts the experiment.

### 3. Future Plans

The model proposed here has been tested for simple homogeneous flows. We will extend the model to wall bounded flows, such as a heated flat plate.

### 4. References

- <sup>1</sup> Nagano, Y. and C. Kim. "A two equation model for heat transport in wall turbulent shear flows", J. Heat Transfer, 110, 583-589, (1988).
- <sup>2</sup> Youssef, M.S., Y. Nagano and M. Tagawa. "A two-equation heat transfer model for predicting turbulent thermal fields under arbitrary wall thermal conditions", Int. J. Heat Mass Transfer, 35, 11, 3095-3104, (1992).
- <sup>3</sup> Newman, G.R., B.E. Launder and J.L. Lumley. "Modeling the behaviour of homogeneous scalar turbulence", J. Fluid Mech., 111, 217-232, (1981).
- <sup>4</sup> Yang, Z. and T.H. Shih. "A  $k - \epsilon$  model for turbulent and transitional boundary layers", Proceedings of the International conference on Near-Wall Turbulent Flows, Edited by R.M. So, C.G. Speziale and B.E. Launder, 165-175, (1993).

- <sup>5</sup> Tennekes, H., and J.L. Lumley. "A First Course in Turbulence". The MIT Press, (1972).
- <sup>6</sup> Warhaft, Z., and J.L. Lumley. "An experimental study of the decay of temperature fluctuations in grid-generated turbulence", *J. Fluid Mech.*, 88, 659-684, (1978).
- <sup>7</sup> Jones, W.P., and P. Musonge. "Closure of the Reynolds stress and scalar flux equations", *Phys. Fluids*, 31, 3589-3604, (1988).
- <sup>8</sup> Sirivat, A., and Z. Warhaft. "The effect of a passive cross-stream temperature gradient on the evolution of temperature variance and heat flux in grid turbulence", *J. Fluid Mech.*, 128, 326-346, (1983).
- <sup>9</sup> Tavoularis, S., and S. Corrsin. "Experiments in nearly homogeneous turbulent shear flow with a uniform mean temperature gradient", Part 1, *J. Fluid Mech.*, 104, 311-347, (1981).
- <sup>10</sup> Shih, T.-H., and J.L. Lumley. "Remarks on turbulent constitutive relations", NASA TM 106116, (1993).
- <sup>11</sup> Yoshizawa, A. "Statistical modelling of passive-scalar diffusion in turbulent shear flows", *J. Fluid Mech.*, 195, 541-555, (1988).
- <sup>12</sup> Rubinstein, R., and J.M. Barton. "Renormalization group analysis of anisotropic diffusion in turbulent shear flows", *Phy. Fluids A*, 3, 415-421, (1991).
- <sup>13</sup> Shih T.-H., and J.L. Lumley. "Influence of timescale ratio on scalar flux relaxation: modelling Sirivat & Warhaft's homogeneous passive scalar fluctuations", *J. Fluid Mech.*, 162, 211-22, (1986).
- <sup>14</sup> Shih, T.-H., W.W. Liou, A. Shabbir, Z. Yang and J. Zhu. "A vorticity dynamics based model for the turbulent dissipation", NASA TM 106177, (1993).

### Appendix A

The model used in the present study is summarized below for homogeneous flows. (Note that the  $k - \epsilon$  model used is that of Shih *et al.*<sup>14</sup>.)

$$U_j \frac{\partial k}{\partial x_j} = -\overline{u_i u_j} \frac{\partial U_i}{\partial x_j} - \epsilon \quad (A1)$$

$$U_j \frac{\partial \epsilon}{\partial x_j} = C_1 S \epsilon - C_2 \frac{\epsilon^2}{k} \quad (A2)$$

$$\overline{u_i u_j} = \nu_T (U_{i,j} + U_{j,i}) - \frac{2}{3} k \delta_{ij} \quad (A3)$$

$$\nu_T = C_\mu \frac{k^2}{\epsilon}, \quad C_\mu = \frac{2/3}{1.25 + \eta + 0.9\xi} \quad (A4)$$

where

$$\eta = \frac{kS}{\epsilon}, \quad \xi = \frac{k\Omega}{\epsilon}, \quad S = \sqrt{S_{ij}S_{ij}}, \quad \Omega = \sqrt{2\Omega_{ij}^*\Omega_{ij}^*} \quad (A5)$$

and

$$S_{ij} = \frac{1}{2} \left( \frac{\partial U_i}{\partial x_j} + \frac{\partial U_j}{\partial x_i} \right), \quad \Omega_{ij}^* = \frac{1}{2} \left( \frac{\partial U_i}{\partial x_j} - \frac{\partial U_j}{\partial x_i} \right) \quad (A6)$$

The constants in the  $\epsilon$  equation are:  $C_1 = 0.42$  and  $C_2 = 1.9$ .

$$U_j \frac{\partial \overline{\theta^2}}{\partial x_j} = -2\overline{u_i \theta} \frac{\partial \Theta}{\partial x_i} - 2\epsilon_\theta \quad (A7)$$

$$U_j \frac{\partial \epsilon_\theta}{\partial x_j} = C_{\theta 1} \epsilon_\theta S + C_{\theta 2} \frac{\sqrt{\epsilon_\theta \epsilon \Phi}}{\sqrt{Pr}} - C_{\theta 3} \frac{\epsilon_\theta \epsilon}{k} \quad (A8)$$

$$\overline{u_i \theta} = a_1 \frac{k^2}{\epsilon} \left( \frac{2}{r} \right)^{1/2} \Theta_{,i} + \frac{k^3}{\epsilon^2} \left( \frac{2}{r} \right)^{1/2} (a_2 U_{i,j} + a_3 U_{j,i}) \Theta_{,j} \quad (A9)$$

where

$$a_1 = -0.72 \frac{\epsilon \epsilon_\theta}{4k^2 \Phi^2 \sqrt{r}} (r^2 + 2r + 2) + \frac{\epsilon_\theta}{\theta^2 \epsilon \sqrt{r}} \frac{(2k/3 - .55S \sqrt{\theta^2 q^2 / \Phi})}{(r^2 + 2r + 2)} \quad (A10)$$

and  $\Phi = \sqrt{\Theta_{,i} \Theta_{,i}}$ . The constants in the  $\epsilon_\theta$  equation are:

$$C_{\theta 1} = 0.1, \quad C_{\theta 2} = 1.28, \quad C_{\theta 3} = C_2 - 1 + r \quad (A11)$$

The evolution equation for the time scale ratio  $r = \frac{2k}{\epsilon} \frac{\epsilon_\theta}{\theta^2}$  (used in section 2.2) can be obtained by differentiating this relation by parts and then substituting the equations for  $k$ ,  $\epsilon$ ,  $\overline{\theta^2}$  and  $\epsilon_\theta$  as given above. The result is

$$\begin{aligned} \frac{Dr}{Dt} = & (C_{\theta 1} S - C_1 S - \frac{\overline{u_i u_j}}{k} \frac{\partial U_i}{\partial x_j}) r + [C_{\theta 2} (Pr \frac{\epsilon}{\epsilon_\theta})^{1/2} \Phi - 2 \frac{\overline{u_i \theta}}{\theta^2} \frac{\partial \Theta}{\partial x_i}] r \\ & + (-2C_{\theta 3} - 2 + 2C_2 + 2r) \frac{\epsilon_\theta}{\theta^2} \end{aligned} \quad (A12)$$

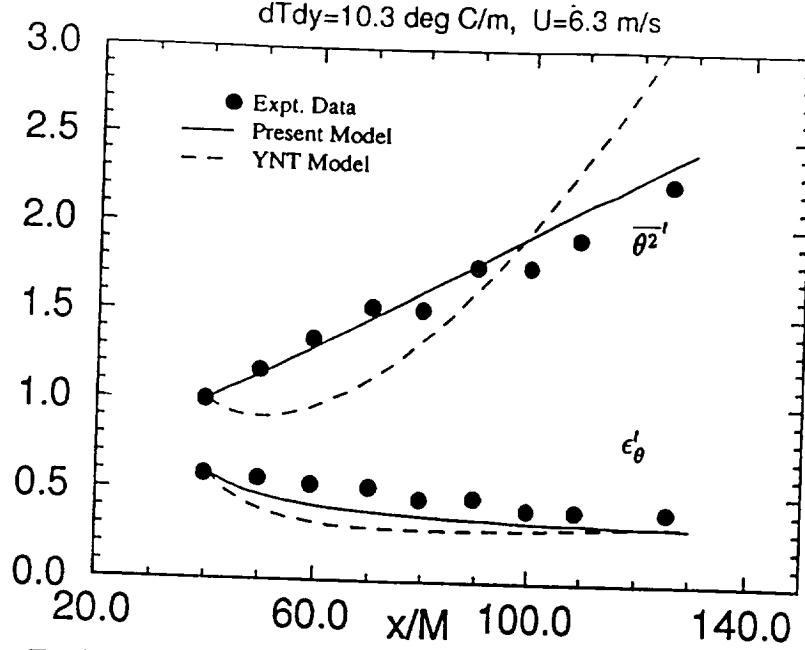


Figure 1. Evolution of the normalized temperature variance and thermal dissipation rate in the experiment of Sirivat and Warhaft (1983). The temperature variance is normalized as  $\overline{\theta^2}' = \overline{\theta^2}/\overline{\theta^2}_0$  and the thermal dissipation is normalized as  $\epsilon'_\theta = \frac{\epsilon_\theta}{\overline{\theta^2}_0 u_0/l_0}$ . For this case  $\overline{\theta^2}_0 = 0.0128 \text{ } ^\circ\text{C}^2$ ,  $u_0 = 0.145515 \text{ m/s}$ , and  $l_0 = 0.011937 \text{ m}$ .

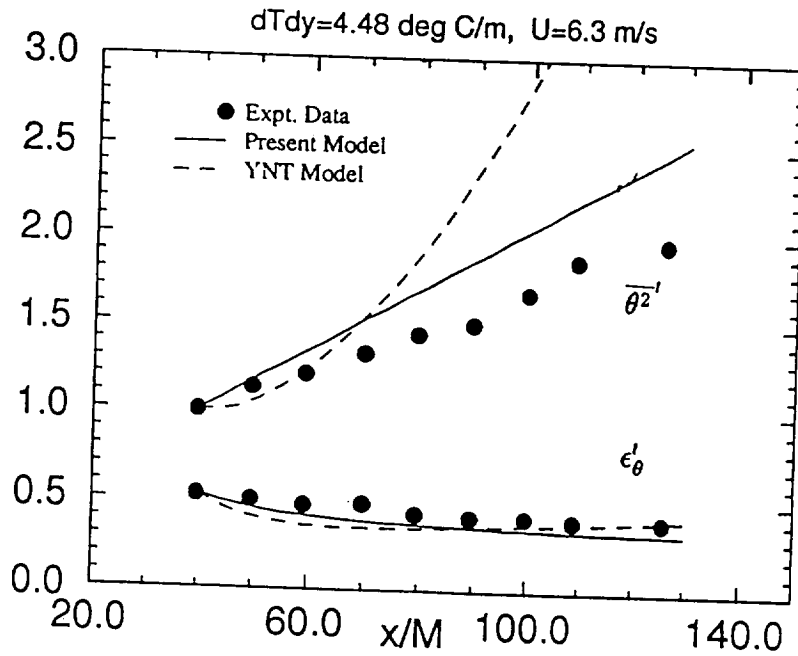


Figure 2. Evolution of the normalized temperature variance and thermal dissipation rate in the experiment of Sirivat and Warhaft (1983). The temperature variance is normalized as  $\overline{\theta^2}' = \overline{\theta^2}/\overline{\theta^2}_0$  and the thermal dissipation is normalized as  $\epsilon'_\theta = \frac{\epsilon_\theta}{\overline{\theta^2}_0 u_0/l_0}$ . For this case  $\overline{\theta^2}_0 = 0.002287 \text{ } ^\circ\text{C}^2$ ,  $u_0 = 0.145515 \text{ m/s}$ , and  $l_0 = 0.011937 \text{ m}$ .

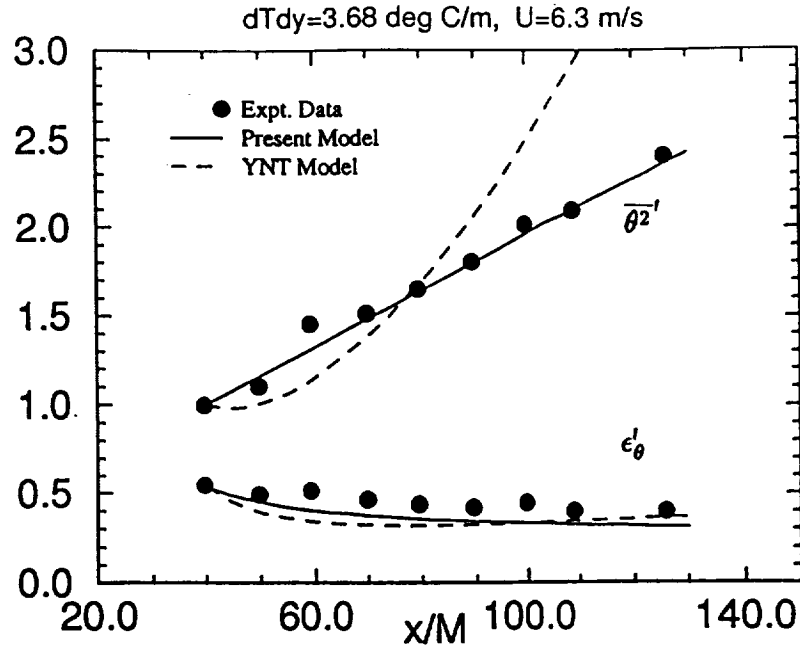


Figure 3. Evolution of the normalized temperature variance and thermal dissipation rate in the experiment of Sirivat and Warhaft (1983). The temperature variance is normalized as  $\overline{\theta^2}' = \overline{\theta^2}/\overline{\theta^2}_0$  and the thermal dissipation is normalized as  $\epsilon_\theta' = \frac{\epsilon_\theta}{\overline{\theta^2}_0 u_0/l_0}$ . For this case  $\overline{\theta^2}_0 = 0.001705 \text{ } ^\circ\text{C}^2$ ,  $u_0 = 0.145515 \text{ m/s}$ , and  $l_0 = 0.011937 \text{ m}$ .

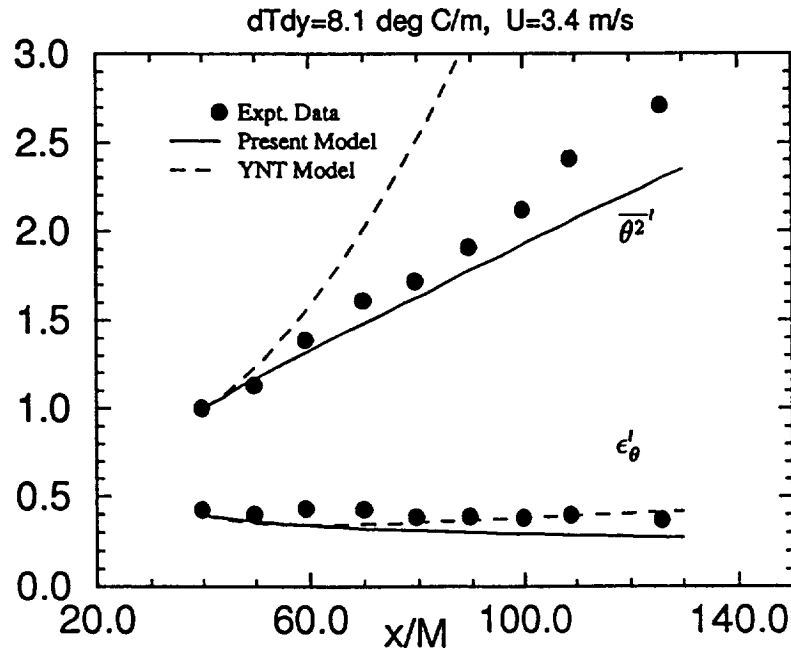


Figure 4. Evolution of the normalized temperature variance and thermal dissipation rate in the experiment of Sirivat and Warhaft (1983). The temperature variance is normalized as  $\overline{\theta^2}' = \overline{\theta^2}/\overline{\theta^2}_0$  and the thermal dissipation is normalized as  $\epsilon_\theta' = \frac{\epsilon_\theta}{\overline{\theta^2}_0 u_0/l_0}$ . For this case  $\overline{\theta^2}_0 = 0.009059 \text{ } ^\circ\text{C}^2$ ,  $u_0 = 0.074701 \text{ m/s}$ , and  $l_0 = 0.011071 \text{ m}$ .

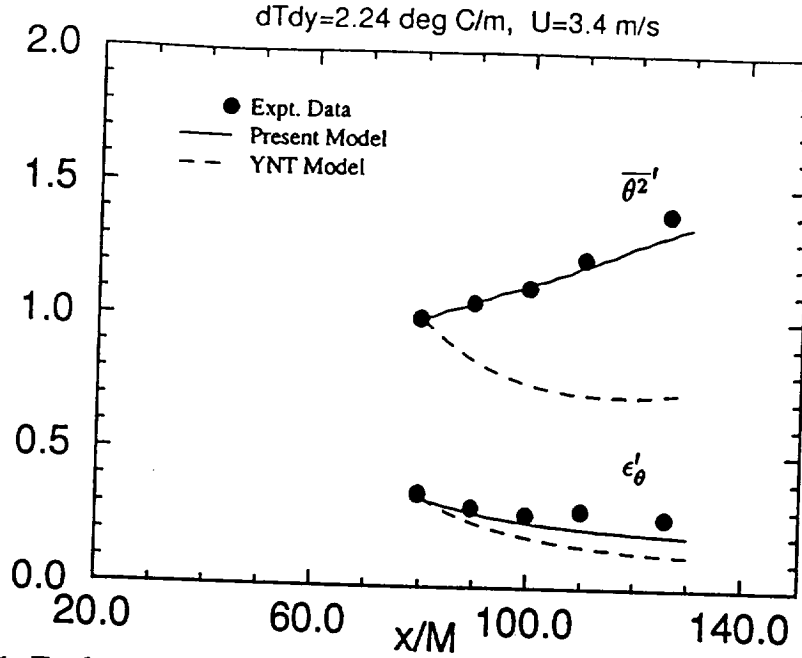


Figure 5. Evolution of the normalized temperature variance and thermal dissipation rate in the experiment of Sirivat and Warhaft (1983). The temperature variance is normalized as  $\overline{\theta'^2} = \overline{\theta^2}/\overline{\theta^2}_0$  and the thermal dissipation is normalized as  $\epsilon'_\theta = \frac{\epsilon_\theta}{\overline{\theta^2}_0 u_0/l_0}$ . For this case  $\overline{\theta^2}_0 = 0.000924 \text{ } ^\circ\text{C}^2$ ,  $u_0 = 0.074701 \text{ m/s}$ , and  $l_0 = 0.011071 \text{ m}$ .

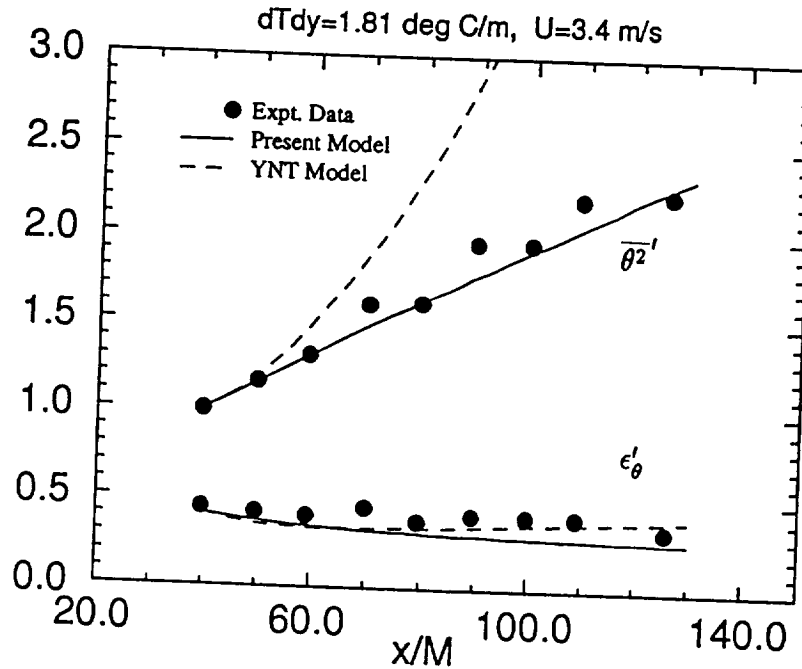


Figure 6. Evolution of the normalized temperature variance and thermal dissipation rate in the experiment of Sirivat and Warhaft (1983). The temperature variance is normalized as  $\overline{\theta'^2} = \overline{\theta^2}/\overline{\theta^2}_0$  and the thermal dissipation is normalized as  $\epsilon'_\theta = \frac{\epsilon_\theta}{\overline{\theta^2}_0 u_0/l_0}$ . For this case  $\overline{\theta^2}_0 = 0.0004471 \text{ } ^\circ\text{C}^2$ ,  $u_0 = 0.074701 \text{ m/s}$ , and  $l_0 = 0.011071 \text{ m}$ .

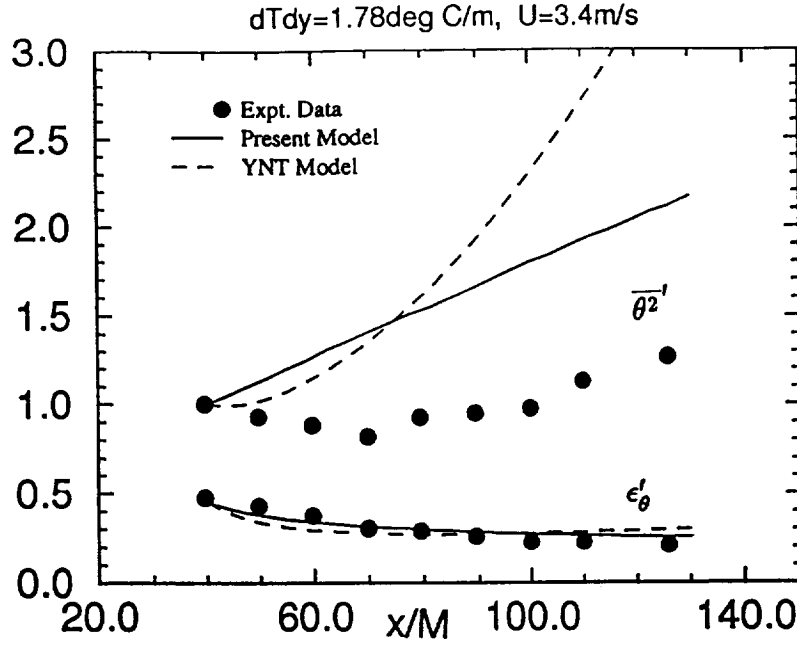


Figure 7. Evolution of the normalized temperature variance and thermal dissipation rate in the experiment of Sirivat and Warhaft (1983). The temperature variance is normalized as  $\overline{\theta^2}' = \overline{\theta^2}/\overline{\theta^2}_0$  and the thermal dissipation is normalized as  $\epsilon'_\theta = \frac{\epsilon_\theta}{\overline{\theta^2}_0 u_0/l_0}$ . For this case  $\overline{\theta^2}_0 = 0.0004955 \text{ } ^\circ\text{C}^2$ ,  $u_0 = 0.074701\text{m/s}$ , and  $l_0 = 0.011071\text{m}$ .

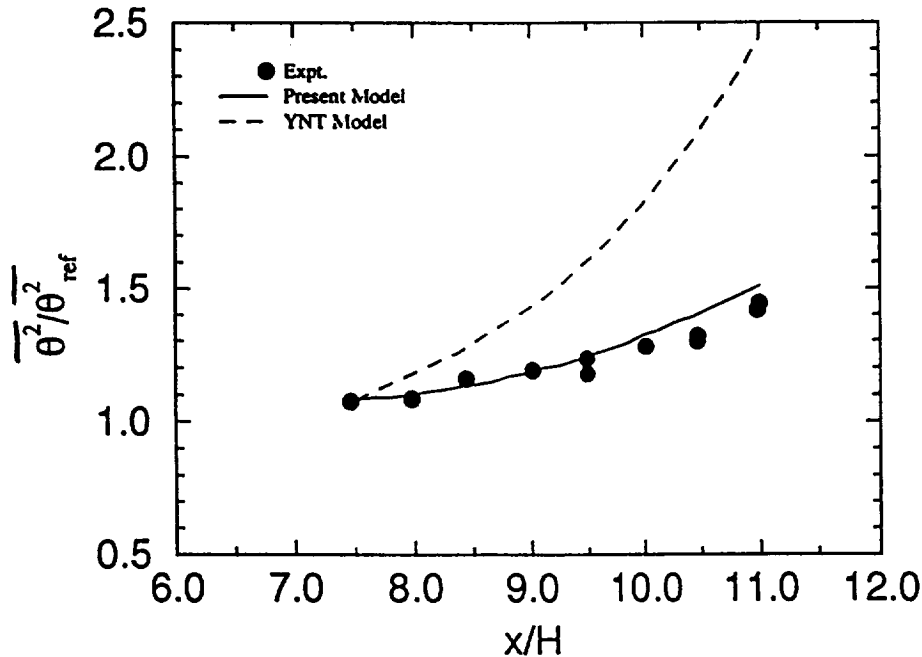


Figure 8a. Evolution of the normalized temperature variance in the experiment of Tavoularis and Corrsin (1981). The temperature variance is normalized with  $\overline{\theta^2}_{ref} = 0.01 \text{ } ^\circ\text{C}^2$ .



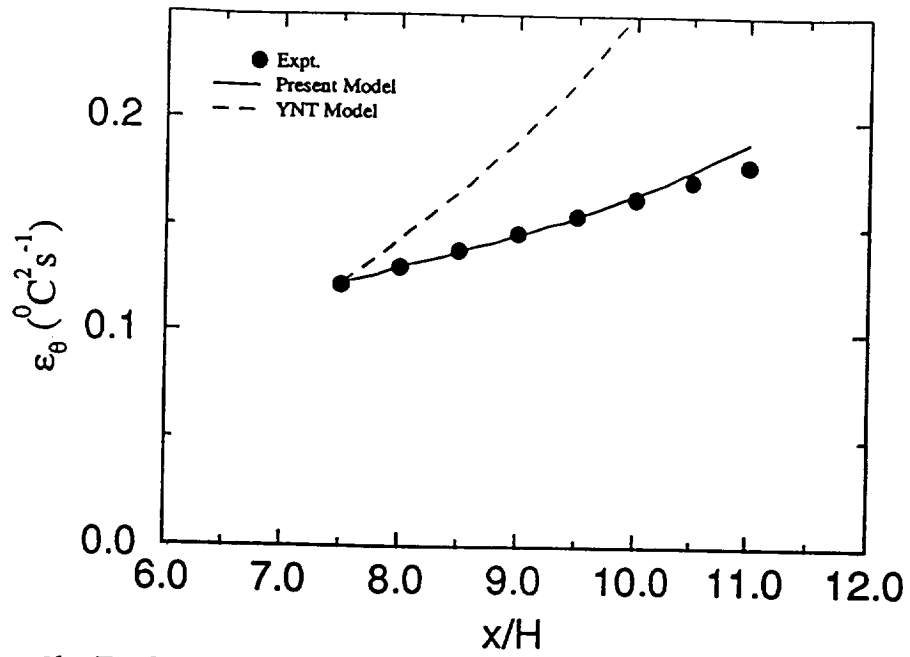


Figure 8b. Evolution of the thermal dissipation rate in the experiment of Tavoularis and Corrsin (1981).



# A Multiple-Scale Turbulence Model for Incompressible Flow

B. S. Duncan

## 1. Motivation and Objective

In turbulent flows, the mean flow performs deformation work which transfers energy from the mean flow to the large-scale turbulent eddies. The turbulent kinetic energy contained within these large eddies is passed to the smaller eddies by vortex stretching. Once the energy has been passed into eddies near the Kolmogorov scale, it is then dissipated by the molecular viscosity. This process can be thought of as a turbulent kinetic energy cascade<sup>1</sup>. In other words, the turbulent kinetic energy is passed through the wave number spectrum as it cascades from large to small eddies.

The multiple-scale turbulence model which is proposed in this study splits the energy spectrum into low and high wave number regions. The low wave number region contains the large-scale eddies and the high wave number region consists of the smaller, less energetic eddies. A division of this nature models the cascade of energy from the production region, where the energy is initially created by the mean straining work, to the dissipation region where this energy is eventually dissipated. This concept is illustrated in Figure 1. Although a simple two-part division of the energy spectrum cannot fully model the cascade of energy, it can simulate the nonequilibrium energy transfer process which is beyond the capability of all single-scale models.

This concept was incorporated into an earlier multiple-time scale turbulence model by Hanjalic, Launder and Schiestel<sup>2</sup> (hereafter HL&S). Based on the same modeling methodology that was used in the development of the "standard"  $k$ - $\epsilon$  model<sup>3</sup>, HL&S derived four transport equations to describe the turbulent characteristics of the two regions. Consequently, HL&S formulated two transport equations for the partitioned turbulent kinetic energies. They also developed transport equations for the rate of energy transfer between the two scales and for the rate of energy transfer to the small-scale eddies. In this model, the coefficients were written as functions of both the ratio of the partitioned energies and the ratio of the spectral energy transfer rates. A term containing the mean vorticity was included in the energy transfer rate equation to account for the increased energy transfer rates in irrotational shear flows. Their results<sup>2</sup> showed fairly good agreement between the model predictions and the experimental data for jets and boundary layers.

Kim and Chen<sup>4</sup> (hereafter K&C) developed another multiple-scale model based on the energy partitioning idea introduced by HL&S. In this model, the transport equations were modified to include an extra source term in both the energy transfer rate equation and the energy dissipation rate equation. In addition, the turbulent velocity scale was characterized by the total turbulent kinetic energy. K&C calibrated the model constants which appear in the energy transfer equations for

simple, wall-bounded turbulent flow problems. This model has been used for several boundary-layer flow problems using the appropriate near-wall corrections.

The model in this study is also based on the energy partitioning concept of HL&S. In particular, the model coefficients are dynamically dependent upon the partitioning of the energy spectrum. The variable nature of the coefficients adjusts the model to different flow situations. There is no need for the extra source terms used in K&C's model or the rotational straining term in the HL&S model. These model coefficients have been calibrated for homogeneous shear flow and decaying grid turbulence. The present multiple-scale turbulence model has been tested for boundary-free shear flows. Two mixing layers at different speed ratios, a planar jet and a round jet have been evaluated. All the computations show reasonably good agreement with the data.

## 2. Work Accomplished

### 2.1 Model Equations

#### Mean Flow Equations

For incompressible turbulent flow, the ensembled-averaged equations for continuity of mass and momentum are written as

$$\frac{\partial U_i}{\partial x_i} = 0$$

and

$$\frac{DU_i}{Dt} = \frac{\partial}{\partial x_j} \left( \nu \frac{\partial U_i}{\partial x_j} - \overline{u_i u_j} \right) - \frac{1}{\rho} \frac{\partial P}{\partial x_i}$$

where  $-\overline{u_i u_j}$  is the turbulent Reynolds stress tensor. Using the eddy viscosity concept, the Reynolds stress can be related to the mean strain rate and a turbulent eddy viscosity,

$$-\overline{u_i u_j} = \nu_t \left( \frac{\partial U_i}{\partial x_j} + \frac{\partial U_j}{\partial x_i} \right) - \frac{2}{3} k \delta_{ij}.$$

Now, the momentum equation can be written as

$$\frac{DU_i}{Dt} = \frac{\partial}{\partial x_j} \left( (\nu + \nu_t) \frac{\partial U_i}{\partial x_j} \right) - \frac{1}{\rho} \frac{\partial P}{\partial x_i}.$$

The turbulent eddy viscosity,  $\nu_t$ , can be characterized by the local turbulent kinetic energy and the local length scale of the energy containing eddies,

$$\nu_t \propto k^{\frac{1}{2}} l.$$

The definition used for this length scale is the primary discriminating factor of eddy viscosity turbulence models. For instance, in a  $k$ - $\epsilon$  model this length scale is written in terms of the turbulent kinetic energy,  $k$ , and its dissipation rate,  $\epsilon$ ,

$$l = \frac{k^{\frac{3}{2}}}{\epsilon}.$$

In the present model, the length scale is described by the total turbulent kinetic energy and the rate of spectral energy transfer, i.e.  $l = \frac{k^{\frac{3}{2}}}{\epsilon_p}$ . The turbulent kinetic energies and the rates of energy transfer are determined by modeled transport equations similar to the "standard"  $k$ - $\epsilon$  equations. These transport equations are described in the following section.

### Turbulence Equations

In this multiple-scale turbulence model, the energy spectrum has been split into a region where the turbulent kinetic energy has been produced by interaction with the mean flow and a region where the turbulent energy has been transferred from the production region. This division can be graphically represented by Figure 1. Now,  $k_p$  is the kinetic energy contained within the production region and  $\epsilon_p$  is the rate at which energy is passed from the low wave number range into the high wave number range. At the high wave number end of the spectrum,  $k_t$  is the kinetic energy contained in the smaller eddies and  $\epsilon_t$  is taken to be equivalent to the dissipation rate. The modeled transport equations are

$$\frac{Dk_p}{Dt} = \frac{\partial}{\partial x_j} \left[ \left( \nu + \frac{\nu_t}{\sigma_{k_p}} \right) \frac{\partial k_p}{\partial x_j} \right] + P_{k_p} - \epsilon_p \quad (1)$$

$$\frac{D\epsilon_p}{Dt} = \frac{\partial}{\partial x_j} \left[ \left( \nu + \frac{\nu_t}{\sigma_{\epsilon_p}} \right) \frac{\partial \epsilon_p}{\partial x_j} \right] + c_{p1} \frac{\epsilon_p}{k_p} P_{k_p} - c_{p2} \frac{\epsilon_p^2}{k_p} \quad (2)$$

$$\frac{Dk_t}{Dt} = \frac{\partial}{\partial x_j} \left[ \left( \nu + \frac{\nu_t}{\sigma_{k_t}} \right) \frac{\partial k_t}{\partial x_j} \right] + \epsilon_p - \epsilon_t \quad (3)$$

$$\frac{D\epsilon_t}{Dt} = \frac{\partial}{\partial x_j} \left[ \left( \nu + \frac{\nu_t}{\sigma_{\epsilon_t}} \right) \frac{\partial \epsilon_t}{\partial x_j} \right] + c_{t1} \frac{\epsilon_t \epsilon_p}{k_t} - c_{t2} \frac{\epsilon_t^2}{k_t} \quad (4)$$

where,

$$P_{k_p} = \nu_t \left( \frac{\partial U_j}{\partial x_i} + \frac{\partial U_i}{\partial x_j} \right) \frac{\partial U_i}{\partial x_j}.$$

Here,  $P_{k_p}$  is the production of kinetic energy by the large scale eddies. Note that the  $\epsilon_p$  term serves as a sink in the equation for  $k_p$  and a source in the  $k_t$  equation. The source and sink terms in the energy transfer rate equations ( $\epsilon_p$  and  $\epsilon_t$ ) are related to those in the turbulent kinetic energy equations by their corresponding time scales, i.e.,  $\frac{k_p}{\epsilon_p}$  and  $\frac{k_t}{\epsilon_t}$ .

These transport equations, equations (1) through (4), possess several differences from the earlier multiple-scale models. HL&S include a rotational straining term in the  $\epsilon_p$  energy transfer equation (2) to improve their model's performance in axisymmetric flows. Based on dimensional reasoning, K&C<sup>4</sup> include additional terms in the  $\epsilon_p$  and  $\epsilon_t$  equations which are nonlinear in  $P_{k_p}$  and  $\epsilon_p$ , respectively. The present model is the least complicated as it uses neither the rotational straining term nor the nonlinear production terms for energy transfer rates in the model equations.

Accounting for the multiple partitions in the turbulent kinetic energy spectrum and the spectral energy transfer rates, the eddy viscosity in the present model is defined as

$$\nu_t = c_\mu \frac{(k_t + k_p)^2}{\epsilon_p}$$

and  $c_\mu = 0.09$ . This is the same relationship for eddy viscosity used by K&C. With this formulation, the single scale eddy viscosity model will be recovered when  $\epsilon_p$  approaches  $\epsilon$  in equilibrium turbulence. The  $\sigma$  coefficients in equations (1) through (4) are assumed to be the following constants,

$$\sigma_{k_p} = \sigma_{k_t} = 1.0 \text{ and } \sigma_{\epsilon_p} = \sigma_{\epsilon_t} = 1.3.$$

The other coefficients in equations (1) through (4), namely  $c_{p1}$ ,  $c_{p2}$ ,  $c_{t1}$ , and  $c_{t2}$ , are the modeling coefficients discussed in the following section.

## 2.2 Model Coefficients

The coefficients for this incompressible model have been determined from analyses of homogeneous and decaying turbulence.

### Grid Turbulence

In homogeneous decaying grid turbulence, the turbulent quantities are functions of time only and equations (1) through (4) can be simplified to

$$\frac{dk_p}{dt} = -\epsilon_p \quad (5)$$

$$\frac{d\epsilon_p}{dt} = -c_{p2} \frac{\epsilon_p^2}{k_p} \quad (6)$$

$$\frac{dk_t}{dt} = \epsilon_p - \epsilon_t \quad (7)$$

$$\frac{d\epsilon_t}{dt} = c_{t1} \frac{\epsilon_t \epsilon_p}{k_t} - c_{t2} \frac{\epsilon_t^2}{k_t}. \quad (8)$$

Most of the experimental evidence suggests that the turbulent kinetic energy decays in time and can be represented by

$$\frac{k_p}{k_{p0}} = \left( \frac{t}{t_0} \right)^{-n}$$

and

$$\frac{k_t}{k_{t0}} = \left( \frac{t}{t_0} \right)^{-n}$$

where  $n$  is the decay rate and is typically of the order 1.2. From the above kinetic energy equations, (5) and (7), the energy transfer rates must decay as

$$\frac{\epsilon_p}{\epsilon_{p0}} = \left( \frac{t}{t_0} \right)^{-n-1}$$

and

$$\frac{\epsilon_t}{\epsilon_{t0}} = \left( \frac{t}{t_0} \right)^{-n-1}.$$

Therefore, the  $c_{p2}$  coefficient from equation (6) can be related to the decay rate,

$$c_{p2} = \frac{n+1}{n}. \quad (9)$$

Manipulating the simplified transport equations, (5) through (8), and using the above relations yields a relationship between  $c_{t2}$  and the other coefficients,

$$c_{t2} = \frac{c_{t1} + \frac{k_t}{k_p} c_{p2}}{\frac{k_t}{k_p} + 1}. \quad (10)$$

### **Homogeneous Shear Flow**

Guidelines can be established for determining the remaining two constants,  $c_{p1}$  and  $c_{t1}$ , by examining the physical behavior of homogeneous shear flows. In this flow situation, the turbulent transport equations reduce to

$$\frac{dk_p}{dt} = P_{kp} - \epsilon_p \quad (11)$$

$$\frac{d\epsilon_p}{dt} = c_{p1} \frac{\epsilon_p}{k_p} P_{kp} - c_{p2} \frac{\epsilon_p^2}{k_p} \quad (12)$$

$$\frac{dk_t}{dt} = \epsilon_p - \epsilon_t \quad (13)$$

$$\frac{d\epsilon_t}{dt} = c_{t1} \frac{\epsilon_t \epsilon_p}{k_t} - c_{t2} \frac{\epsilon_t^2}{k_t}. \quad (14)$$

If we define

$$\alpha = \frac{P_{kp}}{\epsilon_t} \quad (15)$$

and

$$\beta = \frac{\epsilon_p}{\epsilon_t}, \quad (16)$$

then equation (11) can be combined with equation (12) to give

$$\frac{\epsilon_p}{k_p} \frac{dk_p}{d\epsilon_p} = \frac{(\alpha - \beta)}{c_{p1}\alpha - c_{p2}\beta}.$$

Likewise, equations (13) and (14) can be combined to give the following result,

$$\frac{\epsilon_t}{k_t} \frac{dk_t}{d\epsilon_t} = \frac{\beta - 1}{c_{t1}\beta - c_{t2}}.$$

Assuming that  $\beta$  and the percentages of the kinetic energy contained in  $k_p$  and  $k_t$  remain nearly constant, then

$$\frac{\epsilon_p}{k_p} \frac{dk_p}{d\epsilon_p} = \frac{\epsilon_t}{k} \frac{dk}{d\epsilon_t} = \frac{(\alpha - \beta)}{c_{p1}\alpha - c_{p2}\beta} \quad (17)$$

and

$$\frac{\epsilon_t}{k_t} \frac{dk_t}{d\epsilon_t} = \frac{\epsilon_t}{k} \frac{dk}{d\epsilon_t} = \frac{\beta - 1}{c_{t1}\beta - c_{t2}}. \quad (18)$$

From the experiment<sup>5</sup>, the ratio  $\frac{\epsilon_t}{k} \frac{dk}{d\epsilon_t}$  has been deduced to be 1.065. In a similar experiment, Tavoularis and Corrisin<sup>6</sup> found this ratio to be between 0.82 and 0.94. Clearly, this ratio is on the order of one. For simplicity, this term,  $\frac{\epsilon_t}{k} \frac{dk}{d\epsilon_t}$ , has been assumed to be unity. Therefore, the following expressions for  $c_{p1}$  and  $c_{t1}$  can be found from equations (17) and (18),

$$c_{p1} = \left(1 - \frac{\beta}{\alpha}\right) + \frac{\beta}{\alpha} c_{p2}$$

$$c_{t1} = \frac{\beta - 1}{\beta} + \frac{c_{t2}}{\beta}.$$

Equation (10) is now

$$c_{t2} = \frac{\beta - 1 + c_{p2}\beta \frac{k_t}{k_p}}{\beta + \beta \frac{k_t}{k_p} - 1}$$

and  $c_{p2}$  is defined in equation (9). The coefficients,  $c_{p1}$ ,  $c_{t1}$  and  $c_{t2}$  are functions of  $\frac{P_{kp}}{\epsilon_t}$ ,  $\frac{\epsilon_p}{\epsilon_t}$ , and  $\frac{k_t}{k_p}$ . In the present model, the ratios described in equations (15) and (16) are assumed to be the following constants

$$\alpha = \frac{P_{kp}}{\epsilon_t} = 2.2$$

and

$$\beta = \frac{\epsilon_p}{\epsilon_t} = 1.05.$$

These constants have been calibrated considering that experimental measurements of homogeneous shear flow suggest that the ratio  $\frac{\alpha}{\beta}$  should be near two. The coefficients of the present model are summarized in Table 1.

Notice that the value of  $\frac{k_t}{k_p}$  is allowed to vary as the ratio of the turbulent kinetic energy in the small scales to the energy contained in the large scales changes. Since most of the energy is contained in the large scales, this ratio should remain less than one<sup>1</sup>. This coefficient adaptability allows the model to adjust to different flow situations and is a unique characteristic of multiple-scale eddy viscosity models.



## 2.3 Results and Discussions

The present multiple-scale model has been tested for two planar mixing layers and two jet flows. As part of these tests, the model has been compared to experimental data and to the multiple-scale models of Hanjalic, Launder and Schiestel<sup>2</sup> (HL&S), Kim and Chen<sup>4</sup> (K&C), and the “standard”  $k$ - $\epsilon$  model. In all cases, the parabolic solution technique is started with an initial plane and the flow field evolves as the computations march in the axial direction. The solutions are checked to insure that they maintain a self-preserving profile. The results of these calculations are presented in Figures 2 through 16 and in Table 2.

### 2.2.1 Planar Mixing Layers

For the planar mixing layers, the flow is assumed to have a thin shear layer profile at the interface between the still air and the jet. Zero gradient boundary conditions for the turbulence quantities are applied at the edges of the flow field and an equally spaced grid is used.

#### Speed ratio = 0.0

In Figure 2, the three multiple-scale models and the “standard”  $k$ - $\epsilon$  model are compared to the experimental data of Wygnanski and Fiedler<sup>7</sup> and Patel<sup>8</sup>. At the high speed edge, none of the four models predicts the diffusive characteristic indicated by the data. Away from this area, however, the present model, HL&S’s model and the “standard”  $k$ - $\epsilon$  model all are very close to Patel’s data. The data due to Wygnanski and Fiedler is considerably more diffusive than either Patel’s data or the computations. The spreading rates predicted by the four eddy viscosity models and the spreading rate measured by Patel are listed in Table 2. For mixing layers, the spreading rate is defined as  $\frac{d(y.9 - y.1)}{dx}$ . The spreading rate predictions by the present model and the “standard”  $k$ - $\epsilon$  model are closest to the data. K&C’s model significantly underestimates the growth rate of the mixing layer.

The tendency of K&C’s model to under-predict the growth of the turbulent mixing region is further seen in Figures 3 and 4. The shapes of the kinetic energy curves and the shear stress distributions are correct, but the peak levels are well below the data. The “standard”  $k$ - $\epsilon$  model, HL&S’s model, and the present model predict turbulent kinetic energy levels slightly below the data but they correctly predict the peak levels for shear stress. Apparently, the computational shear layers tend to shift further towards the low speed side of the flow than the experimentally measured shear layers.

In Figure 5, the ratios of the partitioned kinetic energies and the energy transfer rates are shown. Notice that the ratio,  $\frac{\epsilon_t}{\epsilon_p}$ , is one through the mixing layer where the turbulence spectrum is in equilibrium. The fact that  $\frac{k_t}{k_p}$  remains much less than one indicates that most of the energy is contained by the large scale eddies as stated by Tennekes and Lumley<sup>1</sup>.

#### Speed ratio = 0.3

The next case considered is a mixing layer with a speed ratio of 0.3. In Figure 6, the mean velocity profiles predicted by all four models are in very good agreement with the experimental data measured by Spencer et. al.<sup>9</sup>. The present model and

the “standard”  $k-\epsilon$  model predict an almost identical velocity profile. HL&S’s and K&C’s models under-predict the growth of the mixing region, which is indicated by the narrower mean velocity profile and also by the lower spreading rates listed in Table 2.

As can be seen in Figure 7, the “standard”  $k-\epsilon$  and the present  $k_p-\epsilon_p-k_t-\epsilon_t$  model predict the kinetic energy distribution very well. Although the models due to HL&S and K&C yield good mean velocity predictions, they both under-predict the peak turbulent kinetic energy level. The present model and the “standard”  $k-\epsilon$  model yield better predictions of the turbulent kinetic energy profile. All the eddy viscosity models in this study under-predict the peak shear stress shown in Figure 8. Here, the “standard”  $k-\epsilon$  and the present model do a better job of predicting the shear stress profile than HL&S or K&C; however, they are both slightly low in their predictions of the peak value.

#### Grid Resolution Analysis

Since the mixing layer with a speed ratio of 0.3 gives the thinnest shear layer and the slowest growth rate, this case would be the most dependent upon grid resolution. For all the calculations discussed thus far, there were 65 points across the flow field. Figure 9 compares the solution obtained with 65 points to the same calculation with 101 points across the domain. As this Figure indicates, the result is essentially unchanged as the grid is refined.

#### 2.2.2 Planar Jet

For the jet flow simulations, the initial plane is split with a uniform velocity and kinetic energy profile comprising approximately half of the domain, and quiescent air comprising the other half. Zero gradient boundary conditions are applied at the centerline of the jet and the grid has been clustered towards the centerline to improve the accuracy of this boundary condition. Stable, self-similar profiles could not be obtained for the HL&S model; therefore this model has not been included in the following comparisons.

As can be seen in Figure 10, the mean velocity profiles predicted by the present model, K&C’s model, and the “standard”  $k-\epsilon$  model lie within the scatter of the experimental data<sup>10,11,12</sup>. The present multiple-scale model is particularly close to the data of Heskestad<sup>12</sup>. There is very little disagreement between the predicted spreading rates and experimental spreading rate given in Table 2. For jet flows, the spreading rate is defined as the rate of change of the half velocity point, i.e.,  $\frac{dy_{0.5}}{dx}$ . The predicted spreading rates range from 0.103 by K&C’s model to 0.114 by the “standard”  $k-\epsilon$  model. All these spreading rates are in reasonably good agreement with the experimentally determined rates.

There is considerably more disagreement between the models for the predicted turbulent kinetic energy levels, shown in Figure 11. Both the present model and K&C’s model predict relatively flat profiles which match the data of Heskestad<sup>12</sup>. The “standard”  $k-\epsilon$  model is in very good agreement with the experimental data, being especially close to Bradbury’s measurements.

Both multiple-scale models and the “standard”  $k-\epsilon$  model predict closest to the peak shear stress, shown in Figure 12, although they tend to exaggerate the width

of the jet.

### 2.2.3 Round Jet

Using the “standard”  $k$ - $\epsilon$  turbulence model often gives poor predictions for the spreading rate and flow properties of a round jet. There are several methods to adjust the “standard”  $k$ - $\epsilon$  model, e.g., by changing the coefficient in the dissipation equation or by adding a vortex stretching term<sup>13</sup>. The “standard”  $k$ - $\epsilon$  model predictions given in Figures 13 through 15 have applied no correction methods. Neither the present model nor K&C’s model uses a three-dimensional correction term; yet, as shown in Figure 13, they give the best match to the experimental data of Rodi<sup>14</sup> and Wagnanski & Fiedler<sup>15</sup> for mean velocity.

The turbulent kinetic energy is over-predicted by the “standard”  $k$ - $\epsilon$  model as shown in Figure 14. Closer to the data, but still not giving good predictions, are the present model and K&C’s model. Both models predict the correct centerline turbulent kinetic energy, however, the outer edges of the jet are over-predicted. None of the models in this report does a good job of predicting the turbulent kinetic energy for an axisymmetric jet.

Figure 15 shows that there is also a wide spread in the shear stress predictions. Without adjusting the modeling coefficients or adding correction terms, the “standard”  $k$ - $\epsilon$  model predicts shear stress levels almost 1.5 times those given by the data. Both the present model and K&C’s model are relatively close to the data compared to the “standard”  $k$ - $\epsilon$  model, although both models over-predict the peak level by approximately 25 percent. The two multiple-scale models, i.e. the present model and K&C’s model, predict spreading rates which are, respectively, 17 and 24 percent too large in comparison to the data.

Figure 16 shows the ratios of  $\frac{k_t}{k_p}$  and  $\frac{\epsilon_t}{\epsilon_p}$  across the jet for the present multiple-scale model. Notice that the ratio of kinetic energy are much less than one, indicating that most of the energy is in the larger scales. Looking at the ratio of energy transfer rate, the energy transfer to the dissipative scales increases near the centerline of the jet indicating that the flow field is not in equilibrium. The “standard”  $k$ - $\epsilon$  model has no means to account for the increase in energy transfer rate near the centerline of the jet and consequently over-predicts the turbulent kinetic energy and the spreading rate.

## 3. Future Work

This model will be extended to wall bounded flow using both wall functions and near wall damping functions.

$$\begin{aligned}
c_\mu &= 0.09 & n &= 1.2 & \alpha &= 2.2 & \beta &= 1.05 \\
c_{p1} &= \frac{\left(\frac{1-\beta}{\alpha}\right)\beta}{\alpha c_{p2}} & c_{p2} &= \frac{n+1}{n} & c_{t1} &= \frac{\beta-1}{\beta} + \frac{c_{t2}}{\beta} & c_{t2} &= \frac{\beta-1+c_{p2}\beta\frac{k_t}{k_p}}{\beta+\beta\frac{k_t}{k_p}-1} \\
\sigma_{k_p} &= 1.0 & \sigma_{k_t} &= 1.0 & \sigma_{\epsilon_p} &= 1.3 & \sigma_{\epsilon_t} &= 1.3
\end{aligned}$$

Table 1. Multiple-Scale Turbulence Model Coefficients

	Experiment	HL&S $k_p-\epsilon_p-k_t-\epsilon_t$	K&C $k_p-\epsilon_p-k_t-\epsilon_t$	present $k_p-\epsilon_p-k_t-\epsilon_t$	standard $k-\epsilon$ Model
Planar Jet	0.11-0.12	—	0.103	0.104	0.114
Round Jet	0.085-0.095	—	0.118	0.111	0.126
2D Mix. Layer r=0.0	0.179	0.146	0.126	0.152	0.159
2D Mix. Layer r=0.3	0.052	0.061	0.064	0.078	0.082

Table 2. Spreading Rate Comparisons for Free Shear Flow

#### 4. References

- <sup>1</sup> Tennekes, H. and Lumley, J. L., *A First Course in Turbulence*, The MIT Press (1972).
- <sup>2</sup> Hanjalic, K., Launder, B.E., and Schiestel, R., "Multiple-time-scale concepts in modeling turbulent flows," *Turbulent Shear Flows*, Springer-Verlag (1980).
- <sup>3</sup> Jones, W.P. and Launder, B.E., "The prediction of laminarization with a two-equation model of turbulence," *Journal of Heat and Mass Transfer* **15**, 301-314 (1972).
- <sup>4</sup> Kim, S.W. and Chen, C.P., "A multiple-time-scale turbulence model based on variable partitioning of turbulent kinetic energy spectrum," NASA CR-179222, (1987).
- <sup>5</sup> Harris, V.G. Graham, J.A.H. and Corrsin, S., "Further experiments in nearly homogeneous turbulent shear flow," *Journal of Fluid Mechanics* **81**, 577-612 (1977).
- <sup>6</sup> Tavoularis, S. and Corrsin, S., "Experiments in nearly homogeneous shear flow with a uniform mean temperature gradient. part 1," *Journal of Fluid Mechanics* **104**, (1981).
- <sup>7</sup> Wygnanski, I. and Fiedler, H. E., "The two-dimensional mixing region," *Journal of Fluid Mechanics* **41**, 327-361 (1970).
- <sup>8</sup> Patel, R., "An Experimental Study of a Plane Mixing Layer," *AIAA Journal* **11**, (1), 69-71, (1973).
- <sup>9</sup> Spencer, B.W and Jones, B.G., "Statical investigation of pressure and velocity

- fieldss in the turbulent two-stream mixing layer," AIAA paper 71-0613, (1991).
- <sup>10</sup> Gutmark, E. and Wygnanski, I., "The planar turbulent jet," *Journal of Fluid Mechanics* **73**, 465-495 (1976).
  - <sup>11</sup> Bradbury, L. J. S., "The stucture of the self-preserving jet," *Journal of Fluid Mechanics* **23**, 31-64 (1965).
  - <sup>12</sup> Heskestad, G., "Hot-wire measurements in a plane turbulent jet", *Journal of Applied Mechanics* **42**, 721-734 (1965).
  - <sup>13</sup> Pope, S. B., "An explanation of the turbulent round-jet/plane-jet anomaly", *AIAA Journal* **16**, (1978).
  - <sup>14</sup> Rodi, W., "A new method of analyzing hot-wire signals in highly turbulent flow and its evaluation in round jet", *Disa Information* No. 17 (1975).
  - <sup>15</sup> Wygnanski, I. and Fiedler, H. E., "Some measurements in the self preserving jet", *Journal of Fluid Mechanics* **38**, 577-612.

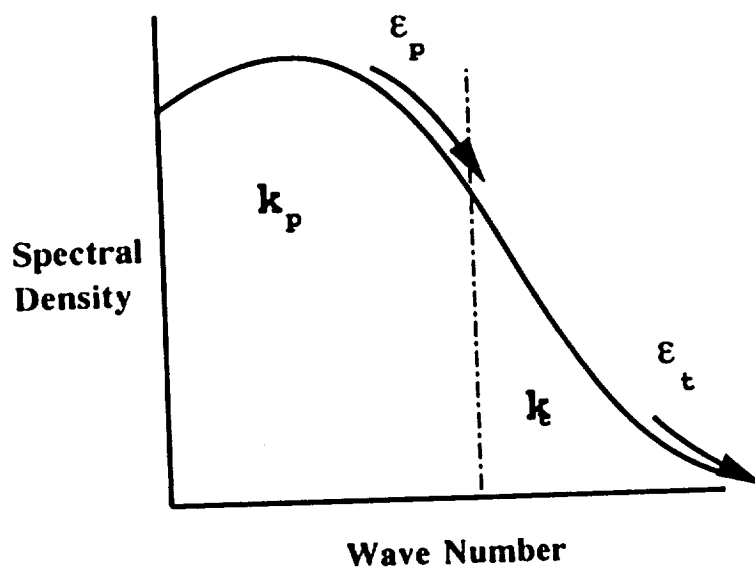
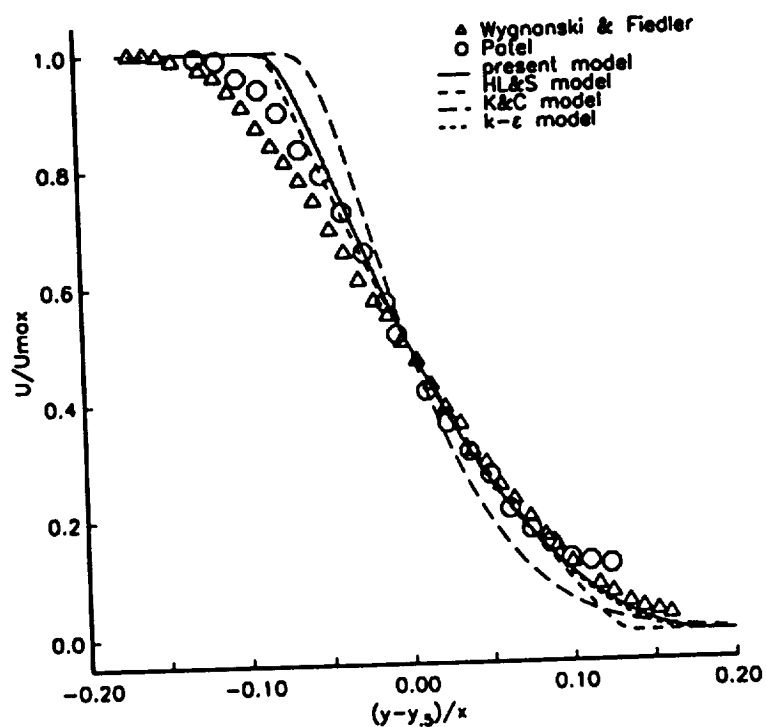


Figure 1. Energy cascade process.

Figure 2. Mean velocity profile for a planar mixing layer with a speed ratio of 0.  $U_{max}$ : maximum velocity.

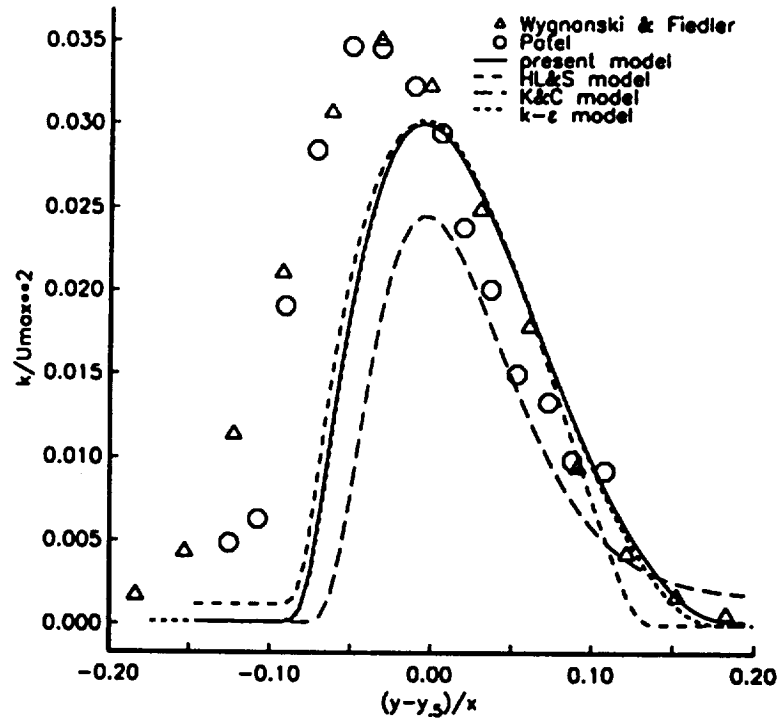


Figure 3. Turbulent kinetic energy profile for a planar mixing layer with a speed ratio of 0.  $U_{max}$ : maximum velocity.

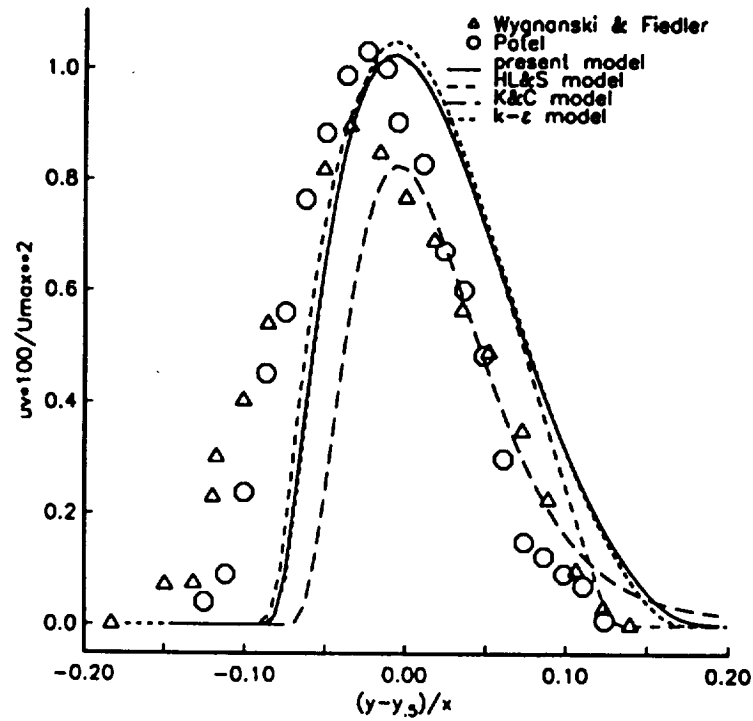


Figure 4. Shear stress profile for a planar mixing layer with a speed ratio of 0.  $U_{max}$ : maximum velocity.

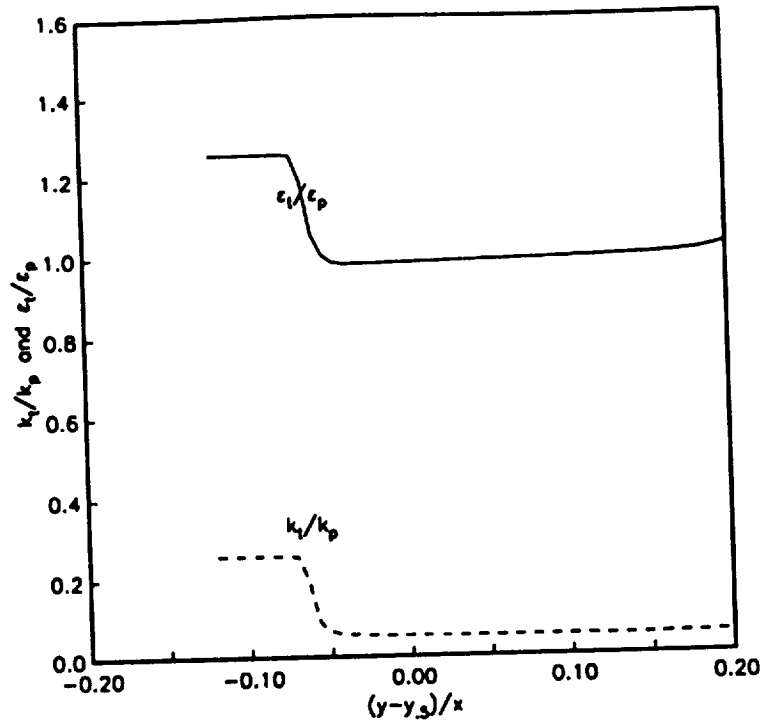


Figure 5. Energy transfer rate and kinetic energy ratios for a plane mixing layer with a speed ratio of 0.

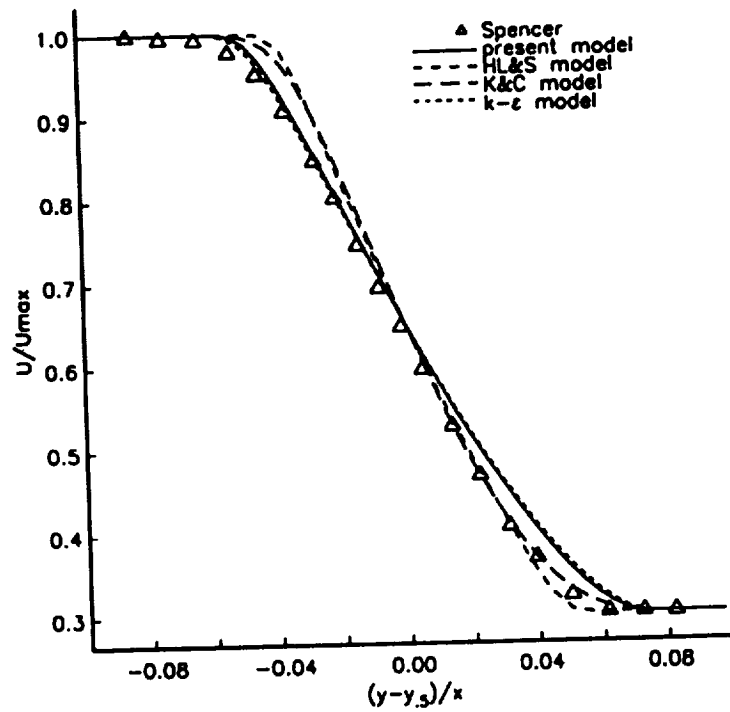


Figure 6. Mean velocity profile for a planar mixing layer with a speed ratio of .3.  $U_{max}$ : maximum velocity.



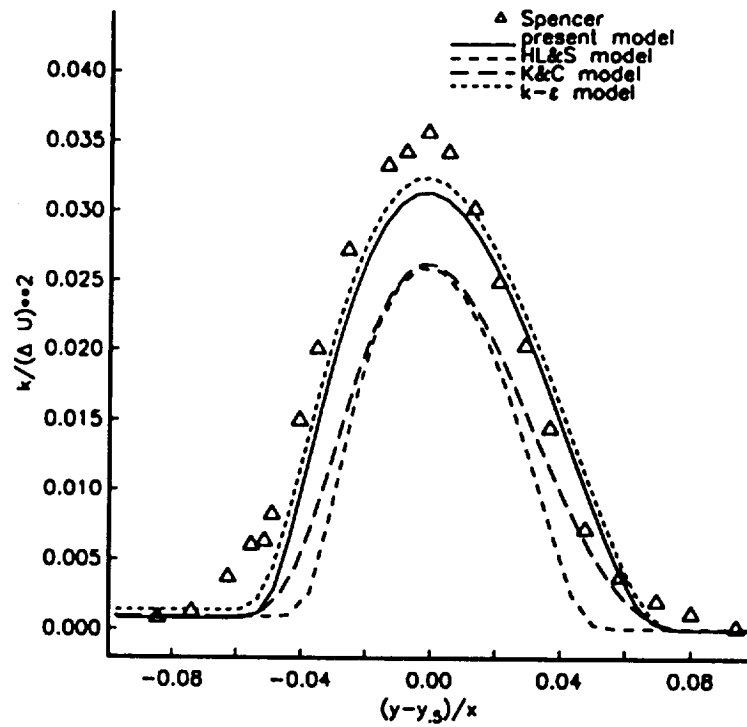


Figure 7. Turbulent kinetic energy profile for a planar mixing layer with a speed ratio of .3.  $\Delta U = U_{max} - U_{min}$ .

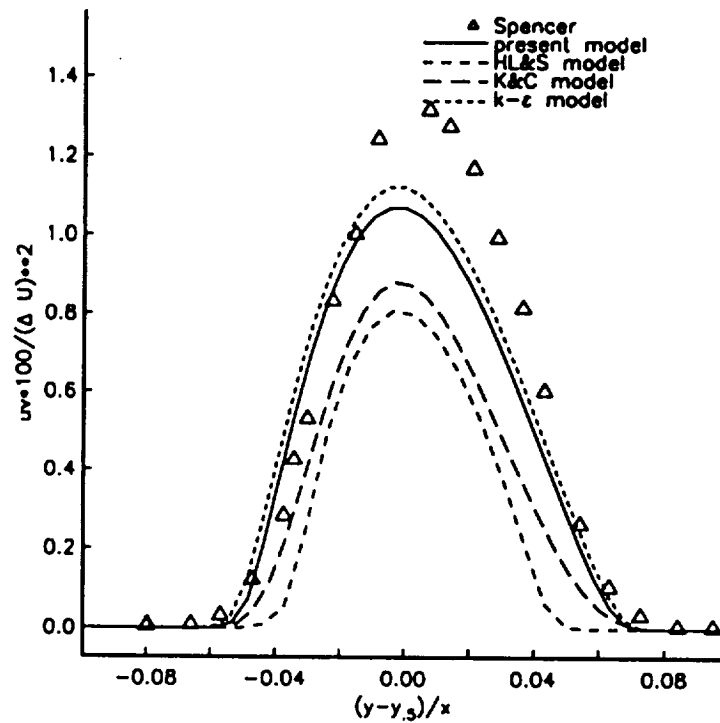


Figure 8. Shear stress profile for a planar mixing layer with a speed ratio of .3.  $\Delta U = U_{max} - U_{min}$ .

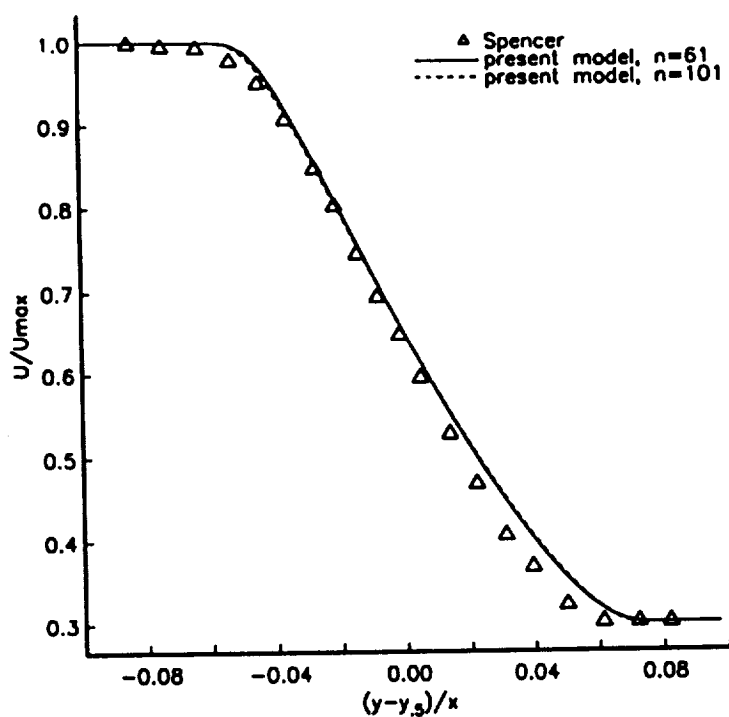


Figure 9. Grid resolution analysis of the mean velocity profile for a planar mixing layer with a speed ratio of .3.  $U_{max}$ : maximum velocity.

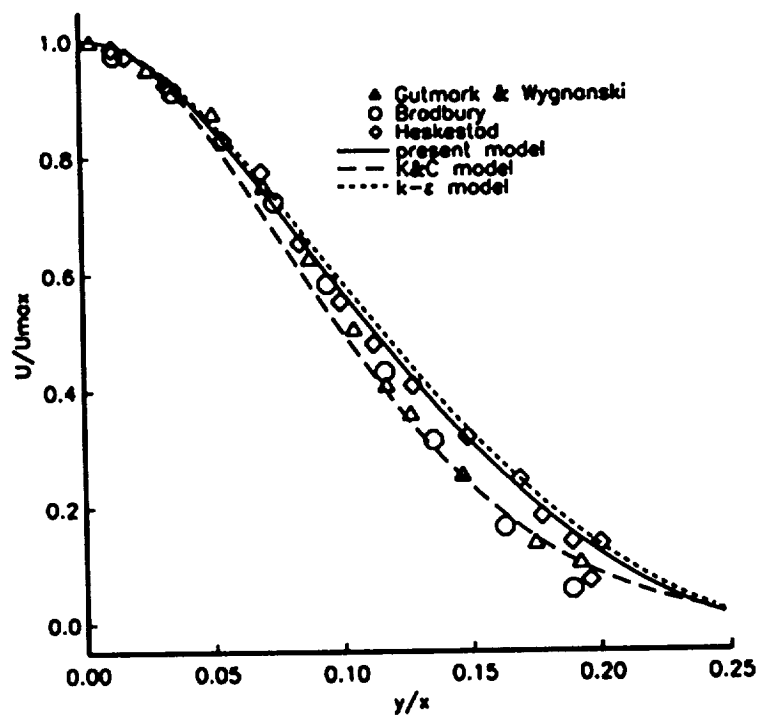


Figure 10. Mean velocity profile for a turbulent, planar jet.  $U_{max}$ : centerline velocity.

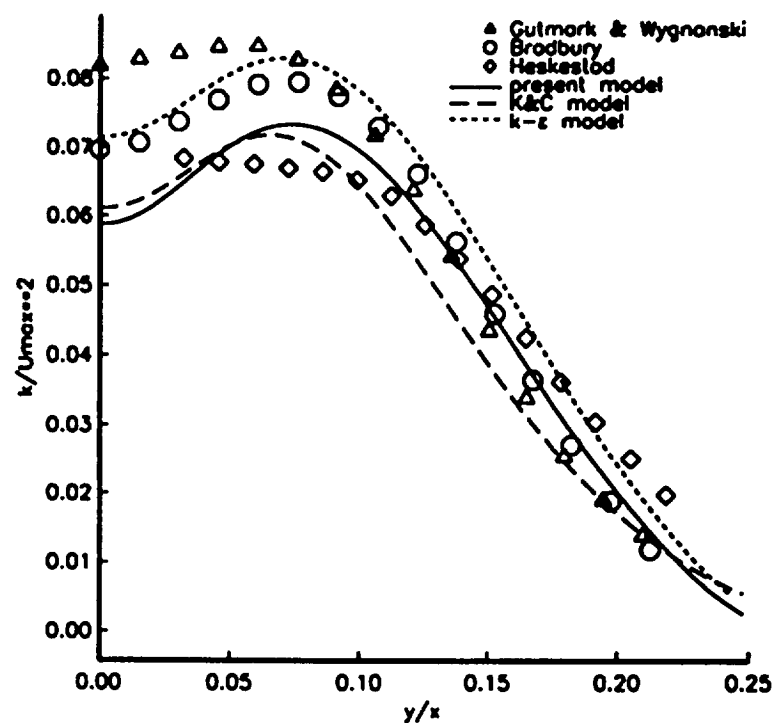


Figure 11. Turbulent kinetic energy profile for a planar jet.  
 $U_{max}$ : centerline velocity.

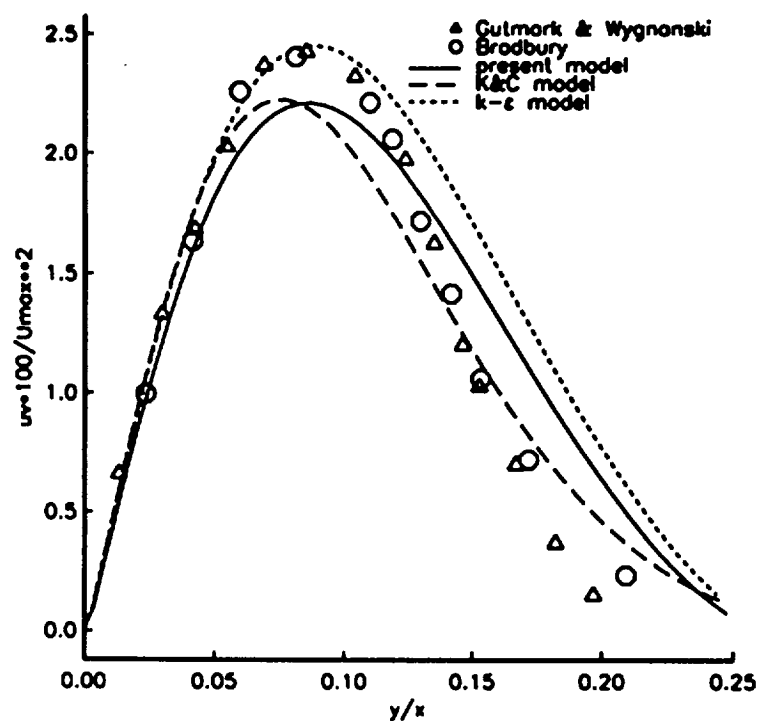


Figure 12. Shear stress profile for a planar jet.  
 $U_{max}$ : centerline velocity.

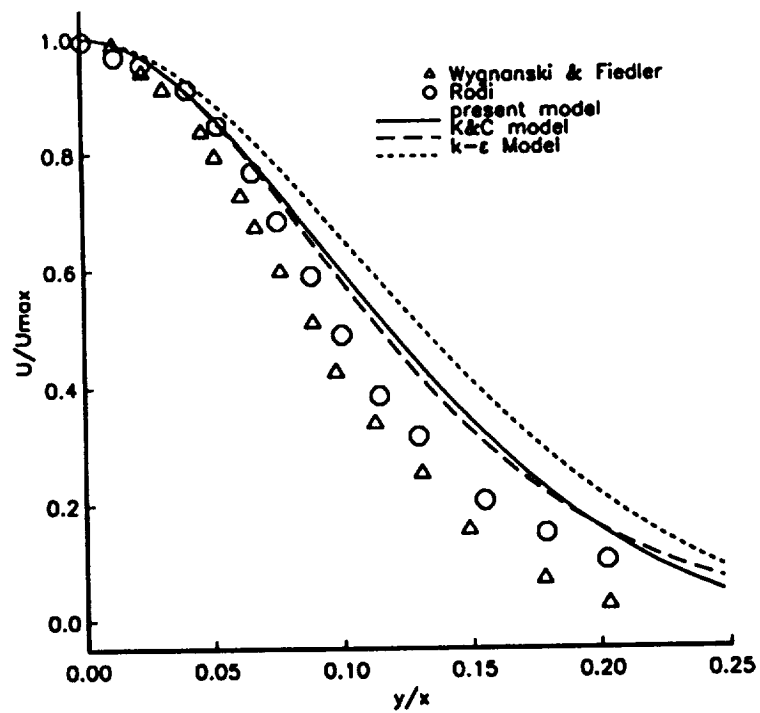


Figure 13. Mean velocity profile for a round jet.  
 $U_{max}$ : centerline velocity.

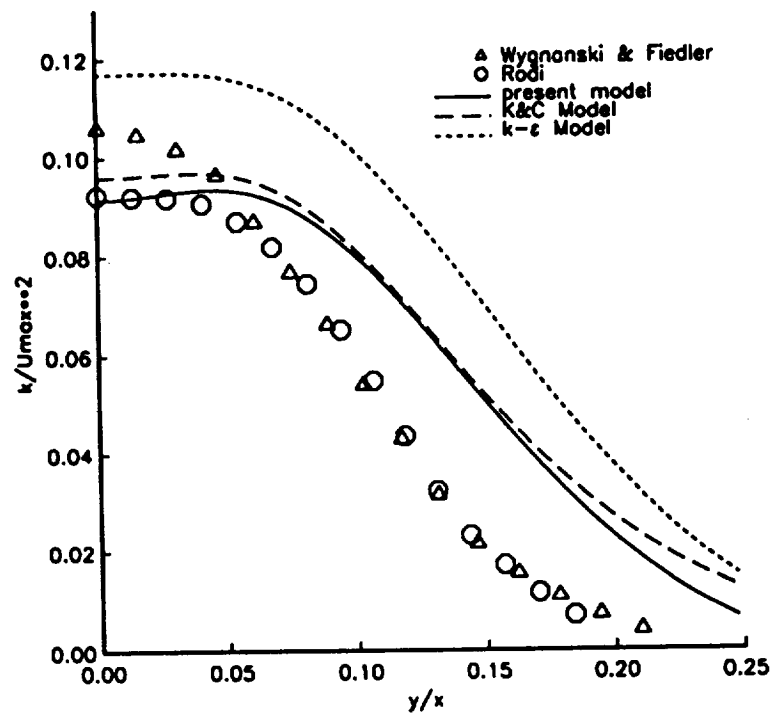


Figure 14. Turbulent kinetic energy profile for a round jet.  
 $U_{max}$ : centerline velocity.

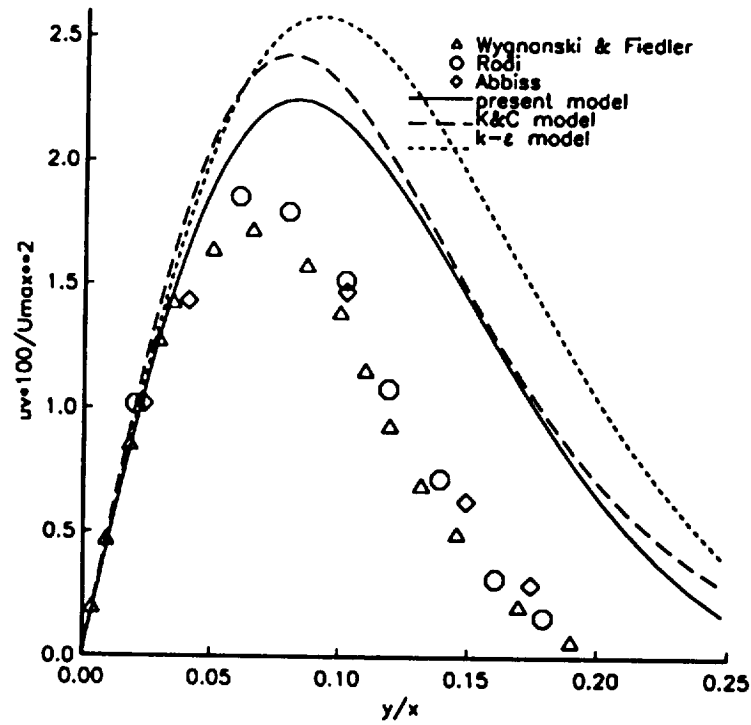


Figure 15. Shear stress profile for a round jet.  
 $U_{max}$ : centerline velocity.

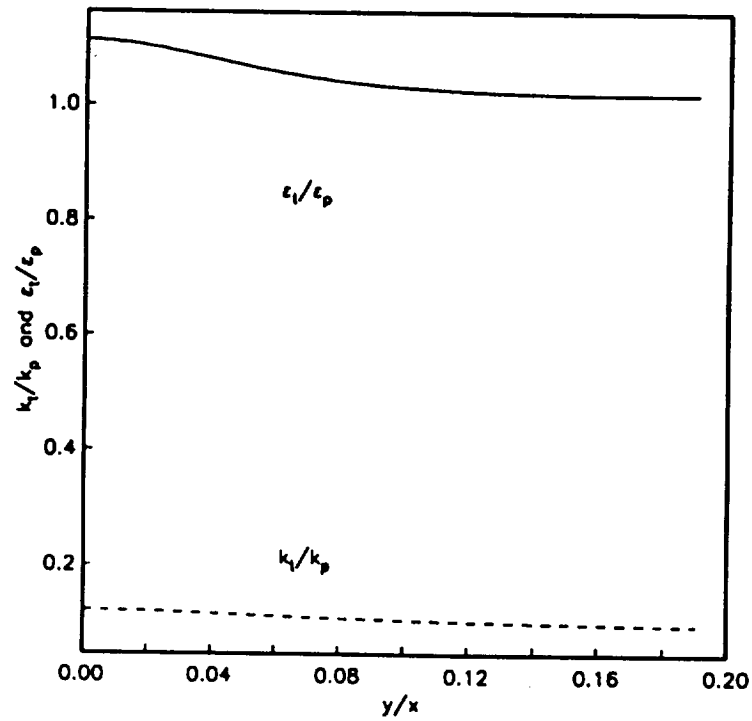


Figure 16. Dissipation and kinetic energy ratios for a round jet.



# Modeling of Turbulent Shear Flows

William W. Liou

## 1. Motivation and Objective

The development of advanced propulsion systems for high speed aerospace vehicles will require accurate computational models of turbulence that can be used in the CFD calculation of individual flow components. The immediate objective of the research activity described here is to identify robust modeling techniques for compressible turbulent flows. The main goal is to develop second-order Reynolds-stress models for compressible flows.

## 2. Work Accomplished

Several approaches are now being pursued. A two-scale eddy-viscosity model was developed earlier<sup>1,2</sup> and successfully applied to the calculation of compressible shear layers. In this reporting period, the model was further assessed in the solution of compressible boundary layers<sup>3</sup>.

A new modeling technique that describes the large-scale coherent structures in free shear flows using a weakly nonlinear theory is also being studied. The model was shown to be capable of providing a deterministic description of the time-dependent turbulent motions at the large scale in incompressible free mixing layers. To further assess the model in describing the coherent structures generated by a more complex flow mechanism, a simple linear analysis was performed for curved mixing layers in the past year<sup>4</sup>. It was found that some observed characteristics of the large-scale structures might very well be described by the simple analysis.

Also, a part of the research activity involves the development and validation of a new model equation for the turbulent dissipation rate<sup>5</sup>. The new model dissipation rate equation may increase the numerical stability of the second-order Reynolds-stress model in complex flow calculations. In the following, progress made on the individual research subjects in the current reporting period is briefly reviewed. The complete analyses are given in the related cited reports.

### 2.1 Validation of compressible two-scale model in boundary layers

The rationale for exploring the two-scale approach in the modeling of compressible turbulent flows is described in detail in a NASA TM<sup>LS</sup>. Briefly, the observed eddy shocklets and the modification of the energy transfer process due to flow compressibility render compressible turbulence non-equilibrium, i.e., the energy is not transferred at the same rate between the eddies of different scales. Therefore, single-scale modeling of the non-equilibrium compressible turbulence is not sufficient. The two-scale model approach adopted here relinquishes the assumption that the energy is transferred from the large scale to the small scale at the same rate as it is dissipated by the molecular viscosity. This allows the eddies of different sizes to respond

differently to compressibility effects. Since the eddy shocklets were observed in numerical experiments to be scaled mainly with the large eddies, compressibility effects were applied explicitly to the transport equations governing the kinetic energy of the large scale and the rate of energy transfer from the large scale to the small scale. The model equations, with the boundary-layer approximation, were written as,

$$\bar{\rho} \frac{D\tilde{k}_p}{Dt} = \frac{\partial}{\partial y} \left[ \left( \bar{\mu} + \frac{\mu_T}{\sigma_{\tilde{k}_p}} \right) \frac{\partial \tilde{k}_p}{\partial y} \right] + (1 - \alpha_2 M_t) \mu_T \left( \frac{\partial \tilde{u}}{\partial y} \right)^2 - (1 - \alpha_3 M_t^2) \bar{\rho} \tilde{\epsilon}_p \quad (1)$$

$$\bar{\rho} \frac{D\tilde{\epsilon}_p}{Dt} = \frac{\partial}{\partial y} \left[ \left( \bar{\mu} + \frac{\mu_T}{\sigma_{\tilde{\epsilon}_p}} \right) \frac{\partial \tilde{\epsilon}_p}{\partial y} \right] + C_{p1} \frac{\tilde{\epsilon}_p}{\tilde{k}_p} \mu_T \left( \frac{\partial \tilde{u}}{\partial y} \right)^2 - (C_{p2} - C_{p3} M_t^2) \bar{\rho} \frac{\tilde{\epsilon}_p^2}{\tilde{k}_p} \quad (2)$$

$$\bar{\rho} \frac{D\tilde{k}_t}{Dt} = \frac{\partial}{\partial y} \left[ \left( \bar{\mu} + \frac{\mu_T}{\sigma_{\tilde{k}_t}} \right) \frac{\partial \tilde{k}_t}{\partial y} \right] + \bar{\rho} \tilde{\epsilon}_p - \bar{\rho} \tilde{\epsilon}_t \quad (3)$$

$$\bar{\rho} \frac{D\tilde{\epsilon}_t}{Dt} = \frac{\partial}{\partial y} \left[ \left( \bar{\mu} + \frac{\mu_T}{\sigma_{\tilde{\epsilon}_t}} \right) \frac{\partial \tilde{\epsilon}_t}{\partial y} \right] + C_{t1} \bar{\rho} \frac{\tilde{\epsilon}_t \tilde{\epsilon}_p}{\tilde{k}_t} - C_{t2} \bar{\rho} \frac{\tilde{\epsilon}_t^2}{\tilde{k}_t} \quad (4)$$

where  $\tilde{k}_p$  and  $\tilde{k}_t$  denote the turbulent kinetic energy of the large and the small scale, respectively.  $\tilde{\epsilon}_p$  denotes the energy transfer between the different scales and  $\tilde{\epsilon}_t$  represents the turbulent dissipation. This model has been successfully applied in the prediction of compressible shear layers. This includes the observed reduction of growth rate as well as the mean velocity profile. In this reporting period, the model was further assessed in the solution of compressible boundary layers. To account for the effects of the wall, a compressible wall-function was introduced. For turbulent boundary layers with adiabatic wall or cooled wall, it has been shown that the mean velocity in the fully turbulent region near the wall can be described by a log function, similar to the log-law of the wall for incompressible boundary layers. The use of the wall function to bridge from the high Reynolds number region to the wall also eliminates the need for devising near-wall damping functions and the compressibility model can be truly put to test. The results of the assessment of the two-scale model in compressible boundary layers are included in a NASA TM<sup>3</sup>. The following two figures are extracted from that report. Figure 1 shows the comparison of the predicted mean velocity profiles with measurement for a compressible boundary layer. The flow Mach number is 2.831 and the Reynolds number based on the momentum thickness is 424,070. The flow was studied in an experiment and the measurement was reviewed by Fernholz and finly. The designated flow number is 65020101. Figure 1 shows that both the present model and the standard  $k - \epsilon$ , with Sarkar's compressibility correction, predict well the mean velocity profile. Figure 2 shows the comparison of the calculated skin friction coefficients,  $C_f$ , using the present model and the standard  $k - \epsilon$  model, with the Van Driest II correlation. The Reynolds number based on the momentum thickness is 10,000. The wall is adiabatic. There is a good agreement between the present



model and the Van Driest II formula at all the Mach numbers tested. The standard  $k - \epsilon$  model, with Sarkar's compressibility corrections, underpredicts  $C_f$ . Overall, the present two-scale model produces good agreement with measurements in both compressible shear layers and compressible boundary layers with the same model coefficients, which has been shown to be not feasible using the single-scale  $k - \epsilon$  model in conjunction with other compressibility corrections.

## 2.2 Linear analysis of curved mixing layers

In a plane mixing layer, it has been shown that the profile distributions of the large-scale structure can be described by linear disturbances generated by shear instability, or Kelvin-Helmholtz instability. In an earlier report<sup>6</sup>, the author has further shown that a predictive turbulence model can be obtained by using a weakly nonlinear wave theory in which the local structural characteristics are described by linear wave disturbances and their amplitudes are determined by their kinetic energy evolution. For a curved mixing layer, the effect of centrifugal forces is introduced. The centrifugal force may stabilize or destabilize fluctuations, depending on the velocity distribution of the flow. The additional, yet identifiable, complexity in the incompressible curved mixing layer presents a good test for the applicability of the wave model in cases where flow fluctuations can be affected by more complicated mechanisms, such as flow compressibility. Large-scale spanwise vortical structures have been observed in both stably and unstably curved turbulent mixing layers. These structures appear to be less two-dimensional in an unstably curved mixing layer than they are in a stably curved mixing layer. Stationary vortical structures have also been observed in experiments in a unstably curved mixing layer. A simple linear analysis was performed for curved mixing layers. We are unaware of any previously reported work studying this particular problem. The governing equations for the disturbance can be reduced to the following single equation<sup>4</sup> for the vertical velocity fluctuation,  $v(y)$ ,

$$(\alpha U - \sigma) \frac{d^2 v}{dy^2} + \frac{2\alpha U}{R} \frac{dv}{dy} - [(\alpha U - \sigma)(\alpha^2 + \beta^2) + \alpha \frac{d^2 U}{dy^2} - \frac{2U}{R} \frac{\beta^2}{\alpha U - \sigma} \frac{dU}{dy}] v = 0. \quad (5)$$

Figure 3 shows the distributions of the eigenfunction,  $v(y)$ , for the most unstable modes with two different stabilizing curvatures. The shapes of the eigenfunction for the curved cases are seen to be similar to those of a plane shear layer. With the centrifugal forces also becoming a destabilizing factor, or when the mixing is unstably curved, more than one linear instability mode can exist in the flow. In addition to the spatially convecting Kelvin-Helmholtz modes, stationary modes that assume no periodicity in the streamwise direction are also found. Figure 4 shows the countour of the streamwise vorticity of one such mode that has the highest growth rate among the hierarchy of instability modes found at the same spanwise number. The vorticity pattern shows that this mode is a vortex pair counterly rotating in the streamwise direction, similar to the Gortler vortices that are observed in a flow along

a concave wall (destabilizing curvature). It was also found that the number of the vortex pair increases for the mode with lower growth rate in the same hierarchy. In a recent experiment, spatially stationary streamwise counter-rotating vortex pairs were observed in the near field mixing region of underexpanded jets, where the flow was also subjected to curvature effects. These preliminary results seem to indicate that linear analyses can be used to provide local profile description of the large-scale structure under the influence of streamline curvature.

### 2.3 Assessment of a new model dissipation rate equation

The new model dissipation rate equation was derived from the equation for the mean square of fluctuation vorticity ( or enstrophy ). Models for the dominant terms in the equation, such as the source and sink for the production of enstrophy, were developed by examining the dynamics of vorticity fluctuations. This first-principle based model dissipation rate equation was applied to a variety of turbulent flows as part of a two-equation model. The details of the two-equation model and the results of model application are described by T.H. Shih in this report and in a NASA TM<sup>5</sup>. Figure 5 shows the comparison of the present model predictions of the mean velocity profile with measurements for incompressible round jets. The  $k - \epsilon$  model prediction is also included for comparison. The agreement between the predictions and the measurement is better for the present model than it is for the standard  $k - \epsilon$  model. The same is also true for the spreading rate of the jet. It should be noted that the new dissipation rate model equation can be used in conjunction with advanced second-order models. In fact, it is expected that the new model equation may improve the numerical stability problem associated with the Reynolds stress equations.

### 3. Future Plans

- (1) Identify a number of appropriate complex compressible flows as bench-mark test cases for model assessment and validation. Preliminary candidates include, but are not limited to, supersonic ramp flows, transonic flow over an airfoil, and flows about turbine blades.
- (2) Implement the two-scale compressible model into Navier-Stokes CFD codes.
- (3) Perform linear analyses for compressible plane and curved shear layers to investigate the effects of compressibility on the characteristics of the coherent large-scale structure.

**4. References**

- <sup>1</sup> Duncan, B. S., Liou, W.W., and Shih, T.-H., "A Multiple-Scale Turbulence Model for Incompressible Flow," AIAA 93-0086 (1993).
- <sup>2</sup> Liou, W.W. and Shih, T.-H., "A Multiple-Scale Model for Compressible Turbulent Flows," NASA TM 106072 (1993).
- <sup>3</sup> Liou, W.W. and Shih, T.-H., "Compressible Turbulent Boundary Layer Predictions Using a Multiple-Scale Model," to appear in NASA TM (1993)
- <sup>4</sup> Liou, W.W., "Linear Instability of Curved Free Shear Layers," AIAA 93-3253 (1993).
- <sup>5</sup> Shih, T.-H., Liou, W.W., Shabbir, A., Yang, Z., and Zhu, J., "A Vorticity Dynamics Based Model for the Turbulent Dissipation," NASA TM 106177 (1993).
- <sup>6</sup> Liou, W.W. and Morris, P.J., "Weakly Nonlinear Models for Turbulent Mixing in a Plane Mixing Layer," *Phys. Fluids*, 4, pp. 2798-2808 (1992).

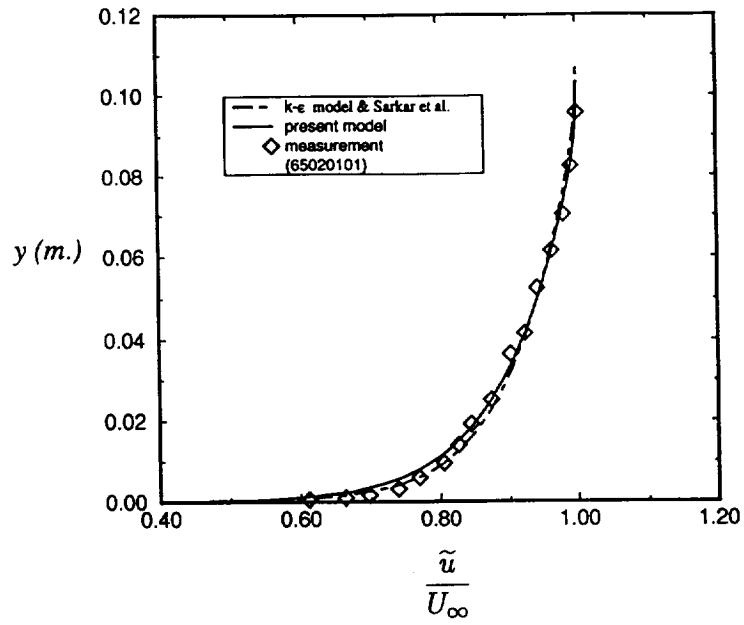


Figure 1. Comparison of mean velocity profiles.  $M_\infty = 2.831$ ,  $Re_\theta = 424,070$ .

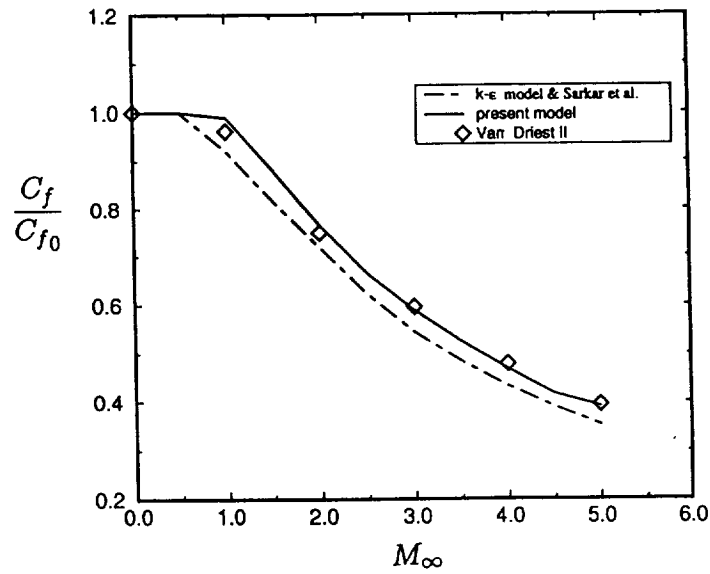


Figure 2. Comparison of skin friction coefficients.  $M_\infty = 5.0$ ,  $Re_\theta = 10,000$

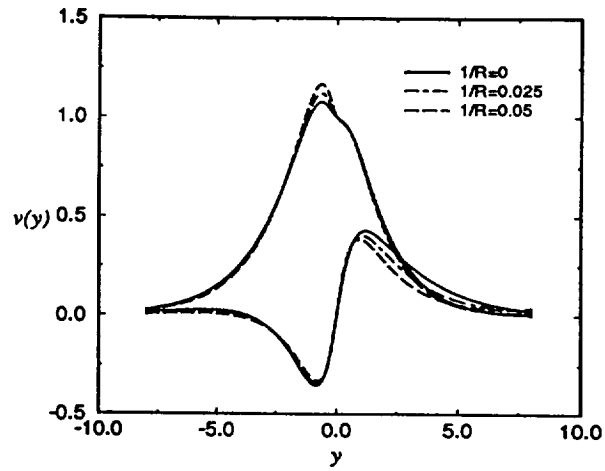


Figure 3. Distributions of the eigenfunction  $v(y)$  for the most unstable Kelvin-Helmholtz modes with  $\beta = 0.3$ . Stably curved.

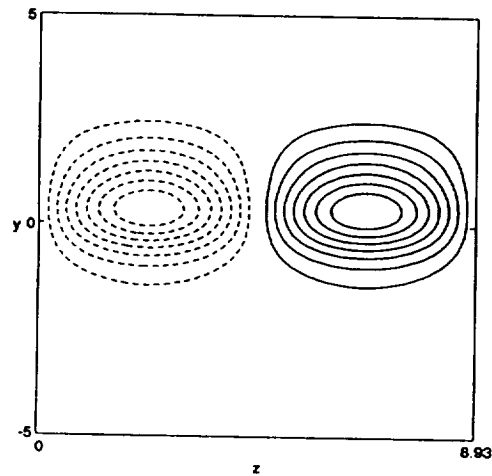


Figure 4. Streamwise vorticity  $\omega_x$  of the first modes of  $\beta = 0.7$  of zero frequency. Unstably curved.

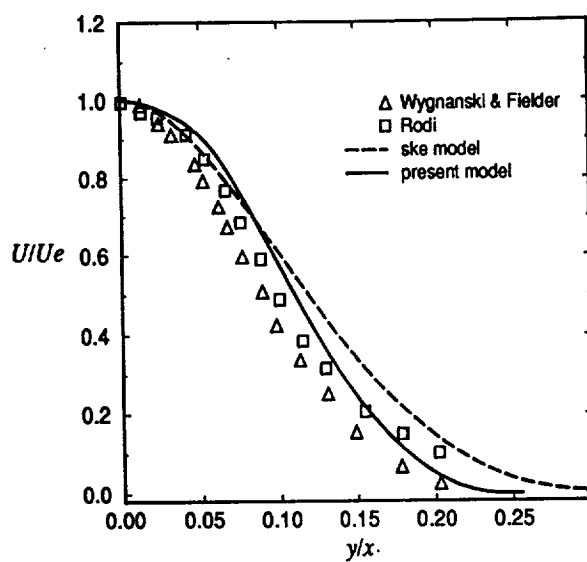


Figure 5. Self-similar mean velocity profiles for a round jet.

# PDF Models for Compressible Reactive Flows and DNS

A.T. Hsu

## 1. Motivation and Objective

1) **PDF.** The objective of the present work is to develop a probability density function (pdf) turbulence model for compressible reacting flows for use with a finite-volume flow solver. The probability density function of the species mass fraction and enthalpy are obtained by solving a pdf evolution equation using a Monte-Carlo scheme. The pdf solution procedure is coupled with a compressible finite-volume flow solver which provides the velocity and pressure fields. A modeled pdf equation for compressible flows, capable of capturing shock waves and suitable to the present coupling scheme, is proposed and tested. Convergence of the combined finite-volume Monte-Carlo solution procedure is discussed, and an averaging procedure is developed to provide smooth Monte-Carlo solutions to ensure convergence. Two supersonic diffusion flames are studied using the proposed pdf model and the results are compared with experimental data; marked improvements over solutions without pdf are observed.

2) **DNS.** Direct numerical simulation results and theoretical analysis are presented for the effect of the Coriolis force on compressible homogeneous isotropic turbulence. It is shown that the Coriolis force serves as a frequency modulator on turbulence. While the Coriolis force neither creates nor destroys turbulent kinetic energy, it redistributes energy by eliminating low frequency waves and transferring energy to waves with a frequency of  $2\Omega$ . The dissipation rate of turbulent kinetic energy can be either reduced or enhanced depending on whether or not the ratio between the rotation time scale and the Kolmogorov time scale is much greater than one. It has been demonstrated both theoretically and numerically that the Taylor-Proudman theorem is applicable to homogeneous turbulence only when the time scale of rotation, defined as the inverse of the frequency of the inertial waves, approaches the Kolmogorov time scale, and that two-dimensionalization occurs in this regime.

## 2. Work Accomplished

In the past year, a pdf model for compressible reactive flows has been developed and validated in 2D supersonic hydrogen-air flames. The analysis of compressible homogeneous turbulence under rotation is completed.

### 2.1 A PDF Model for Compressible Reactive Flows

The most attractive feature of the probability density function (pdf) method is its ability to overcome the chemistry closure problem in turbulent reacting flow computations. Much progress has been made in both pdf theory and application

during the past decade<sup>1</sup>. However, most of the previous developments of pdf models (using a pdf evolution equation) were restricted to low speed combustion. The objective of the present work is to develop a pdf model for high speed compressible flows that can be coupled with existing finite-volume or finite-difference flow solvers.

High speed compressible reacting flows present some unique challenges to pdf modeling because of the existence of shocks and strong dilatation terms. In principle, the joint pdf of velocity, pressure, temperature, and species mass fraction can be solved using a self-contained Monte-Carlo solver, and such a scheme should be sufficient for solving compressible reacting flow problems<sup>2</sup>. Unfortunately, a shock capturing pdf pressure solver is currently unavailable, and it may be a while before shock capturing schemes using pdf method would be developed, and a even longer time for these schemes to mature to the extent that they could be regularly used in industry. Thus, it appears that the only alternative currently available for immediate application of the pdf method to high speed flows calls for the decoupling of the aerodynamics from the scalar field. Since shock capturing finite-difference and finite-volume codes have reached a certain degree of maturity, and are widely used in industry, it seems, at least from the standpoint of practical application, that the use of the composition pdf together with a finite-difference or finite-volume code is more beneficial.

The pdf model and the corresponding Monte-Carlo solver developed in the present work is general enough to be applied with any existing finite-volume or finite-difference codes. To demonstrate the portability of the pdf solver, we have applied it in conjunction with two distinctly different versions of a finite-volume code known as RPLUS<sup>3</sup>: The first version is the original RPLUS designed specifically for high speed combustion problems. It solves the full compressible Navier-Stokes equations and species transport equations using an LU scheme. Algebraic and two-equation turbulence models are available in the code. The second version is a modified RPLUS code developed for the modeling of turbulent reacting flows with sprays occurring inside a Wankel engine<sup>4</sup>; sufficient changes in the numerical algorithm and code structures have been made in this version for it to be regarded as a different code. When using a pdf algorithm to solve for chemical reactions, the species transport equations in the finite-volume code are replaced by the composition pdf equation.

Since the flow field, including the mean velocity, density, pressure, turbulent kinetic energy, etc., are provided by the finite-volume flow solver, we only need to solve for the species mass fractions and energy (or enthalpy, temperature, etc.) in the Monte-Carlo pdf solver. For low speed reacting flows, there are two unclosed terms in the species and temperature joint pdf equation; namely, the turbulent diffusion term and the molecular diffusion term. For high speed flows, depending on the specific formulation chosen for the energy equation, many more unclosed terms could appear<sup>5</sup>. The pros and cons of various formulations are discussed in the present work. The formulation best suited for the present objective is studied in detail, and a modeling procedure is proposed and tested.

In incompressible flow computations, the flow equations can essentially be solved



independently of the pdf equation since the momentum and energy equations are decoupled; one only needs to transfer information from the flow solver to the pdf solver, but not vice versa. In contrast, the presence of the strong pressure and density gradients makes the coupling between flow equations and the pdf equation very important for compressible flows. Because the finite-volume solution of the flow field is smooth, the transfer of information from the flow solver to the Monte-Carlo pdf solver is straightforward, but information transfer the other way around presents a challenge because of the relatively large statistical error. A way of obtaining smooth averaged solutions from a Monte-Carlo pdf solver, using a relatively small number of samples that is within the capacity of today's computing facilities, becomes an important issue in the finite-volume/Monte-Carlo coupling process.

An issue related to the problem of coupling mentioned in the previous paragraph is the convergence of a Monte-Carlo procedure in solving an elliptic flow problem. Applications of pdf models to elliptic flow computations are few<sup>6,7,8,9</sup>. When a Monte-Carlo solver is used to simulate elliptic flows, both the definition and the criteria of convergence are unclear, and little discussed. Since the statistical error in a Monte-Carlo method is often much larger than the truncation error in a finite-volume or finite-difference scheme, the convergence of a combined finite-volume Monte-Carlo scheme is difficult to measure. Without special treatment, the solution often appears non-convergent.

A combined ensemble and time-averaging procedure for the solution is proposed in the present work. This averaging scheme makes the measurement of the convergence of a Monte-Carlo scheme possible, and provides sufficiently smooth solutions to be fed back into the finite-volume flow solver, making the coupling between Monte Carlo and finite-volume solvers feasible.

The compressible pdf model is validated using a non-reacting supersonic flow over a ten degree ramp, where the temperature rise across the shock is computed using the modeled pdf equation and compared with the theoretical solution. Two cases of supersonic hydrogen combustion are studied using the proposed model: A two-dimensional supersonic wall jet and a supersonic axisymmetric jet. Results compare well with experimental data. In both of these supersonic jet cases it was shown that with the pdf model, the solutions are markedly improved over those obtained from a conventional CFD combustion code. Preliminary results from 3D applications are also reported in this paper.

### 2.1.1 Pdf Formulation for Compressible Flows

For compressible flows, the energy equation can be cast in a number of different forms. Pope chose to use total enthalpy<sup>2</sup>:

$$\rho H_{,t} + \rho u_j H_{,j} = -p_{,t} - q_{j,j} + (\tau_{ji} u_i)_{,j}. \quad (1.1)$$

In the above equation, as well as in the equations that follow, repeated indices imply summation over the range of the indices. By neglecting molecular diffusion effects and assuming steady flow, the energy equation reduces to constant total enthalpy

for a given sample particle. The total enthalpy formulation provides the simplest form of the energy equation and, if the pdf for pressure and velocities are known, the formulation can be applied to compressible flows without introducing any new modeled terms<sup>2</sup>. However, in the present case, the velocity field is obtained from a finite-volume solver, and the pdf for the velocity field is unknown. Without the velocity pdf, one cannot back out the temperature of each sample point from a given total enthalpy.

Kollmann<sup>5</sup> suggested the use of specific internal energy, which leads to a formulation with  $\Delta = u_{j,j}$ , the velocity divergence as a random variable. In order to solve for  $\Delta$ , Kollmann introduced a transport equation for the velocity divergence into the pdf formulation. The resulting pdf equation produces a large number of new unknown terms that need modeling. Without enough experimental or direct numerical simulation data to establish models for these new terms, it is hard to estimate the viability of this approach.

In the present study, considering the fact that the velocity pdf is not known in our solution, we choose to use the specific enthalpy formulation to minimize the need of devising new models. As we shall show in the following, the specific enthalpy formulation allows us to use existing models from previous works on second order closure models for compressible turbulence.

The energy equation in terms of enthalpy is:

$$\rho h_{,t} + \rho u_j h_{,j} = -\frac{Dp}{Dt} - q_{j,j} + \Phi \quad (1.2)$$

where  $\Phi$  is the dissipation due to viscosity. Neglecting  $\Phi$  from the energy equation, the evolution equation for the joint pdf of species mass fractions and specific enthalpy,  $P(Y_1, \dots, Y_N, h; x_i, t)$ , can be written as:

$$\begin{aligned} &(\rho P)_{,t} + (\rho < u_j > P)_{,j} + (\rho w_j P)_{,Y_j} = \\ & - (\rho < u'_j | Y_i, h > P)_{,j} - (\rho D_j Y_{j,ii} | Y_i, h > P)_{,Y_j} - \left( \left\langle \frac{Dp}{Dt} | Y_i, h \right\rangle P \right)_{,h} \end{aligned} \quad (1.3)$$

Where the right hand side terms represent turbulent diffusion, molecular diffusion, and the pressure effect, respectively. All the conditional means on the right hand side of the equation are extra unknowns and need to be modeled.

In what follows the modeling of the unknown conditional means is discussed. Since comparing with the pdf equation for low speed flows the only new term is the conditional mean of the material derivative of pressure, we start by deriving an appropriate model for this term.

Using  $C$  to denote the conditions in the mean, the new term can be written as

$$\left\langle \frac{Dp}{Dt} | C \right\rangle = \langle p | C \rangle_{,t} + \langle u_i p_{,i} | C \rangle; \quad (1.4)$$

decomposing the random variables into means and fluctuations,  $p = \langle p \rangle + p'$  and  $u_i = \langle u_i \rangle + u'_i$ , we have

$$\left\langle \frac{Dp}{Dt} | C \right\rangle = \langle p \rangle_{,t} + \langle u_i \rangle \langle p \rangle_{,i} + \langle u'_i p' | C \rangle_{,i} + \langle p' u'_{i,i} | C \rangle. \quad (1.5)$$

To use existing models for the last two terms in the above expression, we need first to assume that the product of the fluctuating velocity and fluctuating pressure is statistically independent of the species mass fractions and specific enthalpy.

With this assumption, the last two unknown terms can be readily modeled: The first of the two terms,  $\langle u'_i p' \rangle_{,i}$ , is the trace of the pressure-strain rate tensor in second order closure models. Most second order closure models give the following expression for this term <sup>8</sup>:

$$\langle u'_i p' \rangle_{,i} = 0.8\rho \langle k \rangle \langle u_i \rangle_{,i}, \quad (1.6)$$

where  $\langle k \rangle$  is the mean turbulent kinetic energy.

The last term,  $\langle p' u'_{i,i} \rangle$ , is the so called pressure dilatation term in second order closure models for compressible flows. Following Sarkar<sup>9</sup>, we write:

$$\langle p' u'_{i,i} \rangle = -\alpha_2 \rho Pr M_t + \alpha_3 \rho \epsilon M_t^2 \quad (1.7)$$

where  $Pr$  is the turbulent production,  $\epsilon$  is the dissipation of turbulent kinetic energy,  $M_t$  is the turbulent Mach number, and  $\alpha_1$  and  $\alpha_2$  are model constants given by Sarkar as 0.15 and 0.2, respectively. All the information needed in the above models is available from a flow field solution using a  $k - \epsilon$  model.

The final modeled pdf equation then becomes:

$$(\rho P)_{,t} + (\rho \langle u_j \rangle P)_{,j} + (\rho w_j P)_{,Y_j} = (D_t P)_{,j} + M(P) - (S_p P)_{,h}. \quad (1.8)$$

where the first two terms on the right hand side of the equation are the modeled terms for turbulent diffusion and molecular mixing, of which details can be found in refs. <sup>12,13</sup>; the last term is the term representing the compressible effect, with a new source term defined as

$$S_p = \langle p \rangle_{,t} + \langle u_i \rangle \langle p \rangle_{,i} + 0.8\rho \langle k \rangle \langle u_i \rangle_{,i} - \alpha_2 \rho Pr M_t + \alpha_3 \rho \epsilon M_t^2, \quad (1.9)$$

which can be regarded as the convection velocity of a sample particle in the  $h$ -direction in the space spanned by  $h$  and  $Y_i$ 's.

The new term in the pdf equation simulates the compressibility effect; in other words, it transfers information of a compressible flow field to the pdf solution. As a test case for the above model, a non-reacting supersonic flow over a ten degree ramp is calculated using a  $40 \times 50$  grid. The pdf solution of the temperature across the oblique shock is shown in Fig. 1.1. The pdf solutions are taken from several different times in the solution procedure. Since only 100 particles per cell were used for the calculation and no time-averaging or smoothing schemes were used, the oscillation in the solution is expected. A step function in the figure shows the theoretical solution of temperature for the same shock. The results show that the new model picks up the temperature rise across the shock fairly accurately.

A word of caution must be given here: The source term  $S_p$  can be very large for high Mach number flows or flows with strong shocks. When using an explicit time

marching scheme in the Monte-Carlo simulation, time step must be carefully chosen such that the "CFL number" does not exceed one to ensure a converged solution.

### 2.1.2 Solution Procedure

Since the Monte-Carlo method used for solving the pdf evolution equation has been given in a previous paper<sup>12</sup>, and the numerical schemes used in the finite-volume code are well documented, we will only describe those details that are important or new for the present work on compressible pdf modeling and elliptic flow solvers.

### Coupling

When coupling a pdf solver with RPLUS, the species transport equations in the RPLUS code are no longer needed. The information we need, at each marching time step, from the flow solver (RPLUS) includes the mean velocity, pressure, density, and a turbulence time scale or quantities such as the turbulent kinetic energy and dissipation rate. The species transport and chemical reactions are simulated by solving the pdf evolution equation. At every time step, the species mass fraction field from the pdf solution is fed back to the mean flow solver for the computation of temperature and pressure. The Monte Carlo and finite-volume solvers are run in parallel, and information exchange occurs at every time step until a converged solution is obtained.

The finite-volume code requires smooth temperature and pressure fields as input, but a Monte-Carlo solution is usually not smooth unless the number of sample particles used is extremely large. Therefore, the transfer of information from a Monte-Carlo solver to a finite-volume solver could either require a prohibitive amount of computer memory, or cause divergence in the finite-volume solution. An economical way of obtaining smooth solutions from a Monte-Carlo solver becomes a key issue in the coupling procedure.

Pope and coworkers (e.g., <sup>12</sup>) use spline curve fitting in their parabolic flow calculations to generate smooth 1D Monte-Carlo solutions. For 2D and 3D data, splines are difficult to apply and a different way of smoothing must be found. A combined ensemble and time-averaging scheme, as described in the following section, is used in the present study to solve this problem.

### Convergence

The convergence criteria for a Monte-Carlo simulation of a steady elliptic flow problem is not well defined. When we use  $N$  events to simulate a random process, it is probable that the error is smaller than  $1/\sqrt{N}$ , which is still a rather large number compared to the truncation errors of a finite-volume solution. The top curve in Fig. 1.2 shows the L2 norm convergence history of the ensemble averaged solution of a jet-in-cross-flow calculation, where the error is defined as

$$Error = \int_R (\langle \phi^{n+1} \rangle - \langle \phi^n \rangle)^2 dR \quad (1.10)$$

where  $\langle \phi \rangle$  is the ensemble mean of an unknown variable,  $\phi$ ,  $n$  denotes the time step, and  $R$  the solution domain. Using ensemble average only, the error curve levels off before a converged solution is obtained.

The reason for this inconsistency between the L2 error curve and actual convergence history is that the relatively large statistical error ( $1/\sqrt{500}$  for the present simulation) becomes dominant before a converged solution is obtained. Another major problem caused by the relatively large statistical error is that when the Monte-Carlo solution is transferred to the finite-volume flow solver, the statistical error may cause the finite-volume solution to diverge. We clearly need more sampling points; however, the computer cpu time and memory requirements become prohibitive when we further increase the number of samples.

For steady flow problems, a combined ensemble and time-averaging is used to overcome this problem: Time averaging is performed over a set of ensemble-averaged solutions to obtain a smoother solution. This averaging procedure is performed continuously at every time step; for instance, supposing that we are averaging over  $m$  time steps, at the  $n^{\text{th}}$  time step, the information from time step  $n-m$  is discarded, and the ensemble averaged solution from the current time step is added to the time averaging process. A similar time averaging method has been used by Correa and Pope<sup>9</sup>.

The curves in Fig. 1.2 shows the convergence history from averaging over 1 to 1000 iteration steps. The large jumps of the curves are caused by abandoning the sample from the initial condition; for instance, for the error curve of averaging over 1000 time steps, the jump occurs at  $N = 1000$ , where  $N$  is the number of iteration. This type of large excursion in the error only happens when  $N = N_{\text{average}}$ , and does not appear again at larger iterations. It appears that increasing the number of time steps averaged by approximately three fold cause the error to reduce an order of magnitude. The use of 100 time steps is sufficient in obtaining a smooth solution for the purpose of transferring information to the finite-volume flow solver. Our sample size is 500 per cell. The use of 1000 iteration steps is equivalent to the use of 500,000 particles per cell, a number that can not possibly be handled by today's supercomputers. This scheme provides a powerful tool for one to obtain huge samples with limited computer resources.

In the above example, we have assumed the time step used in the Monte-Carlo computation to be large enough that the errors in the solutions of two consecutive time steps are statistically independent. When time steps used are very small, this assumption may not be valid, and the effect of time averaging is greatly diminished. In which case, we chose to select solutions from every  $M$  time steps for the time averaging process, and make sure that the correlation of the random error reaches zero for a time  $t > M\Delta t$ . In some of the computations reported in this paper, we used solutions from every ten time steps in the averaging process.

## Efficiency

A flow trace analysis of the pdf solver revealed that an overwhelming portion of the cpu time was spent in selecting particles randomly for convection and diffusion

simulations; this is because the selecting process can not be vectorized effectively as is. In the case of non-reacting flow computations, more than 95% of the cpu time is spent on this process. The computational burden lies on the need to generate five random vectors of length  $N$ , for a sample size of  $N$ . A novel approach was devised to accelerate the solution procedure: At the beginning of each iteration, five random vectors of length  $2N$  are selected. For each cell, five random indices are selected, starting from which the samples are selected using the given random arrays. This removed the need to generate five random arrays for each cell, and allowed vectorization of the procedure. With this procedure, the cpu required is reduced by a factor of four.

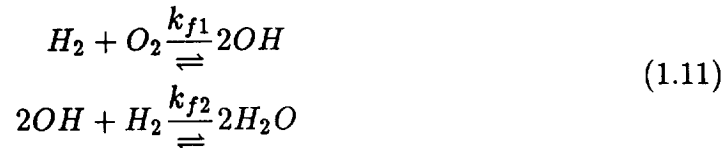
### 2.1.3 Results and Discussion

The pdf procedure is validated using experimental data for two cases of supersonic hydrogen diffusion flames: a supersonic hydrogen round jet and supersonic wall jet. The solution procedures used and the results are presented in the following sections. To demonstrate the applicability of the pdf model in general 3D flows, a 3D jet-in-cross flow is presented.

#### Supersonic Round Jet

The numerical computations for the case involving the injection of a supersonic hydrogen jet coaxially into a high-temperature, vitiated air-stream have been performed by the code that was originally developed for the modeling of turbulent, reacting flows with sprays occurring inside of a Wankel engine, which evolved from the RPLUS code. The finite-difference formulation is based on an Eulerian-Lagrangian approach where the unsteady, Navier-Stokes equations for a perfect gas-mixture with variable properties together with the standard two-equation  $k-\epsilon$  turbulence equations are solved in generalized, Eulerian coordinates on a moving grid by making use of an implicit finite-volume, Steger-Warming flux vector splitting scheme, and the liquid-phase equations are solved in Lagrangian coordinates. The turbulent viscosity is computed by a compressibility correction as proposed by Villasenor et al<sup>14</sup>. A complete description of the code can be found in Ref. 4. The code has recently been modified to accommodate axisymmetric flow fields before being coupled with the pdf solver.

Combustion is modeled by the following global, five-species, two-step model developed by Rogers and Chinitz<sup>15</sup> for  $H_2$ - $O_2$  combustion:



where the forward reaction rates are given as

$$k_{fi} = A_i T_{N_i} \exp(-E_i/RT) \quad (1.12)$$

with the coefficients given as:

$$\begin{aligned}
 A_1 &= 11.4 \times 10^{47} \\
 N_1 &= -10. \\
 E_1 &= 20.35 \times 10^6 \\
 A_2 &= 2.5 \times 10^{64} \\
 N_2 &= -13. \\
 E_2 &= 177.82 \times 10^6
 \end{aligned}
 \tag{1.13}$$

The units of  $A_i$  is  $m^3/mole \cdot sec$ , and the units of  $E_i$  is  $J/kg - mole$ . The backward reaction rates are calculated from the Gibbs free energy and the equilibrium coefficients.

The global model is reported to predict the oxidation of hydrogen adequately in flows that are not dominated by long ignition delay times. The model is tested for pressures at 1 atm, initial mixture temperatures of 1000-2000 K, and fuel/oxidizer equivalence ratios ranging between 0.2-2.0.

The geometry and flow conditions for the coaxial-jet case are given in Fig. 1.3. The test conditions are taken from Evans et al <sup>16</sup>. This test case has been the subject of investigation by several authors <sup>17,18</sup>, where the flow field is modeled by different assumptions: (1) turbulence is modeled by making use of either algebraic or two equation  $k-\epsilon$  models, (2) combustion is modeled by either finite-rate or equilibrium chemistry models, and/or (3) the effect of turbulence on reaction rates is modeled by either the eddy-breakup model or the assumed probability density functions approach to describe the species fluctuations.

The computational grid used in the flow calculations is 51x61 with the grid extending 30.0 fuel-injector diameters in the flow direction and 6.5 fuel-injector diameters in the transverse direction. The grid is stretched in such a way so that more resolution is obtained within 1.75 fuel-injector diameters about the nonindent in the transverse direction and also more resolution is provided near the inflow in the axial direction. The flow computations are initiated at  $x/d = 0.33$ , the nearest point at which the measurements are made. At the inflow all the flow variables are specified. The initial conditions used in the computations are similar to those chosen by Evans et al <sup>16</sup>, except the gas composition of central jet, which is assumed to contain small amounts of  $H_2O$  and  $N_2$  mass fractions ( $=0.1$ ) instead of pure hydrogen. The specification of inflow conditions contains a slight degree of uncertainty since the only available information at this location is the measured Pitot pressures. And all the other variables are chosen approximately to fit the measured pressure data. At the exit all the flow variables are extrapolated from the interior. The treatment of the upper boundary is determined by applying inviscid wall conditions. Values along the nonindent are obtained by applying zero gradient extrapolation, except the radial velocity, which is set equal to zero.

The pdf solution is obtained by making use of 100 particles per cell. The species mass-fraction field that is supplied to the finite-volume solver from the Monte-Carlo

solver is obtained from averaging the pdf solutions over the previous 100 time steps. The combined Monte Carlo and finite-volume solver required about 0.7 ms of cpu time per time-step per cell on a CRAY Y-MP. The inclusion of the pdf solver is found to increase the computational effort by a factor of 2.2. For the case examined, less than 2000 time-steps are required for the computations to reach a converged solution.

Figs. 1.4a-d show the radial profiles of four major species,  $H_2$ ,  $O_2$ ,  $H_2O$ , and  $N_2$ , from the combined Monte Carlo/finite-volume computations compared with experimental data at four different axial locations,  $x/d = 8.26, 15.5, 21.7$ , and  $27.9$ , respectively. The numerical results match fairly well with the experimental data considering the fact that the estimated error in measurements could be as large as 15%<sup>14</sup> and the uncertainty involved in specifying the inflow conditions. The estimated error in the measurements is reportedly due to the possibility that the gas composition might be altered because of additional reactions being taking place in the gas sampling probes as a gas chromatograph is used to measure the species concentrations<sup>16</sup>. The disagreement in the calculated results showing lower than the experimental values for the mass fractions of  $H_2O$ ,  $O_2$ , and  $H_2$  at axial locations of  $x/d = 21.7$  and  $27.9$  might also be attributed to the uncertainty involved in the specification of the inflow conditions in the jet region. However, no effort is made in the present computations to study the effect of different inflow conditions on the ensuing flow field.

To examine the effect of the pdf model on the predicted results, a separate set of finite-volume computations were performed without the pdf solver, with the chemiscal source term evaluated using the mean temperature and species mass fractions. The assumption of equal diffusivity is made in the computation. Combustion in these computations is also modeled by the global, 2-step combustion model of Rogers and Chinitz. And the corresponding results are summarized in Figs. 1.5a-d. The combined Monte Carlo and finite-volume computations seem to predict the position of the peak  $H_2O$  mass fraction rather accurately while in the finite-volume computations the position of the flame zone is shifted radially outward into the high-temperature region indicating that much more  $O_2$  is consumed than what is observed experimentally. While Monte Carlo/finite-volume computations predict negligible amounts of oxygen within the central-jet region, the non-pdf computations predict substantial amounts of  $O_2$  within this region at axial locations of  $x/d = 8.26$  and  $15.5$ . The reasons for this discrepancy could be attributed to a lack of consideration of the temperature fluctuations on the reaction rate. If the neglected temperature fluctuations are large, the reaction rates based on the mean gas temperatures are likely to lead to smaller oxidation rates as the calculated gas temperatures in this region remain lower than 600 K. At succeeding axial locations, the  $H_2O$  mass fraction grows and spreads much faster in the non-pdf solution as compared with the pdf solution. Similar to the findings in the present non-pdf computations, most if not all the previous computations, reported a radially-outward shift in the location of the peak  $H_2O$  mass fraction into the high-temperature region and, also, reported that  $O_2$  is consumed more rapidly in the calculated results. The



most likely cause for this disagreement may be due to incorrect temperature dependence on some of the reaction rates, leading to rapid combustion as the temperature rises in the flame zone<sup>18</sup>.

The above results demonstrated that the use of pdf turbulence model can improve the accuracy of combustion computations considerably.

### Supersonic Wall Jet

The second test case is the experiment reported by Burrows and Kurkov<sup>19</sup> in 1973. This experiment has been investigated numerically by several authors<sup>17,18</sup>. Figure 6 shows its flow configuration. The two-dimensional test section measures 35.6 cm downstream of a  $H_2$  wall jet. The jet is mixed with a vitiated air stream and burned. A high pressure gas generator supplied Mach 2.44 vitiated air at approximately 1270K. The composition of the air is 25.8%  $O_2$ , 25.6%  $H_2O$ , and 48.6%  $N_2$  by mass.

The simulation of the wall-jet is performed by coupling the pdf solver with RPLUS<sup>3</sup>. The Baldwin-Lomax algebraic turbulence model is used in this calculation. The turbulence diffusivity used is calculated based on the eddy viscosity and the assumption that the turbulence Schmidt number equals one. The time scale needed in the molecular mixing model of the pdf equation is calculated using  $\tau = y^2/\nu_t$ , where  $\nu_t$  is the turbulent viscosity from the algebraic model, and  $y$  is the distance from the wall.

The numerical results reported in the present paper are obtained using a  $71 \times 61$  grid in the test section. A finer grid had been tested with little change in the solution observed. The pdf solver uses 100 samples per cell and the solution is obtained by averaging over 100 time steps. The cpu time required on a CRAY Y-MP is approximately 0.7 ms per time-step per cell. The calculation of the chemical reaction accounts for 68% of the total cpu time. The required cpu-time is proportional to the number of samples used, but is unrelated to the number of time steps being averaged.

The overview of the solution by the coupled Monte Carlo/finite-volume computation for the wall-jet case is depicted in Fig. 1.7a-d show the temperature and the mass fraction of hydrogen, oxygen, and water vapor. The peak temperature in this case is approximately 2500K. The water vapor contour shows that ignition occurs immediately after hydrogen comes in contact with the vitiated air streams. In reality, an ignition delay was observed in the experiment. This failure to predict the ignition point is expected because partial equilibrium is assumed in the global chemistry model used. The comparison of the numerical solution and experimental data measured at the test-section exit is shown in Fig. 1.8a-b. The computed species mole fractions shown in Fig. 1.8a agree very well with the experimental data. The computed total temperature profile, compared to the experimental measurement in Fig. 1.8b, appears to be shifted away from the wall. However, we believe that the numerical solution for the total temperature is reasonable for the following reason: The profile of water vapor indicates that the distance between the flame surface (peak of water vapor) and the wall is more than 2 cm; since the vitiated air stream

has larger total temperature, the peak of total temperature should be farther away from the wall than the flame surface; yet the experimental data seem to indicate otherwise.

In the course of this application, we noticed the following. The accuracy of the Monte Carlo/finite-volume calculation relies on a good estimation of the turbulence diffusivity. For the present test case, the Baldwin-Lomax model seems to be adequate. To understand the effect of the turbulence diffusivity, we experimented with various Schmidt numbers and observed significant changes in species composition. Also noticed is the importance of the lip above the inlet of the hydrogen jet. The lip has a thickness of 0.076 cm. For convenience, we were tempted to ignore this thickness in the computation. However, our experience shows that shrinking the lip thickness to zero can result in a 0.2-0.3 cm shift of the flame surface toward the wall. The presence of any shock wave in the flow field could also cause the flame surface to shift. As indicated earlier, the chemistry model allows immediate ignition at the lip. The shock wave generated by ignition can reflect from the upper wall and strike the flame, resulting in a shift of flame surface away from the lower wall. In reality, the ignition point is located a certain distance downstream of the lip, and the reflected shock wave does not interact with the flame in the test section. In our numerical simulation, a non-reflective boundary condition is used at the the upper wall to avoid the shock wave interference.

#### **2.1.4 Conclusions**

A compressible pdf turbulence model has been developed and implemented in a Monte-Carlo solver for two- and three-dimensional elliptic flows. A combined ensemble and time-averaging scheme is applied, which enables one to use a relatively small sample in the Monte-Carlo computation; this averaging scheme greatly improves the efficiency and convergence of the pdf solution and, thereby, making large scale computations feasible. The pdf solver can be easily coupled with any existing finite-volume solvers for compressible flows. Numerical results show that, for chemically reacting flows, the pdf method performed consistently better than conventional CFD methods.

### **2.2 Effect of the Coriolis Force on Compressible Turbulence**

Rotation is an important factor in many flow phenomena in nature and in engineering. Problems that are affected strongly by rotation include flows in turbomachinery, large scale motions in the atmosphere and oceans, and galactic motions. Turbulence is important in all these examples. In order to model turbulence in a rotating frame, a better understanding of the effects of rotation on turbulence is required.

Experiments studying the effect of rotation on turbulence had been carried out by various researchers (Ibbetson & Tritton (1975), Traugott (1958), Wigeland & Nagib (1978), Hopfinger, Browand & Gagne (1982) Jacquin , Leuchter & Geffroy (1987)). These experimental results suggest the following two effects of rotation on turbulence: (1) rotation hampers energy cascade in turbulence, resulting in a

decreased dissipation rate for turbulent kinetic energy (Traugott (1958), Wigeland & Nagib (1978), Jacquin, Leuchter & Geffroy (1987)); and (2) two-dimensionalization occurs under rotation (Hopfinger, Browand & Gagne (1982) Jacquin, Leuchter & Geffroy (1987)).

Numerical studies of incompressible turbulence in a rotating frame have been carried out by Bardina, Ferziger & Rogallo (1985), Dang & Roy (1985), Speziale, Mansour & Rogallo (1987), and Teissedre and Dang (1987).

Bardina et al. (1985) performed both large eddy and full simulations of incompressible isotropic turbulence. Their results show that, in the case of incompressible turbulence, the dissipation rate decreases with increasing rotation rate, and that two-dimensionalization does not occur as a result of the Coriolis force. Speziale et al. (1987) confirmed these results using a smaller Rossby number, i.e., a faster rotation, and suggested that no Taylor-Proudman reorganization would occur for homogeneous turbulence.

Studies other than the present one dealing with compressible flows in a rotating frame are not known to the authors.

In general, compressible turbulence in a rotating frame is not homogeneous or isotropic because of the existence of centrifugal force and density fluctuations. However, when the rotation rate is low, or when the solution domain is very close to the rotation axis, the centrifugal force can be neglected and the flow is approximately homogeneous. In the present study, our goal is to identify the effects of the Coriolis force, as opposed to the effects of the centrifugal force or the combined effects of the centrifugal and Coriolis forces. Therefore, the centrifugal force is artificially dropped from the governing equations, regardless of whether or not it is negligible. The resulting problem is a hypothetical one, but nonetheless important.

The theoretical and numerical results presented in the following show that although the Coriolis force does not appear explicitly in the turbulent kinetic energy equation, its effect can be significant. Anisotropy does develop as a result of the Coriolis force. Two-dimensionalization is observed from DNS data for the first time.

It is shown that the Coriolis force serves as a frequency modulator on turbulence. While the Coriolis force neither creates nor destroys turbulent kinetic energy, it redistributes energy by eliminating low frequency waves and transfers energy to waves with a frequency of  $2\Omega$ . The energy distribution in the wave space is modified accordingly: energy is shifted and restricted to either the large scale or the small scale, depending on the rotation rate. This shift of energy spectrum could cause either an increase or a decrease in the dissipation rate of turbulent kinetic energy.

It has been demonstrated both theoretically and numerically that the Taylor-Proudman theorem is applicable to homogeneous turbulence only when the time scale of rotation, defined as the inverse of the frequency of the inertial waves, approaches the Kolmogorov time scale, and that two-dimensionalization occurs in this regime.

### 2.2.1 The Applicability of the Taylor-Proudman Theorem

There is experimental evidence that a homogeneous turbulence would undergo a two-dimensionalization process under high rotation rates (Hopfinger, Browand and

Gagne (1982), Jacquin, Leuchter and Geffroy (1987)). Lesieur (1990) used a Rossby number expansion to prove that at the zeroth order, turbulence is two-dimensional. However, previous numerical simulations have not predicted this phenomenon, and Speziale, Mansour, and Rogallo (1987) argued, based on rapid distortion theory, that the Taylor-Proudman theorem does not apply in rotating isotropic turbulence.

The original Taylor-Proudman theorem is derived under the assumption that, beside a small Rossby number,  $Ro$ , the flow is steady, see, e.g., Chandrasekhar (1961). Turbulence is an unsteady phenomenon with a broadband frequency spectrum. We shall show in what follows that the Taylor-Proudman theorem is valid only for a certain flow regime.

For simplicity we start with the incompressible Navier-Stokes equation in a rotating frame:

$$u_{i,t} + u_j u_{i,j} = -p_{,i} - 2\epsilon_{ijk}\Omega_j u_k + \nu u_{i,jj} \quad (2.1)$$

where  $p$  is the modified pressure. For small  $Ro$ , the convection term is negligible. Taking the curl of the above equation (with the convection term neglected) yields

$$\omega_{i,t} = 2\Omega_j u_{i,j} + \nu \omega_{i,jj} \quad (2.2)$$

where  $\omega_i = \epsilon_{ijk} u_{k,j}$ . If, at the limit of a very small Ekman number,  $\omega_{i,t} = 0$ , then we obtain the standard Taylor-Proudman theorem. However, in general,  $\omega_{i,t} \neq 0$ .

We start our argument by assuming that a decaying homogeneous turbulence can be decomposed into waves of the following form

$$u_i(\mathbf{x}, t) = \sum_{\mathbf{k}} \sum_{\alpha} \tilde{u}_i(\mathbf{k}, \alpha) \exp[i(k_j x_j + \alpha t)] \quad (2.3)$$

Where  $\mathbf{k}$  and  $\alpha$  are the wave number and angular frequency, respectively, and  $i$  denotes the imaginary unit (not to be confused with  $i$  and  $k$  in the subscripts).

The Taylor-Proudman theorem would be applicable if  $\Omega_j u_{i,j} = 0$ , and with waves of the type given by eq. (2.3), it would suffice if  $\Omega_j k_j = 0$  for all wave numbers  $k_j$ . Substituting one wave component of (2.3) to eq. (2.2), we have

$$\epsilon_{ijk}\alpha k_j \tilde{u}_k = i2\Omega_j k_j \tilde{u}_i + i\nu k^2 \epsilon_{ijk} k_j \tilde{u}_k \quad (2.4)$$

which can be rearranged as

$$\hat{\Omega}_j k_j = - \left( \frac{\nu k^2 + i\alpha}{2\Omega} \right) \epsilon_{ijk} k_j \frac{\tilde{u}_k}{\tilde{u}_i} \quad (2.5)$$

where  $\hat{\Omega}_j \equiv \Omega_j / \Omega$  denotes a unit vector in the direction of rotation. Note that  $2\Omega$  is the intrinsic angular frequency of inertial waves in a fluid under solid body rotation.

The Taylor-Proudman theorem is valid when

$$\frac{|\nu k^2 + i\alpha|}{2\Omega} = \frac{\sqrt{\alpha^2 + \nu^2 k^4}}{2\Omega} \ll 1 \quad (2.6)$$

for all the possible  $\alpha$  and  $k$  values. Eq. (2.6) shows that the Taylor-Proudman theorem is applicable only to low frequency waves with  $\sqrt{\alpha^2 + \nu^2 k^4} \ll 2\Omega$ , and does not apply to all waves in turbulence in general.

In what follows we try to find a criterion for which the Taylor-Proudman theorem is valid in turbulence. The turbulence time scale is limited from below by the Kolmogorov time scale  $\tau$ , and the length scale is limited from below by the Kolmogorov length scale  $\eta$ . Any waves with frequencies  $|\alpha| \geq 2\pi/\tau$  or wave numbers  $k \geq 2\pi/\eta$  will be damped by viscosity. Thus, noticing that  $\tau = \eta^2/\nu$ , we can make the following estimation on the upper limit of  $\sqrt{\alpha^2 + \nu^2 k^4}/(2\Omega)$ :

$$\frac{\sqrt{\alpha^2 + \nu^2 k^4}}{2\Omega} \leq 2\pi\sqrt{1 + 4\pi^2} E_\eta \quad (2.7)$$

where  $E_\eta$  is the Ekman number defined by the Kolmogorov microscales:

$$E_\eta \equiv \frac{\nu}{2\Omega\eta^2} = \frac{1}{2\Omega\tau} \quad (2.8)$$

which is the ratio between the rotation time scale and the Kolmogorov time scale. From the above analysis, we see that for the Taylor-Proudman theorem to be valid in turbulence, one needs not only to have  $Ro \rightarrow 0$ , but also  $E_\eta \rightarrow 0$ .

Eq. (2.8) does not mean that at the limit of zero viscosity, or infinite Reynolds number, the Taylor-Proudman theorem is valid; in fact, a careful examination shows that the opposite is true. Let  $Ro_\ell$  and  $Re_\ell$  be the turbulence Rossby number and turbulence Reynolds number based on the turbulent integral length scale  $\ell$  and turbulent velocity scale  $u$ . Then the regular turbulence Ekman number can be written as  $E_\ell = \nu/\Omega\ell^2 = Ro_\ell/Re_\ell$ . Thus one may have a zero Ekman number by either letting  $Ro_\ell$  go to zero or letting  $Re_\ell$  go to infinity. But the Ekman number defined by the Kolmogorov microscale is different:

$$E_\eta = \frac{Ro_\ell}{Re_\ell} \left( \frac{\ell}{\eta} \right)^2 = A Ro_\ell Re_\ell^{\frac{1}{2}} \quad (2.9)$$

where  $A$  is an undetermined constant. Therefore, in order to have  $E_\eta \rightarrow 0$ , one must have  $Ro_\ell$  go to zero faster than  $Re_\ell^{-1/2}$ . For finite but small Rossby numbers, there is no Taylor-Proudman reorganization at the limit of infinite Reynolds number, a fact remarkably different from the case of steady flows.

Using the Taylor microscale,  $\lambda$ , we obtain a simple relation between  $E_\eta$  and  $Ro_\lambda$ :

$$E_\eta = \frac{\nu}{2\Omega\lambda^2} \left( \frac{\lambda}{\eta} \right)^2 = 15^{\frac{1}{2}} E_\lambda Re_\lambda = 15^{\frac{1}{2}} Ro_\lambda \quad (2.10)$$

This relation shows that the criterion for the Taylor-Proudman theorem to be valid in turbulence is  $Ro_\lambda \ll 1$ , and that  $Ro_\ell \ll 1$  is not sufficient.

Define a modified microscale Ekman number as

$$\hat{E}_\eta = 2\pi\sqrt{1 + 4\pi^2 E_\eta} \quad (2.11)$$

According to the above analysis, turbulence subject to rotation can be divided into the following regimes:

(1)  $\hat{E}_\eta \gg 1$ . Turbulence will not undergo any two-dimensionalization. When  $Ro \rightarrow 0$ , the convection term is negligible and the energy cascade process is hampered, resulting in a slowing down of energy dissipation.

(2)  $\hat{E}_\eta \sim 1$ . Waves with small wave numbers and small frequencies will undergo a two-dimensionalization process. However, since the Coriolis force neither generates nor destroys turbulent kinetic energy, yet according to eq. (2.5) the low frequency waves are eliminated, one may conclude that the effect of the Coriolis force is to transfer energy from low frequency waves to waves with  $\sqrt{\alpha^2 + \nu^2 k^4} \sim 2\Omega$ . Because of this shift in energy spectrum, one expects an increase in the dissipation rate of turbulence kinetic energy. Because the energy containing eddies are of low frequency and small wave numbers, the effect of rotation can be significant in this regime.

(3)  $\hat{E}_\eta \ll 1$ . The Taylor-Proudman theorem is valid for this regime since all the turbulence waves satisfy the inequality  $\sqrt{\alpha^2 + \nu^2 k^4} \ll 2\Omega$  and the right hand side of eq. (2.5) goes to zero for all the waves. This regime may not be physically feasible because it requires an extremely large rotation rate. For example, for  $\hat{E}_\eta = 0.1$ , one needs a turbulence Rossby number  $Ro_\lambda$  of the order of  $10^{-3}$ , a number difficult to reach in the laboratory or in nature.

In the experiments of Wigeland & Nagib (1978) and the numerical simulations of Bardina et al. (1985), the minimum  $\hat{E}_\eta$  is greater than 40. In the simulation of Speziale et al. (1987), the value of  $\hat{E}_\eta$  is about 10. For these relatively high values of the microscale Ekman number, no two-dimensional reorganization is possible, and none was observed.

Finally, let us look at the implications of the Taylor-Proudman theorem in isotropic homogeneous turbulence. Assume that, in a Cartesian coordinate system,  $\Omega = (0, 0, \Omega)$ ; then the Taylor-Proudman theorem requires that fluid particles along any line in the  $z$ -direction move with the same velocity. However, because the flow field is initially random with  $\langle u \rangle = \langle v \rangle = 0$ , and because there is no preferred  $x - y$  plane in the flow field, the only way for the Taylor-Proudman theorem to be satisfied is for the fluctuation velocities in the  $x$ - and  $y$ -directions to go to zero.

### 2.2.2 Turbulence Equations for Rotating Fluids

The governing equations for compressible flows subjected to a constant rotation are

$$\begin{aligned} \rho_{,t} + (\rho u_j)_{,j} &= 0 \\ (\rho u_i)_{,t} + (\rho u_j u_i)_{,j} &= -p_{,i} + \tau_{ij,j} - \rho \epsilon_{ijk} \epsilon_{klm} \Omega_j \Omega_l x_m - 2\rho \epsilon_{ijk} \Omega_j u_k \\ (\rho e)_{,t} + (\rho u_j e)_{,j} &= -p u_{j,j} + u_{i,j} \tau_{ij} - (kT_{,j})_{,j} \\ p &= \rho RT \end{aligned} \quad (2.12)$$

The last two terms in the second equation represent, respectively, the effects of centrifugal force and the Coriolis force. The centrifugal force is a nonuniform body force which would induce nonuniform pressure and density distributions; its effect on turbulence is to destroy homogeneity. The Coriolis force, on the other hand, is a uniform body force, provided that the velocity field is uniform. In the case of incompressible flows, the centrifugal force can be included into a modified pressure term and thus does not appear explicitly; however, this can not be done in the case of compressible flows.

In order to identify the effect of the Coriolis force alone, and to compare results with incompressible flow simulations, we artificially drop the centrifugal force in our study. This, of course, greatly simplifies the problem: with a homogeneous initial condition, the flow field remains homogeneous under the Coriolis force. The simplified problem is a hypothetical one and can not normally be found in nature. Nevertheless, it allows one to identify the effects of the Coriolis force without ambiguity.

The Reynolds stress equation for a homogeneous turbulence without mean flow is

$$\begin{aligned} (\overline{u_i u_j})_{,t} = & -\overline{u_k (u_i u_j)_{,k}} - \frac{1}{\rho} \overline{(u_i p_{,j} + u_j p_{,i})} + \overline{u_i \tau_{jk,k}} \\ & + \overline{u_j \tau_{ik,k}} - 2\epsilon_{ilm} \Omega_l \overline{u_m u_j} - 2\epsilon_{jlm} \Omega_l \overline{u_m u_i} \end{aligned} \quad (2.13)$$

The equation for the turbulent kinetic energy, for a constant  $\nu$ , is

$$k_{,t} = \frac{1}{2} \overline{u_i u_i u_{j,j}} - \overline{u_i p_{,i}} - \nu \overline{u_{i,j} u_{i,j}} - \frac{\nu}{3} \overline{u_{i,i} u_{j,j}} \quad (2.14)$$

We define an incompressible dissipation rate as  $\epsilon^i \equiv \nu \overline{u_{i,j} u_{i,j}}$  and a compressible dissipation rate as  $\epsilon^c \equiv \frac{\nu}{3} \overline{u_{i,i} u_{j,j}}$ . The equation for incompressible dissipation is

$$\begin{aligned} \epsilon^i_{,t} = & -2\nu \overline{u_{i,j} u_{k,j} u_{i,k}} + \nu \overline{u_{i,j} u_{i,j} u_{k,k}} - 2\nu \overline{u_{i,j} p_{,ij}} \\ & - 2\nu^2 \overline{u_{i,jk} u_{i,jk}} - \frac{2}{3} \nu^2 \overline{u_{i,ij} u_{k,kj}} \end{aligned} \quad (2.15)$$

We notice that rotation does not appear explicitly in the above equations. However, this does not mean that rotation has no effect on turbulent kinetic energy and dissipation. A careful analysis shows that rotation affects most of the triple correlations in the above equations. For example, the first term on the right hand side of the energy equation is governed by

$$(\overline{u_i u_i u_{j,j}})_{,t} = -\epsilon_{jlm} \Omega_j \overline{u_i u_i u_{m,j}} + OT \quad (2.16)$$

where  $OT$  stand for "Other Terms" unrelated to rotation. The triple correlations in the dissipation equation are governed by

$$(\overline{u_{i,j} u_{i,j} u_{l,l}})_{,t} = -2\epsilon_{lmn} \Omega_m \overline{u_{n,l} u_{i,j} u_{i,j}} + OT \quad (2.17)$$

$$(\overline{u_{i,l}u_{j,l}u_{i,j}})_{,t} = -2\epsilon_{jlm}\Omega_l\overline{u_{m,l}u_{i,j}u_{i,l}} + OT \quad (2.18)$$

The last two triple correlations represent the production of dissipation. For turbulence under rotation, the change in dissipation rate is caused mainly by these triple correlations.

### 2.2.3 Inertial Waves and Anisotropy

It is known that the Navier-Stokes equations for incompressible fluid subjected to solid body rotation admit wave solutions, known as inertial waves (Chandrasekhar, 1961). For homogeneous, anisotropic turbulence, the existence of inertial waves is manifested in Reynolds stresses. In order to explain our numerical results later, we derive the wave solutions for the Reynolds stresses here, starting with the Reynolds stress equations for incompressible homogeneous turbulence, assuming the rotation to be in the  $x_3$ -direction:

$$\frac{d\overline{u_1^2}}{dt} = 4\Omega\overline{u_1u_2} + OT \quad (2.19)$$

$$\frac{d\overline{u_2^2}}{dt} = -4\Omega\overline{u_1u_2} + OT \quad (2.20)$$

$$\frac{d\overline{u_1u_2}}{dt} = 2\Omega(\overline{u_2^2} - \overline{u_1^2}) + OT \quad (2.21)$$

In the following analysis, we neglect the terms unrelated to rotation ( $OT$ ). Taking time derivatives of eqs. (2.19) and (2.20), and applying eq. (2.21), we have

$$\frac{d^2}{dt^2}(\overline{u_2^2} - \overline{u_1^2}) = -16\Omega^2(\overline{u_2^2} - \overline{u_1^2}) \quad (2.22)$$

It is easy to see that a solution of the above equation is

$$\overline{u_2^2} - \overline{u_1^2} = A \exp(i4\Omega t) \quad (2.23)$$

where  $A$  is an undetermined constant. With  $OT$  neglected, eqs. (2.19) and (2.20) give

$$\frac{d}{dt}(\overline{u_2^2} + \overline{u_1^2}) = 0 \quad (2.24)$$

or

$$\overline{u_2^2} + \overline{u_1^2} = C \quad (2.25)$$

From this equation and eq. (2.23), we obtain the following solutions:

$$\overline{u_1^2} = \frac{A}{2} \exp(i4\Omega t) + \frac{C}{2} \quad (2.24)$$

$$\overline{u_2^2} = -\frac{A}{2} \exp(i4\Omega t) + \frac{C}{2} \quad (2.25)$$

$$\overline{u_1u_2} = \frac{A}{2} \exp\left[i\left(4\Omega t - \frac{\pi}{2}\right)\right] \quad (2.26)$$



The frequency of the wave solutions for the Reynolds stresses is twice that of the inertial waves, which is expected. We note that if the turbulence is strictly isotropic, i.e.,  $\overline{u_2^2} - \overline{u_1^2} = 0$ , then the waves will not appear in the solutions of Reynolds stresses.

#### 2.2.4 DNS Results

The governing equations solved in this study are those given in eq. (2.12) with the centrifugal force neglected. An 8th order compact difference scheme is used to solve the equations numerically. This scheme has been shown to give spectral-like resolutions (Lele 1990), and has been successfully used in DNS (Lee, Lele, & Moin, 1991). The numerical results presented in the following are obtained using a  $64^3$  grid over a box of size  $2\pi$ . The initial conditions for all the cases are the same, and are obtained by carrying the calculation of a homogeneous, isotropic flow field to a point where the velocity-derivative skewness reaches a constant value of about -0.5 (Tavoularis, Bennett & Corrsin, 1978). The initial turbulence Mach number for all the cases studied is  $M_t = 0.31$  and the initial turbulent Reynolds number is  $Re_\lambda = 12.8$ . The parameters of cases studied are listed in the following table.

Modified Ekman No. $\hat{E}_\eta$	Rossby No $Ro_\lambda = \frac{u}{2\Omega\lambda}$	Rotation Rate $\Omega$
$\infty$	$\infty$	0.
22	0.14	2.74
11	0.07	5.48
4.2	0.028	13.7
2.2	0.014	27.4
0.8	0.005	68.5

The modified Ekman numbers are either much larger than, or in the neighborhood of, unity. We have not been able to compute cases for  $\hat{E}_\eta \ll 1$  because such cases require extremely small time steps to resolve the rotation time scale, and are too time consuming.

#### Reynolds Stresses

Figs. 2.1, 2.2, and 2.3 are the time evolution of the diagonal terms of the Reynolds stresses for  $\hat{E}_\eta = \infty$ , 22, and 2.2, respectively. The velocity component  $w$  is parallel to  $\Omega$ , and  $u$  and  $v$  are perpendicular to  $\Omega$ . For a relatively small rotation rate, with  $\hat{E}_\eta = 22$ , there is no appreciable anisotropy in terms of the Reynolds stresses. However, as  $\hat{E}_\eta$  approaches one, as shown in Fig. 2.3, there is a distinct trend of faster decay for the energy components in the plane perpendicular to the rotation. As the analysis of Section 2 suggested, the only possible route of two-dimensionalization

for a homogeneous turbulence is for  $\langle u \rangle$  and  $\langle v \rangle$  to approach zero. The numerical results given in Fig. 2.3 support that conclusion.

The  $\langle uu \rangle$  and  $\langle vv \rangle$  curves in Fig. 2.3 show considerable oscillation as a result of inertial waves. To show that the oscillation is indeed caused by the inertial waves, we plotted  $\langle v^2 \rangle - \langle u^2 \rangle$  versus time in Fig. 2.4, where the time is not nondimensionalized by eddy turn over time. The angular frequency is found to be  $4\Omega$  from Fig. 2.4, which agrees with the theoretical analysis given in Section 4.

### Turbulent Kinetic Energy

Fig. 2.5 shows three curves of the ratio between the initial turbulent kinetic energy and energy at time  $t$ . For  $\hat{E}_\eta = 22$ , there is a noticeable reduction in the turbulent energy decay rate, while for  $\hat{E}_\eta = 2.2$ , the decay rate has increased.

The decrease of the decay rate is expected: it is attributed to the hampering of energy cascade by rotation, and has been demonstrated previously by both experiments and DNS. But the decrease is rather small compared to the incompressible results. To see why this is the case, we try to analyze the compressible and incompressible turbulent kinetic energy separately. While actually decomposing the energy into a compressible part and an incompressible part is very difficult, one can estimate the trend by looking at the dilatation field and vorticity field. Since the incompressible component of the velocity can be written as an integral of the vorticity field,  $\omega_i$ , and the compressible component of the velocity can be written as an integral of the dilatation,  $\Delta$ , one expect the quantities  $\langle |\omega|^2 \rangle$  and  $\langle \Delta^2 \rangle$  to be a good indicator of the incompressible and compressible energy, respectively. These quantities are plotted in Figs. 2.6 and 2.7. The results show that while the Coriolis force reduces the decay rate of the incompressible turbulent kinetic energy, its effect on the compressible energy is the opposite.

A clearer picture of the effect of rotation is gained by plotting the turbulent kinetic energy, the mean vorticity square,  $\langle |\omega|^2 \rangle$ , and the mean velocity divergence square,  $\langle \Delta^2 \rangle$ , at  $t/t_{eddy} = 1$  as a function of the modified Ekman number (Fig. 2.8). For the sake of comparison, the variables are normalized by their respective values for  $\Omega = 0$ . The total energy curve has a maximum at  $\hat{E}_\eta \sim 20$ , where the dissipation rate of the turbulent energy reaches a minimum. For the incompressible energy, represented by  $\langle |\omega|^2 \rangle$ , the dissipation reaches a minimum at  $\hat{E}_\eta \sim 5$ .

The analysis given in Section 2 suggested that depending on the value of  $\hat{E}_\eta$ , the dissipation rate of turbulent kinetic energy will be either reduced or enhanced: For  $\hat{E}_\eta \gg 1$ , the dissipation rate decreases with the rotation rate, and for  $\hat{E}_\eta \sim 1$ , the dissipation rate increases with the rotation rate. The numerical results presented here agree well with that prediction.

The compressible energy always decreases as rotation rate increases, which seems to contradict our theoretical prediction. One plausible explanation is that the compressible waves are more readily converted to non-random inertial waves. The evidence of this can be observed from Figs. 2.6 and 2.7, where the curve for  $\langle \Delta_0^2 \rangle / \langle \Delta^2 \rangle$  at  $\hat{E}_\eta = 2.2$  shows a much stronger influence from inertial waves than the curve for  $\langle |\omega_0|^2 \rangle / \langle |\omega|^2 \rangle$ . Since the mean values  $\langle . \rangle$  at any

given time are obtained by averaging over the computational domain, energy contained in non-random inertial waves is not included in the mean turbulent kinetic energy.

### Dissipation Rate

Fig. 2.9 shows the dissipation rates per unit energy or  $\hat{E}_\eta = \infty$  and  $\hat{E}_\eta = 0.8$ . One can see that, as was predicted in Section 2, the dissipation rate has indeed increased for  $\hat{E}_\eta \sim 1$ .

### Spectrum

To understand the phenomena described above, and to relate them to the analysis given in Section 2, it is best to look at both the time and spatial spectra of the flow field.

Fig. 2.10 shows the time spectra, at  $t/t_{eddy} = 1$ , of the u-velocity, defined as

$$\psi_1 = \int \langle u(t)u(t+\tau) \rangle \exp(i\alpha\tau) d\tau \quad (2.27)$$

The spectra show that the Coriolis force serves as a frequency modulator for turbulence. The Coriolis force caused a considerable amount of energy to be removed from the low frequency range, where the energy containing eddies are, and shifted to the angular frequency of  $2\Omega$ . Rotation prevents energy from being transferred away from frequency  $2\Omega$ .

When the inertial angular frequency,  $2\Omega$ , coincides with the frequencies of the energy containing eddies, turbulent kinetic energy is prevented from cascading to higher frequencies. If we associate high frequencies with large wave numbers, then this restriction reduces the amount of energy transferred to small eddies, and thus reduces dissipation. However, when  $2\Omega$  approaches the Kolmogorov time scale, energy is transferred to small eddies, and the dissipation rate is increased.

To show that the transfer of energy to higher frequencies is accompanied by energy transfer to smaller eddies, we plotted the one-dimensional energy spectra in Fig. 2.11, where  $F_{21}$  is defined as

$$F_{21}(k_1) = \frac{1}{2\pi} \int \frac{\langle v(x, y, z)v(x+r, y, z) \rangle}{\langle v(x, y, z)^2 \rangle} \exp(ik_1 r) dr \quad (2.28)$$

The areas under all the curves in Fig. 2.11 are the same and equal to unity (if we integrate from  $-\infty$  to  $\infty$ ).

Compared with the spectrum for  $\Omega = 0$  (solid line), the curves show that for large Ekman numbers, or small rotation rates, the energy spectrum is shifted to the left, meaning more energy is concentrated in large eddies. Since the Reynolds numbers are initially the same for all the cases, a decrease in the energy contained in the small eddies means less dissipation.

As the Ekman number decreases, the energy spectra are shifted to the right, to small eddies. In fact, the spectra for flows with rotation crosses the spectrum of zero rotation at about  $\hat{E}_\eta = 4.4$ , suggesting that for  $\hat{E}_\eta < 4.4$ , the dissipation rate

should increase. This is consistent to both what was observed in Fig. 2.8 and what was predicted in Section 2.

### 2.2.5 Conclusions

In the governing equations of turbulent kinetic energy and dissipation rate, rotation does not appear explicitly; the dissipation rate is affected by rotation through the triple correlations in the equation. For anisotropic turbulence subjected to solid body rotation, the solutions for the turbulent shear stresses oscillate with a frequency equal to twice the frequency of the inertial waves.

We have shown that the Coriolis force serves as a frequency modulator on turbulence. The turbulent kinetic energy shifts from low frequencies to the frequency of the inertial waves. The shift of energy in the frequency space is accompanied by a shift of energy in the wave number space. Using both theoretical arguments and DNS data, we have shown that an appropriate parameter in categorizing homogeneous turbulence subjected to solid body rotation is the modified microscale Ekman number,  $\hat{E}_\eta$ . For  $\hat{E}_\eta \gg 1$ , the dissipation rate of turbulent kinetic energy is reduced by rotation due to a shift of energy to large scales. As  $\hat{E}_\eta$  approaches one, energy is shifted to the dissipative scales, and thus dissipation is enhanced by rotation. Strictly speaking, the Taylor-Proudman theorem is applicable to turbulence only when  $\hat{E}_\eta \ll 1$ .

### 3. Future Plans

The near term goal is the application of pdf method to three-dimensional supersonic flows. In addition to 3D applications, the pdf model for compressible flows will be further developed. Direct numerical simulation will be performed to assist the development of new pdf models.

### 4. References

- <sup>1</sup> Pope, S.B., "PDF Methods for Turbulent Reactive Flows." Prg. Energy Combust. Sci., 1985, 11, 119-192.
- <sup>2</sup> Pope, S.B., Private communication, May, 1992.
- <sup>3</sup> Shuen, S. and Yoon, S., "Numerical Study of Chemically Reacting Flows Using a Lower-Upper Symmetric Successive Overrelaxation Scheme." AIAA Journal, Vol 27, No 12, pp. 1752-1760, December, 1989.
- <sup>4</sup> Raju, M.S., "Heat Transfer and Performance Characteristics of a Dual-Ignition Wankel Engine," SAE paper 920303, Feb. 1992, also accepted for publication in The SAE Transactions.
- <sup>5</sup> Kollmann, W., "The PDF Approach to Turbulent Flow." Theoret. Comput. Fluid Dynamics, 1990, 1, 249-285.
- <sup>6</sup> Anand, M.S., Pope, S.B., and Mongia, H.C., "Pressure Algorithm for Elliptic Flow Calculations with the PDF Method." CFD Symposium on Aeropropulsion, NASA Lewis Research Center, April 24-26, 1990.

- <sup>7</sup> Haworth, D.C. and El Tahry, S.H., "Probability Density Function Approach for Multidimensional Turbulent Flow Calculations with Application to in-Cylinder Flows in Reciprocating Engines." AIAA Journal, Vol. 29, pp.208-218, 1991.
- <sup>8</sup> Roekaerts, D., "Use of a Monte Carlo PDF Method in a Study of the Influence of Turbulent Fluctuations on Selectivity in a Jet-stirred Reactor," *Applied Scientific Research*, Vol.48, pp. 271-300, October, 1991.
- <sup>9</sup> Correa, S.M. and Pope, S.B., "Comparison of a Monte Carlo PDF/Finite-Volume mean flow model with bluff-body Raman data." 24th Int'l Symp. on Combust., The Combustion Institute, 1992, in press.
- <sup>10</sup> Shih, T-H and Lumley, J.L., "A Critical Comparison of Second Order Closures with Direct Numerical Simulation of Homogeneous Turbulence." NASA TM 105351, November, 1991.
- <sup>11</sup> Sarkar, S., Erlebacher, G., Hussaini, M.Y., "Compressible Homogeneous Shear: Simulation and Modeling." NASA CR-189611, 1992.
- <sup>12</sup> Hsu, A.T., "A Study of Hydrogen Diffusion Flames Using PDF Turbulence Model," AIAA Paper 91-1780, June, 1991.
- <sup>13</sup> Hsu, A.T. and Chen, J.Y., "A Continuous Mixing Model for PDF Simulations and its Applications to Combusting Shear Flows." 8th Symposium on Turbulent Shear Flows, Munich, September, 1991.
- <sup>14</sup> Pope, S.B. and Gadh, R., "Fitting Noisy Data Using Cross Validated Cubic Smoothing Splines." *Communications in Statistics, Part B*, Vol.17, pp. 349-376, 1988.
- <sup>15</sup> Villasenor, R., Chen, J.-Y., and Pitz, R.W., "Modeling Ideally Expanded Supersonic Turbulent Jet Flows With Nonpremixed  $H_2$ -Air Combustion," AIAA Journal, Vol.30, No. 2, Feb. 1992.
- <sup>17</sup> Rogers, R.C., and Chinitz, W., "Using a Global Hydrogen-Air Combustion Model in Turbulent Reacting Flow Calculations," AIAA Journal, Vol.21, No.4, April 1983.
- <sup>18</sup> Evans, J.S., Schexnayder, C.J., and Beach, H.L., "Application of a Two-Dimensional Parabolic Computer Program to Prediction of Turbulent Reacting Flows," NASA TP-1169, March 1978.
- <sup>19</sup> Eklund, D.R., Drummond, J.P., and Hassan, H.A., "Calculation of Supersonic Turbulent Reacting Coaxial Jets," AIAA Journal, Vol.28, No. 29, Sept. 1990.
- <sup>20</sup> Evans, J.S., and Schexnayder, C.J., "Influence of Chemical Kinetics and Unmixedness on Burning in Supersonic hydrogen Flames," AIAA Journal, Vol.18, No.7, Feb. 1980.
- <sup>21</sup> Burrows, M. C. and Kurkov, A. P., "Analytical and Experimental Study of Supersonic Combustion of Hydrogen in a Vitiated Air Stream," TM X-2828, NASA, 1973.
- <sup>22</sup> Bardina, J., Ferziger, J.H. and Rogallo, R.S. 1985 Effect of Rotation on Isotropic Turbulence: Computation and Modeling. *J. Fluid Mech.* 154, 321-336.

- <sup>23</sup> Chandrasekhar, S. 1961 Hydrodynamic and Hydromagnetic Stability. Oxford Press.
- <sup>24</sup> Dang, K. and Roy, Ph., 1985 Direct and large eddy simulation of homogeneous turbulence submitted to solid body rotation. *Turbulence Shear Flows*, 1985.
- <sup>25</sup> Hopfinger, E.J., Browand, F.K. and Gagne, Y., 1982 Turbulence and waves in a rotating tank. *J. Fluid Mech.* 125, 505-534.
- <sup>26</sup> Ibbetson, A. and Tritton, D.J., 1975, Experiments on Turbulence in a Rotating Fluid. *J. Fluid Mech.* 56, 639-672.
- <sup>27</sup> Jacquin, L. Leuchter, O. and Geffroy, P. 1987 Experimental study of homogenous turbulence in the presence of rotation. *Turbulence Shear Flow*, Toulouse, France.
- <sup>28</sup> Lee, S., Lele, S.K. and Moin, P., 1991, Direct Numerical Simulation and Analysis of Shock Turbulence Interaction. AIAA Paper 91-0523.
- <sup>29</sup> Lele, S.K., 1990, Compact Finite Difference Scheme with Spectral-like Resolution. CTR Manuscript 107, Stanford University.
- <sup>30</sup> Lesieur, M., 1990 Turbulence in Fluids, 2nd Ed. Kluwer Academic Publishers.
- <sup>31</sup> Speziale, C.G., Mansour, N.N. and Rogallo, R.S., 1987 The Decay of Isotropic Turbulence in a Rapidly Rotating Frame, Center for Turbulence Research, *Proceedings of the Summer Program*
- <sup>32</sup> Tavoularis, S., Bennett, J.C., and Corrsin, S., 1978, Velocity-derivative skewness in small Reynolds number, nearly isotropic turbulence. *J. Fluid Mech.* vol. 88, Part 1, 63-69.
- <sup>33</sup> Teissedre, C. and Dang, K., 1987 Anisotropic behavior of rotating homogeneous turbulence by numerical simulation. AIAA paper 87-1250.
- <sup>34</sup> Traugott, S.C., 1958 Influence of Solid-body Rotation on Screen-produced Turbulence. NACA TN 4135.
- <sup>35</sup> Wigeland, R.A. and Nagib, H.M. 1978 Grid-generated Turbulence With and Without Rotation About the Streamwise Direction. *IIT Fluids and Heat Transfer Rep. R78-1*, Illinois Inst. of Tech., Chicago, Illinois.

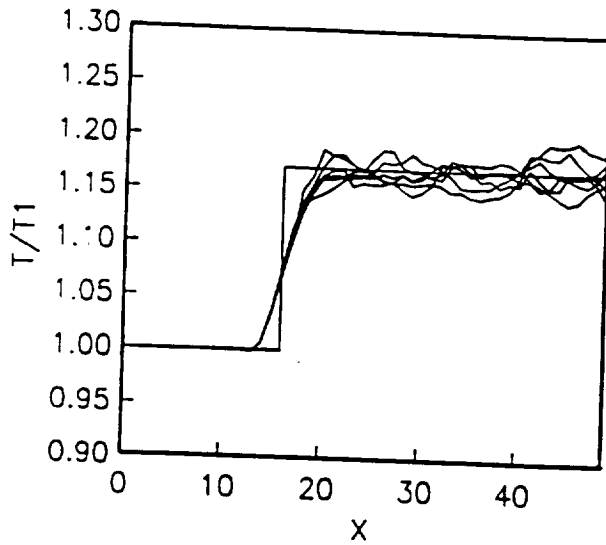


Fig 1.1 Temperature rise through an oblique shock predicted by the pdf turbulence model compared with an analytical solution.

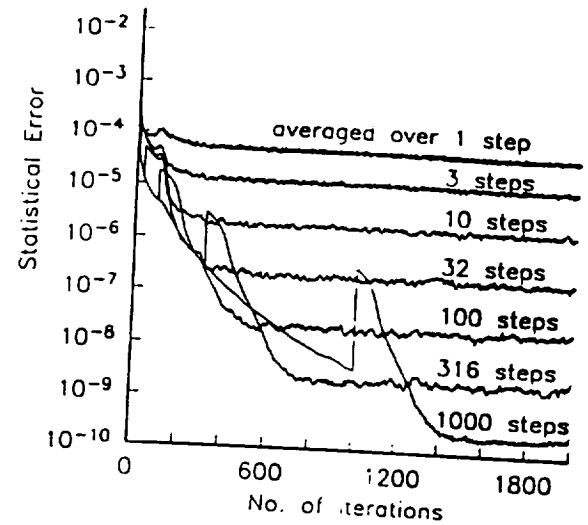


Fig 1.2 Convergence history of the pdf solver measured by an L2 norm; combined time and ensemble averaged solutions.

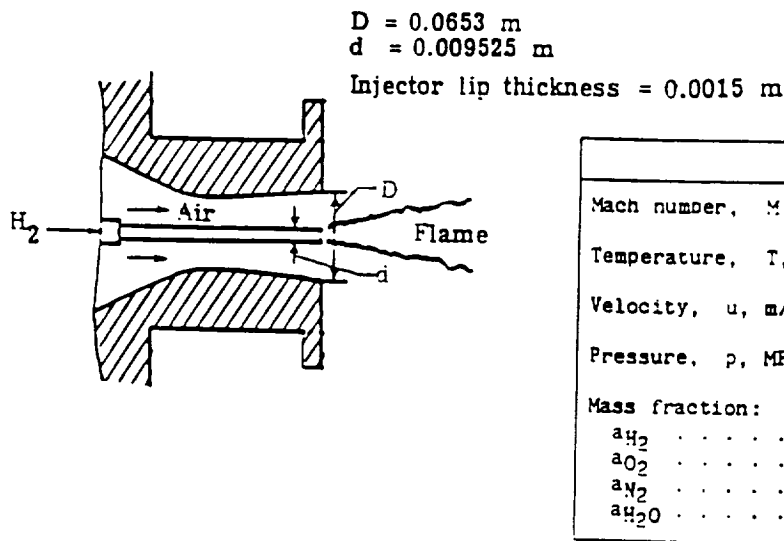


Fig 1.3 Geometry and test conditions for the coaxial hydrogen jet combustion.

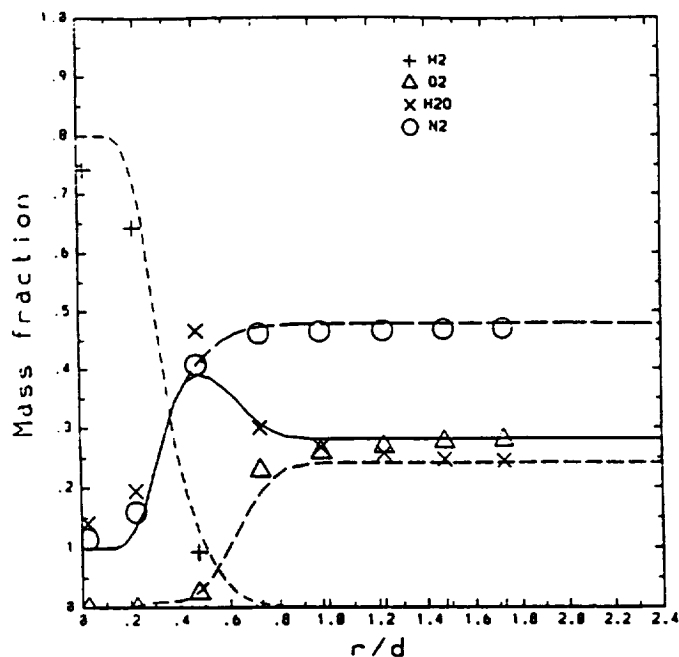


Fig 1.4a Radial profiles of the predicted and measured mass fractions of major species for the pdf-CFD solver at  $x/d = 8.26$ .

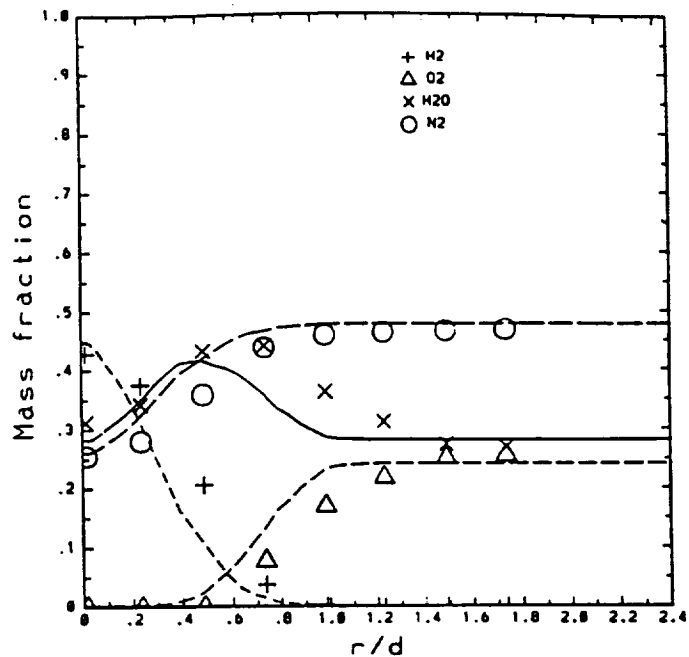


Fig 1.4c Radial profiles of the predicted and measured mass fractions of major species for the pdf-CFD solver at  $x/d = 21.7$ .

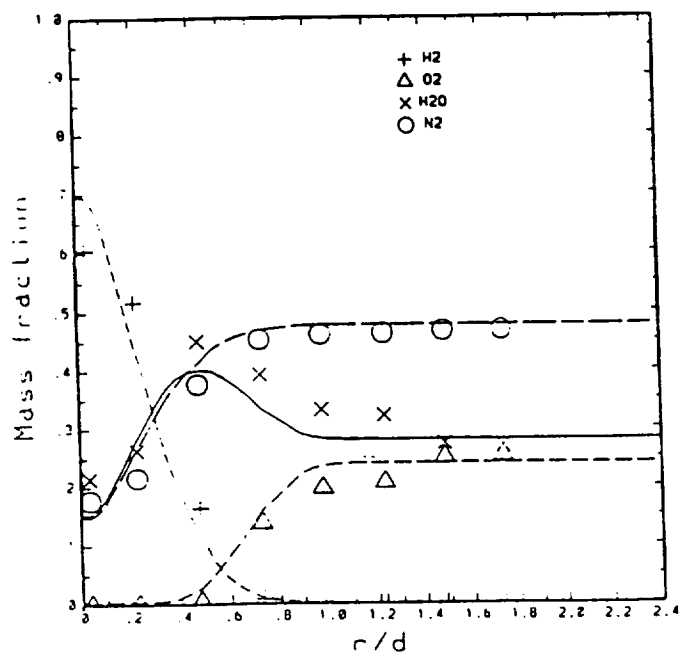


Fig 1.4b Radial profiles of the predicted and measured mass fractions of major species for the pdf-CFD solver at  $x/d = 15.5$ .

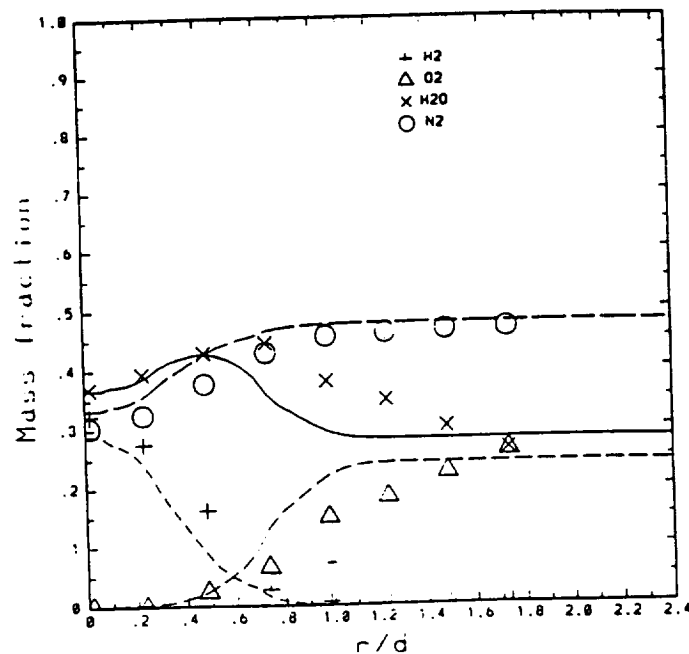


Fig 1.4d Radial profiles of the predicted and measured mass fractions of major species for the pdf-CFD solver at  $x/d = 27.9$ .



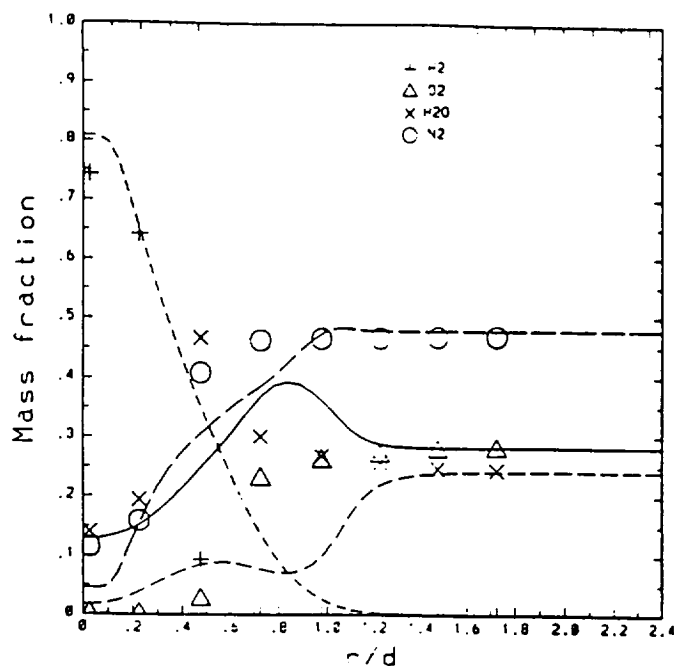


Fig 1.5a Radial profiles of the predicted and measured mass fractions of major species for the CFD solver at  $x/d = 8.26$ .

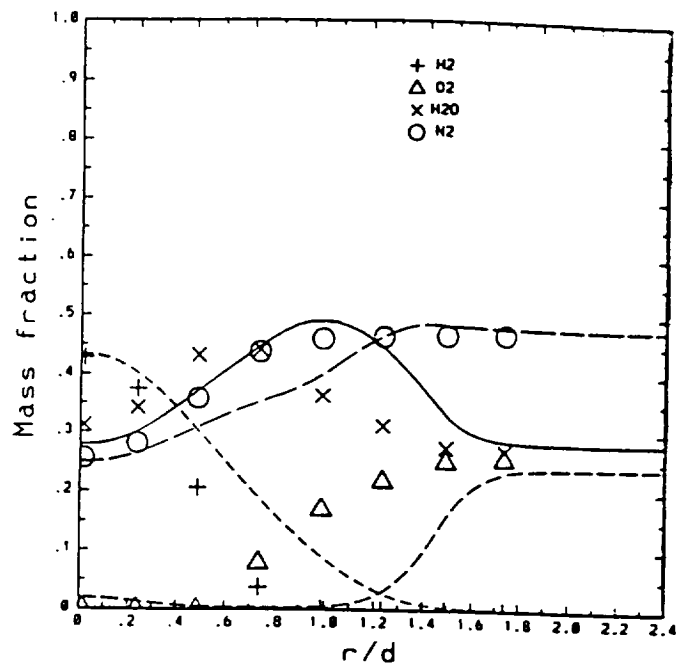


Fig 1.5c Radial profiles of the predicted and measured mass fractions of major species for the CFD solver at  $x/d = 21.7$ .

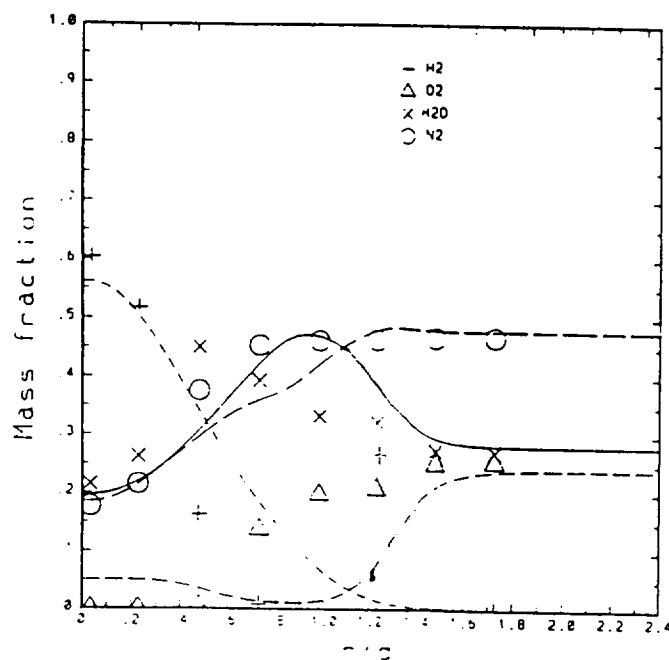


Fig 1.5b Radial profiles of the predicted and measured mass fractions of major species for the CFD solver at  $x/d = 15.5$ .

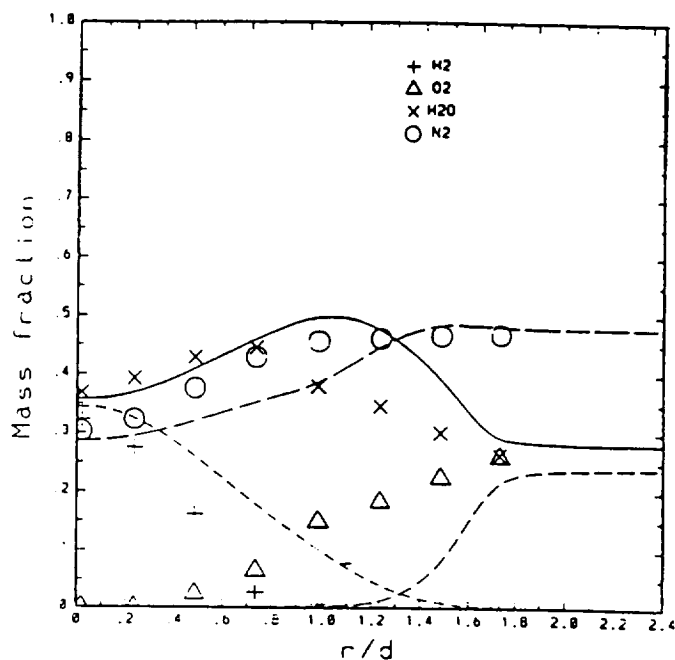


Fig 1.5d Radial profiles of the predicted and measured mass fractions of major species for the CFD solver at  $x/d = 27.9$ .

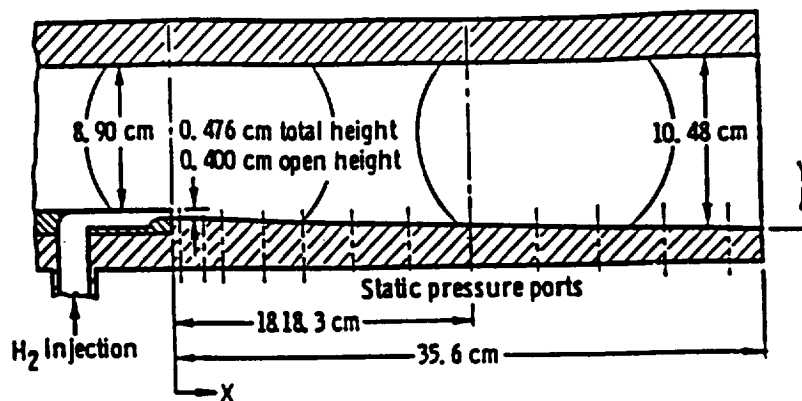


Fig 1.6 Flow Configuration of Burrows and Kuckov's Experiment.

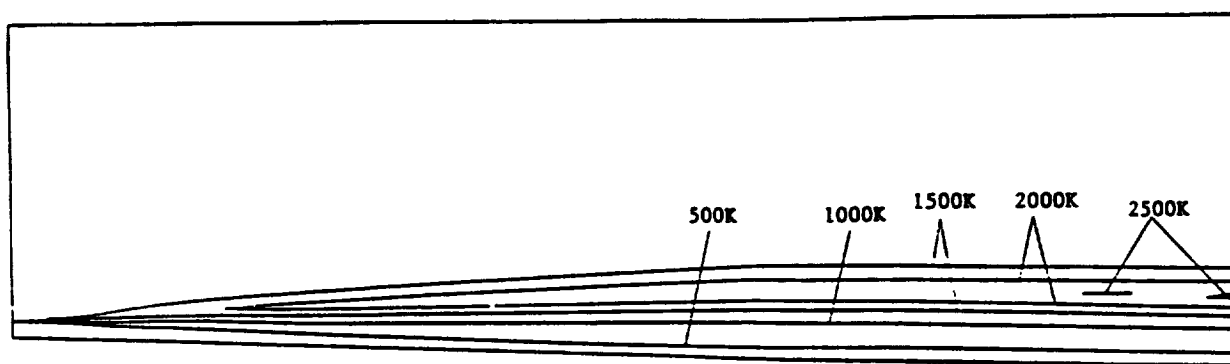


Fig 1.7a Temperature Contour of Numerical Solution Using PDF.

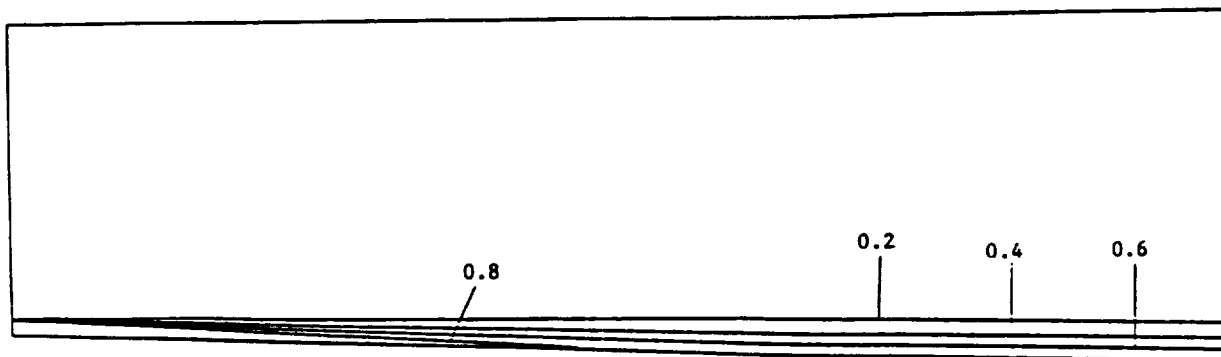


Fig 1.7b Hydrogen Mass Fraction Contour of Numerical Solution Using PDF.

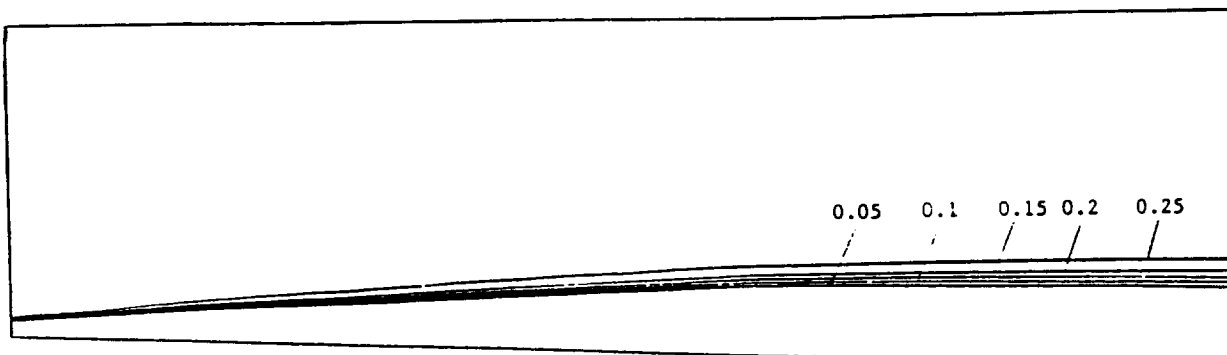


Fig 1.7c Oxygen Mass Fraction Contour of Numerical Solution Using PDF.

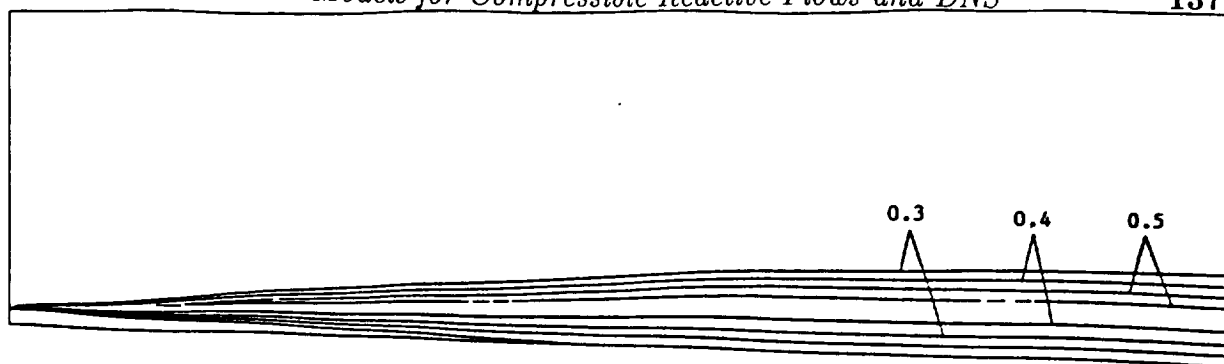
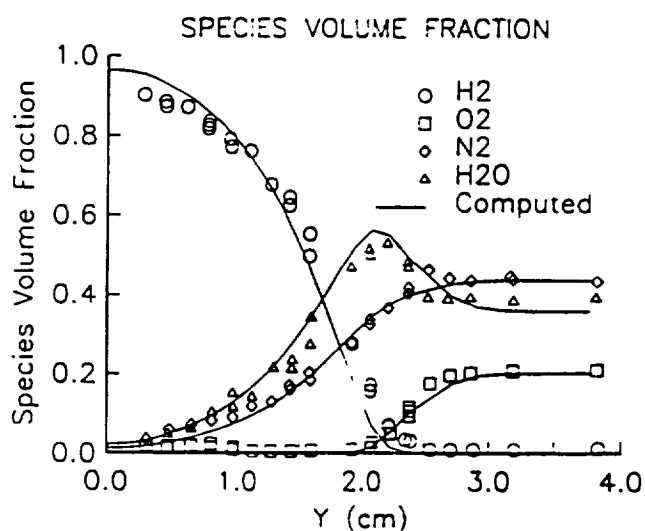
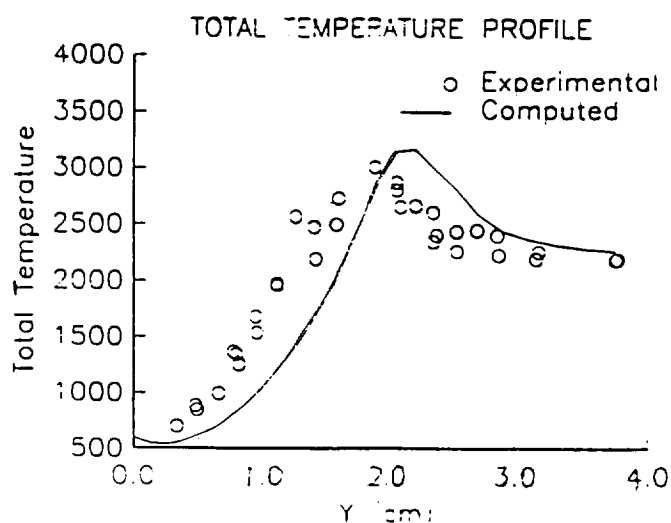
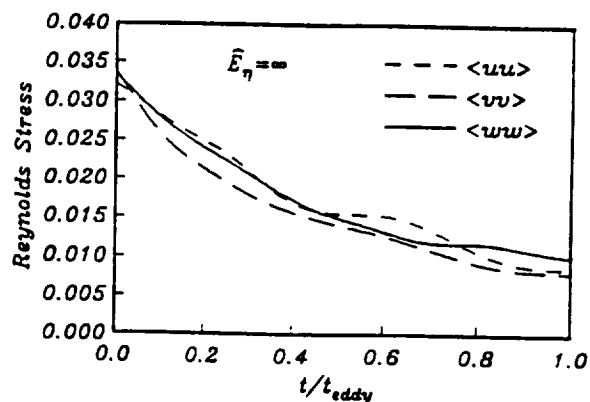
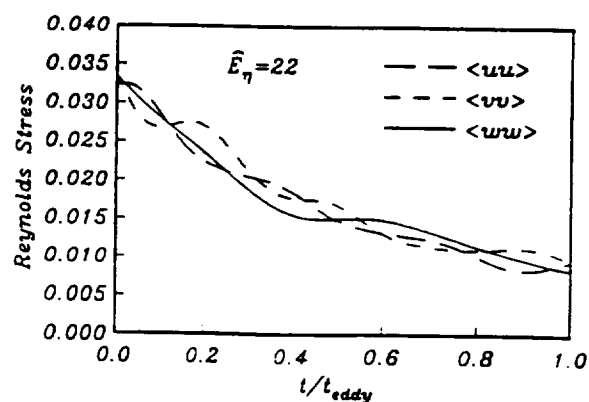


Fig 1.7d Water-Vapor Mass Fraction Contour of Numerical Solution Using PDF.

Fig 1.8a Composition Profile of Measured Data and Numerical Solution Using PDF. (  $x = 35.6$  cm )Fig 1.8b Total Temperature Profile of Measured Data and Numerical Solution Using PDF. (  $x = 35.6$  cm )Fig 2.1 Time history of Reynolds stresses for  $\Omega = 0$ .Fig 2.2 Time history of Reynolds stresses for a moderate rotation rate of  $\Omega = 2.74$ .

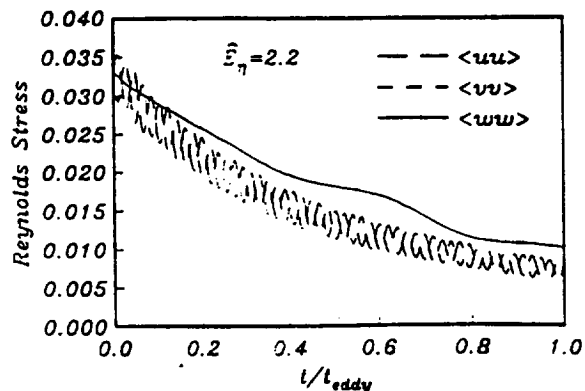


Fig 2.3 Time history of Reynolds stresses for a high rotation rate of  $\Omega = 68.5$ .

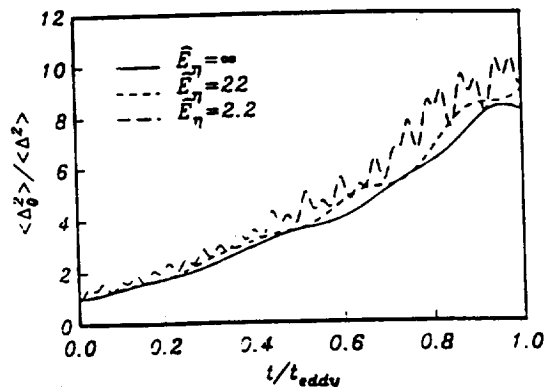


Fig 2.6 The ratio of velocity divergence square, representing compressible turbulent kinetic energy.

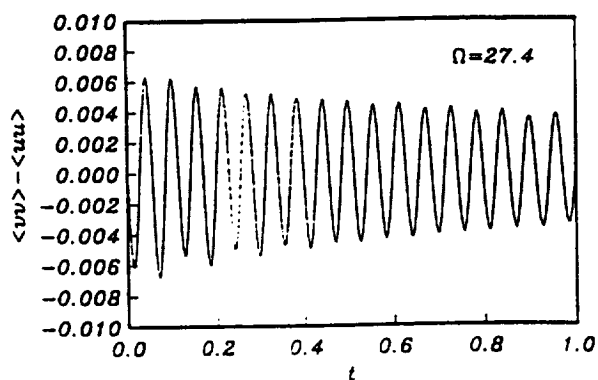


Fig 2.4 Time history of  $\langle vv \rangle - \langle uu \rangle$  with an angular frequency of  $4\Omega$ .

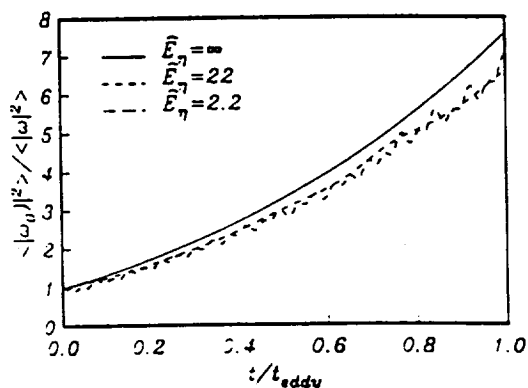


Fig 2.7 The ratio of vorticity square, representing incompressible turbulent kinetic energy.

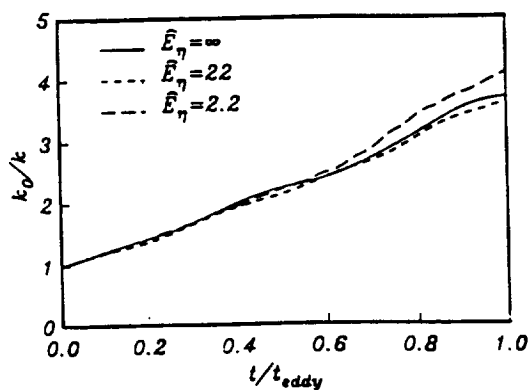


Fig 2.5 Total turbulent kinetic energy ratio.

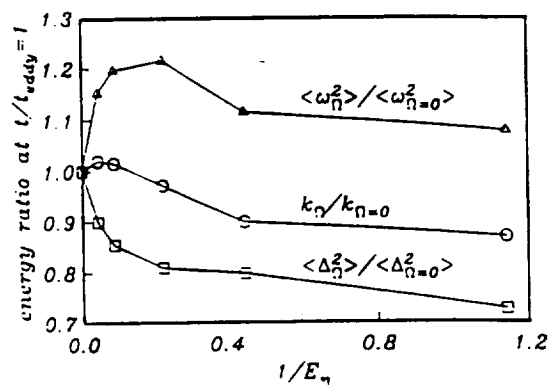


Fig 2.8 Turbulence kinetic energy, velocity divergence square, and vorticity square at  $t/t_{eddy} = 1$ , normalized by their corresponding values for  $\Omega = 0$ .

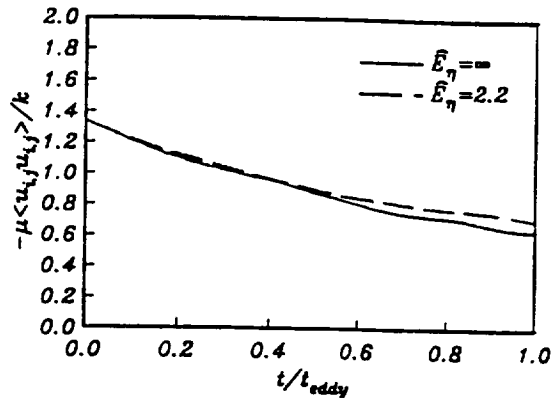


Fig 2.9 Dissipation rate of turbulent kinetic energy, normalized by energy.

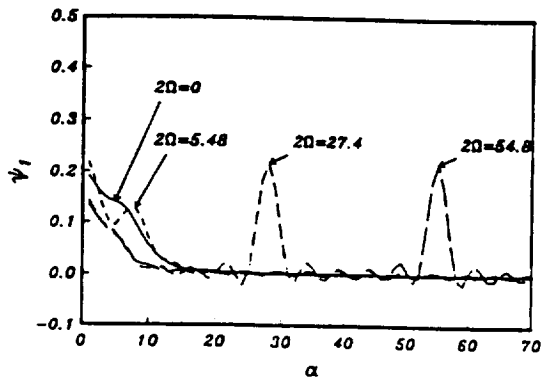


Fig 2.10 Time spectra of turbulent kinetic energy.

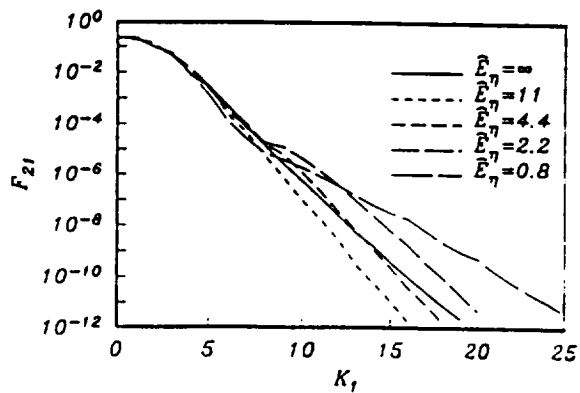


Fig 2.11 One-dimensional energy spectra for the flow field at  $t/t_{eddy} = 1$ .



# Modeling of Turbulent, Reacting Flows by PDF Methods

A. T. Norris

## 1. Motivation and Objective

The objective of this work is to further the development of Probability Density Function (PDF) models for turbulent, reacting flows. To achieve this, work will be performed in two different areas. The first area will involve developmental work on an existing scalar PDF model for compressible flows. Specific areas to be worked on are the implementation of chemical kinetics and extending the model to include axisymmetric and 3D flows. The second area of work will involve the development and implementation of other PDF models. Proposed topics include the development of new models for molecular mixing and state variables such as enthalpy, and work on parallel implementation of PDF methods. In addition, the development of a velocity-scalar PDF method for compressible flows is proposed.

In all cases, the performance of the PDF model will be verified by application to a variety of real flows, and comparing the predictions to the experimental data.

## 2. Work Proposed

In the following section, a brief background of PDF methods is presented. This is followed by the details of the proposed work for the 1993-1994 year.

### 2.1 Background

Probability Density Function (PDF) methods involve solving a transport equation for the joint PDF of quantities of interest, such as velocity, dissipation, enthalpy and composition. For all but the simplest of flows, solutions of the joint PDF transport equation are obtained by Monte Carlo schemes, where the PDF is represented by an ensemble of particles that evolve in time by some stochastic process. The principle advantage of this form of modeling over moment closure approaches is that the chemical reaction is treated exactly<sup>1</sup>, thus making PDF methods particularly attractive for calculating turbulent reactive flows.

As a generalization, PDF methods can be divided into two types: The scalar PDF method and the velocity-scalar PDF method. The scalar PDF method consists of a modeled transport equation for the joint PDF of composition only, with the velocity field solved by a moment closure model. This model was developed by Pope<sup>2</sup> (1981) and Dopazo and O'Brian<sup>3</sup> (1974). This form of model was also used by Chen et al<sup>4</sup> and was extended to compressible flows by Hsu et al<sup>5</sup>. In the velocity-scalar PDF method, the transport equation for the joint PDF of velocity and composition is solved. This model was developed by Pope et al<sup>6,7</sup> in 1986, and has the advantage over the scalar PDF method in that convective transport is treated exactly.

## 2.2 Existing Code Development

Despite the ability of the PDF method to treat chemical reaction exactly, the implementation of the numerical chemical kinetics in a Monte Carlo scheme is a non-trivial matter. First, the solution of the full system of rate equations for the thermochemistry in turbulent reacting flows requires obtaining solutions for of order 50 chemical species, governed by of order 200 stiff, non-linear rate equations. At present this task is computationally infeasible, and so reduced mechanisms are employed. These reduced mechanisms represent the full composition by a few representative species, typically two to five, and the reaction rates of these species are quasi-global equations derived from the full mechanism. However even the solution of a reduced mechanism is a computationally expensive task. In a typical PDF calculation<sup>5</sup>, there are on order 100,000 particles and 1,000 time steps, resulting in the code performing  $10^9$  solutions of the reduced mechanism. A computationally efficient way of reducing this task to manageable proportions is to use a look-up table. In this table, the reduced mechanism is integrated for discrete time and composition increments, and stored in a table. Thus integration is replaced by interpolation, at a considerable saving in computer time. By the use of adaptive tabulation techniques<sup>8</sup> the size of the tables can also be minimized.

To illustrate the form of a look-up table, it is useful to consider a simple function, representing a one step, finite rate reaction of an arbitrary fuel, F, with air, A, forming product, P;



Assuming equal diffusivity of all species, the rate of creation of product (reaction rate) is just a function of the mixture fraction  $\xi$  and the mass fraction of the product,  $Y_P$ . Figure 1 shows a contour plot of reaction rate as a function of  $\xi$  and  $Y_P$ . Overlaid is a grid representing the adaptive look-up table used to store the data. Reaction rates for some arbitrary composition are obtained by identifying the cell that contains the composition, and interpolating from the four nodes.

It is proposed that the existing scalar PDF model be modified to incorporate the use of look-up tables. Apart from an expected speed-up of the code, a library of tables of different fuels can be generated and stored, providing users with a more versatile tool for reactive flow calculations. In addition to the look-up table implementation of the chemical reaction, a useful contribution would be to make the code compatible with the CHEMKIN<sup>10</sup> code. CHEMKIN is a chemical kinetics software package, designed to help incorporate gas-phase chemical reaction schemes in fluid mechanics models. While CHEMKIN would not provide the computational speed-up of the look-up tables, it would allow the user to quickly and simply select any fuel-oxidizer combination required for the calculations.

The extension of the scalar PDF code to allow axisymmetric and 3D calculations is relatively trivial, code modification being the main work, and so requires no elaboration.



### 2.3 Model Development

In PDF methods, the modeling of the molecular diffusion term is a region of current research. For the case of a single scalar,  $\phi$ , in constant density, homogeneous, isotropic turbulence, the evolution equation for the scalar PDF,  $f_\phi$  is given by:

$$\frac{\partial f_\phi}{\partial t} = -\frac{\partial}{\partial \psi} [f_\phi < (\Gamma/\rho) \nabla^2 \phi | \psi = \phi >], \quad (2)$$

where  $\Gamma/\rho$  is the diffusion coefficient divided by the density, and  $< Q(q) | p = q >$  is the expectation of some function of  $q$ , conditional upon the sample space variable  $p$  being equal to  $q$ . Many different models have been developed for this term<sup>1,8</sup>, none of which perform entirely satisfactorily. One common assumption made in these models is that the time scale of the mixing,  $\tau_\phi$  is half the turbulent time scale,  $\tau = k/\epsilon$ , where  $k$  is the turbulent kinetic energy and  $\epsilon$  is the dissipation. While this assumption has been shown to be reasonable for free shear flows<sup>1</sup>, experiments have shown it not to hold for more complex flows<sup>1</sup>. It is proposed to remove this problem by providing a separate model for  $\tau_\phi$ , based on the scalar dissipation,  $\epsilon_\phi$ . The expected benefits of this model are to improve the performance of the mixing model in regions where the mixing and turbulent time scales are not proportional, such as areas of intermittency.

Another area of potential for modeling improvement is in the area of state variables. In the compressible scalar PDF model, the evolution of the PDF of composition and specific enthalpy is calculated, while the density and velocity calculations are input from a finite difference moment closure model. A useful development would be to model both state variables in the PDF part of the calculation. To achieve this, a stochastic model for density (or another state variable, such as entropy) would need to be developed. The next logical step after this would be to provide stochastic models for the velocity, resulting in a velocity-composition PDF model. The advantage of this type of model is that convection is now treated exactly, and so gradient diffusion models no longer need to be used. This is particularly important for reacting flows, where counter-gradient diffusion has been shown to occur<sup>9</sup>.

The final area of proposed work is in parallel implementation of PDF methods. One of the concerns with PDF methods is ensuring there are enough particles to ensure statistical accuracy, with the constraint being the amount of memory available on a computer. For the compressible scalar PDF method of Hsu et al<sup>5</sup>, a time averaging procedure is employed, however of order 100 particles per cell is still required. However PDF methods are particularly suitable for parallel implementation as the same program, with fewer particles, can be run on many different processors at once, and the results averaged at the end of the runs. For full velocity-composition PDF methods, the only change from a serial program is including the averaging process, a simple task. Apart from very simple implementation, there is no need for processors to communicate with each other, except at the end of the program, making PDF parallel computing effective on distributed systems. For the scalar PDF model, the parallel implementation of the finite difference velocity code is the

only complication. One solution is to employ a parallel implementation for the scalar PDF calculations, with the mean quantities being passed to a serial velocity calculation. This method takes advantage of the statistical accuracy of the parallel PDF calculations, while minimizing the changes required to a serial code.

### 3. References

- <sup>1</sup> Pope, S.B., "PDF Methods for Turbulent Reactive Flows," *Prog. Energy Combust. Sci.*, **11**, 119-192 (1985).
- <sup>2</sup> Pope, S.B., "A Monte Carlo Method for the PDF Equations of Turbulent Reacting Flows," *Combust. Sci. Tech.*, **25**, 159-174 (1981).
- <sup>3</sup> Dopazo, C. & O'Brian, E.E., "An Approach to the Autoignition of a Turbulent Mixture," *Acta Astronautica*, **1**, 1239-1266 (1974).
- <sup>4</sup> Chen, J.Y., Kollmann, W. & Dibble, R.W., "PDF Modeling of Turbulent, Non-Premixed Methane Jet Flames," *Combust. Sci. Tech.*, **64**, 315-346 (1989).
- <sup>5</sup> Hsu, A.T., Tsai, Y.L.P. & Raju, M.S., "A PDF Approach for Compressible Turbulent Reacting Flows," *Proc. AIAA 31st Aerospace Sciences Meeting and Exhibit*, Reno, Nevada, AIAA-93-0087 (1993).
- <sup>6</sup> Pope, S.B. & Correa, S.M., "Joint PDF Calculations of a Non-Equilibrium Turbulent Diffusion Flame," In *21st Symposium (International) on Combustion*, 1341-1348 (1986).
- <sup>7</sup> Anand, M.S. & Pope, S.B., "Calculations of Premixed Turbulent Flames by PDF Methods," *Combustion and Flame*, **67**(2), 127-142 (1987).
- <sup>8</sup> Norris, A.T., *The Application of PDF Methods to Piloted Diffusion Flames*, PhD Thesis, Cornell University, Ithaca, 1993.
- <sup>9</sup> Pope, S.B., "Computations of Turbulent Combustion: Progress and Challenges," In *23rd Symposium (International) on Combustion*, 591-612 (1990).
- <sup>10</sup> Kee, R.J., Rupley, F.M. & Miller, J.A., "CHEMKIN-II: A Fortran Chemical Kinetics Package for the Analysis of Gas-Phase Chemical Kinetics," Report SAND89-8009, Sandia National Laboratories, Livermore, CA 94551

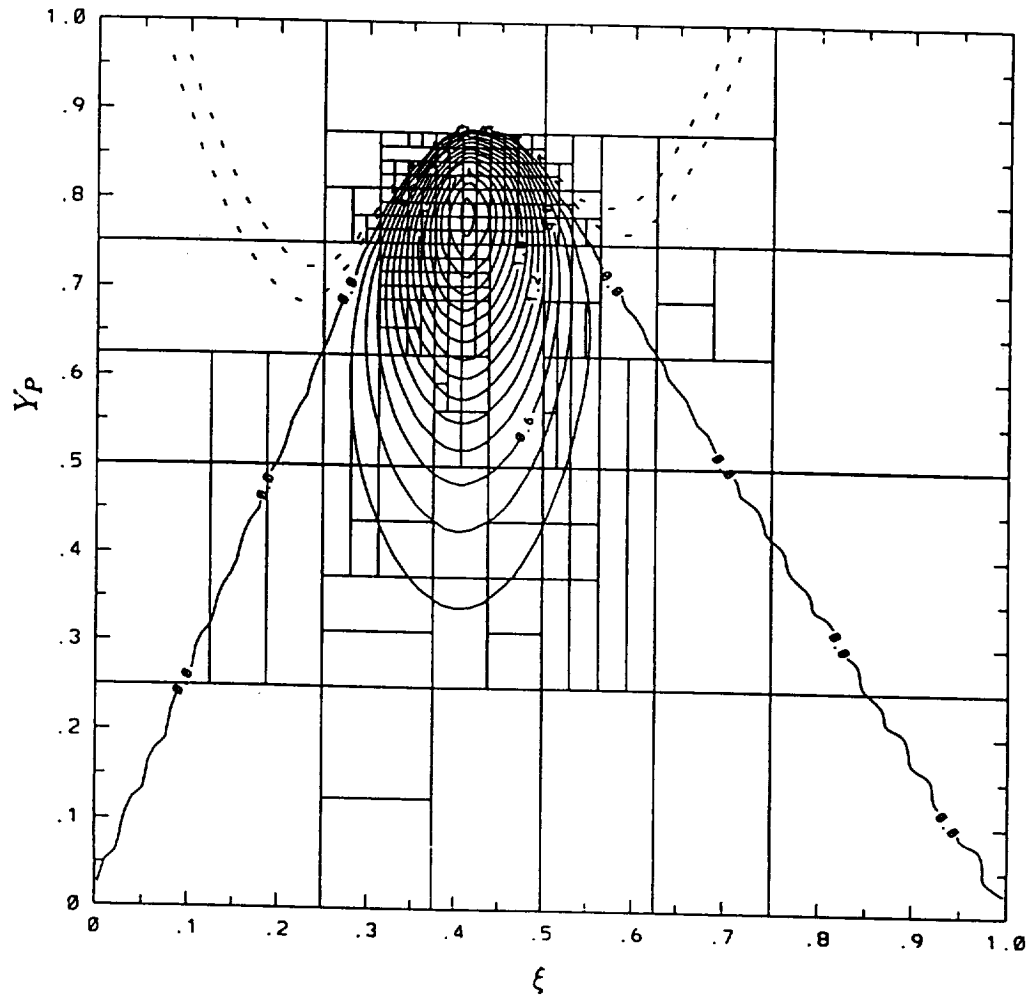


Fig 1: Contour plot of reaction rate as a function of  $\xi$  and  $Y_P$  with the grid for the adaptive lookup table overlaid.



# A Time Dependent Generalization of the Nonlinear Eddy Viscosity Representation of Turbulence

R. Rubinstein

## 1. Motivation and Objective

Standard two equation turbulence models are derived in an equilibrium limit which assumes a local Kolmogorov steady state. This assumption rules out the possibility of correctly capturing the response of turbulence to sudden changes in external conditions which occur when a flow is impulsively sheared or subject to rapidly oscillating shear. Moreover, such models also do not incorporate memory effects associated with the viscoelasticity of turbulence. Although stress transport models do incorporate some memory effects, it will be shown that they misstate the short time response. The goal of this work is to analyze the time dependence of turbulence from the viewpoint of the direct interaction approximation. This is a natural viewpoint because the direct interaction approximation is the only fully time dependent analytical theory of turbulence now available. Models valid for arbitrarily large strains will be introduced. These models demonstrate that both rapid distortion theory and the Kolmogorov steady state theory are required in a complete picture of shear turbulence.

## 2. Work Accomplished

The goal of this work is to derive a time dependent generalization of the nonlinear eddy viscosity formula

$$\begin{aligned}\tau = & \frac{2}{3}KI - C_\nu \frac{K^2}{\epsilon} (\nabla U + \nabla U^T) \\ & + C_{\tau 1} \frac{K^3}{\epsilon^2} (\nabla U \nabla U^T - \frac{1}{3} \nabla U : \nabla U^T I) \\ & + C_{\tau 2} \frac{K^3}{\epsilon^2} (\nabla U^2 + \nabla U^{T2} - \frac{2}{3} \nabla U : \nabla U I) \\ & + C_{\tau 3} \frac{K^3}{\epsilon^2} (\nabla U^T \nabla U - \frac{1}{3} \nabla U : \nabla U^T I)\end{aligned}\tag{1}$$

The symbols have the standard meanings:  $\tau_{ij} = \overline{u_i u_j}$  is the stress tensor,  $K$  is the turbulence kinetic energy,  $\epsilon$  the dissipation rate,  $\nabla U$  the mean velocity gradient, and  $C_\nu, C_{\tau 1}, C_{\tau 2}, C_{\tau 3}$  are model constants. The generalization is a nonlinear viscoelastic representation of the stress in which these constants are replaced by integrals over the strain rate history. A typical application of such a theory would be to normal stress effects in oscillating duct flow. It will be shown that this model predicts time dependent response quite distinct from the time dependent response of the

standard stress transport models. The theory reduces to Eq. (1) for constant strain rates maintained for long times, but reduces to rapid distortion theory for suddenly applied and rapidly varying strains. The implications of the model for oscillating shear flows are discussed. This work also helps clarify the relation between rapid distortion theory and the Kolmogorov theory of turbulence. A time dependent form of Eq. (1) cannot be valid when the dimensionless strain rate  $K(\nabla u : \nabla u)^{1/2}/\varepsilon$  is large. Some preliminary extensions of Eq. (1) applicable to arbitrary strain rates will be suggested. Rapid distortion theory plays an essential role in these extensions.

### 2.1. Derivation of the Time Dependent Model

Eq. (1) was proposed by Yoshizawa<sup>1</sup> in order to model normal stress effects with an explicit formula for the stress. For other discussions, see Pope<sup>2</sup>, Speziale<sup>3</sup> and Rubinstein and Barton<sup>4</sup>. As the derivations of this formula from analytical theories of Yoshizawa<sup>1</sup> and Rubinstein and Barton<sup>4</sup> suggest, Eq. (1) describes the long-time behavior of turbulence corresponding to establishment of a Kolmogorov steady state; application of this equation in a time-dependent problem requires sufficiently slow changes of the strain rate that this steady state can establish itself at each time. It should be noted that the models of Yoshizawa<sup>1</sup> and Speziale<sup>3</sup> contain convective terms which represent effects of time dependent mean gradients. However, these terms provide low order corrections for time dependence only; these theories do not reduce to rapid distortion theory at very short times.

In contrast to the description by Eq. (1) of the purely viscous response of turbulence to mean strain, the viscoelastic response has been stressed by Crow<sup>5</sup>. In these investigations, the short time response of turbulence is elastic,  $\dot{\tau}_{12} \sim K \partial U_1 / \partial x_2$  and is determined by rapid distortion theory<sup>6</sup>, but the long time response is viscous,  $\tau_{12} \sim \nu_T \partial U_1 / \partial x_2$ . Crow<sup>5</sup> proposed a linear viscoelastic turbulence model with these properties, however, this model assumes purely (molecular) viscous damping, and is therefore of limited applicability. Recently, Smith and Yakhot<sup>7</sup> have proposed a more general theory of this type based on the direct interaction approximation (DIA) of Kraichnan<sup>8</sup>. Since the DIA and its derivatives are fully time dependent theories of the spectral dynamics of turbulence (and are, in fact, the only such theories now available) they provide a natural basis for formulating such theories.

The DIA is a closed system of nonlinear integrodifferential equations for the correlation tensor  $Q_{ij}(\mathbf{k}, t, s)$  and a response function  $G_{ij}(\mathbf{k}, t, s)$ . A fundamental difficulty in DIA is the divergence of the response equation when Kolmogorov scaling is assumed. Smith and Yakhot<sup>7</sup> propose to surmount this difficulty by introducing a regularized DIA in which the correlation equation, which is consistent with Kolmogorov scaling, is not changed, but the response equation is suitably modified. Previous suggestions of this sort are due to Kraichnan<sup>9</sup> and others. Pending a solution of this regularized DIA now in progress, Smith and Yakhot<sup>7</sup> suggest using the response function for isotropic turbulence derived by Avellaneda and Majda<sup>14</sup> for a related problem

$$G_{ij} = GP_{ij}, \quad P_{ij} = \delta_{ij} - k_i k_j / k^2 \quad (2)$$

$$G(k, \tau) = \exp \left\{ -c_1 \varepsilon^{1/3} k^{2/3} \tau [1 - \exp(-c_2 \varepsilon^{1/3} k^{2/3} \tau / 2)] \right\}$$

An important feature of this response function stressed by Smith and Yakhot<sup>7</sup> is that at short times,  $G \sim 1 + O(t^2)$  as required by DIA, but  $G \sim \exp(-ct)$  at long time separations, as assumed (in effect) by static turbulence models. The importance of this short time behavior will be discussed subsequently.

To derive the viscoelastic generalization of Eq. (1), we follow Leslie<sup>11</sup> and begin with the Fourier transform of the equations for the fluctuating velocity in a homogeneous shear flow,

$$\left( \frac{d}{dt} + \nu k^2 \right) u_i(\mathbf{k}, t) - \frac{1}{2} i P_{imn}(\mathbf{k}) \int_{\mathbf{p}+\mathbf{q}=\mathbf{k}} d\mathbf{p} d\mathbf{q} \times \quad (3)$$

$$u_m(\mathbf{p}, t) u_n(\mathbf{q}, t) = S_{im}(\mathbf{k}, t) u_m(\mathbf{k}, t)$$

where

$$P_{imn} = k_m P_{in} + k_n P_{im}$$

$$S_{im} = -A_{im} + 2k^{-2} k_i k_p A_{pm} + \delta_{im} k_s A_{sr} \partial / \partial k_r$$

$$A_{im} = \partial U_i / \partial x_m$$

If Eq. (3) is formally expanded in powers of the mean strain rate about an isotropic background state  $u^{(0)}$ ,

$$u = u^{(0)} + u^{(1)} + \dots \quad (4)$$

then DIA gives the solution for  $u^{(1)}$ ,

$$u_i^{(1)}(k, t) = \int_0^t ds G_{im}^{(0)}(k, t-s) S_{mn}(k, s) u_n^{(0)}(k, s)$$

where  $G_{im}^{(0)} = G^{(0)} P_{im}$  is the response function for isotropic turbulence. If, corresponding to Eq. (4), the correlation function is written as

$$Q = Q^{(0)} + Q^{(1)} + \dots$$

then

$$\begin{aligned} Q_{im}^{(1)}(\mathbf{k}, t) = & \int_0^t ds G^{(0)}(k, t-s) (-A_{ir} + 2k_i k_p k^{-2} A_{pr}) P_{rm} Q^{(0)}(k, t-s) \\ & + (im) + G^{(0)}(\mathbf{k}, t-s) k_r A_{rn} \frac{\partial}{\partial k_n} Q_{im}^{(0)}(k, t-s) \\ & - Q_{im}^{(0)}(k, t-s) k_r A_{rn} \frac{\partial}{\partial k_n} G^{(0)}(k, t-s) \end{aligned} \quad (5)$$

where  $(im)$  denotes index interchange in the immediately preceding term. Of course,

$$\tau = \tau^{(0)} + \tau^{(1)} + \dots = \int d\mathbf{k} Q^{(0)} + Q^{(1)} + \dots$$

The behavior of this model for simple shear flow, in which  $\partial U_1/\partial x_2 = S$  is the only nonzero mean velocity gradient is of particular importance. At short times, Eq. (5) reduces to

$$\tau_{12} = \frac{4}{15} K S t + O(t^3)$$

The lowest order term agrees with rapid distortion theory. The  $O(t^3)$  correction indicates a short time suppression of eddy damping which is characteristic of this theory. In rapid distortion theory, in which eddy damping is absent altogether, the corrections to short time behavior are of order  $O(t^5)$ . Eq. (5) reduces at once to the quantity evaluated by Crow<sup>5</sup> if  $G^{(0)} \equiv 1$ .

To evaluate the stress at long times for constant strain, we adopt the procedures of Yakhot and Orszag<sup>12</sup> and assume that a universal energy spectrum  $E(k)$  exists for  $k \geq k_f$ , where  $k_f$  is an inverse integral scale. We also assume the fluctuation-dissipation relation

$$Q(k, \tau) = Q(k)G(k, |\tau|)$$

Then

$$\tau_{12} = \nu(k_f)S$$

with

$$\begin{aligned} \nu(k, t) &= \frac{1}{15} \int_{k_f}^{\infty} dq \Theta(q, t) [5E(q) + q \frac{dE}{dq}] \\ \Theta(q, t) &= \int_0^t ds [G^{(0)}(q, s)]^2 \end{aligned}$$

in agreement with Kraichnan<sup>10</sup> when  $t = \infty$ . Explicit formulas follow by substituting the Avellaneda-Majda expression Eq. (2) for  $G$  and a Kolmogorov spectrum for  $E$ . Note that  $\nu \sim k^{-4/3}$  as required by Kolmogorov scaling. Whereas the short time response does not depend on the form of the spectrum, a result familiar from rapid distortion theory, the long time response depends on the inertial range exponent through  $dE/dk$ .

The short time behavior of this model can be contrasted to the short time behavior of the standard Launder-Reece-Rodi<sup>13</sup> stress transport model, which gives for simple shear

$$\dot{\tau}_{12} = -C_R \frac{\varepsilon}{K} \tau_{12} + \frac{4}{15} S K + \dots \quad (6)$$

in which the terms indicated by dots are of order  $t^2$  for short times in initially isotropic flow. It is clear that at very short times, Eq. (6) predicts the same stress relaxation as the equation

$$\tau_{12}(t) = \int_0^t G(t-s) S(s) ds$$

with  $G(t-s) = \exp(-C_R \varepsilon(t-s)/K)$ , so that  $G \sim 1 + O(t)$  for small times. It follows that  $\tau_{12} = 4/15 K S t + O(t^2)$  at short times. The short time behavior agrees



with rapid distortion theory to lowest order, but the corrections are of order  $O(t^2)$ . Thus, the stress transport models initiate eddy damping more quickly than the present theory. This is reflected in the excessive short time growth of kinetic energy in highly strained homogeneous shear flow. This difference is also reflected in the response to oscillating mean shear. Suppose conditions are such that  $K$  and  $\varepsilon$  can be considered constant while  $S(\omega) = S_0 + S_1 e^{i\omega t} i\omega$ . Then exactly as in the theory of linear viscoelasticity, the stress is given by the complex modulus

$$G(i\omega) = \int_0^\infty d\tau e^{i\omega\tau} G^{(0)}(k_f, \tau)$$

Of particular interest is the phase lag between stress and strain, which is zero in a purely elastic regime. (The phase lag between stress and strain rate is  $90^\circ$  in this case). The short time behavior  $G \sim 1 + O(t^2)$  causes a very rapid drop in the phase lag as the frequency increases. Thus, this theory predicts a larger frequency range for applicability of rapid distortion theory than the standard model.

This calculation helps clarify the relation between rapid distortion theory and standard static turbulence models based, however implicitly, on a Kolmogorov steady state. Namely, rapid distortion theory is the special case of shear flow DIA that results from setting the response function to its short time value,  $G \equiv 1$  for all times. The replacement of the DIA response function by its short time limit has a twofold significance. First, it is consistent with the picture of rapid distortion theory as a short time theory. Second, since the DIA response function models eddy damping, the result of nonlinear interactions, this assumption means that nonlinear interaction is ignored; neglect of nonlinear interaction in the Navier-Stokes equations of course defines rapid distortion theory.

Calculation of the stress to second order is straightforward. The result has the form

$$\begin{aligned} Q_{ij}^{(2)}(\mathbf{k}, t) = & \sum_{1 \leq N \leq 6} I^{(N)} [a^{(N)} A_{ip}(s) A_{jp}(r) \\ & + b^{(N)} A_{ip}(s) A_{pj}(r) \\ & + c^{(N)} A_{pi}(s) A_{jp}(r) + d^{(N)} A_{pi}(s) A_{pj}(r) \\ & + e^{(N)} \delta_{ij} A_{pq}(s) A_{qp}(r) + f^{(N)} \delta_{ij} A_{pq}(s) A_{pq}(r)] + (ij) \end{aligned}$$

where  $A_{ij} = \partial U_i / \partial x_j$  is the mean velocity gradient, allowed to depend on time,  $a^{(N)}, \dots, f^{(N)}$  are geometric constants, and the  $I^{(N)}$  are integral operators

$$\begin{aligned} I^{(1)} &= \int_0^t ds G^{(0)}(k, t-s) \int_0^s dr G^{(0)}(k, s-r) G^{(0)}(k, t-r) Q^{(0)}(k) \\ I^{(2)} &= \int_0^t ds G^{(0)}(k, t-s) \int_0^s dr G^{(0)}(k, s-r) \frac{d}{dk} [G^{(0)}(k, t-r) Q^{(0)}(k)] \\ I^{(3)} &= \int_0^t ds G^{(0)}(k, t-s) \int_0^s dr G^{(0)}(k, s-r) \frac{d^2}{dk^2} [G^{(0)}(k, t-r) Q^{(0)}(k)] \end{aligned}$$

$$\begin{aligned}
I^{(4)} &= \int_0^t ds G^{(0)}(k, t-s) \int_0^t dr G^{(0)}(k, t-r) G^{(0)}(k, |s-r|) Q^{(0)}(k) \\
I^{(5)} &= \int_0^t ds G^{(0)}(k, t-s) \int_0^t dr G^{(0)}(k, t-r) \frac{d}{dk} [G^{(0)}(k, |s-r|) Q^{(0)}(k)] \\
I^{(6)} &= \int_0^t ds G^{(0)}(k, t-s) \int_0^t dr G^{(0)}(k, t-r) \frac{d^2}{dk^2} [G^{(0)}(k, |s-r|) Q^{(0)}(k)]
\end{aligned}$$

The values of the constants are given by

	(1)	(2)	(3)	(4)	(5)	(6)
$105a^{(N)}$	27	-1	-2	$\frac{19}{2}$	$-\frac{1}{2}$	-1
$105b^{(N)}$	20	6	-2	6	3	-1
$105c^{(N)}$	-15	-15	-2	$\frac{5}{2}$	$-\frac{15}{2}$	-1
$105d^{(N)}$	20	-8	-2	-22	-4	-1
$105e^{(N)}$	10	24	6	3	12	3
$105f^{(N)}$	-4	24	6	10	12	3

The time integrations can be compared with those of Yoshizawa's theory<sup>1</sup>. As in all derivations of this type, the constants  $a^{(N)}, \dots$  arise from integrating even order products  $k_1 k_j, \dots$  over spheres  $|k| = \text{constant}$ . A useful constraint on the calculation is that it must reduce to the rapid distortion results of Maxey<sup>6</sup> when  $G^{(0)} \equiv 1$ . An interesting reduction of this model for slowly varying strains is suggested by the theory of nonlinear viscoelasticity, namely that the time history integrals can be approximated by sums of Rivlin-Ericksen tensors in this case. This replacement should lead to a model of the form proposed by Speziale<sup>3</sup>.

## 2.2. Models Valid for Large Strains

The perturbative derivation of this model restricts its applicability to weak, although possibly rapidly varying, shears. It is natural to try to derive a theory valid for strong shear by summing this series. It proves more convenient to evaluate the exact response function for shear flow than to evaluate the correlation function directly. Thus, define  $G^{(1)}$  by

$$G_{ij}^{(1)} = G_{ip}^{(0)} S_{pj}$$

where  $S$  is the mean strain operator of Eq. (3). The notation abbreviates the integral operator in

$$u_i^{(1)}(t) = \int_0^t G_{im}^{(1)} u_m^{(0)}(s) ds$$

As above, the operator  $G^{(2)}$  can be constructed, and by simple recursions, all  $G^{(n)}$  for  $n \geq 2$ . It is at once evident from the form of this expansion that if we set

$G^{(0)} = 1$ , then the sum  $G = G^{(0)} + G^{(1)} + \dots$  simply defines rapid distortion theory for finite times and finite strain rates. The sum is explicitly known for several standard cases including simple shear and irrotational strain. Consider for example simple shear with  $S(t) = \partial U_1 / \partial x_2$  the only nonvanishing mean velocity gradient. The replacement of  $G^{(0)} = 1$  by a form valid at long times, say by Eq. (2) amounts to a replacement in the formulas of RDT of the total strain

$$\alpha = \int_0^t S(r) dr$$

by the wavenumber dependent quantity

$$\alpha(k) = \int_0^t G^{(0)}(k, r) S(r) dr$$

This defines an "equivalent total strain," a formal device often advocated in the RDT literature, but derived here as a consequence of an analytical theory.

It is not difficult to derive from this theory a long-time modification of Eq. (1) valid at large strains, in which the coefficients  $C_\nu, C_{\tau 1}, C_{\tau 2}, C_{\tau 3}$  are functions of  $\eta = SK/\varepsilon$  as suggested by Yakhot et al.<sup>15</sup> For example, in the case of simple shear flow,

$$C_\nu(\eta) = F(\eta/C_R) / \eta$$

where  $\tau/K = F(\alpha)$  is the solution of RDT for simple shear. Analogs for the normal stress coefficients  $C_{\tau i}(\eta)$  follow at once from RDT.

It must be stressed that this theory only applies to simple shear flow. Derivation of a theory for three-dimensional mean velocity fields will require the solution of RDT for these flows. A phenomenological modification of Eq. (1) has recently been proposed by Zhu and Shih<sup>16</sup> by using realizability constraints to set the functional dependence on  $\eta$ .

We would like to conclude by outlining another approach to developing models valid at arbitrary strain rates, now being developed in collaboration with L. Smith and V. Yakhot. The idea is that RDT may apply not only at short times, but also to scales for which the Kolmogorov inertial range frequency, proportional to  $\varepsilon^{1/3} k^{2/3}$  is smaller than the imposed strain rate  $S$ . The remaining scales are governed by equilibrium eddy damping. This suggests a two-scale form of the response function

$$G(k, t) = \begin{cases} 1, & k \leq k^* \\ \exp - c\varepsilon^{1/3} k^{2/3} t, & k > k^* \end{cases}$$

where the cutoff scale  $k^*$  is chosen so that turbulence in local energy equilibrium has no rapidly distorted scales. It remains to determine the time of rapid distortion. This time is finite both in homogeneous shear flow and in near wall turbulence. In homogeneous shear flow, scales of increasing size  $1/k_f$  are continually being created by the mean shear, but the cutoff scale  $1/k^*$  may also increase with time;

thus, turbulence at scale  $k$  is rapidly distorted from the time that it is created until the time when  $k = k^*$ . A plausible conjecture is that in fully developed homogeneous shear flow,  $1/k^*$  and  $1/k_f$  both increase exponentially with the ratio  $k^*/k_f$  constant. This theory could explain the observation that stress ratios in both fully developed homogeneous shear flow and shear flows in local energy equilibrium are approximately equal.

In steady near wall flows, turbulence is created in the region of high strain near the wall but is then diffused into the equilibrium log layer<sup>17</sup>. Thus, although the flow is steady in time from the usual Eulerian viewpoint, from the Lagrangian viewpoint, turbulence is highly strained only for a finite time. If we assume that imbalance between production and dissipation is entirely the result of rapid straining, then it is reasonable to set this time to  $K/\dot{K} = K/(P - \epsilon)$  where  $P = S\tau$  is production. Preliminary comparisons with data from near wall flows and from highly strained homogeneous shear flow are satisfactory and further development of this model is in progress.

### 3. Future Plans

A two scale model of homogeneous shear flow will be developed to apply both to fully developed flows and to rapidly sheared flows. Current models do not capture the transient period of highly sheared flows correctly. It is hoped that the present methodology, which incorporates the rapid distortion limit in an essential way, will be more successful. Application of the theory to near wall turbulence will also be attempted. This problem is more difficult than homogeneous shear flow because the transients are due to rapid diffusion rather than to convection.

The long time constants in the nonlinear eddy viscosity representation will be derived in this DIA framework. The introduction of the  $\epsilon$  expansion techniques of the Yakhot-Orszag theory into DIA will be required.

### 4. References

- <sup>1</sup> Yoshizawa, A. "Statistical analysis of the deviation of the Reynolds stress from its eddy viscosity representation," *Physics of Fluids* **27**, 1377-1391 (1984).
- <sup>2</sup> Pope, S. B., "A more general effective viscosity hypothesis," *Journal of Fluid Mechanics* **72**, 331-340 (1975).
- <sup>3</sup> Speziale, C. G., "On nonlinear K-1 and K-e models of turbulence," *Journal of Fluid Mechanics* **178**, 459-487 (1987).
- <sup>4</sup> Rubinstein, R. and Barton, J. M., "Nonlinear Reynolds stress models and the renormalization group," *Physics of Fluids A* **2**, 1472-1480 (1990).
- <sup>5</sup> Crow, S., "Viscoelastic properties of fine grained turbulence," *Journal of Fluid Mechanics* **41**, 81-95 (1968).
- <sup>6</sup> Maxey, M. R., "Distortion of turbulence by uniform shear," *Journal of Fluid Mechanics* **124**, 261-282 (1982).
- <sup>7</sup> Smith, L. M. and Yakhot, V., "Short time and long time behavior of eddy viscosity models," *Theoretical and Computational Fluid Dynamics* (to appear)

- <sup>8</sup> Kraichnan, R. H., "The structure of turbulence at very high Reynolds number," *Journal of Fluid Mechanics* **5** 459-491 (1959).
- <sup>9</sup> Kraichnan, R. H., "Kolmogorov's hypothesis and Eulerian turbulence theory," *Physics of Fluids* **7** 1030-1048 (1964).
- <sup>10</sup> Kraichnan, R. H., "Eddy viscosity in two and three dimensions," *Journal of the Atmospheric Sciences* **33** 2315-2338 (1976).
- <sup>11</sup> Leslie, D. C., *Modern developments in the theory of turbulence*, Oxford (1973).
- <sup>12</sup> Yakhot, V. and Orszag, S. A., "Renormalization group analysis of turbulence," *Journal of Scientific Computing* **1** 3-50 (1986).
- <sup>13</sup> Launder, B. L., Reece, G. and Rodi, W. "Progress in the development of a Reynolds stress transport closure," *Journal of Fluid Mechanics* **68** 537-582 (1975).
- <sup>14</sup> Avellaneda, M. and Majda, A., "Approximate and exact renormalization theories," *Physics of Fluids A* **4** 41-63 (1992).
- <sup>15</sup> Yakhot, V., Thangam, S., Gatski, T., Orszag, S. A., and Speziale, C., "Development of turbulence models by a double expansion technique," *Physics of Fluids A* **4** 1510-1532 (1992).
- <sup>16</sup> Zhu, J. and Shih, T. H., "Calculation of turbulent separated flows," NASA Technical Memorandum TM-106154 (1993).
- <sup>17</sup> Yakhot, V. (private communication).



# Higher-Order Accurate Osher Schemes with Application to Compressible Boundary Layer Stability

J. J. W. Van Der Vegt

## 1. Motivation and Objective

The study of boundary layer stability and transition to turbulence is one of the classical topics in fluid mechanics. Linear and weakly non-linear theory, together with experiments, have been successful in describing several of the important instability mechanisms in compressible boundary layers, e.g. Tollmien-Schlichting (TS) waves, or first modes, and higher modes, which come into play at supersonic Mach numbers, Mack<sup>15</sup>, and theory was also successful in describing secondary instability, Herbert<sup>10</sup>.

The complicated phenomena in the non-linear stages, leading to transition and turbulence, however, require further understanding. Direct numerical simulations can provide some of this information, but their application to compressible boundary layers has been hindered by many obstacles. To mention just a few, high order accuracy is required on non-uniform grids and a severe time step limitation is encountered due to the small grid spacing in the boundary layer when using an explicit time integration method; whereas with implicit time integration methods it is difficult to maintain time accuracy. Spectral methods have been very successful in simulating incompressible flows in simple geometries, such as channel flow, e.g. Laurien and Kleiser<sup>11</sup>, but are not easily extended to more complicated geometries. The recently popular compact finite difference schemes, Lele<sup>13</sup>, do not have the geometric limitations of spectral methods and have been successfully applied to mixing layers and shock turbulence interaction, Lee et al.<sup>14</sup>. Unfortunately, compact finite difference schemes and also spectral methods, cannot capture shocks and if they appear they have to be fully resolved, which can require prohibitively small grid spacings, Lee et al.<sup>14</sup>.

There have been several attempts to use finite difference schemes for direct simulation of transition in compressible boundary layers. The most frequently used method is the fourth order accurate version of Mac Cormack's scheme, developed by Gottlieb and Turkel<sup>7</sup>, e.g. Maestrello et al.<sup>16</sup> and Bestek et al.<sup>3</sup>. This method can only achieve higher order accuracy on grids generated as the product of two or more one-dimensional analytic transformations, limiting its applicability to relatively simple, smooth flows.

Most frequently, explicit time integration methods have been used, but for many transitional flows the Courant-Friedrichs-Lewy (CFL) time step limitation is not necessary to maintain time accuracy. Recently Rai and Moin<sup>21</sup> developed a numerical scheme which solves the compressible Navier-Stokes equations using a time

accurate upwind biased implicit method and were able to simulate bypass transition. This method alleviates the time step limitation of explicit methods, but has as main drawback that it uses the non-conservative form of the Navier-Stokes equations and only allows grid stretching in one direction. The grid stretching, however, does not have to be analytically defined because the higher order finite difference approximations are generated numerically in physical space.

In this paper two alternative methods will be discussed. The first method is a higher order accurate extension of the MUSCL scheme, originally developed by Van Leer<sup>27</sup> as a second order accurate extension of Godunov schemes. The scheme is related to the multi-dimensional essentially non-oscillatory (ENO) schemes developed by Casper and Atkins<sup>4</sup> and Harten et al.<sup>9</sup>. The second method is a higher order accurate upwind biased version of the Osher scheme, which maintains its high order accuracy on non-uniform grids. Higher order accurate Osher schemes were also discussed by Rai<sup>20</sup>, but his method is only higher order accurate on a uniform grid.

The discussion in this paper will be restricted to smooth flows, but both schemes have been extensively tested for flows with shocks and other discontinuities in one-dimensional flows. A detailed discussion of the benefits and application of these schemes to non-smooth flows can be found in Van Der Vegt<sup>25</sup>. The purpose of this paper is to investigate if these methods are accurate and efficient enough to be used as tools for direct simulation of boundary layer instability and transition to turbulence. The finite volume scheme has as main benefit that it is a truly multi-dimensional scheme, whereas the finite difference scheme uses dimensional splitting. The finite volume scheme automatically satisfies conservation and is most closely related to the integral formulation of the compressible Euler and Navier-Stokes equations. It also maintains higher order accuracy at sonic points, which is not true for the finite difference formulation. The finite volume method, however, is slightly more costly than the finite difference scheme and requires significantly more effort to implement. The use of an upwind scheme is beneficial for direct simulations of compressible flow, because it automatically controls aliasing errors. There are two types of upwind schemes, those based on flux vector splitting, e.g. Van Leer<sup>28</sup> and Steger-Warming<sup>24</sup>, and those based on a Godunov approach which use the solution of a Riemann problem. Godunov schemes most closely mimic the physics of wave propagation in compressible flow and have excellent shock capturing properties. In this class of schemes the Roe and Osher approximate Riemann solvers are the most popular, see Roe<sup>22</sup> and Osher and Solomon<sup>18</sup>. The Osher scheme has been chosen because it has a very low numerical dissipation in boundary layers, which is crucial for direct simulations, and it has a continuously differentiable flux, which is important for implicit schemes. In addition it satisfies the entropy condition and has good shock capturing properties.

In the next two sections of this paper the basic equations will be discussed and the higher order accurate numerical schemes will be presented. The paper will conclude with a discussion of the results of computations of boundary layer instability at various Mach numbers.



## 2. Work Accomplished

### 2.1 Navier-Stokes Equations

The Navier-Stokes equations can be considered either in integral formulation, leading to the finite volume discretization, or in differential form, which is the basis for the finite difference discretization. The finite volume method automatically satisfies the conservation properties of the equations but care has to be taken that the finite difference method is in the so-called conservation form. It is otherwise not possible to obtain a weak solution with the proper jump relations at discontinuities in the limiting case of vanishing viscosity, as demonstrated by Lax and Wendroff<sup>12</sup>. A detailed discussion of finite volume and finite difference methods and their differences can be found in Vinokur<sup>29</sup>.

The integral formulation of the compressible Navier-Stokes equations is defined as:

$$\int_{\Omega(t_2)} \mathbf{U} dV - \int_{\Omega(t_1)} \mathbf{U} dV + \int_{t_1}^{t_2} \oint_{\partial\Omega(t)} \mathcal{F}(\mathbf{U}) \cdot \mathbf{n} dS dt = 0 \quad (1)$$

Here  $\Omega(t)$  is the flow domain with boundary  $\partial\Omega(t)$  at time  $t$  and  $\mathbf{n}$  the unit outward normal vector at  $\partial\Omega$ . The vector  $\mathbf{U}$  represents the conserved variables:

$(\rho, \rho u, \rho v, \rho w, e)^T$ , with  $\rho$  density,  $\mathbf{u} = (u, v, w)^T$  the Cartesian velocity components, and  $e$  total energy. The matrix  $\mathcal{F}$ , which represents the fluxes through the surface  $\partial\Omega(t)$ , consists of two parts,  $\mathbf{F}$  the inviscid flux, and  $\mathbf{V}$  the viscous flux, with  $\mathcal{F} = \mathbf{F} - \mathbf{V}$ . The inviscid flux contribution  $\mathbf{F}$  has as components:

$$\mathbf{F}_1 = \begin{pmatrix} \rho u \\ \rho u^2 + p \\ \rho uv \\ \rho uw \\ (e + p)u \end{pmatrix}; \quad \mathbf{F}_2 = \begin{pmatrix} \rho v \\ \rho uv \\ \rho v^2 + p \\ \rho vw \\ (e + p)v \end{pmatrix}$$

$$\mathbf{F}_3 = \begin{pmatrix} \rho w \\ \rho uw \\ \rho vw \\ \rho w^2 + p \\ (e + p)w \end{pmatrix} \quad (2)$$

where the dimensionless pressure  $p$  is determined from the equation of state:  $p = \rho c_v T / (\gamma M^2)$ , with  $c_v$  the specific heat at constant volume,  $\gamma$  the ratio of specific heat at constant pressure and constant volume,  $M$  the Mach number and  $T$  temperature. The temperature  $T$  is given by the relation:  $T = \gamma(\gamma - 1)M^2(e - \frac{1}{2}\rho \mathbf{u} \cdot \mathbf{u}) / (\rho c_v)$ .

The viscous contribution  $\mathbf{V}$  has as components:

$$\mathbf{V}_1 = \begin{pmatrix} 0 \\ \tau_{xx} \\ \tau_{xy} \\ \tau_{xz} \\ \beta_x \end{pmatrix} \quad \mathbf{V}_2 = \begin{pmatrix} 0 \\ \tau_{xy} \\ \tau_{yy} \\ \tau_{yz} \\ \beta_y \end{pmatrix} \quad \mathbf{V}_3 = \begin{pmatrix} 0 \\ \tau_{xz} \\ \tau_{yz} \\ \tau_{zz} \\ \beta_z \end{pmatrix} \quad (3)$$

with the stress tensor  $\tau$  and the variables  $\beta_x$ ,  $\beta_y$  and  $\beta_z$  defined as:

$$\begin{aligned}
 \tau_{xx} &= \left( (2\mu + \lambda) \frac{\partial u}{\partial x} + \lambda \left( \frac{\partial v}{\partial y} + \frac{\partial w}{\partial z} \right) \right) / Re \\
 \tau_{xy} &= \left( \mu \left( \frac{\partial u}{\partial y} + \frac{\partial v}{\partial x} \right) \right) / Re \\
 \tau_{xz} &= \left( \mu \left( \frac{\partial u}{\partial z} + \frac{\partial w}{\partial x} \right) \right) / Re \\
 \tau_{yy} &= \left( (2\mu + \lambda) \frac{\partial v}{\partial y} + \lambda \left( \frac{\partial u}{\partial x} + \frac{\partial w}{\partial z} \right) \right) / Re \\
 \tau_{yz} &= \left( \mu \left( \frac{\partial w}{\partial y} + \frac{\partial v}{\partial z} \right) \right) / Re \\
 \tau_{zz} &= \left( (2\mu + \lambda) \frac{\partial w}{\partial z} + \lambda \left( \frac{\partial u}{\partial x} + \frac{\partial v}{\partial y} \right) \right) / Re
 \end{aligned} \tag{4}$$

$$\begin{aligned}
 \beta_x &= u\tau_{xx} + v\tau_{xy} + w\tau_{xz} + \frac{\kappa}{(\gamma - 1)M^2 Pr} \frac{\partial T}{\partial x} \\
 \beta_y &= u\tau_{xy} + v\tau_{yy} + w\tau_{yz} + \frac{\kappa}{(\gamma - 1)M^2 Pr} \frac{\partial T}{\partial y} \\
 \beta_z &= u\tau_{xz} + v\tau_{yz} + w\tau_{zz} + \frac{\kappa}{(\gamma - 1)M^2 Pr} \frac{\partial T}{\partial z}
 \end{aligned} \tag{5}$$

Here  $Re$  represents the Reynolds number,  $Pr$  Prandtl number,  $\kappa$  the coefficient of thermal conductivity and  $\mu$  and  $\lambda$  the first and second viscosity coefficient. All computations were done using the relation  $\lambda = -\frac{2}{3}\mu$ , with  $\mu$  given by Sutherland's law. The non-dimensional variables are defined with respect to the freestream velocity, density, temperature, viscosity, thermal conductivity and specific heat.

If we assume that all variables are continuously differentiable in time it is possible to rewrite equation (1) into:

$$\frac{\partial}{\partial t} \int_{\Omega(t)} \mathbf{U} dV + \oint_{\partial\Omega(t)} \mathcal{F}(\mathbf{U}) \cdot \mathbf{n} dS = 0 \tag{6}$$

A special constraint can be derived from this expression, namely the geometric conservation law. Inserting a uniform flow field in equation (6) we obtain:

$$\oint_{\partial\Omega(t)} \mathbf{n} dS = 0 \tag{7}$$

which states that the cell face  $\partial\Omega(t)$  must be closed. When dividing the total flow field in a set of non-overlapping cells this constraint puts limitations on how to compute the cell faces and volumes. They all have to add up to the total volume and each cell will have to be closed; otherwise a uniform flow field will be disturbed

due to contributions from the metrics. This is a non-trivial problem when deriving higher order schemes and will be discussed in the next sections.

The differential form of the compressible Navier-Stokes equations is directly obtained from the integral formulation, equation (6), using Gauss' theorem and considering an arbitrary volume  $\Omega$ :

$$\frac{\partial \mathbf{U}}{\partial t} + \nabla \cdot \mathcal{F}(\mathbf{U}) = 0 \quad (8)$$

This is the conservative formulation of the compressible Navier-Stokes equations and it is important that the discretization also can be written in conservation form. The geometric conservation law must be satisfied and this requires great care in dealing with the metrical coefficients in a finite difference discretization, especially in three dimensions.

## 2.2 Higher Order Accurate Finite Volume Scheme

Second order accurate finite volume schemes have been around for a long time. When extending the accuracy beyond second order several problems are encountered. It is no longer valid to equate cell averaged values with values at the cell center and a more elaborate algorithm to reconstruct point values from cell averaged values is required. In addition one has to compute the integrals of the fluxes over the cell surfaces more accurately. The standard procedure of multiplying the flux with the cell surface is only second order accurate. The geometry in a higher order accurate finite volume method also has to be represented more accurately, especially at the boundary. The relations for cell area and volume as given by Vinokur<sup>29</sup> are no longer sufficient. They are exact for hexahedrons with straight line edges, but not for cells with curved edges.

Until now very few attempts have been made to develop higher order accurate finite volume methods. For structured grids Harten et al.<sup>9</sup> and Casper and Atkins<sup>4</sup> developed the multi-dimensional ENO schemes and Abgrall<sup>1</sup> and Harten and Chakravarthy<sup>8</sup> studied these schemes for unstructured grids. Despite the fact that the unstructured approach has more flexibility in treating complicated geometries and allows local grid refinement it was decided to use the structured grid approach developed by Casper and Atkins<sup>4</sup>. Both CPU time and memory usage in the unstructured schemes is so large that it is not feasible to use these methods for direct or large eddy simulations of compressible flow. The structured grid approach, however, requires a smooth  $C^3$  grid. It is possible to deal with locally non-smooth boundaries and intersections in the finite volume approach by subdividing the grid into smooth subsections using a multi-block approach. The smoothness requirements of the grid will limit the application of this method to fairly simple geometries, but due to their high cost large eddy and direct simulations will be limited to simple flows for quite a while. The finite volume method is, however, considerably more flexible than spectral methods which require a  $C^\infty$  grid.

The use of a structured grid makes it possible to transform the physical domain to a simpler computational domain. Let  $\xi$ ,  $\eta$ , and  $\zeta$  be the coordinates in the

computational domain then they are related to the physical coordinates  $x, y, z$  by the relations:

$$\begin{aligned}\xi &= \xi(x, y, z) \\ \eta &= \eta(x, y, z) \\ \zeta &= \zeta(x, y, z)\end{aligned}\tag{9}$$

The finite volume discretization on a structured grid is obtained by dividing the domain  $\Omega$  into regular partitions  $\Omega_{i,j,k}$ . Each element  $\Omega_{i,j,k}$  is a hexahedron with coordinates  $x_i, y_j$  and  $z_k$  for the top right corner. The subdomains  $\Omega_{i,j,k}$  are non-overlapping and their sum is equal to the domain  $\Omega$ .

The cell average  $\bar{U}_{i,j,k}$  in a cell with index  $(i, j, k)$  is defined as:

$$\bar{U}_{i,j,k} = \frac{1}{Vol(\Omega_{i,j,k})} \int_{\Omega_{i,j,k}} U dV\tag{10}$$

with  $Vol(\Omega_{i,j,k})$  the volume of cell  $\Omega_{i,j,k}$ . The equation for the cell average is obtained by limiting the integration domain  $\Omega$  to  $\Omega_{i,j,k}$  in equation (6), and is equal to:

$$\frac{\partial}{\partial t} \bar{U}_{i,j,k}(t) + \mathbf{h}_{i,j,k}(\mathbf{U}) = 0\tag{11}$$

with the flux integral  $\mathbf{h}_{i,j,k}$  at the surface  $\partial\Omega_{i,j,k}$  of the cell  $\Omega_{i,j,k}$  defined as:

$$\begin{aligned}\mathbf{h}_{i,j,k}(\mathbf{U}) &= \frac{1}{Vol(\Omega_{i,j,k})} \int_{\partial\Omega_{i,j,k}} \mathcal{F}(\mathbf{U}) \cdot \mathbf{n} dS \\ &\equiv \frac{1}{Vol(\Omega_{i,j,k})} \int_{\partial\Omega_{i,j,k}} \hat{\mathbf{F}}(\mathbf{U}) dS\end{aligned}\tag{12}$$

with  $\hat{\mathbf{F}}$  the flux normal to the cell surface:

$$\hat{\mathbf{F}} = k_1 \mathbf{F}_1 + k_2 \mathbf{F}_2 + k_3 \mathbf{F}_3\tag{13}$$

and  $\mathbf{n} = (k_1, k_2, k_3)^T$ . This relation gives the method of lines formulation for the cell averaged equation  $\bar{U}_{i,j,k}(t)$ . The numerical flux in a higher order finite volume scheme now is constructed such that it approximates the exact flux at time  $t = (n+1)\Delta t$  up to  $O(h^r)$ :

$$\bar{U}_{i,j,k}^{n+1} - \left[ \bar{E}_h(\Delta t) \cdot \bar{U}^n \right]_{i,j,k} = O(h^r)\tag{14}$$

with  $\bar{E}_h(\Delta t)$  the numerical solution operator. The higher order accurate finite volume scheme therefore gives an  $r$ -th order accurate approximation to the cell averages, not the point values as in a finite difference scheme.

The two important ingredients of a higher order accurate finite volume method are the reconstruction of the point values  $\mathbf{U}(\mathbf{x})$  from the cell averaged values  $\bar{U}_{i,j,k}$  and the computation of the flux  $\hat{\mathbf{F}}$  at the cell face. The point values are necessary

to compute the fluxes  $\mathbf{h}_{i,j,k}$  at the cell faces which depend on  $\mathbf{U}(\mathbf{x})$  and not on  $\bar{\mathbf{U}}$ . This is done with the reconstruction method discussed in section 3.1. The fluxes at the cell faces are computed by considering a Riemann problem at each cell face. This method was introduced by Godunov<sup>6</sup> for first order accurate schemes and extended by Van Leer<sup>27</sup> to second order accuracy. Instead of using the exact solution of the Riemann problem the approximate Riemann solver developed by Osher and Solomon<sup>18</sup> is used, because it is less expensive than the exact solution, but has excellent shock capturing properties and minimal dissipation in boundary layers.

### 2.2.1 Reconstruction of Point Values from Cell Averages

In one dimension the most successful reconstruction technique is based on the primitive function method, see e.g. Harten et al.<sup>9</sup>. This method was extended by Harten et al.<sup>9</sup> and Casper and Atkins<sup>4</sup> to multiple dimensions using the one-dimensional primitive function reconstruction technique first to compute line averages from cell averages, after which point values are computed with a second one-dimensional reconstruction. It is, however, possible to define a primitive function directly for the multi-dimensional problem without having to use one-dimensional primitive functions.

Define the primitive function  $\mathcal{U}$  as:

$$\mathcal{U}(\xi, \eta, \zeta) = \int_{\zeta_0}^{\zeta} \int_{\eta_0}^{\eta} \int_{\xi_0}^{\xi} \mathbf{U}(\xi', \eta', \zeta') |J(\xi', \eta', \zeta')| d\xi' d\eta' d\zeta' \quad (15)$$

then the flow field  $\mathbf{U}$  satisfies the relation

$$\mathbf{U}(\xi, \eta, \zeta) = \frac{1}{|J(\xi, \eta, \zeta)|} \frac{\partial^3}{\partial \zeta \partial \eta \partial \xi} \mathcal{U}(\xi, \eta, \zeta) \quad (16)$$

with  $\xi$ ,  $\eta$  and  $\zeta$  the coordinates in computational space and  $J$  the Jacobian of the coordinate transformation. The primitive function  $\mathcal{U}$  can be related to the cell average  $\bar{\mathbf{U}}$  in physical space using the following relation:

$$\begin{aligned} \mathcal{U}(\xi_i, \eta_j, \zeta_k) &= \int_{\zeta_0}^{\zeta_k} \int_{\eta_0}^{\eta_j} \int_{\xi_0}^{\xi_i} \mathbf{U} |J| d\xi' d\eta' d\zeta' \\ &= \sum_{k'=k_0}^k \sum_{j'=j_0}^j \sum_{i'=i_0}^i \int_{k'-1}^{k'} \int_{j'-1}^{j'} \int_{i'-1}^{i'} \mathbf{U} |J| d\xi' d\eta' d\zeta' \\ &= \sum_{k'=k_0}^k \sum_{j'=j_0}^j \sum_{i'=i_0}^i \int_{\Omega_{i',j',k'}} \mathbf{U}(\mathbf{x}, t) dV \\ &= \sum_{k'=k_0}^k \sum_{j'=j_0}^j \sum_{i'=i_0}^i \text{Vol}(\Omega_{i',j',k'}) \bar{\mathbf{U}}_{i',j',k'} \end{aligned} \quad (17)$$

This relation is the basis for the higher order finite volume scheme. It defines the primitive function  $\mathcal{U}$  directly at the corners of each hexahedron in computational space  $(\xi_i, \eta_j, \zeta_k)$  and is conservative. The point values  $\mathbf{U}(\mathbf{x})$  are then obtained using equation (16).

When the flow field is smooth the following procedure can be used to compute the pointwise data: For a surface in the plane  $\xi = \xi^*$ , first approximate the left and right states by differentiating the primitive function  $\mathcal{U}$  with upwind biased differences in both  $\xi$ -directions with fourth order accuracy for all indices  $j$  and  $k$ . Then the  $\eta$  and  $\zeta$ -derivates are computed at the Gauss quadrature points and divided by the local Jacobian to obtain the point values. This process is repeated for the planes with  $\eta = \eta^*$  and  $\zeta = \zeta^*$  and works well for smooth flows. For flows with discontinuities the ENO reconstruction, which tries to use only data from the smooth part of the flow field has to be used. This will be discussed in a future paper.

Although this process is rather simple, care has to be taken to prevent loss of accuracy due to truncation errors, because the primitive function  $\mathcal{U}$  frequently becomes very large or small. The way to prevent this is to construct the primitive function using only those cells around the cell with index  $(i, j, k)$  which are needed to compute the derivatives in equation (16) and adjust the indices  $i_0, j_0$  and  $k_0$  for each cell. Accuracy is further improved by combining the process of summation and differentiation, e.g. first compute the sum with  $i$ -index, then differentiate this result and compute the summation with  $j$ -index, and so on.

In order to preserve uniform flow it is necessary to compute the Jacobian of the coordinate transformation at the Gauss quadrature points the same way as done for the flow field  $\mathbf{U}$ . This can be accomplished most easily by multiplying equation (16) with the Jacobian and inserting a uniform flow field in equations (16-17). This will give the Jacobian at the Gauss quadrature points with the same reconstruction process as for  $\mathbf{U}$ . This procedure is important because otherwise the reconstruction process will generate small errors which can be very annoying on stretched grids.

### 2.2.2 Higher Order Accurate Flux Integrals

The discretization of the integral formulation of the compressible Navier-Stokes equations (11) is completed with the approximation of the flux integrals given by equation (12). Casper and Atkins<sup>4</sup> gave a detailed analysis of the accuracy required in the reconstruction problem and the computation of the flux integrals to obtain an accurate solution with an error of order  $h^r$ . In this paper we limit the discussion to fourth order accuracy. The use of a Gauss quadrature method is the most efficient way to compute the flux integrals with fourth order accuracy. First the integral over the cell boundary is split into the sum of integrals over the six cell faces:

$$\mathbf{h}_{i,j,k}(\mathbf{U}) = \frac{1}{Vol(\Omega_{i,j,k})} \sum_{l=1}^6 \int_{\partial\Omega_{i,j,k}^l} \hat{\mathbf{F}}(\mathbf{U}) dS \quad (18)$$

here the index  $l$  refers to one of the six faces of the hexahedron. Then the flux integrals at each cell face can be further evaluated using the Gauss quadrature rule

at each cell face and the Osher approximate Riemann solver<sup>17,18</sup> is used to compute the flux at each quadrature point:

$$\begin{aligned} \int_{\partial\hat{\Omega}_{i,j,k}^l} \hat{\mathbf{F}}(\mathbf{U})dS &= \frac{1}{2} \int_{\partial\hat{\Omega}_{i,j,k}^l} \left( \hat{\mathbf{F}}_L + \hat{\mathbf{F}}_R - \int_{\Gamma} |\partial\hat{\mathbf{F}}|dU \right) |J|d\hat{S} \\ &\cong \frac{1}{8} \sum_{m=1}^4 \left( \hat{\mathbf{F}}_L + \hat{\mathbf{F}}_R - \int_{\Gamma} |\partial\hat{\mathbf{F}}|dU \right)_{g_{m,l}} |J_{g_{m,l}}|d\hat{S} \end{aligned} \quad (19)$$

with  $\partial\hat{\Omega}_{i,j,k}^l$  the cell face with index  $l$  in computational space. The indices  $g_{m,l}$  refer to the quadrature points with index  $m$  in the cell face where the fluxes of the left and right states  $\mathbf{F}_{L,R}$  and the Osher path integral are computed. The quadrature points have coordinates  $(\frac{1}{2} \pm \frac{1}{2}\sqrt{\frac{1}{3}}, \frac{1}{2} \pm \frac{1}{2}\sqrt{\frac{1}{3}})$ , assuming that the hexahedrons sides have unit length. This relation is used by Casper and Atkins<sup>4</sup> and requires four calculations of the approximate Riemann flux for each cell face which significantly increases the computing time. Harten and Chakravarthy<sup>8</sup> suggested that only one computation of the (approximate) Riemann flux is required to maintain accuracy in smooth flows. Due to the fact that both the Riemann flux and also the approximate Riemann flux according to Osher are Lipschitz continuous and  $|\mathbf{U}_L - \mathbf{U}_R| = O(h^r)$  in smooth flows, it is easy to show that the third component in the integral, equation(19), can be approximated as:

$$\int_{\partial\hat{\Omega}_{i,j,k}^l} \int_{\Gamma} |\partial\hat{\mathbf{F}}|dU |J|d\hat{S} = \int_{\Gamma} |\partial\hat{\mathbf{F}}_{c_l}|dU |J_{c_l}| + O(h^r) \quad (20)$$

Here the index  $c_l$  refers to center of the cell face with index  $l$ . This relation significantly reduces the computing time, while maintaining the total accuracy at the slight expense of computing  $\mathbf{U}_{L,R}$  at the cell face center. In regions with discontinuities it is, however, advisable to use the (approximate) Riemann solution at all the Gauss quadrature points.

### 2.3 Higher Order Accurate Finite Difference Scheme

The most difficult problem in deriving a higher order accurate finite difference scheme is to find a way to maintain that accuracy on a non-uniform grid. In upwind finite difference schemes, either based on flux vector splitting or using approximate Riemann solvers, the flux is a function of more than one grid point. When deriving the expression for the higher order differences care has to be taken to account for the changing metrics, but this is frequently neglected. For instance the higher order Osher scheme derived by Rai<sup>20</sup> is only higher order accurate on a uniform grid. In addition to the accuracy requirement, care has to be taken that the scheme is in conservation form and maintains uniform flow, which is a non-trivial requirement for a finite difference scheme. The conservation property is important on physical

grounds; the equations express conservation of mass, momentum and energy. It is also important when dealing with discontinuities. In this paper, however, only smooth flow fields will be considered.

Before deriving the higher order Osher scheme it is necessary to study the first order Osher scheme in more detail. The conservative approximation to  $\partial_\xi \hat{\mathbf{E}}$  using Osher's scheme is defined as:

$$\partial_\xi \hat{\mathbf{E}}_i = \frac{1}{\Delta \xi} (\hat{\mathbf{E}}_{i+\frac{1}{2}} - \hat{\mathbf{E}}_{i-\frac{1}{2}}) \quad (21)$$

where the conservative flux is defined as:

$$\begin{aligned} \hat{\mathbf{E}}_{i+\frac{1}{2}} = & \frac{1}{2} (\hat{\mathbf{E}}_{i+1}(\xi_{i+\frac{1}{2}}) + \hat{\mathbf{E}}_i(\xi_{i+\frac{1}{2}}) - \\ & \int_{\Gamma_i} \partial_{\mathbf{U}} \hat{\mathbf{E}}^+(\xi_{i+\frac{1}{2}}) d\mathbf{U} + \int_{\Gamma_i} \partial_{\mathbf{U}} \hat{\mathbf{E}}^-(\xi_{i+\frac{1}{2}}) d\mathbf{U}) \end{aligned} \quad (22)$$

with equivalent relations for  $\partial_\eta \hat{\mathbf{F}}$  and  $\partial_\zeta \hat{\mathbf{G}}$ . The symbol  $\partial_{\mathbf{U}}$  represents partial differentiation with respect to  $\mathbf{U}$  and for ease of notation the  $j$  and  $k$  indices are omitted. In this relation  $\xi_{i+\frac{1}{2}}$  refers to the metrical coefficients which are computed at the point with index  $i + \frac{1}{2}$ . The integrals in equation (22) are computed along a path in phase space,  $\Gamma_i$ , and using the fact that the Riemann invariants are constant along this path Osher was able to derive exact analytic expressions for these integrals, see<sup>20,22</sup>. It is important to note that although the path integral  $\Gamma_i$  is from  $i$  to  $i + 1$ , only metrical coefficients at one point must be used for consistency. As can be seen directly from equation (22), the flux  $\hat{\mathbf{E}}_{i+\frac{1}{2}}$  depends on the positions with indices  $i$ ,  $i + \frac{1}{2}$  and  $i + 1$ . Using a Taylor series expansion with respect to both  $i$  and  $i + 1$  Rai<sup>20</sup> was able to derive higher order conservative expressions for  $\partial_\xi \hat{\mathbf{E}}_i$ . The dependency on  $i + \frac{1}{2}$ , however, was neglected, which reduces the order of accuracy of the scheme on a non-uniform grid, even on mildly stretched grids. The analytical derivations necessary to obtain Rai's higher order Osher scheme are already tedious and taking care of the changing metrical coefficients, which would require Taylor series expansions up to at least fourth order in three independent variables, becomes unwieldy.

An alternative is to compute the higher order accurate flux approximations numerically. This is done using the flux-ENO scheme discussed in Van Der Vegt<sup>25</sup>, but the stencil switching, which is part of ENO schemes, is eliminated in this paper. As starting point a different formulation of the first order Osher scheme is used:

$$\partial_\xi \hat{\mathbf{E}}_i = \int_{\Gamma_{i-1}} \partial_{\mathbf{U}} \hat{\mathbf{E}}^+(\xi_{i-\frac{1}{2}}) d\mathbf{U} + \int_{\Gamma_i} \partial_{\mathbf{U}} \hat{\mathbf{E}}^-(\xi_{i+\frac{1}{2}}) d\mathbf{U} \quad (23)$$

It is easy to show that both formulations are equivalent, see Osher and Solomon<sup>18</sup>. The higher order scheme is derived using a Newton interpolation to the fluxes. The Newton interpolation, however, cannot be directly applied to the integrals in



equation (23) because of the path integrals. In order to use the Newton interpolation we use some simple relations, which were derived by Shu and Osher<sup>23</sup>: the function  $\mathbf{f}(x)$  can always be expressed as:

$$\mathbf{f}(x) = \frac{1}{\Delta x} \int_{x-\frac{\Delta x}{2}}^{x+\frac{\Delta x}{2}} \mathbf{h}(x') dx' \quad (24)$$

and using its primitive function:  $\mathbf{F}(x) = \frac{1}{\Delta x} \int_{-\infty}^x \mathbf{h}(x') dx'$  the following relation is obtained:

$$\mathbf{f}(x_i) = \mathbf{F}(x_i + \frac{\Delta x}{2}) - \mathbf{F}(x_i - \frac{\Delta x}{2}) \quad (25)$$

These relations can be used to link the primitive function  $\mathbf{F}$  to the flux integrals  $d\mathbf{f}_i^{\pm}$ :

$$\begin{aligned} d\mathbf{f}_i^+ &= \mathbf{f}_i^+ - \mathbf{f}_{i-1}^+ \\ &= \mathbf{F}^+[x_{i+\frac{1}{2}}, x_{i-\frac{1}{2}}] - \mathbf{F}^+[x_{i-\frac{1}{2}}, x_{i-\frac{3}{2}}] \\ &= 2\mathbf{F}^+[x_{i+\frac{1}{2}}, x_{i-\frac{1}{2}}, x_{i-\frac{3}{2}}] \end{aligned} \quad (26)$$

$$\begin{aligned} d\mathbf{f}_i^- &= \mathbf{f}_{i+1}^- - \mathbf{f}_i^- \\ &= \mathbf{F}^-[x_{i+\frac{3}{2}}, x_{i+\frac{1}{2}}] - \mathbf{F}^-[x_{i+\frac{1}{2}}, x_{i-\frac{1}{2}}] \\ &= 2\mathbf{F}^-[x_{i+\frac{3}{2}}, x_{i+\frac{1}{2}}, x_{i-\frac{1}{2}}] \end{aligned} \quad (27)$$

with:

$$\begin{aligned} d\mathbf{f}_i^- &= \int_{\Gamma_i} \partial_U \hat{\mathbf{E}}^-(\xi_{i+\frac{1}{2}}) dU \\ d\mathbf{f}_i^+ &= \int_{\Gamma_{i-1}} \partial_U \hat{\mathbf{E}}^+(\xi_{i-\frac{1}{2}}) dU \end{aligned}$$

and  $\mathbf{F}[x_{i+k}, \dots, x_i]$  the  $k$ -th divided difference defined as:

$$\mathbf{F}[x_{i+k}, \dots, x_i] = \frac{1}{k} (\mathbf{F}[x_{i+k}, \dots, x_{i+1}] - \mathbf{F}[x_{i+k-1}, \dots, x_i])$$

In the derivation of the higher order accurate scheme the specific functional form of the functions  $\mathbf{f}^{\pm}$  and  $\mathbf{F}^{\pm}$  is not needed, only their divided differences.

The primitive function  $\mathbf{F}$  is now approximated with a fifth order Newton polynomial using the divided differences defined in equations (26-27). The higher order divided differences can be easily obtained by further extending the divided difference tables given by equations (26-27). The nodes in the Newton interpolation are chosen such that an upwind biased scheme is obtained. This relation is then differentiated at  $x_{i+\frac{1}{2}}$ :

$$\begin{aligned} \partial_{\xi} \mathbf{F}^+(x_{i+\frac{1}{2}}) &= \mathbf{F}^+[x_{i+\frac{1}{2}}, x_{i-\frac{1}{2}}] + \mathbf{F}^+[x_{i+\frac{1}{2}}, \dots, x_{i-\frac{3}{2}}] \\ &\quad + 2\mathbf{F}^+[x_{i+\frac{3}{2}}, \dots, x_{i-\frac{3}{2}}] \\ &\quad - 2\mathbf{F}^+[x_{i+\frac{3}{2}}, \dots, x_{i-\frac{5}{2}}] \end{aligned} \quad (28)$$

$$\begin{aligned}
\partial_{\xi} \mathbf{F}^{-}(x_{i+\frac{1}{2}}) = & \mathbf{F}^{-}[x_{i+\frac{3}{2}}, x_{i+\frac{1}{2}}] - \mathbf{F}^{-}[x_{i+\frac{5}{2}}, \dots, x_{i+\frac{1}{2}}] \\
& + 2\mathbf{F}^{-}[x_{i+\frac{5}{2}}, \dots, x_{i-\frac{1}{2}}] \\
& + 2\mathbf{F}^{-}[x_{i+\frac{7}{2}}, \dots, x_{i-\frac{1}{2}}]
\end{aligned} \tag{29}$$

The higher order approximation to  $\partial_{\xi} \hat{\mathbf{E}}_i$  is obtained using equation (25) and adding the positive and negative contributions in equations (28-29):

$$\partial_{\xi} \hat{\mathbf{E}}_i = \partial_{\xi} \mathbf{F}(x_{i+\frac{1}{2}}) - \partial_{\xi} \mathbf{F}(x_{i-\frac{1}{2}}) \tag{30}$$

This relation is conservative, fourth order accurate, and maintains its higher order accuracy on a non-uniform grid because the change in metrical coefficients is properly taken care of by means of the Newton interpolation. It satisfies the geometrical conservation law because for each of the integrals  $\mathbf{df}_i^{\pm}$ ,  $i \in \{i-2, i+2\}$ , appearing in the divided differences, the metrics are chosen at indices  $i + \frac{1}{2}$ ,  $i \in \{i-2, i+2\}$ . The geometric conservation law then is automatically satisfied because for uniform flow each of the integrals gives a zero contribution independent of the metrical coefficients. The additional cost of computing the divided differences is negligible compared to the computation of the integrals  $\mathbf{df}^{\pm}$  and the scheme is as efficient as a scheme with analytically derived coefficients. One additional remark must be made about the first divided difference in equations (28-29). Their value is unknown, but not needed, because in equation (30) only their difference is used, which is exactly the first order contribution and given by equations (26-27).

## 2.4 Implementation of Higher Order Schemes

In order to obtain the high accuracy necessary for direct simulations a large number of grid points is required. In order to efficiently run the program with such large grids a general three-dimensional multi-block code has been written. This gives more flexibility in managing the large memory requirements and it is easier to generate grids for more complicated geometries. The inviscid contribution in the compressible Navier-Stokes equations is discretized using the procedure described in the previous sections. The viscous terms are implemented using fourth order accurate, conservative central differences for the finite difference scheme, but the viscous contribution is only second order accurate for the finite volume scheme. The development of a fourth order accurate viscous discretization for the finite volume scheme is currently in progress. Second order accurate implicit time integration is used and in order to maintain time accuracy a Newton procedure is chosen, equivalent to the one used by Rai and Moin<sup>21</sup> and Rai<sup>20</sup>. In this method the equations are discretized with all the fluxes computed at the new time level  $n+1$ . The resulting non-linear equations are linearized using a Newton procedure and the large system of linear equations is solved iteratively. In <sup>20,21</sup> the diagonal form of approximate factorization according to Pulliam and Chaussee<sup>19</sup> was chosen, which only gives a crude approximation to the solution of the linear system. In this paper a more accurate iterative scheme based on the zebra line Gauss-Seidel method is used and for each step in the Newton procedure the system is solved up to

machine accuracy. This method is used plane by plane and fits well into the Newton procedure.

The Newton procedure makes it possible to have an implicit spatial discretization which is of lower accuracy than the explicit part, but because each time step the Newton procedure is iterated time accuracy is maintained and the higher order spatial accuracy is preserved. Usually four Newton iterations are sufficient, but for convergence of the Newton scheme it is necessary to solve the linear system of the implicit time integration with high accuracy.

The Newton procedure requires the computation of the Jacobian of the flux vector, which is quite cumbersome to derive, especially for the viscous terms. Currently, both the exact Jacobian of the Osher fluxes and the approximation using the Jacobian of the Steger-Warming<sup>24</sup> flux vector splitting are used in the implicit time integration. The exact Jacobian of the Osher fluxes improves the convergence rate compared with the approximate Jacobian. It is, however, approximately three times more expensive to compute the exact Jacobian and for most cases the computing time for both schemes is about equal. For steady flows, where the Jacobian has to be updated only after a certain number of time steps the exact Jacobian is more efficient.

The boundary conditions for the Osher scheme are implemented using the procedure proposed by Osher and Chakravarty<sup>17</sup>. In this method a Riemann initial-boundary value problem is solved instead of an initial value problem, which is used in the interior of the domain. This method is very robust and elegant, but a significant effort is required to derive all relations to compute the boundary fluxes and Jacobians.

## 2.5 Results and Discussion

In this section results will be presented of two simulations of ribbon induced boundary layer instability to demonstrate the ability of the two numerical schemes discussed in this paper to accurately predict boundary layer instability and their possible use for simulations of turbulent and transitional boundary layers. Although the results in this section are all two dimensional the full three-dimensional discretization was used.

As a first step it is crucial to have extremely accurate solutions of the mean flow, which constitute the base flow for the stability calculations. In many previous studies an analytically defined mean flow was used, but this becomes difficult for flows in more general geometries. The use of an analytically defined mean flow also has as disadvantage that it does not exactly satisfy the discretized equations and will generate numerical transients.

In Figures 1 and 2 the mean flow profiles obtained with the finite difference scheme discussed in section 4 are plotted at 10 equally spaced stations with  $Re_x$ , the Reynolds number based on the distance from the nose of the plate, ranging from 50,000 to 320,000 versus the similarity parameter  $\eta = \frac{y}{x} \sqrt{Re}$ , with  $Re$  the Reynolds number based on plate length,  $x$  the streamwise distance from the nose of the plate and  $y$  the normal distance. The freestream Mach number is .08. The dimensionless normal velocity in Figure 2 is defined as:  $\hat{v} = v \sqrt{Re_x}$ . At the inlet a boundary layer

solution was specified and the grid was chosen to approximately follow the streamlines and generated with the GridGen2d package. The grid is non-orthogonal in the interior and the normal grid spacing increases downstream. In the same plot also the compressible Blasius solution is plotted and it is clear that all lines completely collapse for the mean flow streamwise component, Figure 1. The same is true for the normal velocity, Figure 2, except for the asymptotic value outside the boundary layer, which is slightly higher than the Blasius solution. This slight difference is correct because in the boundary layer solution the small displacement of the boundary layer is not accounted for. The comparison between the theoretical and numerical solutions is remarkable considering the high Reynolds number of the base flow. Especially the accurate solution of normal velocity component is noteworthy, because its value is much smaller than the streamwise component and more difficult to compute. Most tests of numerical schemes on a flat plate boundary layer use a Reynolds number which is considerably lower and only show the streamwise velocity component. Accurate boundary layer profiles were already obtained with 35 points in the normal direction, but the total grid consisted of  $336 \times 80$  points to provide sufficient accuracy for the direct simulations, discussed in the next part. This demonstrates that the Osher scheme is considerably more accurate in boundary layers than schemes based on flux vector splitting, Van Der Vegt<sup>26</sup>.

The mean flow profiles obtained with the finite volume scheme discussed in section 3 are similar, but the finite volume scheme turns out to be more sensitive to the smoothness of the grid on highly stretched meshes. Care has to be taken that the grid for the finite volume scheme is at least three times differentiable. The sensitivity to the grid smoothness of the finite volume scheme is caused by the fact that in the reconstruction process the cell averaged flow field  $\bar{U}_{i,j,k}$  in equation (17) is multiplied with the cell volume. The cell volume changes much more rapidly than the grid spacing. The finite difference scheme is less sensitive to the grid, because it uses dimensional splitting and depends therefore only on the smoothness of the grid in each coordinate direction. The sensitivity to the grid smoothness of the finite volume scheme certainly needs further attention before this scheme can be used for more general applications.

Another problem when using a high order accurate scheme to obtain steady solutions for high Reynolds number flows is the slow convergence to steady state. Due to the minimal amount of numerical dissipation it takes a significant amount of computing time to eliminate all transients. Convergence to steady state was improved using an implicit scheme and CFL numbers between 1000 and 5000 were used to obtain steady results with the fourth order accurate schemes. In order to further speed up convergence the computations were started with a first order accurate scheme till the residue was significantly reduced, followed by the fourth order scheme till machine accuracy was obtained.

The first simulation of boundary layer instability is a comparison with the direct simulations of incompressible flow about a flat plate done by Fasel et al.<sup>5</sup>. All parameters were chosen as close as possible to the one used in their computations. The free stream Mach number was .08 and the Reynolds number based on flat plate

length  $Re$  was  $100.000/m$ . The plate started at  $x = .5$  and ended at  $x = 3.2$  and was extended with a buffer region with slowly increased grid spacing to  $x = 8.0$  for the finite difference calculations and to  $x = 5.0$  for the finite volume calculations. The plate has 300 grid points in streamwise direction and the buffer region consisted of 36 points. The purpose of the buffer region was to damp out transients and thereby minimizing reflections. Accurate non-reflecting boundary conditions for the compressible Navier-Stokes equations are not yet available.

First a steady boundary layer solution was computed and the maximum pointwise value of the residual was less than  $10^{-8}$ . The flow was then disturbed in a small region by periodic suction and blowing. The suction strip started at  $x_1 = .908$  and ended at  $x_2 = 1.13$ . The amplitude is given by the relation:

$$f_v = A \sin(\tilde{x})(1 - \cos(\tilde{x})) \sin(\beta t)$$

with:

$$\tilde{x} = \frac{2\pi(x - x_1)}{x_2 - x_1}$$

The amplitude  $A$  for the computations is .0001. The parameter  $\beta$  is equal to 10, which results in a frequency parameter  $F = 100$ . Here the frequency parameter is defined as:  $F = \beta \times 10^6 / Re$ .

The blowing and suction starts in the region where the boundary layer is linearly stable. This has as benefit that transients, which occur due to the suction and blowing, will damp out and a cleaner Tollmien-Schlichting wave is obtained. The time trace of all the flow variables along a line which corresponds to the position of maximum amplification was written to a file and Fourier analyzed. The Fourier analyzed signal was then used to compute the growth rate of the TS wave. Figure 3 shows the comparison of the growth rate  $-\alpha_i$  of the streamwise disturbances with the results of Fasel et al.<sup>5</sup>. A negative value of the growth rate means that the disturbance is growing. The large initial disturbances are caused by the suction and blowing, but after  $x = 1.4$  the result from the finite difference scheme compares well with that from Fasel et al.<sup>5</sup>, which also agree with the theoretical non-parallel results of Gastner. The finite volume results are slightly less accurate than the finite difference results. This is partly due to the fact that the viscous contribution in the finite volume scheme is only second order accurate. The second simulation, a boundary layer at  $M = 0.5$ , which is at a considerably higher Reynolds number gives virtually identical results for both methods. The growth rates of the disturbances of the normal velocity component, Figure 4, also compare well with the results from Fasel et al.<sup>5</sup>, but the curves are shifted slightly upstream. This component becomes unstable earlier in the simulation than that of Fasel et al.<sup>5</sup>. The growth rate of the normal velocity disturbances, however, strongly depends on the vertical position and further research is required to obtain more accurate results for this component. Contrary to the streamwise component there are no theoretical results for the growth rate of the normal velocity disturbances.

The same procedure as used for the  $M = .08$  boundary layer was used for a simulation of a flat plate boundary layer at Mach number  $M = .5$ . The parameters were chosen equal to the calculations done by Bertolotti<sup>2</sup> using the linear

Parabolic Stability Equations (PSE). This method takes the non-parallel effects of the boundary layer into account contrary to linear stability theory. The Reynolds number based on plate length was  $500.000/m$ . The simulations with the finite difference scheme were done on two grids. The coarse grid has  $336 \times 80$  grid points and the plate started at  $x = .5$  and ended at  $x = 3.2$ . Suction and blowing was started at  $x = .725$  and ended at  $x = .86$ . The second grid consisted of  $436 \times 80$  points and the plate started at  $x = .5$  and ended at  $x = 2.3$ . Suction and blowing started at  $x = .5225$  and ended at  $x = .6125$ . The buffer region ends at  $x = 8$  for the coarse grid and at  $x = 5.1$  for the fine grid. The first grid has about 10 grid points per TS wave and the fine grid has 20 point per wavelength. The frequency parameter  $F$  was equal to 20 and the free stream temperature  $T_\infty = 206K$ .

This case is more difficult than the incompressible simulation because of the higher Reynolds number and many more TS wave periods have to be covered. The initial amplitude of the disturbances  $A$  was .0001 and Figure 5 shows a contour plot of the pressure on the fine grid. The regular pattern of the TS waves is clearly visible. The initial amplitude is very small and decays because the disturbance is in the stable part of the boundary layer. More downstream the disturbance grows very regularly, saturates and decays. The decay is partly physical and at the end of the plate further increased by the coarsening of the grid to minimize reflections from the outflow boundary.

Figures 6 and 7 show the spatial growth rates obtained with the finite difference and finite volumes scheme on the fine grid and compare them with the PSE results of Bertolotti<sup>2</sup>. They are virtually identical till the disturbances reach the buffer region, where the growth rate suddenly changes and the Tollmien-Schlichting wave rapidly decays. The CPU time used for both schemes was approximately equal for the implicit calculations, with the finite volume scheme 1.1 times more expensive than the finite difference scheme. The approximation of the flux integral in the finite volume method, equation (20), however, is crucial to minimize computing time for the finite volume scheme. These plots also show that the buffer region is quite effective in minimizing reflections from the outer wall. The simulation was continued in all cases till the leading wave front would have travelled at least twice the length of the domain. The sound waves, which travel faster, then would have a chance to reflect several times through the domain, with no apparent effect on the growth rates. The use of a buffer region is, however, not without pitfalls. One has to be very careful to create a smooth transition with the flow domain.

The accuracy of the simulation also depends on the time step and time integration scheme used. The time integration method is a second order 3 point implicit multi-step scheme. Four Newton iterations were used to improve time accuracy of the implicit scheme. The residual decreased two orders of magnitude and was approximately  $5 \times 10^{-7}$  at the end of the Newton iterations. Figures 8 and 9 show the growth rate of the normal and streamwise velocity component for simulations with different time steps using the finite volume scheme, but all on the  $436 \times 80$  grid. The time step  $\Delta t$  is equivalent with a CFL number 80. As can be seen from these plots the accuracy is bounded by the time integration scheme and not by the

spatial resolution. Significant improvement should be obtained by using a higher order accurate time integration method.

The results of computations with the finite difference scheme on the coarse and fine grid are presented in Figure 10. They show that the coarse grid simulation is underresolved, while the fine grid simulation compares well with the PSE results of Bertolotti<sup>2</sup>. It should be emphasized that it is very important to perform the computations on different grid levels to test accuracy, especially when there are no theoretical results available. The coarse grid results do show that the flow becomes unstable but the growth rate is not correct and can only be checked by increasing the resolution.

Finally, the effect of the location of suction and blowing was investigated. Figure 11. shows results of simulations with the finite difference scheme with suction and blowing applied directly after the inflow boundary or just before the region where the flow becomes unstable. It can be seen that the growth rates are not sensitive to the location of suction and blowing.

To summarize the results discussed in this section it can be stated that both the finite volume and finite difference schemes can be used for simulations of boundary layer instability. The results for the incompressible flow were slightly better for the finite difference scheme, but this can be attributed to the second order viscous contribution in the finite volume scheme. The biggest advantage of the finite difference scheme is that it is less sensitive to grid stretching, but this scheme is not easily extended to flows with sonic points, because it will lose accuracy at these points, which is not the case for the finite volume scheme. It was also found that using a higher order accurate time integration method will be more efficient and extreme care has to be taken to guarantee numerical accuracy, preferably by using grids with different resolution.

### 3. References

- <sup>1</sup> Abgrall, R., "On Essentially Non-Oscillatory Schemes on Unstructured Meshes: Analysis and Implementation", ICASE Report 92-74, (1992).
- <sup>2</sup> Bertolotti, F. P., "Linear and Nonlinear Stability of Boundary Layers with Streamwise Varying Properties", Diss., Ohio State University, Columbus, Ohio, (1990).
- <sup>3</sup> Bestek, H., Thumm, A. and Fasel, H., "Direct Numerical Simulation of the Three-Dimensional Breakdown to Turbulence in Compressible Boundary Layers", Proceedings 13th International Conference on Numerical Methods in Fluid Dynamics", Rome, (1992).
- <sup>4</sup> Casper, J. and Atkins, H.L., "A Finite Volume High-Order ENO Scheme for Two-Dimensional Hyperbolic Systems", Journal of Computational Physics, **106**, pp. 62-76, (1993).
- <sup>5</sup> Fasel, H. F., Rist, U. and Konzelmann, U., "Numerical Investigation of the Three-Dimensional Development in Boundary Layer Transition", AIAA Journal, **28**, pp. 29-37, (1990).

- <sup>6</sup> Godunov, S.K., "Difference Method of Numerical Computations of Discontinuous Solutions in Hydrodynamic Equations", *Matematicheskiy Sbornik*, **47**, pp. 271-306, (1959), Translated US Joint Publ. Res. Service, JPRS 7226, (1969).
- <sup>7</sup> Gottlieb, D. and Turkel, E., "Dissipative Two-Four Methods for Time Dependent Problems", *Mathematics of Computation*, **30**, pp. 703-723, (1976).
- <sup>8</sup> Harten, A. and Chakravarthy, S.R., "Multi-Dimensional ENO Schemes for General Geometries", ICASE Report 91-76, (1991).
- <sup>9</sup> Harten, A., Osher, S., Engquist, B. and Chakravarthy, S.R., "Uniformly High Order Accurate Essentially Non-Oscillatory Schemes III", *Journal of Computational Physics*, **71**, pp. 231-303, (1987).
- <sup>10</sup> Herbert, Th., "Secondary Instability of Boundary Layers", *Annual Review of Fluid Mechanics*, **20**, pp. 487-526, (1988).
- <sup>11</sup> Laurien, E. and Kleiser, L., "Numerical Simulation of Boundary-Layer Transition and Transition Control", *Journal of Fluid Mechanics*, **199**, pp. 403-440, (1989).
- <sup>12</sup> Lax, P. and Wendroff, B., "Systems of Conservation Laws", *Communications on Pure and Applied Mathematics*, **13**, pp. 217-237, (1960).
- <sup>13</sup> Lele, S. K., "Compact Finite Difference Schemes with Spectral-like Resolution", *Journal of Computational Physics*, **103**, pp. 16-42, (1992).
- <sup>14</sup> Lee, S., Moin, P. and Lele, S. K., "Interaction of Isotropic Turbulence with a Shock Wave", Thesis, Stanford University, Report TF-52 Thermosciences Division, Dept. Mech. Eng., (1992).
- <sup>15</sup> Mack, L. M., "Boundary Layer Stability Theory", in "Special Course on Stability and Transition of Laminar Flow", AGARD Report 709, (1984).
- <sup>16</sup> Maestrello, L., Bayliss, A. and Krishnan, R., "Numerical Study of Three-Dimensional Spatial Instability of a Supersonic Flat Plate Boundary Layer", ICASE Report 89-74, (1989).
- <sup>17</sup> Osher, S. and Chakravarthy, S.R., "Upwind Schemes and Boundary Conditions with Applications to Euler Equations in General Geometries", *Journal of Computational Physics*, **50**, pp. 447-481, (1983).
- <sup>18</sup> Osher, S. and Solomon, F., "Upwind Difference Schemes for Hyperbolic Systems of Conservation Laws", *Mathematics of Computation*, **38**, pp. 339-374, (1982).
- <sup>19</sup> Pulliam, T. H. and Chaussee, D. S., "A Diagonal Form of an Implicit Approximate Factorization Algorithm", *Journal of Computational Physics*, **39**, (1981).
- <sup>20</sup> Rai, M. M., "Navier-Stokes Simulations of Blade-Vortex Interaction using High-Order Accurate Upwind Schemes", AIAA paper 87-0543, (1987).
- <sup>21</sup> Rai, M. M. and Moin, P., "Direct Numerical Simulation of Transition and Turbulence in a Spatially Evolving Boundary Layer", AIAA paper 91-1607-CP, (1991).
- <sup>22</sup> Roe, P. L., "Approximate Riemann Solvers, Parameter Vectors and Difference Schemes", *Journal of Computational Physics*, **43**, pp. 357-372, (1981).



- <sup>23</sup> Shu, C.-W. & Osher, S., "Efficient Implementation of Essentially Non-Oscillatory Shock Capturing Schemes, II", *Journal of Computational Physics*, **83**, pp. 32-78, (1989).
- <sup>24</sup> Steger, J.L. and Warming, R.F., "Flux Vector Splitting of the Inviscid Gas-dynamic Equations with Application to Finite-Difference Methods", *Journal of Computational Physics*, **40**, pp. 263-293, (1981).
- <sup>25</sup> Van Der Vegt, J.J.W., "ENO-Osher Schemes for Euler Equations", AIAA Paper 93-0335, (1993).
- <sup>26</sup> Van Der Vegt, J.J.W., "Assessment of Flux Vector Splitting for Viscous Compressible Flows", AIAA Paper 91-0243, (1991).
- <sup>27</sup> Van Leer, B., "Towards the Ultimate Conservative Difference Scheme V. A Second Order Sequel to Godunov's Method", *Journal of Computational Physics*, **32**, pp. 101-136, (1979).
- <sup>28</sup> Van Leer, B., "Flux Vector Splitting for the Euler Equations", *Proc. 8th Int. Conf. on Num. Meth. in Fluid Dyn.*, Berlin, Springer Verlag, (1982).
- <sup>29</sup> Vinokur, M., "An Analysis of Finite-Difference and Finite-Volume Formulations of Conservation Laws", *Journal of Computational Physics*, **81**, pp. 1-52, (1989).

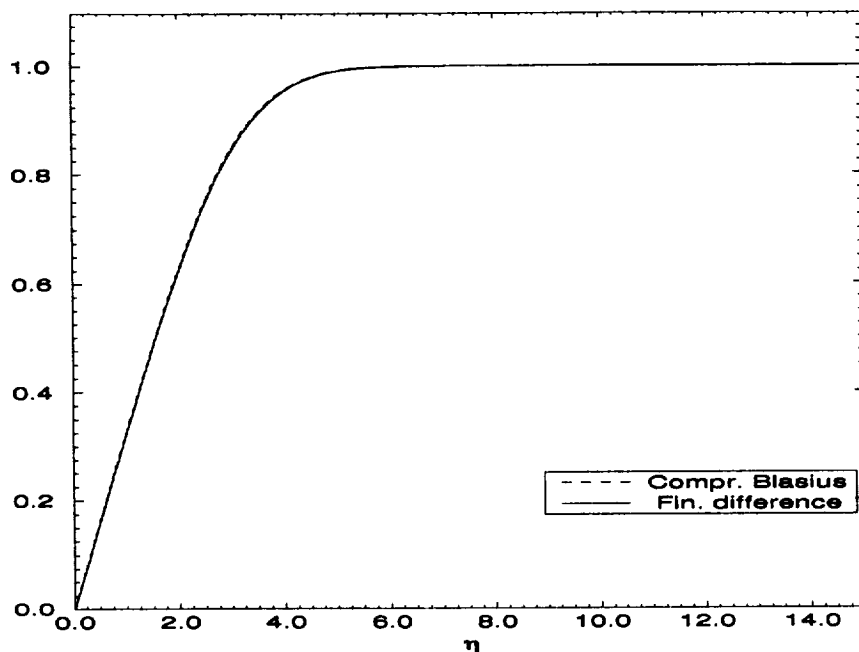


**Figure 1.** Streamwise velocity  $U$  at 10 equally spaced stations,  $Re_x = 50.000 - 320.000$ ,  $M_\infty = .08$ , versus similarity parameter  $\eta = \frac{y}{x}\sqrt{Re}$ , compared with compressible Blasius solution (dashed line).

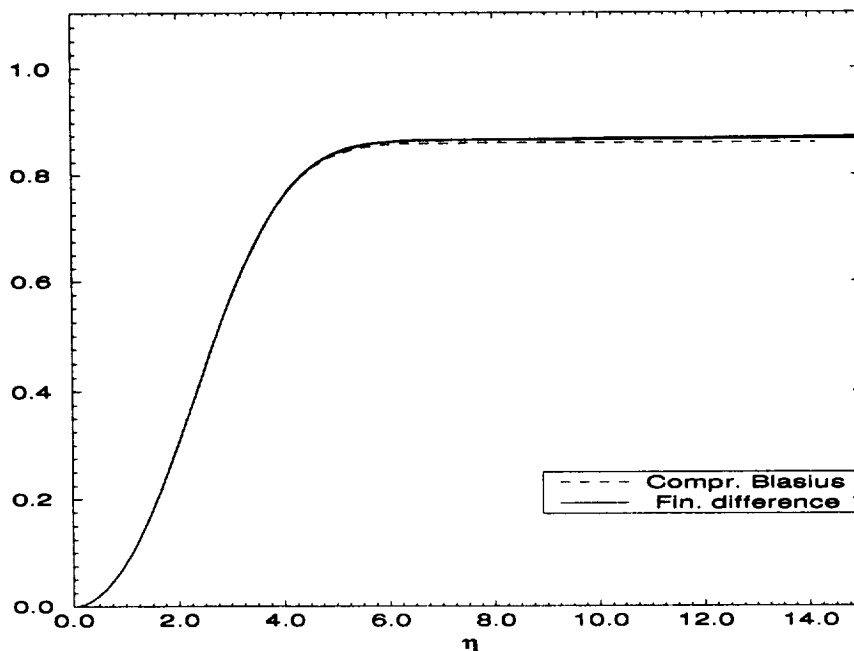


**Figure 2.** Normal velocity  $V\sqrt{Re_x}$  at 10 equally spaced stations,  $Re_x = 50.000 - 320.000$ ,  $M_\infty = .08$ , versus similarity parameter  $\eta = \frac{y}{x}\sqrt{Re}$ , compared with compressible Blasius solution (dashed line).

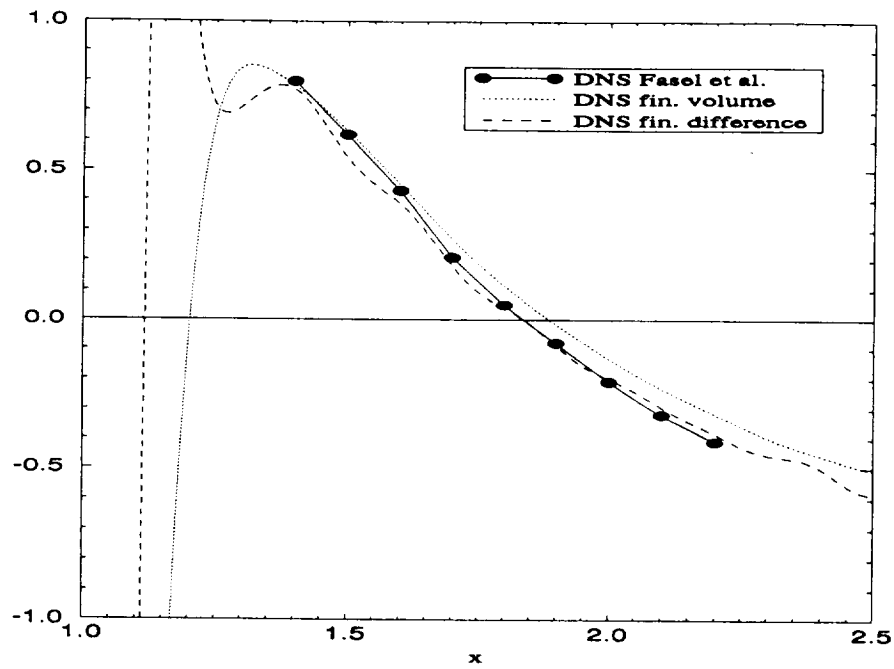


**Figure 3.** Spatial growth rate  $-\alpha_i$  of streamwise velocity disturbances compared with results from Fasel et al.<sup>5</sup>.  $M_\infty = .08$

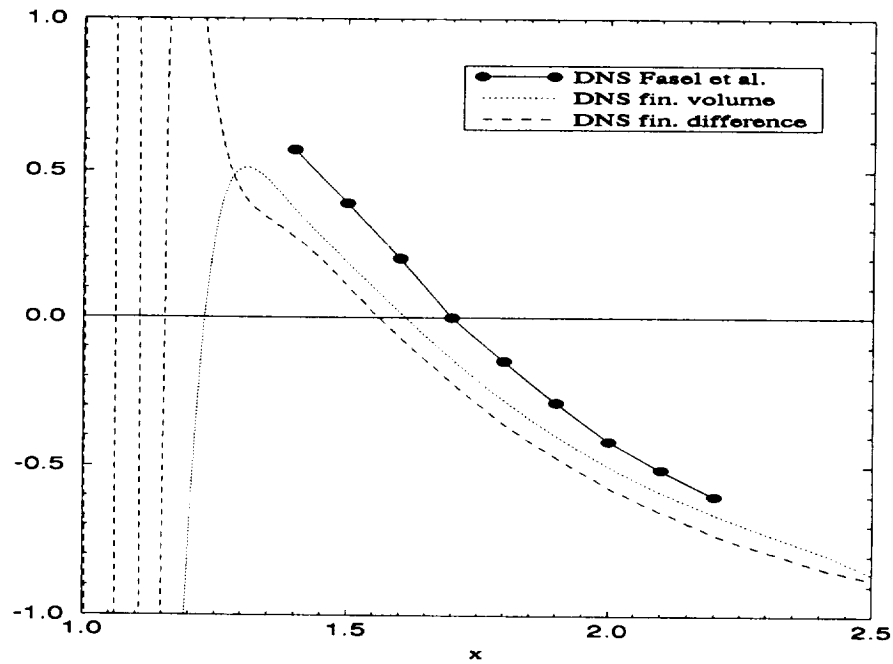


**Figure 4.** Spatial growth rate  $-\alpha_i$  of normal velocity disturbances compared with results from Fasel et al.<sup>5</sup>.  $M_\infty = .08$

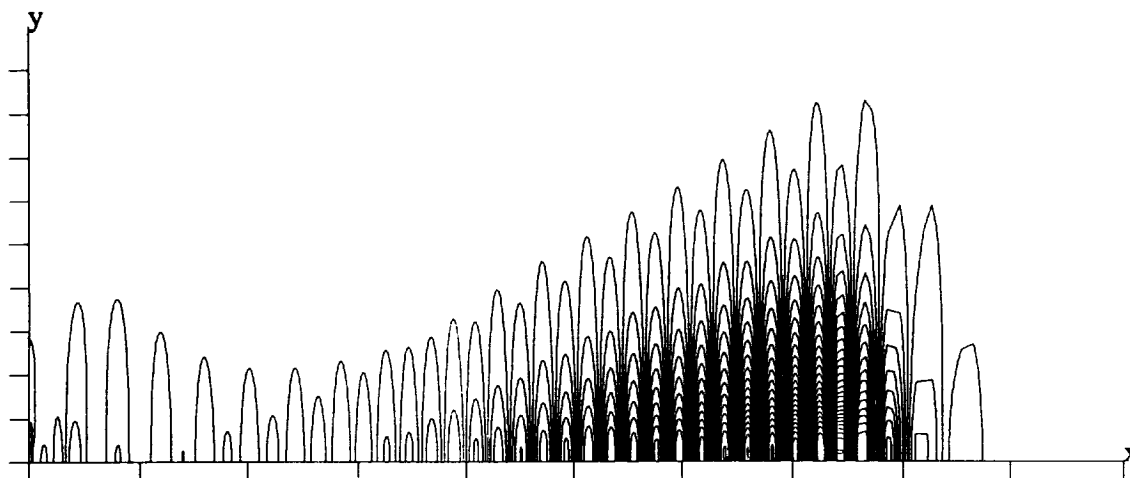


**Figure 5.** Pressure contours in flat plate boundary layer,  $M_\infty = .5$ , initial amplitude suction and blowing at wall .0001.

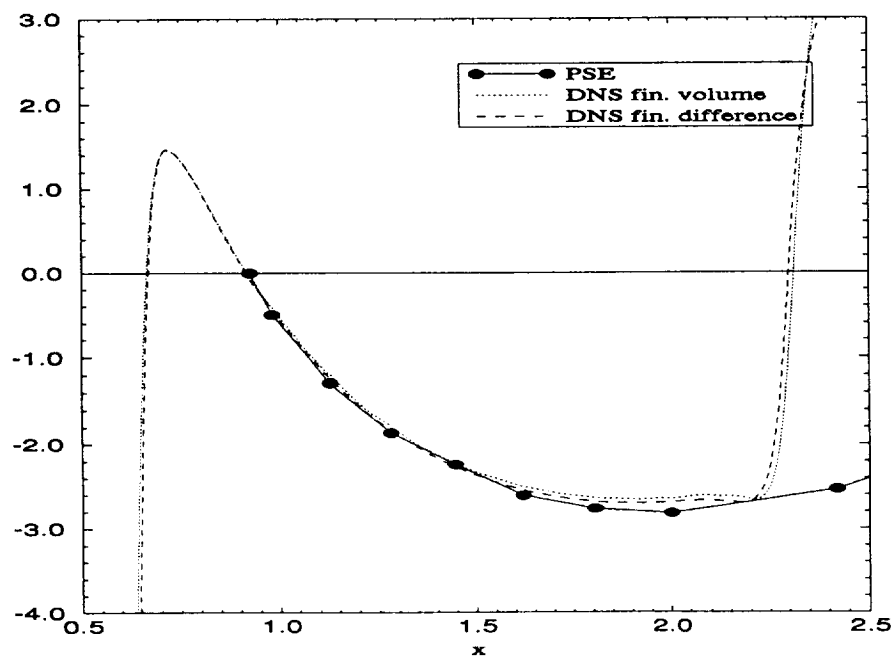


**Figure 6.** Spatial growth rate  $-\alpha_i$  of streamwise velocity disturbances using finite volume and finite difference schemes compared with PSE results Bertolotti<sup>2</sup>,  $M_\infty = .5$

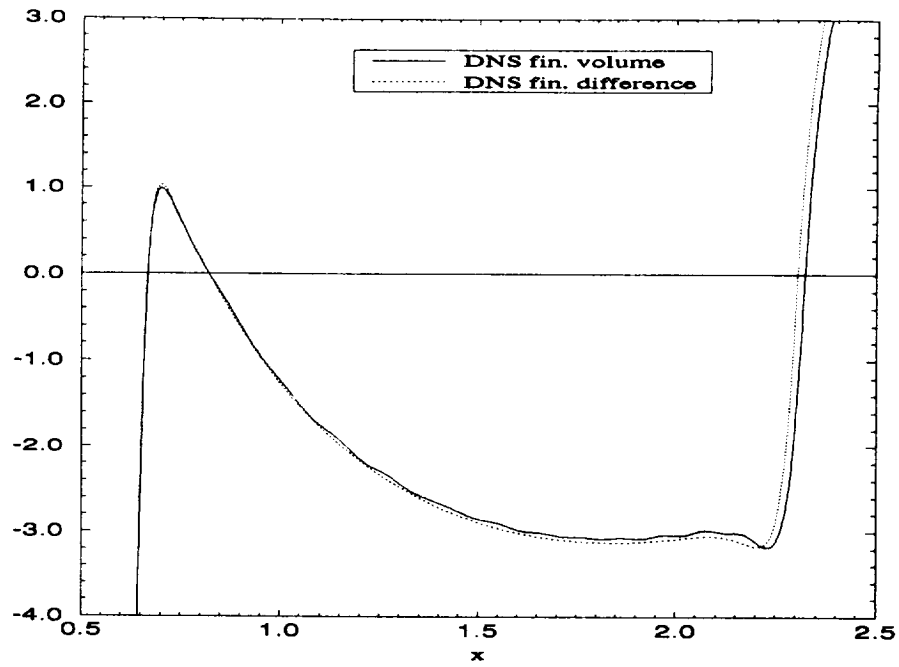


Figure 7. Spatial growth rate  $-\alpha_i$  of normal velocity disturbances using finite volume and finite difference schemes compared with PSE results Bertolotti<sup>2</sup>,  $M_\infty = .5$

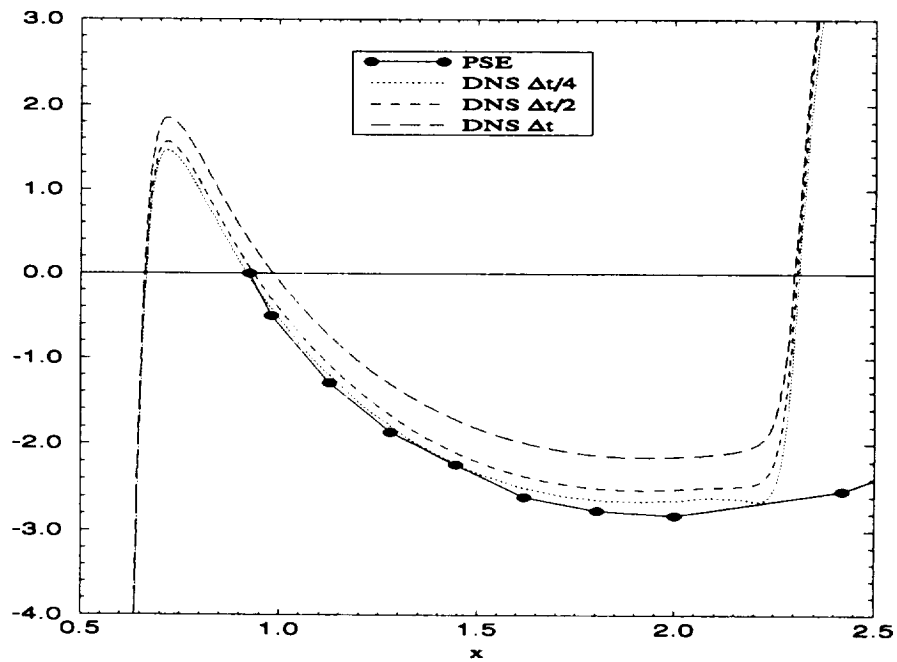
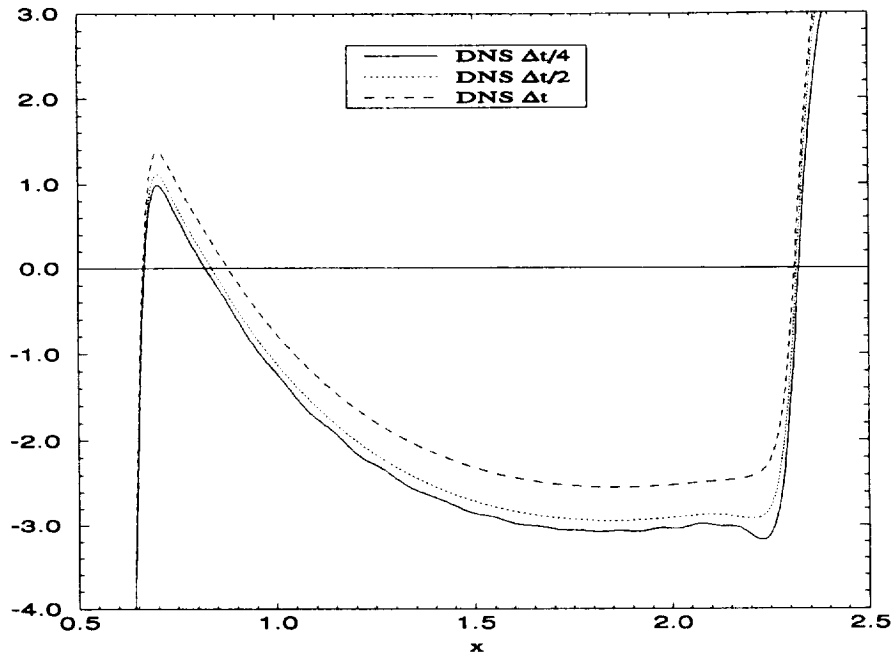
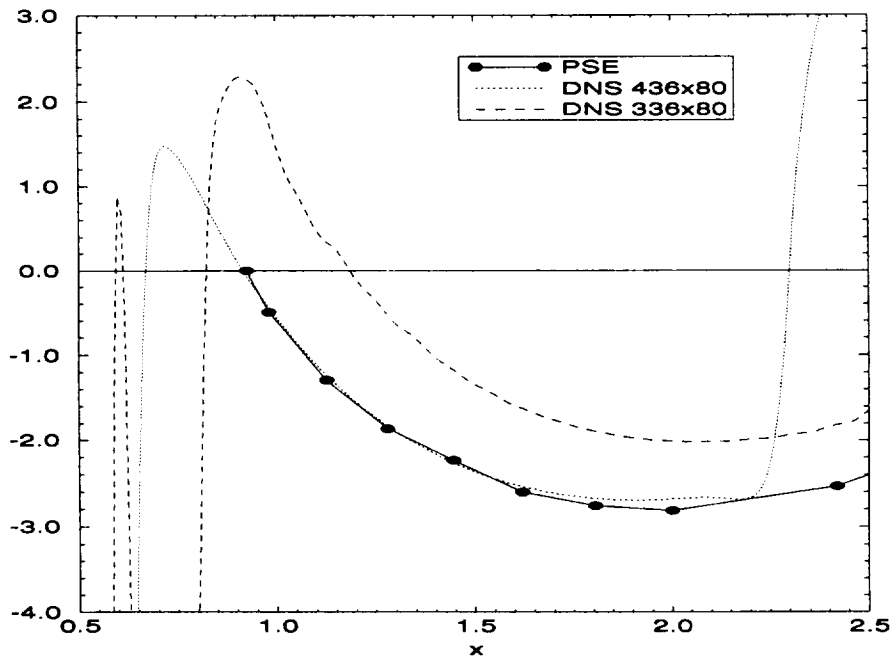


Figure 8. Spatial growth rate  $-\alpha_i$  of streamwise velocity disturbances using finite volume scheme with different time steps,  $M_\infty = .5$



**Figure 9.** Spatial growth rate  $-\alpha_i$  of normal velocity disturbances using finite volume scheme with different time steps,  $M_\infty = .5$



**Figure 10.** Spatial growth rate  $-\alpha_i$  of streamwise velocity disturbances using finite difference scheme on coarse and fine grid,  $M_\infty = .5$

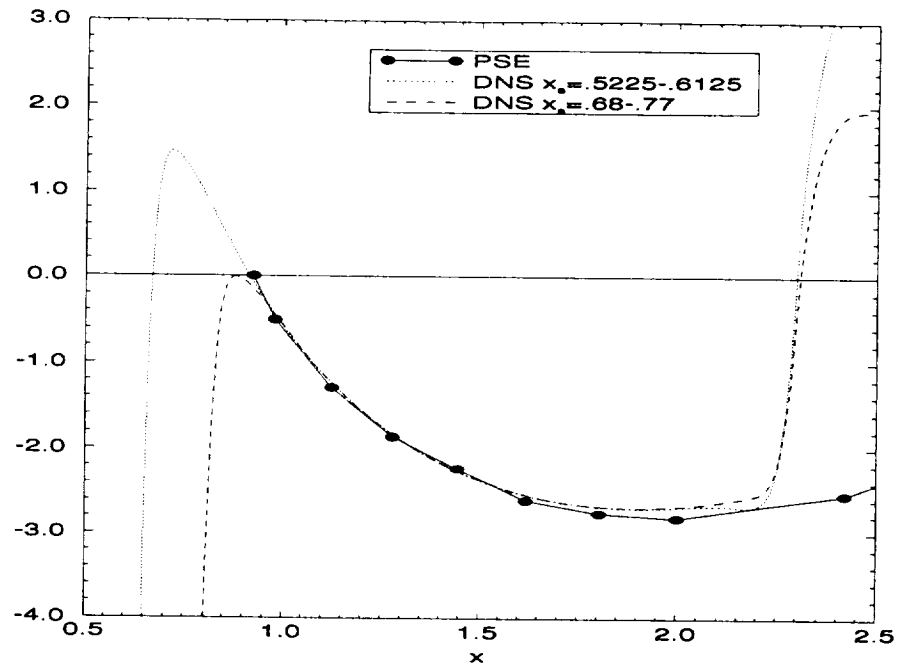


**Figure 11.** Spatial growth rate  $-\alpha_i$  of streamwise velocity disturbances using finite difference scheme for different locations wall suction-blowing,  $M_\infty = .5$





# Calculation of Waves in Fluids Using A High-Order Compact Difference Scheme

Sheng-Tao Yu

## 1. Motivation and Objective

The unsteady Euler equations are solved by a sixth-order compact difference scheme combined with a fourth-order Runge-Kutta method. First, the accuracy of the numerical scheme is assessed by Fourier analysis of the fully discretized, two-dimensional Euler equations. A close form of the amplification factors and their corresponding dispersion correlations are derived. The numerical dissipation, dispersion, and anisotropic effects are assessed. It is found that the CFL limit for stable calculations is about 0.8. For CFL number equal to 0.6, the smallest wave length which is resolved without numerical damping is about 6 to 8 grid nodes. For phase speed in the same order of acoustic waves, the corresponding time period is resolved by about 200 to 300 time steps. Three numerical examples of waves in fluid flows are included: (1) sound propagation in a linear shear layer posed by Pridmore-Brown, (2) linear wave growth in a two-dimensional, compressible free shear layer, and (3) eddy-pairing in a compressible free shear layer perturbed by two frequencies. The results compare favorably to the analytical solutions for all three cases. While analytical solutions of linearized flow equations are indispensable, the adopted finite difference scheme provides comparable accuracy in simulating wave motions in the linear regime and beyond.

## 2. Work Accomplished

We study the numerical characteristics when using the sixth-order compact differencing (CD6) combined with a fourth-order Runge-Kutta method (RK4) to solve the two-dimensional Euler equations for simulating wave motions in fluid flows. For multiple dimensional simulations, anisotropic effect in addition to the dissipation and dispersion errors must be assessed to estimate the accuracy of the numerical scheme. To this end, Fourier analysis of the fully discretized, two-dimensional Euler equations must be performed.

In our previous work [2], a one-dimensional wave equation was adopted as a model upon which Fourier analysis was performed to obtain the CFL limits and dispersion correlations. Since one can perform similarity transformation to decouple the one-dimensional Euler equations to three scalar wave equations, this approach is appropriate for one-dimensional calculations. On the contrary, no similarity transformation is available to decouple the two-dimensional Euler equations. Therefore, the adoption of a two-dimensional wave equation as a model of the Euler equations for Fourier analysis can not be justified. In this paper, we apply Fourier analysis directly to the fully discretized, two-dimensional Euler equations. A close form

of the amplification factors and their corresponding dispersion correlations are derived. Consequently, the numerical accuracy in terms of dissipation, dispersion, and anisotropic errors can be assessed.

To demonstrate the performance of the numerical method, three numerical examples are included in the present paper:

- (1) Sound waves propagation in a linear shear layer. The Euler solver is applied to simulate the problem proposed by Pridmore-Brown [4]. The wave motion is neutrally stable and the harmonic content of this flow field is limited to one frequency mode. From the finite difference solution, the eigenfunctions are reconstructed by Fourier transformation and compared favorably with the analytical solution.
- (2) Linear wave growth in a compressible free shear layer. We first solved the compressible Rayleigh equation for the flow conditions of concern and obtain the full spectrum of viable eigenvalues and eigenfunctions. We then arbitrarily choose an eigenvalue of relatively long wave length and smaller growth rate. The corresponding eigenfunctions and frequency are used to perturb the prescribed mean flow at the upstream. The growth rate of the wave in the down stream region is then obtained from the numerical results and compared with the analytical solution. The simulation is restricted to the linear regime, therefore, similar to Case 1, the harmonic content of this case is limited to one Fourier mode.
- (3) Nonlinear mechanisms of a compressible free shear layers. In this case, we focus on the most unstable mode for the mean flow conditions of interest. Several perturbation schemes are applied: single frequency perturbation with small amplitude (weakly nonlinear), single frequency perturbation with relatively large amplitude to show the eddy roll-up, and double frequencies perturbation with the most unstable mode and its subharmonic to show the eddy pairing.

In all cases, numerical results show favorable comparison to the analytical solutions of the Rayleigh equation in the linear regime. For nonlinear wave motions, numerical solution show crisp resolution of the vortex roll-up and pairing.

## 2.1 Numerical Method

The two-dimensional Euler equations in Cartesian coordinates can be cast into a vector form:

$$\frac{\partial \mathbf{Q}}{\partial t} + \frac{\partial \mathbf{E}}{\partial x} + \frac{\partial \mathbf{F}}{\partial y} = 0, \quad (1)$$

where  $\mathbf{Q}$  is the unknown vector and  $\mathbf{E}$  and  $\mathbf{F}$  are inviscid fluxes in the  $x$  and  $y$  directions, respectively. A RK4 method is applied as the temporal discretization and a CD6 scheme is applied to the spatial discretization.

The adopted RK4 method is originally attributed to Kutta [5] for solving ODEs. Previously, Jameson et al. [6] used this scheme to solve the flow equations. The algorithm is given by

$$\begin{aligned}
\mathbf{Q}^1 &= \mathbf{Q}^n + \frac{\Delta t}{2} \mathbf{R}^n, \\
\mathbf{Q}^2 &= \mathbf{Q}^n + \frac{\Delta t}{2} \mathbf{R}^1, \\
\mathbf{Q}^3 &= \mathbf{Q}^n + \Delta t \mathbf{R}^2, \\
\mathbf{Q}^{n+1} &= \mathbf{Q}^n + \frac{\Delta t}{6} (\mathbf{R}^n + 2\mathbf{R}^1 + 2\mathbf{R}^2 + \mathbf{R}^3).
\end{aligned} \tag{2}$$

The superscripts 1, 2, and 3 denote intermediate steps of the RK method.  $\mathbf{R}^i$  is the numerical value of  $\partial \mathbf{E} / \partial x + \partial \mathbf{F} / \partial y$  calculated from the flow properties at step  $i$ . As shown in our previous paper [2], the algorithm is fourth-order accurate for nonlinear equations and is suitable for the calculations of unsteady flows.

A CD6 scheme is used for spatially differencing the inviscid fluxes. According to Hermite's generalization of the Taylor's series [7], one can get

$$\begin{aligned}
&u'_{i-1} + 3u'_i + u'_{i+1} \\
&= \frac{1}{12\Delta x} (u_{i+2} + 28u_{i+1} - 28u_{i-1} - u_{i-2}) + O(\Delta x^6),
\end{aligned} \tag{3}$$

where  $u$  could be any flow property, and the superscript ' represents the spatial derivatives. The treatment of the boundary condition is similar to that in our previous work [2], namely, the fourth-order compact scheme is used at locations one grid node away from the boundary, and a third-order biased scheme is used at the boundary.

Note that the method of characteristic (MOC) type non-reflecting boundary condition [2,8] incorporated with the one-sided biased difference is used at the computational boundary. Therefore, all numerical waves pass through the boundary without reflection. In addition, numerical grids are stretched near boundaries to enlarge the computational domain and enhance the non-reflection effect. As a result, lowering the order of the spatial discretization in the vicinity of the computational boundary is not detrimental to the numerical accuracy at interior nodes. For details of the non-reflective boundary conditions and their implementation into the present finite difference scheme, we refer the interested readers to Ref. [2]. The application of the CD6 scheme with the aforementioned boundary conditions involves the inversion of a scalar tridiagonal matrix. The inversion of the matrix incurs little penalty in terms of CPU time.

## 2.2 Fourier Analysis

Fourier analysis of a two-dimensional, finite difference scheme assumes that the solution is periodic over an infinite domain with the spatial period equal to the computational domain ( $L_x$  and  $L_y$ ) in  $x$  and  $y$  directions, respectively. The computational domain is decomposed into  $K_x$  and  $K_y$  grid nodes in  $x$  and  $y$  directions, respectively. The harmonic content of the discretized equation is limited to the number of grid nodes used in the computational domain. A discrete solution  $\mathbf{Q}_{i,j}^n$

at a location  $(i, j)$  and time  $(n)$  is a linear combination of  $K_x$  times  $K_y$  wave modes. Fourier analysis is performed by substituting each wave mode of the discrete Fourier expansion into the discretized Euler equations to calculate the amplification matrix,  $G(p, q)$ , which is defined as

$$G(p, q) = \frac{\hat{Q}^{n+1}(p, q)}{\hat{Q}^n(p, q)}. \quad (4)$$

where  $\hat{Q}$  denotes the Fourier component of the object function  $Q$  and  $p$  and  $q$  are the wave numbers in the  $x$  and  $y$  directions, respectively. To obtain the amplification factors of the numerical scheme, one has to diagonalize  $G$  to obtain its eigenvalues. Since  $G$  is a  $4 \times 4$  matrix, we expect to obtain four amplification factors. The procedure is repeated for all wave modes, and the amplification factors over the full spectrum of the wave numbers are obtained. In this process, we map the function  $Q$  defined by the spatial coordinates  $x$  and  $y$  on the domain  $[-L_x/2, L_x/2] \times [-L_y/2, L_y/2]$  to the wave number space  $[-\pi, \pi]$  for both  $p$  and  $q$ . The amplification factors in terms of wave numbers in the first quadrant of the  $(p, q)$  plane is most representative; solutions in other quadrants are merely alias. For this reason, the results of our Fourier analyses are presented in the first quadrant of the  $(p, q)$  plane.

In what follows, the procedure to obtain the amplification factors of the Euler equations discretized by the CD6-RK4 method is illustrated. First, the generalized form of the amplification matrix  $G$  for the RK4 method, as shown in Ref. [2], is provided by

$$G = I + Z + \frac{1}{2}Z^2 + \frac{1}{6}Z^3 + \frac{1}{24}Z^4, \quad (5)$$

where  $I$  is the identity matrix.  $Z$  is the Fourier component of the spatial discretization applied to the convective terms  $(-\partial E/\partial x - \partial F/\partial y)$  in the wave number space. To proceed, we linearize the inviscid fluxes  $E$  and  $F$ , such as

$$\begin{aligned} \frac{\partial E}{\partial x} &= \frac{\partial E}{\partial Q} \frac{\partial Q}{\partial x} = A \frac{\partial Q}{\partial x}, \\ \frac{\partial F}{\partial y} &= \frac{\partial F}{\partial Q} \frac{\partial Q}{\partial y} = B \frac{\partial Q}{\partial y}, \end{aligned} \quad (6)$$

where  $A$  and  $B$  are the Jacobian matrices of the inviscid fluxes. Since the analysis is linear,  $A$  and  $B$  are assumed to be constant. As shown in our previous work [2], the discrete Fourier transformation of  $\partial Q/\partial x$  and  $\partial Q/\partial y$  is given by

$$\begin{aligned} F\left(\frac{\partial Q}{\partial x}\right) &= -Z_x = -\frac{[4 \sin(p) \cos(p) + 56 \sin(p)] \Delta t i}{12[2 \cos(p) + 3] \Delta x}, \\ F\left(\frac{\partial Q}{\partial y}\right) &= -Z_y = -\frac{[4 \sin(q) \cos(q) + 56 \sin(q)] \Delta t i}{12[2 \cos(q) + 3] \Delta x}, \end{aligned} \quad (7)$$

where  $F(\partial Q/\partial x)$  is the Fourier transformation of the spatially discretized  $\partial Q/\partial x$  and is defined as  $-Z_x$ . As a result,  $Z$  can be represented as

$$\mathbf{Z} = \mathbf{A}Z_x + \mathbf{B}Z_y. \quad (8)$$

Substitute Eqn. (8), into the amplification matrix for the RK4 method, Eqn. (5), and  $\mathbf{G}(p, q)$  is obtained for all wave numbers. The remaining task is to diagonalize  $\mathbf{G}$ .

To proceed, we perform similarity transformation of  $\mathbf{G}$  to obtain its eigenvalues as the numerical amplification factors of the adopted numerical scheme,

$$\begin{aligned} \mathbf{T}^{-1}\mathbf{G}\mathbf{T} = & \mathbf{I} + \mathbf{T}^{-1}\mathbf{Z}\mathbf{T} + \frac{1}{2}(\mathbf{T}^{-1}\mathbf{Z}\mathbf{T})^2 + \\ & \frac{1}{6}(\mathbf{T}^{-1}\mathbf{Z}\mathbf{T})^3 + \frac{1}{24}(\mathbf{T}^{-1}\mathbf{Z}\mathbf{T})^4. \end{aligned} \quad (9)$$

For completeness, the matrices  $\mathbf{T}^{-1}$  and  $\mathbf{T}$  which diagonalize  $\mathbf{G}$  are given by

$$\mathbf{T}^{-1} = \begin{pmatrix} 1 & 0 & 0 & -1/c^2 \\ 0 & \beta & -\alpha & 0 \\ 0 & \alpha/\sqrt{2} & \beta/\sqrt{2} & 1/(\sqrt{2}\rho c) \\ 0 & -\alpha/\sqrt{2} & -\beta/\sqrt{2} & 1/(\sqrt{2}\rho c) \end{pmatrix}, \quad (10)$$

$$\mathbf{T} = \begin{pmatrix} 1 & 0 & \rho/(\sqrt{2}c) & \rho/(\sqrt{2}c) \\ 0 & \beta & \alpha/\sqrt{2} & -\alpha/\sqrt{2} \\ 0 & -\alpha & \beta/\sqrt{2} & -\beta/\sqrt{2} \\ 0 & 0 & \rho c/\sqrt{2} & \rho c/\sqrt{2} \end{pmatrix}, \quad (11)$$

where  $\rho$  is density,  $c$  is the speed of sound,  $\alpha = Z_x/(Z_x^2 + Z_y^2)^{1/2}$ , and  $\beta = Z_y/(Z_x^2 + Z_y^2)^{1/2}$ . The  $\ell$ th row of  $\mathbf{T}^{-1}$  is the  $\ell$ th left eigenvector of  $\mathbf{G}$ , corresponding to the eigenvalue  $g_\ell$ . Finally, the amplification factor  $g_\ell$  is

$$\begin{aligned} g_\ell = 1 + \lambda_\ell + \frac{1}{2}\lambda_\ell^2 + \frac{1}{6}\lambda_\ell^3 + \frac{1}{24}\lambda_\ell^4, \\ \ell = 1, \dots, 4, \end{aligned} \quad (12)$$

where  $\lambda_\ell$  is the  $\ell$ th eigenvalue of the matrix  $Z_x\mathbf{A} + Z_y\mathbf{B}$  which is also diagonalized by  $\mathbf{T}^{-1}$  and  $\mathbf{T}$ , and are given by

$$\begin{aligned} \lambda_1 &= Z_x u + Z_y v, \\ \lambda_2 &= Z_x u + Z_y v, \\ \lambda_3 &= Z_x u + Z_y v + c(Z_x^2 + Z_y^2)^{\frac{1}{2}}, \\ \lambda_4 &= Z_x u + Z_y v - c(Z_x^2 + Z_y^2)^{\frac{1}{2}}. \end{aligned} \quad (13)$$

As a result, there are only three distinct amplification factors representing three kinds of numerical waves propagating in the dispersive numerical medium, namely,  $g_{1,2}$ ,  $g_3$ , and  $g_4$  waves. As shown in Eqns. (12) and (13),  $g_{1,2}$  represents the numerical waves simulating the flow velocity. Specifically, the velocity vector  $(u, v)$  is

modulated by a inner product with the vector  $(Z_x, Z_y)$  due to the spatial discretization. The numerical wave is further modulated by substituting the inner product into Eqn. (12) for the RK4 method to obtain the amplification factors. Similarly,  $g_3$  and  $g_4$  waves are the numerical counterparts of the acoustic waves superimposed on the flow motion. Unlike the flow velocity waves though, the acoustic waves propagate in all directions from a moving source and the phase speed  $c$  is modulated by the factor  $(Z_x^2 + Z_y^2)^{1/2}$ .

It is interesting to note that the implicit schemes, such as ADI and LU methods, have four distinct amplification factors due to the fact that the approximate factorization is introduced into the solution procedure for efficiently inverting the coefficient matrices. Therefore, in addition to the aforementioned modulation of the wave velocity, additional error is introduced into the numerical results and no one-to-one comparison between the physical and numerical waves such as that of the present finite difference method (Eqns. (12) and (13)) is available.

In what follows, we use the derived amplification factors to assess the numerical characteristics of the adopted scheme. To proceed, defining the amplification factors in terms of frequency,

$$g_\ell(p, q) = e^{i\omega(p, q)}, \quad (14)$$

and we can make the following interpretations:

1. Artificial Dissipation.  $\omega(p, q)$  is a complex number, i.e.,  $\omega = \alpha + i\beta$ . The imaginary part ( $\beta$ ) represents the numerical amplification, i.e.,

$$\begin{aligned} g_\ell(p, q) &= e^{i\omega} = e^{-\beta} e^{i\alpha} \\ |g_\ell(p, q)| &= e^{-\beta} \end{aligned} \quad (15)$$

When  $|g| \geq 1$ , the scheme is unstable. For calculations of unsteady flows, we want  $|g|$  to be less than and close to unity to ensure numerical stability with minimum artificial dissipation. We plot  $|g(p, q)|$  against  $p$  and  $q$  to illustrate the artificial dissipation.

2. Artificial Dispersion. According to Eqn. (15), the real part of the frequency,  $\alpha(p, q)$ , represents the artificial dispersion. Note that Fourier analysis is linear, i.e., the analytical solution is dispersionless. We plot contours of constant  $\alpha$  to show phase velocities which are then used to illustrate the artificial dissipation.
3. Artificial Anisotropy. Certain direction of wave propagation will be favored by the numerical scheme. We use various values of  $c$ ,  $u$ , and  $v$  to calculate  $g_\ell$ ,  $\ell = 2, 3, 4$  according to Eqns. (12) and (13). Changes of the flow direction ( $u$  and  $v$ ) allow us to assess the anisotropy of  $g_{1,2}$ . For the simulated acoustic ( $g_{3,4}$ ) waves, we turn off flow velocity to assess the isotropy of the acoustic waves.

Figure 1 shows the artificial dissipation of three different numerical waves represented by  $|g_{1,2}|$ ,  $|g_3|$  and  $|g_4|$ . In order to obtain the numerical values,  $u$ ,  $v$ , and

$c$  are specified. Here,  $u$  is set to be equal to  $v$  and the flow velocity is at  $45^\circ$  to the coordinate axes. The magnitude of the flow speed is set to be equal to  $c$ . As shown in the figure, there is negligible dissipation of  $g_{1,2}$  and  $g_4$ . On the contrary,  $g_3$  shows significant dissipation at moderate wave numbers. Figure 1a is repeated in 1d in a different scale to show the dissipation effect at the moderate wave numbers. The minim of  $|g|_{2,3,4}$  are 0.98, 0.51, and 0.99, respectively. Therefore, acoustic waves propagating along the same direction as the flow motion suffer from the worst dissipative error. As a result, we defined the critical CFL number by

$$\text{CFL}_c = \max \left\{ \frac{|Z_x u + Z_y v + c(Z_x^2 + Z_y^2)^{\frac{1}{2}}|, |Z_x u + Z_y v - c(Z_x^2 + Z_y^2)^{\frac{1}{2}}|}{\Delta t \sqrt{\Delta x^2 + \Delta y^2}} \right\} \quad (16)$$

For this case,  $\text{CFL}_c$  is 0.6. In Fig. 1b (the dissipation of  $g_3$ ), there is negligible dissipation in the low wave number region, i.e.,  $p, q \leq \pi/3$ . This region corresponds to waves with wave length greater than six grid nodes. Note that little dissipation is also observed in the other three corners of the same plot. For example, for  $p, q = \pi$  which is wave resolved by two grid nodes (or even-odd wave) in both  $x$  and  $y$  directions, there is essentially no artificial dissipation. Later on, we shall show that these waves are undesirable due to significant dispersive errors. Although not shown, it is noted that for  $\text{CFL}_c$  greater than 0.8,  $|g_3(p, q)|$  becomes larger than unity at certain  $p$  and  $q$  and the calculation is numerically unstable. Therefore, the  $\text{CFL}_c$  limit is 0.8 and a value between 0.5 to 0.7 is recommended for accurate calculations.

Figure 2 shows constant  $\alpha$  contours by which numerical phase velocities can be interpreted. The phase velocity vectors point to the direction normal to the contours. The distance between the consecutive contours is an indication of the magnitude of the phase velocity; increase of the distance is a decrease of the phase velocity and vice versa. Figure 2a shows the phase velocities of the  $g_{1,2}$  waves, i.e., flow velocity waves. In this case, the flow direction is  $45^\circ$ . By observation, the region in which the phase velocities are correctly simulated by the numerical scheme is circumscribed by a dashed line. Outside this region, the phase velocities are in erroneous directions. Similar to the dissipation error, there is little dispersive error for  $p, q \leq \pi/3$ . To assess the anisotropic effect, Fig. 2b shows the phase velocities of the  $g_{1,2}$  waves at  $22.5^\circ$  to the  $x$  axis. Inside the dashed line, the waves are well resolved. Again, in the low wave number region ( $p, q \leq \pi/3$ ), there is little dispersive error. Figures. 2c and 2d show the phase velocities of the simulated acoustic waves superimposed on the flow stream at  $45^\circ$ .

Perhaps, it is helpful to temporarily turn off the flow velocity to observe the acoustic velocities alone as shown in Fig. 3. Theoretically, the propagation of the acoustic waves is isotropic and is depicted by circular contours of constant  $\alpha$ . Again, the well resolved region is circumscribed by a dashed line; outside the dashed

line, acoustic waves propagate in wrong directions with erroneous magnitude. For long wave length (at least 6 grid nodes) waves, little preference of the propagation direction of the acoustic wave is observed; there is no evidence of the anisotropic error. Outside the circumscribed region, however, the figure shows an increase of separation between contours along coordinate axes to a maximum followed by a decrease. This indicates that the acoustic waves of moderately high wave numbers propagate too slowly along the numerical grid lines. At very high wave numbers, the acoustic waves travel in the opposite direction of what they should. Fortunately, for the region of  $p, q \leq \pi/3$ , these dispersive errors are negligible.

As discussed above, the CD6-RK4 scheme has no dissipative effect on the high-wave-number waves. Nevertheless, significant dispersive and anisotropic errors are associated with these highest-wave-number waves. Throughout the course of a computation, these high-wave-number waves keep propagating with erroneous directions and phase speeds and eventually destroy the solution. As shown in our previous work [2], it is appropriate to impose a small amount of high-order artificial damping to filter out these waves, at the same time keeping the resolution at low wave modes intact. The eighth-order artificial damping, defined as

$$\begin{aligned} \text{A.D.} = \frac{\eta}{8} & [-u_{i+4} - u_{i-4} + 8(u_{i+3} - u_{i-3}) \\ & - 28(u_{i+2} + u_{i-2}) + 56(u_{i+1} + u_{i-1}) - 70u_i] \end{aligned} \quad (17)$$

is recommended. In the present applications,  $\eta = 0.003$  is used.

## 2.3 Numerical Examples

### 1. Sound Wave Propagation in Linear Shear Layer

The first case is a forced two-dimensional waves propagating in a shear layer with linear velocity profile posed by Pridmore-Brown [3]. The first-order linearized Euler equations can be derived,

$$\begin{aligned} \frac{\partial \rho'}{\partial t} + U \frac{\partial \rho'}{\partial x} + \rho_o \left( \frac{\partial u'}{\partial x} + \frac{\partial v'}{\partial y} \right) &= 0, \\ \frac{\partial u'}{\partial t} + U \frac{\partial u'}{\partial x} + v' \frac{\partial U}{\partial y} + \frac{1}{\rho_o} \frac{\partial p'}{\partial x} &= 0, \\ \frac{\partial v'}{\partial t} + U \frac{\partial v'}{\partial x} + \frac{1}{\rho_o} \frac{\partial p'}{\partial y} &= 0, \end{aligned} \quad (18)$$

where  $\rho_o$  is the mean flow density and is assumed to be a constant. To close the equation set, the isentropic relation is used,

$$p' = c^2 \rho', \quad (19)$$

where  $c$  is the speed of sound of the mean flow. As proposed by Pridmore-Brown [3], the equation set could be manipulated to obtain the equation in terms of  $p'$  and  $v'$ ,



$$\begin{aligned} \frac{1}{c^2} \frac{\partial^2 p'}{\partial t^2} = & (1 - M^2) \frac{\partial^2 p'}{\partial x^2} + \frac{\partial^2 p'}{\partial y^2} - \frac{2M}{c} \frac{\partial^2 p'}{\partial x \partial t} \\ & + 2\rho_0 c \frac{dM}{dy} \frac{\partial v}{\partial x}, \end{aligned} \quad (20)$$

where  $M = U/c$ . The solution of  $p'$  and  $v'$  in the following form is expected,

$$\begin{aligned} p' &= A e^{ik(\kappa x - ct)} F(\kappa, y), \\ v' &= A e^{ik(\kappa x - ct)} G(\kappa, y), \end{aligned} \quad (21)$$

where  $F$  and  $G$  are related by

$$\frac{dF}{dG} = i\rho c k (1 - \kappa M) G. \quad (22)$$

In the above equations,  $k = \omega/c$  and  $\omega$  is the frequency of the sound wave. Substituting Eqns. (21) and (22) into Eqn. (20) and we obtain

$$\frac{d^2 F}{dy^2} + \frac{2\kappa M'}{1 - \kappa M} \frac{dF}{dy} + k^2 [(1 - \kappa M)^2 - \kappa^2] F = 0, \quad (23)$$

where  $M' = dM/dy$ . The boundary conditions are

$$\frac{dF}{dy} = 0 \quad \text{at} \quad y = 0 \quad \text{and} \quad y = L. \quad (24)$$

For a given frequency  $k = \omega/c$ , the eigenvalue  $\kappa$  could be obtained by solving Eqns. (23) and (24) as a boundary value problem. In Ref. [4], Pridmore-Brown solved the eigenvalue problem by an asymptotic expansion and the final solution is presented in the form of the complex Airy functions. In this report, we numerically solve the equation by a finite difference method. The details of the numerical method are beyond the scope of this report. In what follows, only a brief account of the numerical procedure is illustrated. First, we subdivide the computational domain  $[0, L]$  into  $P$  grid nodes. With the aid of the second-order central difference scheme,  $dF/dy$  and  $d^2 F/dy^2$  are replaced by

$$\begin{aligned} \frac{dF}{dy} &\approx [\mathbf{A}] \vec{\mathbf{f}}, \\ \frac{d^2 F}{dy^2} &\approx [\mathbf{B}] \vec{\mathbf{f}}, \end{aligned} \quad (25)$$

where  $[\mathbf{A}]$  and  $[\mathbf{B}]$  are coefficient matrices of the finite difference scheme with a dimension of  $P \times P$ . The column vector  $\vec{\mathbf{f}}$  has element  $f_i$  ( $i = 1, \dots, P$ ) as the discrete solution of  $F$  at grid node  $i$ . As a result of discretization, we can reformulate Eqns. (23) and (24) to become an eigenvalue problem in terms of  $\kappa$  such as

$$[\mathbf{A}]_0 \vec{\mathbf{f}} + \kappa [\mathbf{A}]_1 \vec{\mathbf{f}} + \kappa^2 [\mathbf{A}]_2 \vec{\mathbf{f}} + \kappa^3 [\mathbf{A}]_3 \vec{\mathbf{f}} = 0. \quad (26)$$

Here, the coefficient matrices  $[A]_i$  ( $i = 0, \dots, 3$ ) are combinations of matrices  $[A]$  and  $[B]$  premultiplied by coefficients as shown in Eqn. (23). Equation (26) is a polynomial type eigenvalue problem. We used the standard QZ algorithm to calculate the eigenvalues  $\kappa_i$  ( $i = 1, \dots, P$ ). The numerical convergence is checked by doubling the number of grid nodes.

The Mach number of the mean flow is a linear profile from null at wall to 0.5 at the free stream. With  $k = 2\pi$ , the converged eigenvalue is  $\kappa = 0.842758$ . The height of the computational domain is selected to be one meter and the wave length of the forced perturbation should be  $1/\kappa$  (about 1.19) meters. The length of the computational domain is set to be 5 meters and the whole domain is subdivided into  $200 \times 40$  grid nodes with uniform distance between them. The magnitude of the perturbation ( $A$  in Eqn. (21)) is equal to one hundredth. Figure 4 shows the converged eigenfunctions  $F$  and  $G$  as functions of  $y$ . These eigenfunctions in conjunction with the prescribed frequency  $k$  are used as the upstream perturbation for the CFD calculation. Figure 5 shows the pressure contours of the CFD results and the wave length is correctly simulated; the flow domain covers about  $5\kappa$  (about 4.2) wave lengths. Figure 6 shows the reconstructed eigenfunctions of  $p'$  at two, three, and four wave lengths downstream of the forced perturbation. In the figure, the solid line is the analytical solution. For the solution at the farthest downstream location, less than 3% of error is observed. As it can be seen, the magnitude of the pressure fluctuation is much larger near the wall. This is because that the mean flow distribution compresses the acoustic waves to propagate near the wall.

## 2. Linear Wave Growth in Compressible Free Shear Layer

The flow is defined in Fig. 7 and the fast stream is denoted by the subscript 1. The upstream perturbations (regardless of the source) are selectively amplified by the shear layer and grow exponentially in the linear regime. Eventually, these instability waves cause eddy roll-up and merging at the later stage (nonlinear) of the flow development.

In this numerical example, we first discuss the mean flow solution. Then the solution of the linearized Euler equations (the Rayleigh equation) based on the given mean flow is provided in the form of a full spectrum of eigenvalues and eigenfunctions. Among the available eigenvalues, a relatively long wave-length solution is adopted in the present calculation and the CFD calculation is set up accordingly. The accuracy of the CFD results is assessed by comparing to the analytical solution in terms of growth rate and eigenfunctions.

For all solutions, flow properties of the fast stream are used as the referenced scales and all properties are non-dimensionalized accordingly in the following equations. In addition, the length scale is taken as  $\delta/2$  where  $\delta$  is the vorticity thickness and is defined as

$$\delta = \frac{U_1^* - U_2^*}{\left(\frac{dU^*}{dy^*}\right)_{\max}}, \quad (27)$$

where the superscript \* denotes the dimensional properties. The mean flow velocity distribution is given by

$$U(y) = \frac{1 + R \tanh ay}{1 + R}, \quad (28)$$

where  $R$  is the velocity ratio and is defined as

$$R = \frac{U_1^* - U_2^*}{U_1^* + U_2^*}, \quad (29)$$

and  $a$  is a parameter to control the thickness of the shear layer. According to Buseman and Crocco, the Prandtl number is set to be unity, and the velocity-temperature relationship is given by

$$T = T_2 + \frac{1 - T_2}{1 - U_2}(U - U_2) + \frac{1}{2}(\gamma - 1)M_1^2(U - U_2)(1 - U). \quad (30)$$

For the balance of the mean flow field, pressure is set to be uniform across the shear layer and the mean flow velocity in the transverse direction  $V$  is set to be null. As a result, all mean flow properties are defined.

Under the parallel-mean-flow assumption, the linearized disturbances have the Fourier coefficients independent of  $x$  and  $t$ , such as

$$\begin{pmatrix} u'(x, y, t) \\ v'(x, y, t) \\ p'(x, y, t) \\ \rho'(x, y, t) \end{pmatrix} = \begin{pmatrix} \hat{u}(y) \\ \hat{v}(y) \\ \hat{p}(y) \\ \hat{\rho}(y) \end{pmatrix} e^{i(\alpha x + \omega t)}, \quad (31)$$

where  $\hat{u}(y)$ ,  $\hat{v}(y)$ ,  $\hat{p}(y)$ , and  $\hat{\rho}(y)$  are the eigenfunctions of the posed problem. For each set of eigenfunctions, the corresponding frequency ( $\omega$ ) and wave number ( $\alpha$ ) are the eigenvalues.

For spatial instability problem,  $\omega$  is real and  $\alpha$  is complex in which the imaginary part ( $\alpha_i$ ) is the growth rate of the instability wave. The solution of these disturbances are governed by the compressible Rayleigh equation. We use a shooting method to solve the equation. The details of the solution procedure is out of the scope of this paper. Figure 8 is a typical solution of the equation. In this figure, we plot  $-\alpha_i$  against  $\omega$  as the full spectrum of the eigenvalues. The mean flow conditions are given by

$$T_1^* = 300K,$$

$$M_1 = 1.5,$$

$$U_2 = 0.74,$$

$$T_2 = 1.85.$$

In Fig. 8, we choose the case of  $\omega_r = 0.10101$  and  $\alpha_i = -0.012445$  for the CFD calculation. The chosen  $\omega$  and the corresponding eigenfunctions are used as the

imposed perturbation at the upstream boundary. Note that the eigenfunctions are complex, therefore, the upstream perturbation is of the form,

$$\phi' = \hat{\phi}_r(y) \cos(\omega t) - \hat{\phi}_i(y) \sin(\omega t), \quad (32)$$

where  $\phi'$  could be  $u'$ ,  $v'$ ,  $p'$ , or  $\rho'$ . Since there are four governing equations, only four boundary conditions are needed. The magnitude of the perturbation is set to be one thousandth. The fluctuations of other flow properties, e.g., temperature, are automatically obtained by solving the equation set. It is interesting to note that, for the given mean flow condition, part of the flow is subsonic. According to the MOC type boundary condition for subsonic flow, one can only specify three boundary conditions and let the fourth one be determined by the out-running characteristic equation. However, in the present calculation, all four boundary conditions are specified even for the subsonic flow due to the fact that the flow is a convective instability problem. All flow properties at the upstream boundary are determined by the eigenfunctions and eigenvalues; flow information carried by the out-running characteristic matches these conditions perfectly.

The computational domain is subdivided into a  $700 \times 70$  grid. The flow domain along the streamwise direction covers about six wave lengths of the imposed perturbation. The numerical grid is clustered near the center to provide high resolution of the flow field; the grid near outside boundaries is stretched to enhance the non-reflection effect. Figure 9 shows a instantaneous distribution of  $|u'|$  along the center line of the shear layer. The  $x$ -axis is the normalized streamwise distance. The  $y$ -axis is the normalized  $|u'|$  plotted in natural log scale. As shown in the figure, the growth rate of the wave is linear (in the log scale) and the slope is within 5% of  $-\alpha_i$  predicted by the linear theory. Since we impose the perturbation according to the eigenfunctions, the linear growth (in the log scale) of the instability wave starts from the very beginning of the free shear layer; no transitional region is observed in the vicinity of the upstream boundary.

Figure 10 shows the reconstructed eigenfunctions of  $u'$  and  $p'$  at various downstream locations compared to the prescribed eigenfunctions. Note that the eigenfunctions are normalized by the maximum. It is obvious that the CD6-RK4 finite difference method faithfully preserves the functional shape of the original perturbation.

### 3. Nonlinear Mechanism of Compressible Free Shear Layer

The mean flow conditions specified in Case 2 is adopted in the present calculation. As indicated in Fig. 8, we choose the most unstable mode of the available eigenfunctions and eigenvalue as the prescribed perturbation, i.e.,  $\omega = 0.389$  and  $\alpha_i = -0.026067$ . First, a magnitude of one thousandth is used to show the linear growth (in the natural log scale) of the instability wave. By doing so, we cover the two particular conditions of the whole spectrum, namely, a long wave mode (Case 2) and the most unstable mode, to assess the accuracy of the finite difference scheme

in simulating linear waves. Second, we increase the magnitude of the perturbation to show the eddy roll-up. Finally, the subharmonic of the most unstable mode is imposed in addition to the most unstable mode. Similar to the single frequency perturbation, the corresponding eigenfunctions of the subharmonic mode are used in this calculation to ensure that no undesirable perturbation is introduced into the system.

Figure 11 shows the Fourier coefficients of  $u'$  along the center line of the free shear layer. This figure clearly shows the linear growth (in the natural log scale) of the most unstable mode in the initial phase of the flow development. The slope of the curve compares favorably with the analytical solution. At the later stage of the flow development, the flow motion becomes nonlinear. The energy carried by the most unstable mode starts being transmitted to high harmonics. As a result, the growth of the fundamental mode stalls. Simultaneously, high harmonic modes gain strength as the prelude of the eddy roll-up. Mathematically, the appearance of the high harmonics is due to the convolution of the fundamental mode with itself and its harmonics. Therefore, no subharmonic mode can be produced. Figure 12 shows the reconstructed eigenfunctions of  $u'$  and  $p'$  at 5 and 10 wave lengths of the streamwise locations as compared to the prescribed eigenfunctions. For the streamwise location at 10 wave lengths, the flow is weakly nonlinear and the eigenfunctions show significant deviation from the linear analytical solution.

Figure 13 shows the Fourier coefficient of the harmonic contents for flow perturbed by the most unstable mode at a larger magnitude (one hundredth). The linear growth of the instability wave is limited to the region in the vicinity of the upstream boundary. At the later stage of the flow development, active eddy roll-ups are obvious as shown in Fig. 14, in which the contours of the constant vorticity are plotted. As shown in Fig. 13, at  $x = 160$ , a dip of Fourier coefficients is observed. The significant modulation of the Fourier modes may be attributed to a change of the energy transmission mechanism from the mean flow to the unsteady motions due to the appearance of the eddy roll-up.

Finally, the two-frequency perturbation is imposed on the upstream. The magnitude of both fundamental and its subharmonic is set to be one hundredth. Figure 15 shows the distributions of the Fourier coefficients of the fundamental ( $\omega$ ), second harmonic ( $2\omega$ ), and subharmonic ( $\omega/2$ ) as functions of streamwise locations. The growth rates of both fundamental and its subharmonic waves accurately mimic the analytical solution in the linear region. Compared to Fig. 13, Fig. 15 shows a earlier appearance of the  $2\omega$  wave due to the perturbation of the  $\omega/2$  wave. Again, the fundamental and its high harmonics are modulated due to the eddy roll-up. However, the location of the dip of the  $\omega$  wave occurs at  $x = 140$ . Previously, for the case without subharmonics perturbation the dip occurs at  $x = 160$  (see Fig. 13). As a contrast, the subharmonic mode is not affected and grows continuously. For incompressible flows, the growth rate of the subharmonic mode shows a kink and changes to a steeper slope when the eddy pairing appears in the shear layer. In the present calculation, the growth of  $\omega/2$  wave is levelled when flow motions

become nonlinear. In a later stage, the growth of the  $\omega/2$  wave is reactivated due to the eddy pairing. However, the slope change is much gradual compared to that of incompressible flows. Figure 16 shows the vorticity contours of the present calculation. Compared to Fig. 14, the trend of the eddy pairing is obvious due to the introduction of the subharmonic wave.

### 3. Concluding Remarks

We investigated the performance of the CD6-RK4 finite difference method in simulating linear and nonlinear wave motions in shear layers. The numerical accuracy is assessed by the Fourier analysis and numerical examples. First, a close form of the amplification factors and their corresponding dispersion correlations for the fully discretized, two-dimensional Euler equations are derived. Subsequently, the numerical dissipation, dispersion, and anisotropic effects are assessed. It is found that there are three groups of numerical waves propagating in the numerically dispersive medium, namely, the flow velocity waves and two acoustic waves superimposed on the flow velocity. Although, only the acoustic wave propagates in the direction of the flow velocity suffers from significant dissipation error, all three groups of waves suffer from dispersive errors at high wave numbers. For the present scheme, the CFL number limit for stable and accurate calculations is about 0.8. Under the CFL limit, dissipation, dispersive, and anisotropic artifacts are negligible for wave numbers less than  $\pi/3$  which corresponds to waves resolved by more than 6 grid nodes.

Three numerical examples of waves in fluid flows are presented: (1) sound propagation in a linear shear layer posed by Pridmore-Brown, (2) wave growth in a two-dimensional, compressible free shear layer, and (3) eddy-pairing in a compressible free shear layer perturbed by dual frequencies. The results compare favorably to the analytical solutions for linear wave motions. For nonlinear waves, the CFD results provide crisp resolution of the appearance of high harmonics, modulation of wave modes, eddy roll-up, and eddy pairing.

### 4. References

- <sup>1</sup> Lele, S. K. "Compact Finite Difference Schemes with Spectral-Like Resolution," *J. Comput. Phys.*, **103**, 16-42 (1992).
- <sup>2</sup> Yu, S. T., Tsai, Y.-L. P., and Hsieh, K. C., "Runge-Kutta Methods Combined with Compact Difference Schemes for the Unsteady Euler Equations," AIAA Paper 92-3210 (1992). (also submitted to *JCP*).
- <sup>3</sup> Tsien, H. S., *J. Am. Rocket Soc.*, **22**, 139 (1952).
- <sup>4</sup> Pridmore-Brown, D. C., "Sound Propagation in a Fluid Flowing through an Attenuating Duct," *J. Fluid Mech.*, 393-406 (1958).
- <sup>5</sup> Carnahan, B., Luther, H. A., and Wilkes, J. O., "Applied Numerical Methods," *John Wiley & Sons, Inc.*, 363 (1969).
- <sup>6</sup> Jameson, A., Schmidt, W. and Turkel, E. "Numerical Solutions of the Euler Equations by Finite Volume Methods Using Runge-Kutta Time-Stepping Schemes," AIAA Paper 81-1259 (1981).

- <sup>7</sup> Colatz, L., "The Numerical Treatment of Differential Equations," *Springer Verlag*, 538 (1966).
- <sup>8</sup> Giles, M. B., *AIAA J.* **28**, 12, 2050 (1990).

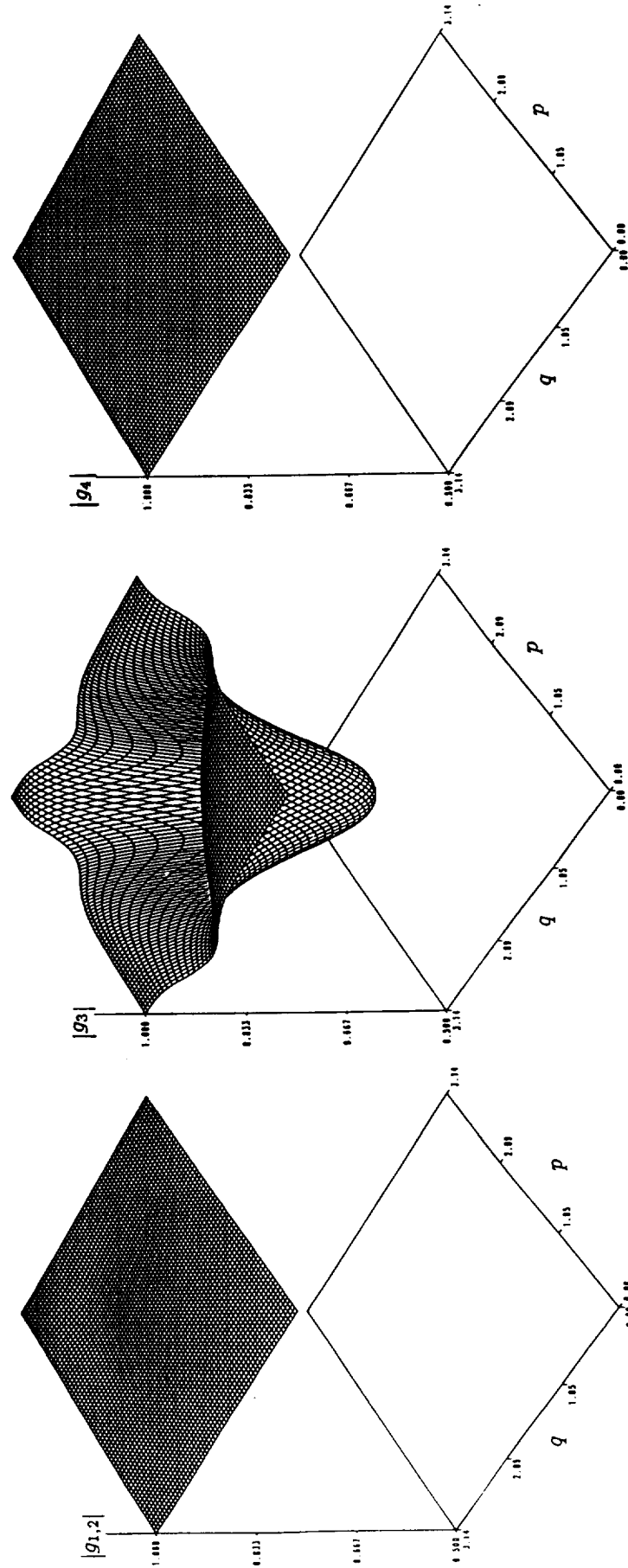


Fig. 1 Dissipation characteristics of the CD6-RK4 scheme for CFL=0.6.

1a  $|g_{1,2}(p, q)|$  for  $u = v$  and  $c = \sqrt{u^2 + v^2}$ .

1b  $|g_3(p, q)|$  for  $u = v$  and  $c = \sqrt{u^2 + v^2}$ .

1c  $|g_4(p, q)|$  for  $u = v$  and  $c = \sqrt{u^2 + v^2}$ .



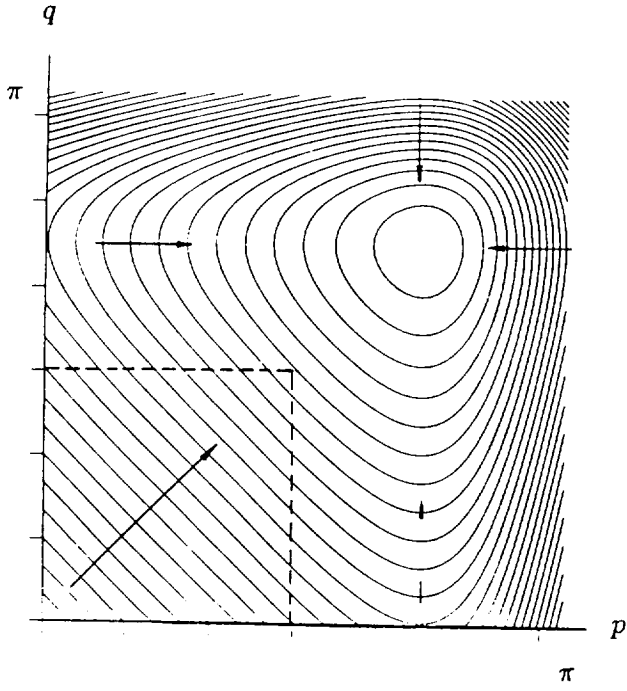
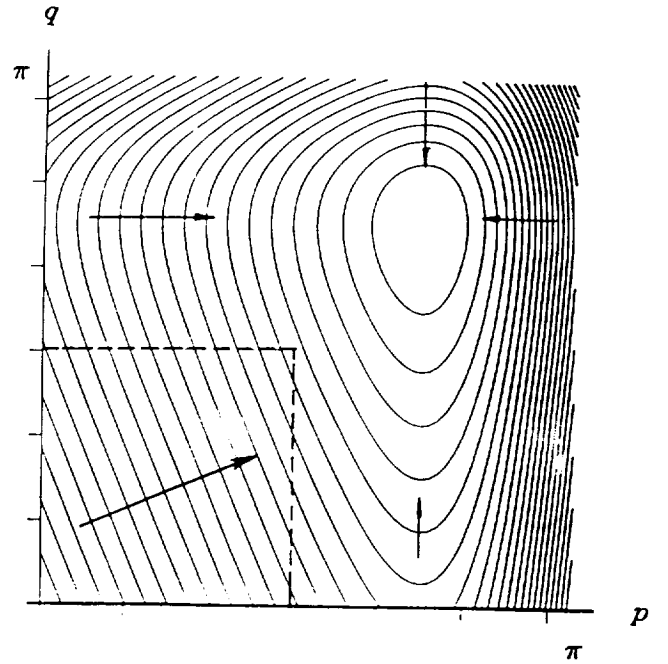
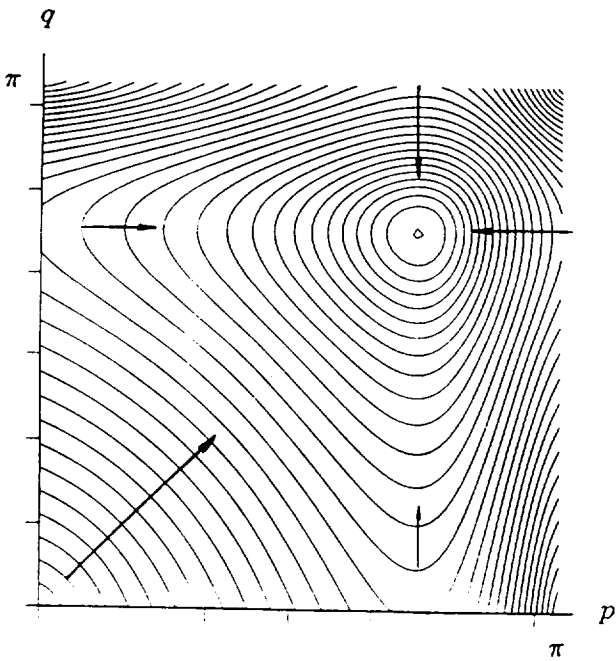
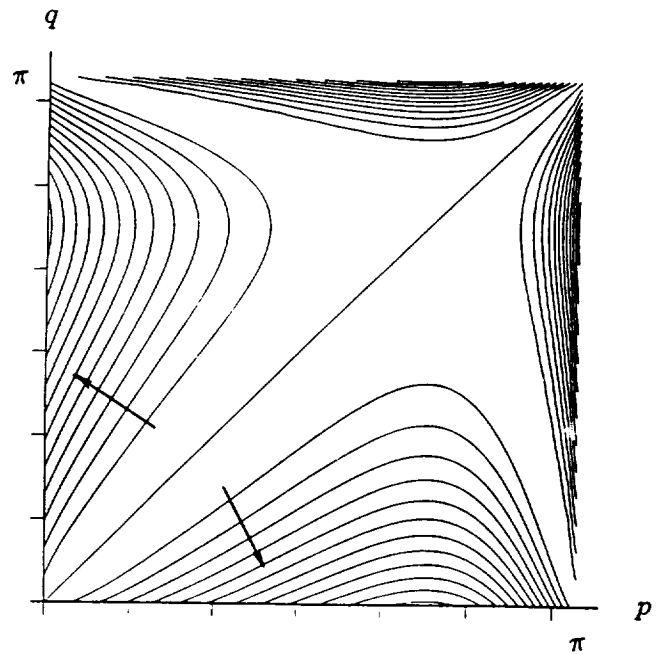
2a  $\alpha_{1,2}$  for  $u = v$  and  $c = \sqrt{u^2 + v^2}$ .2b  $\alpha_{1,2}$  for  $\tan^{-1}(v/u) = 22.5^\circ$  and  $c = \sqrt{u^2 + v^2}$ .2c  $\alpha_3$  for  $u = v$  and  $c = \sqrt{u^2 + v^2}$ .2d  $\alpha_4$  for  $u = v$  and  $c = \sqrt{u^2 + v^2}$ .

Fig. 2 Dispersion characteristics of the CD6-RK46 scheme for CFL=0.6.

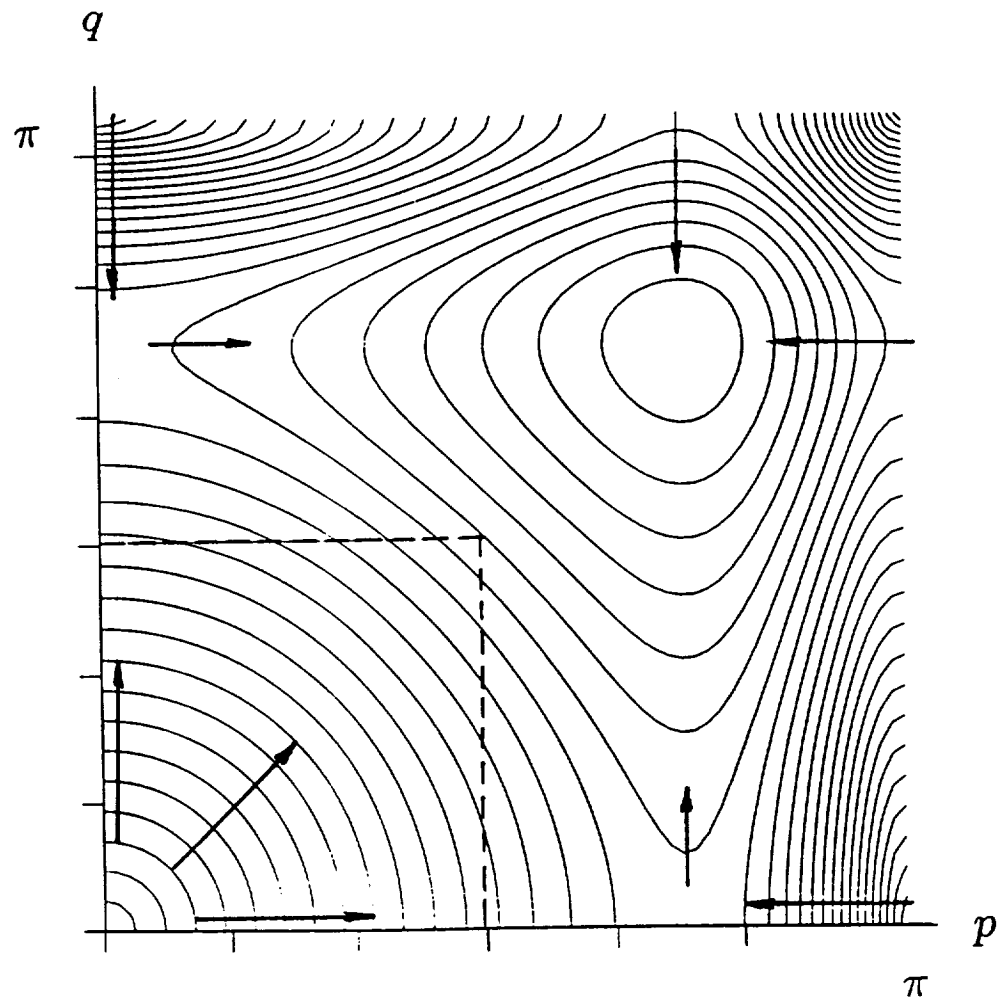


Fig. 3 Dispersion characteristics of the acoustic waves using the CD6-RK46 scheme for CFL=0.6.

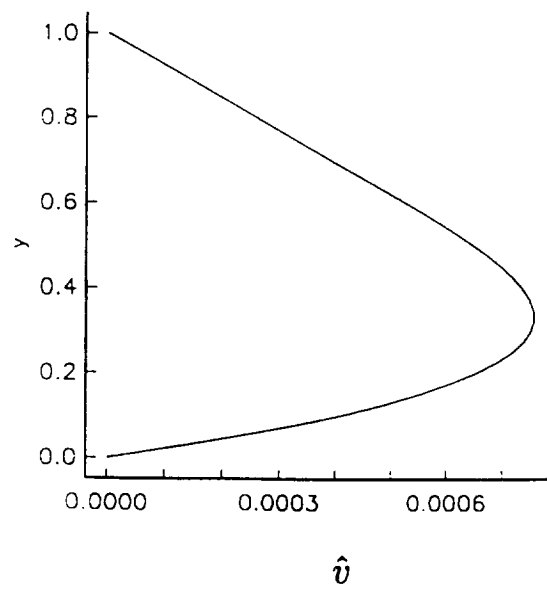
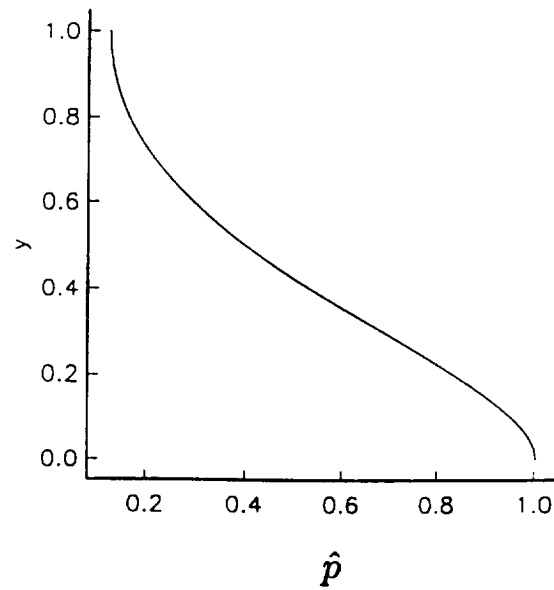


Fig. 4 Theoretical eigenfunction components  $p'$  and  $v'$  for acoustic waves in a duct with linear shear.

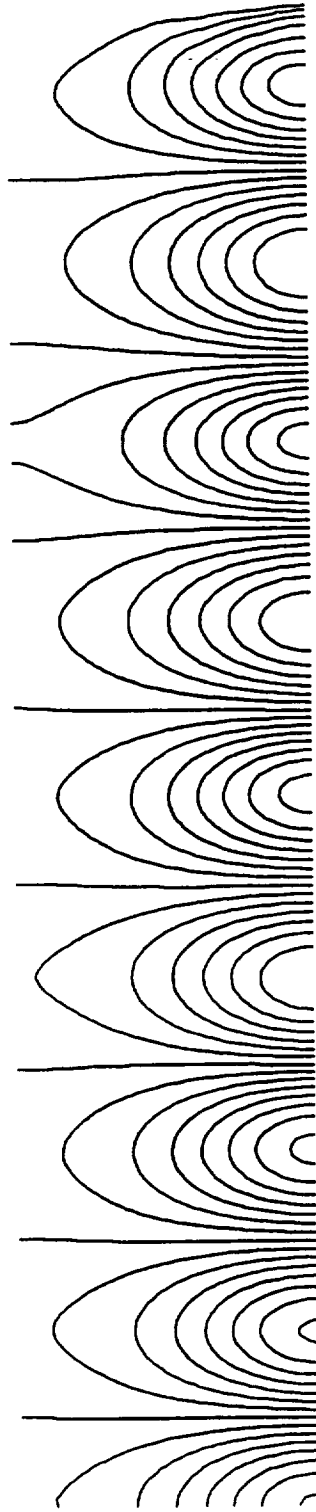


Fig. 5 Contours of constant pressure for acoustic waves in a duct with linear shear from the direct calculation using the CD6-RK4 method.

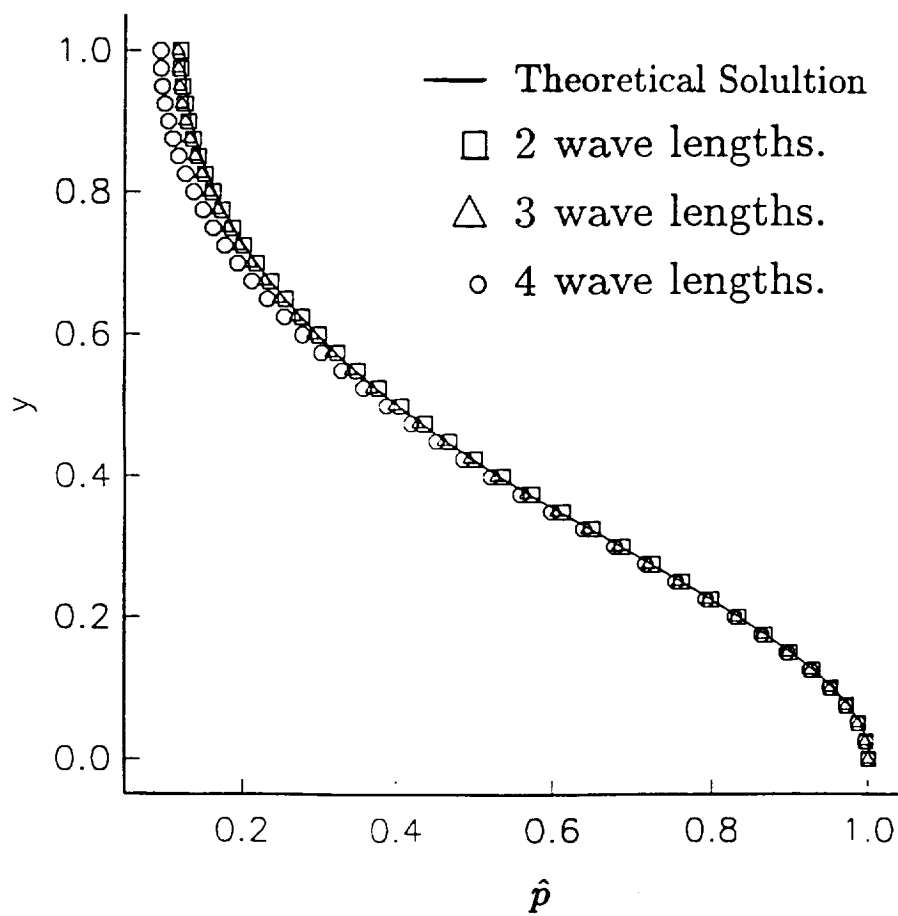


Fig. 6 Reconstructed eigenfunction of  $p'$  from the CFD results using the CD6-RK4 method for acoustic waves in a duct with linear shear.

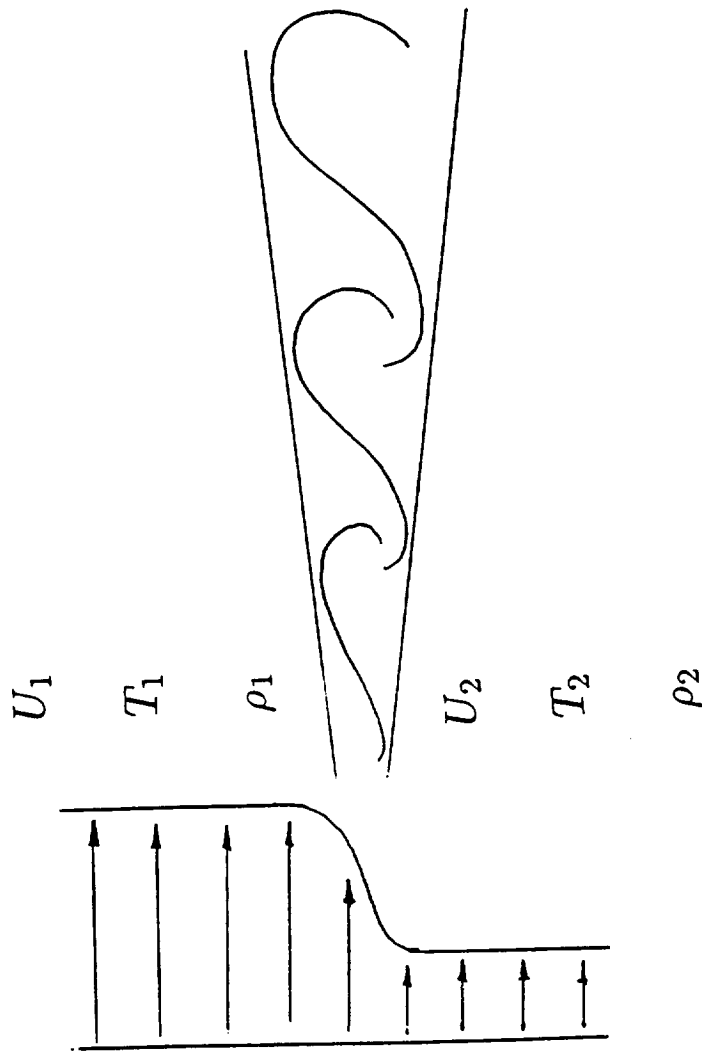


Fig. 7 Schematic of a compressible free shear layer.

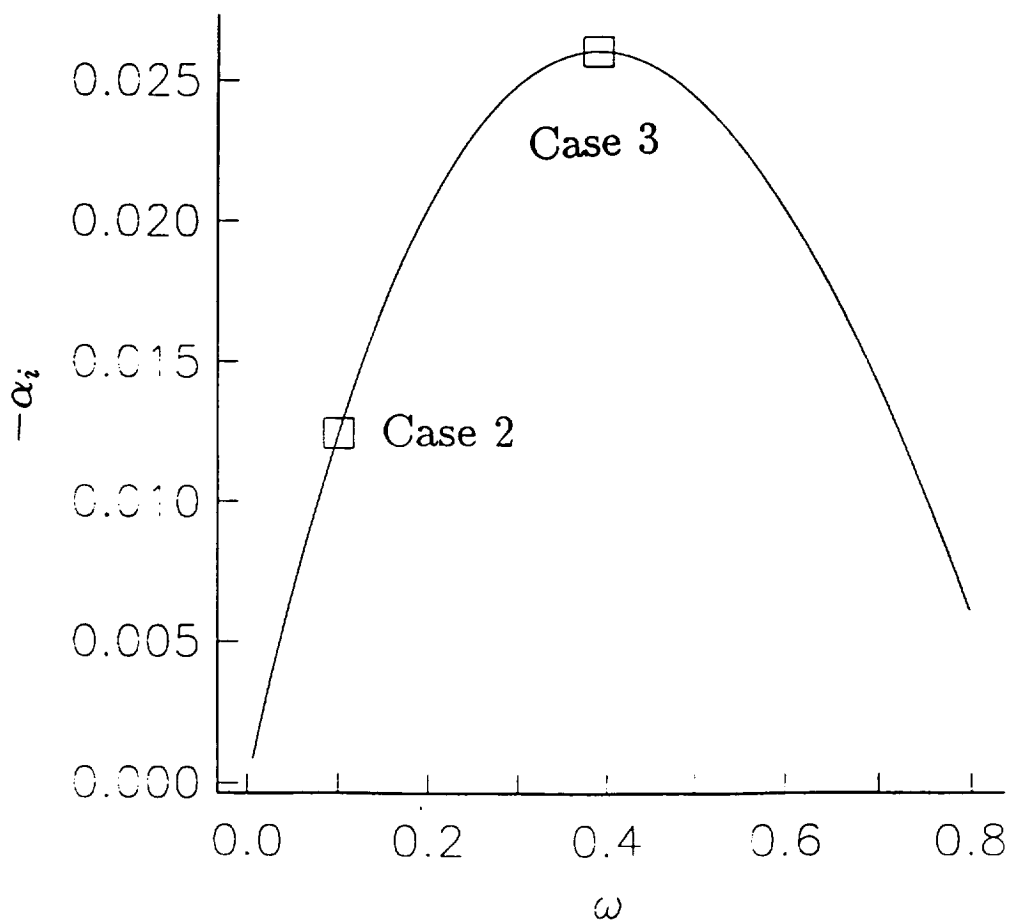


Fig. 8 The spatial growth rate as a function of the angular frequency from linear theory for the compressible free shear layer

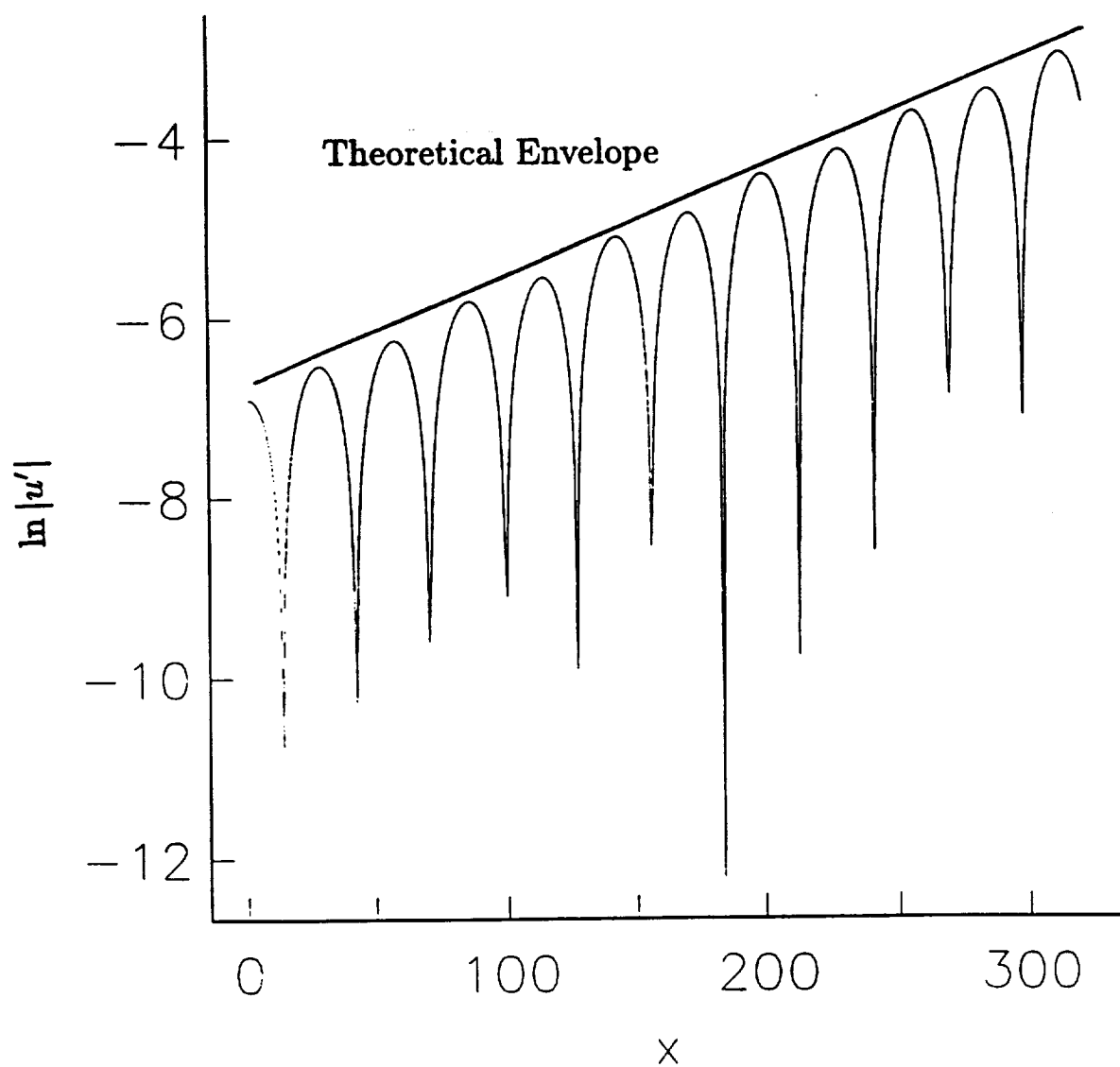


Fig. 9 Instantaneous distribution of  $|u'|$  along the center line of the free shear layer.



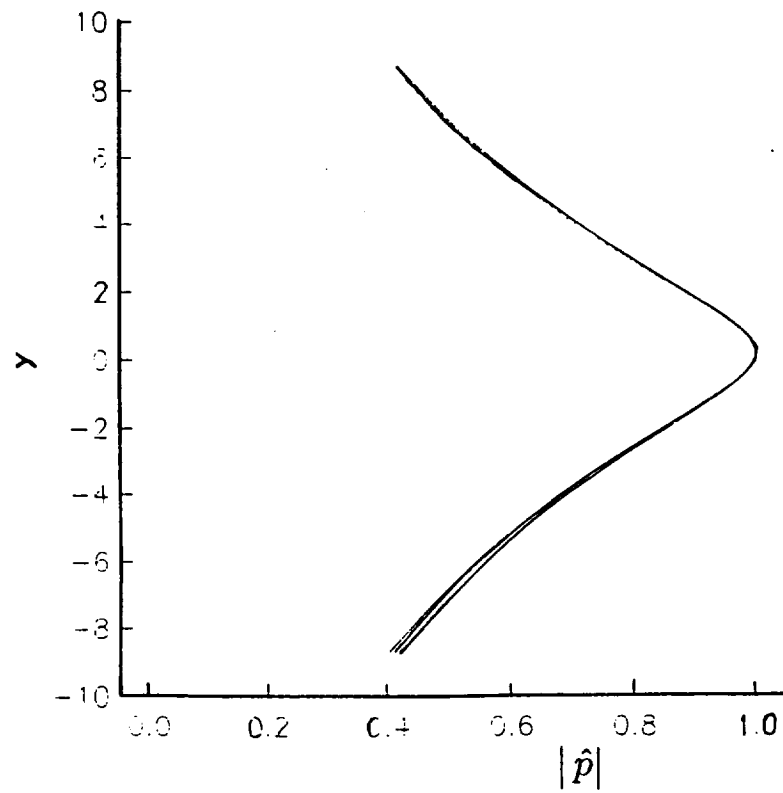
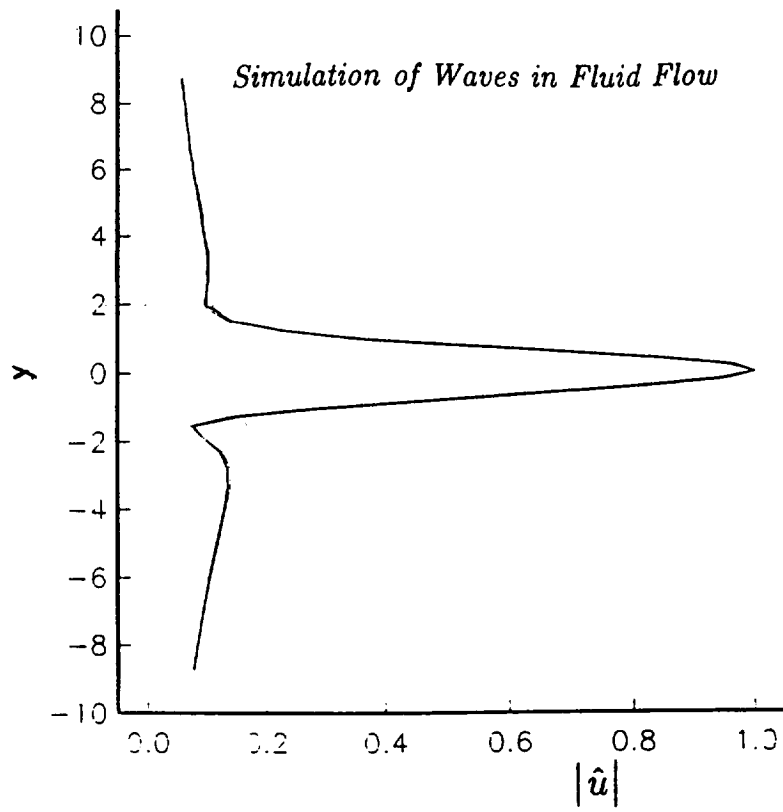


Fig. 10 Reconstructed eigenfunction components  $u'$  and  $p'$  from the CFD results for the compressible shear layer.

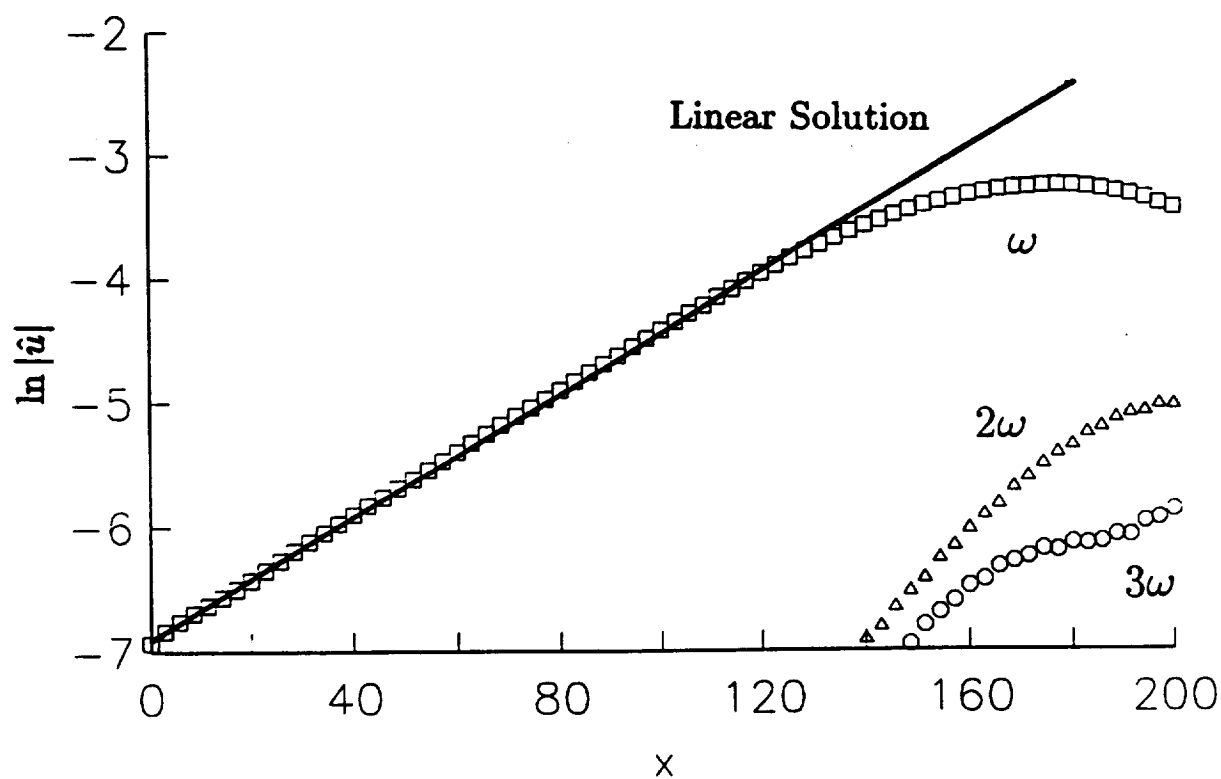


Fig. 11 The Fourier coefficients of the instability waves in a compressible free shear layer perturbed by the most unstable mode at the magnitude of one thousandth.

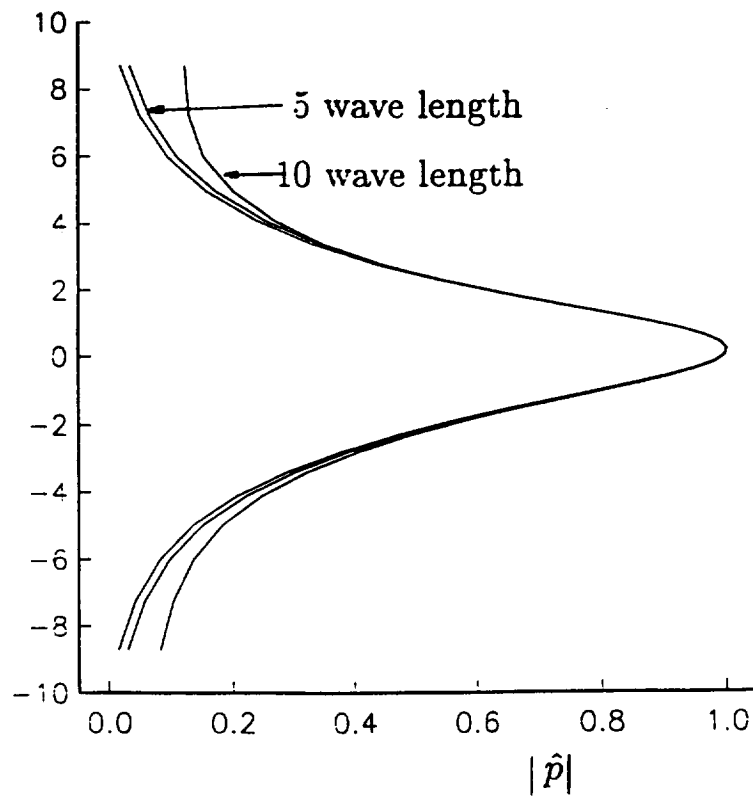
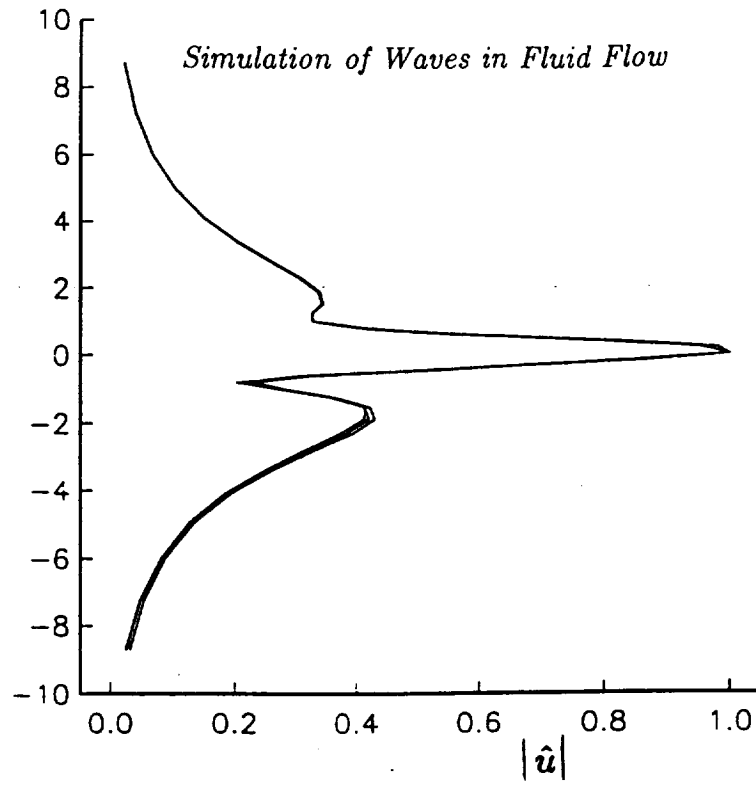


Fig. 12 Reconstructed eigenfunction components  $u'$  and  $p'$  from the CFD results for the free shear layer perturbed by the most unstable mode.

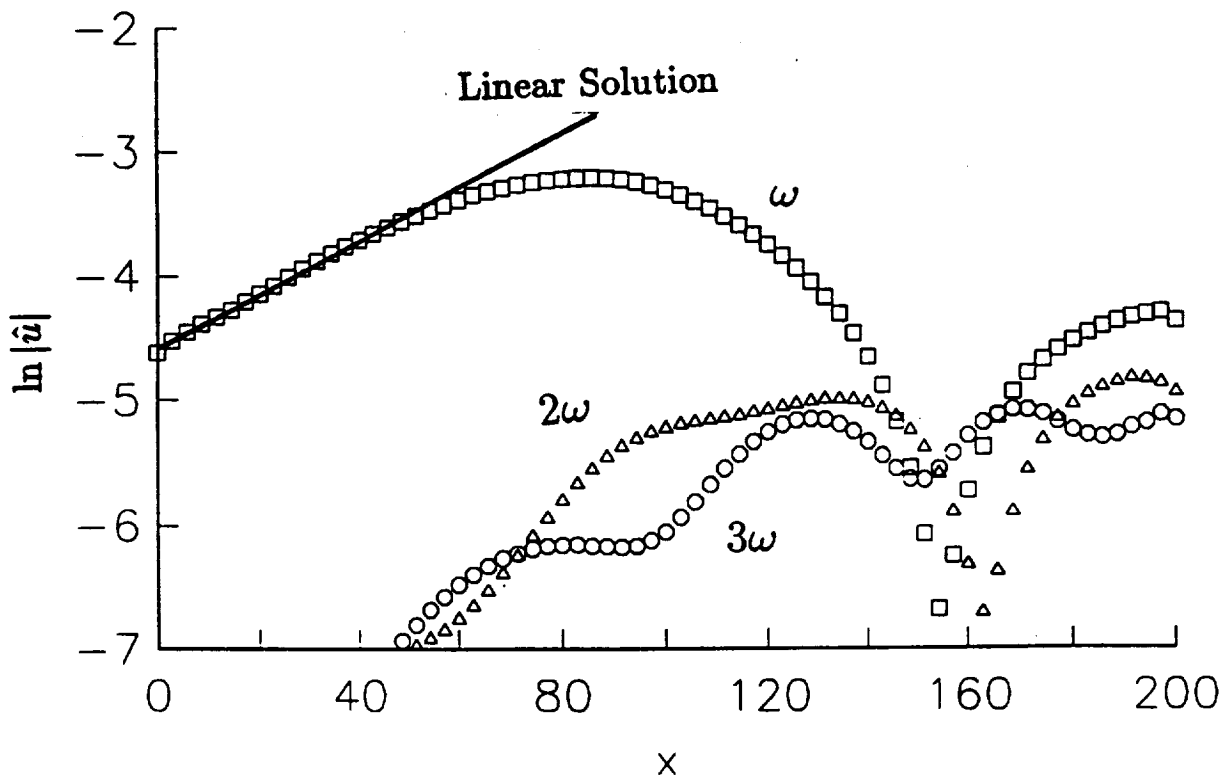


Fig. 13 Fourier coefficients of the unsteady motion in a compressible free shear layer perturbed by the most unstable mode at a magnitude of one hundredth.



Fig. 14 Contours of constant vorticity of the simulated free shear layer perturbed by the most unstable mode at a magnitude of one hundredth.

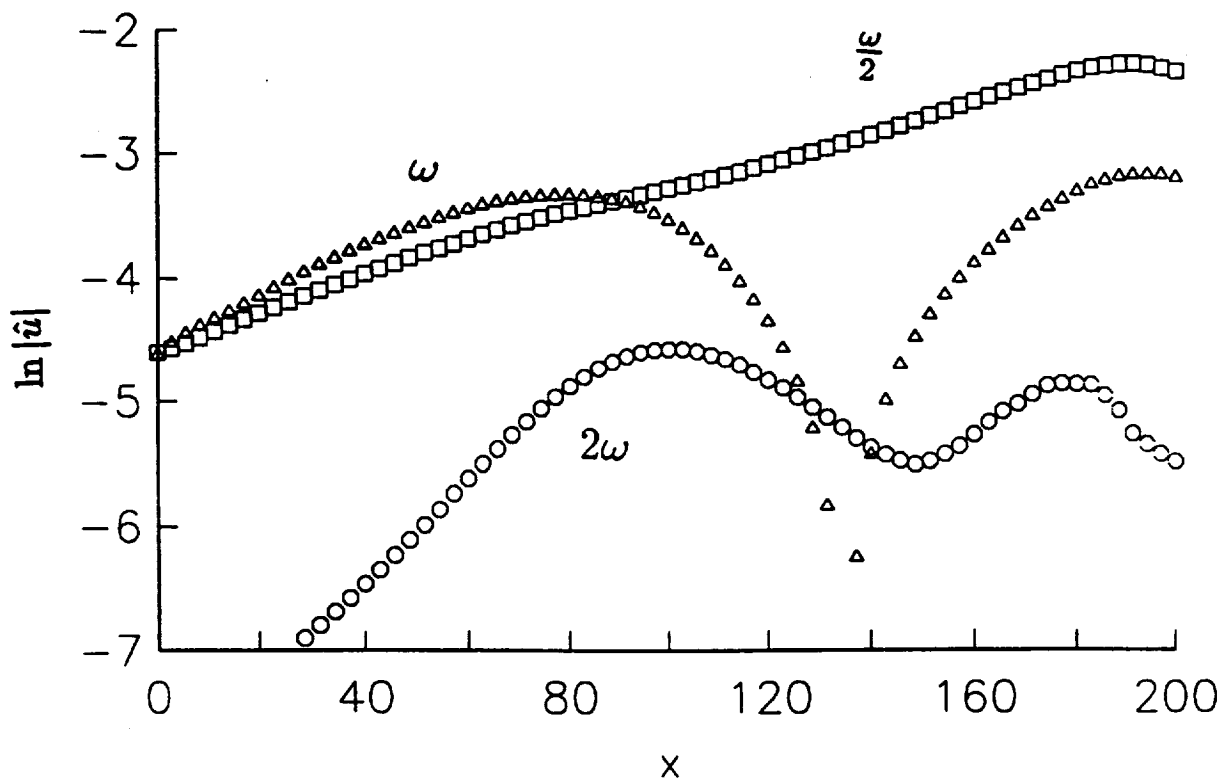


Fig. 15 The Fourier coefficients of the instability waves in a compressible free shear layer perturbed by the most unstable mode and its subharmonic.



Fig. 16 Contours of constant vorticity of the simulated free shear layer perturbed by the most unstable mode and its subharmonic.





## Visitors' Research Activities

A summer visitor program was initiated this year to promote collaborative research with academia. The following describes the technical activities of the visiting researchers.

In addition, CMOTT has also initiated collaborative applied research with the CFD groups in Rockwell Int. (headed by M. Sinder) and General Electric Co. (headed by S. Syed) for the purpose of improving their turbulent flow calculations in propulsion system design. This effort also helps CMOTT establish feedback channels with industry customers and the supply/demand relationship between CMOTT and its customers.

### **J.-Y. Chen ( University of California at Berkeley )**

#### **Direct Numerical Simulation of Turbulent Flows with Realistic Chemistry**

The main objective of this research is to study the interaction between turbulence and realistic chemical kinetics in nonpremixed turbulent flows using Direct Numerical Solutions (DNS). The starting point is the development of a feasible strategy of carrying out realistic chemical kinetics in DNS without adding a significant burden to the computational task. Such a task can be accomplished by considering specially designed fuel mixtures of  $H_2/AR$  and in a specific regime of turbulent combustion. By properly choosing the contents of the fuel mixtures, both the flame thickness and the degree of stiffness caused by chemical kinetics can be adjusted so that the flame will be fully resolved both in time and space. The computational task needed for the realistic chemical kinetics can be made manageable by using reduced chemical reaction mechanisms and efficient algorithms for evaluating chemical kinetics source terms.

The present development includes: (1) construction of a look-up table for the source terms for the hydrogen chemistry  $2H_2 + O_2 \rightarrow 2H_2O$  and for the Zeldovich NO mechanism  $N_2 + O_2 \rightarrow 2NO$ ; (2) implementation of the interpolation scheme into a high-order finite difference DNS code for compressible homogeneous turbulence as well as a spectral code for incompressible flows, and (3) testing of these newly developed computer codes. This development facilitates studies of the effects of density variation, compressibility, and the interaction of chemistry on turbulence. Study have been conducted for homogeneous turbulence with and without a forcing scheme to maintain kinetic energy. The preliminary results reveal that the compressibility causes the flame temperatures in either lean or rich sides higher than the counterparts in incompressible flows. A significant departure from chemistry equilibrium is also observed as the turbulence time scale can be smaller than the characteristic chemistry time scale. Future development is planned to impose a constant shear on the homogeneous turbulence.

**P.G. Huang ( Elore Institute/NASA Ames Research Center )  
Computation of Complex Shock/Boundary Layer Interactions Using A Two-Scale Turbulence Model**

The present consists of two parts: implementation of a two-scale model by Liou and Shih (1993) in to the compressible code by Huang and Coakley (1992) and testing of the model in flows with complex shock/boundary layer interactions.

The first part of the work, i.e., the implementation of the two-scale model into the compressible code, has been completed. The model has been tested successfully on a flat plate flow with zero pressure gradient. for Mach numbers ranging from 0.1 to 5.

The second part of the work has been part of the work has been partially completed. We have tested the model on Settles' 24 degree compressible corner flow, selected based on a recent review article (Settles and Dodson (1993)). The preliminary results have shown that the two-scale model produces results similar to that of the  $k - \epsilon$  model, although the skin friction in the recovery region is slightly higher. The outcome of the study will be submitted to the International Conference on Flow Interaction, to be held in Hong Kong, September 5-9, 1994.

**Arne V. Johansson ( Royal Institute of Technology, Stockholm )**

The cooperation between CMOTT and the Royal Institute of Technology has been started off in the area of turbulence modelling and numerical simulation of turbulence and transition. Several common points of interest were penetrated during the two-week visit, although the main focus was devoted to the study of general formulations of constitutive relations, with application to turbulence modelling. The particular area of interest for such general formulations of efforts in the direction of constructing explicit algebraic Reynolds stress models have shown promising results. The present work of clarifying some of the fundamentals for such relations have partly been written up during this visit. In addition to completing this effort, continued collaboration is planned in e.g. the direct numerical simulation area.

**Chaoqun Liu ( University of Colorado at Denver )**

Flow transition is one the fundamental and unsolved problems in modern fluid mechanics. The existing numerical studies are quite limited for the following reasons:

1. Most of them use temporal approach which is non-physical,
2. The codes blow up at the flow breakdown stage before transition (pre-onset simulation only)
3. Very expensive in cpu cost (around 100 - 1000 CRAY hours for a 3-D flat plate).

A new technology was developed during my visit at ICOMP in May-August, 1993, which led to a successful numerical simulation of the whole process of flow transition at

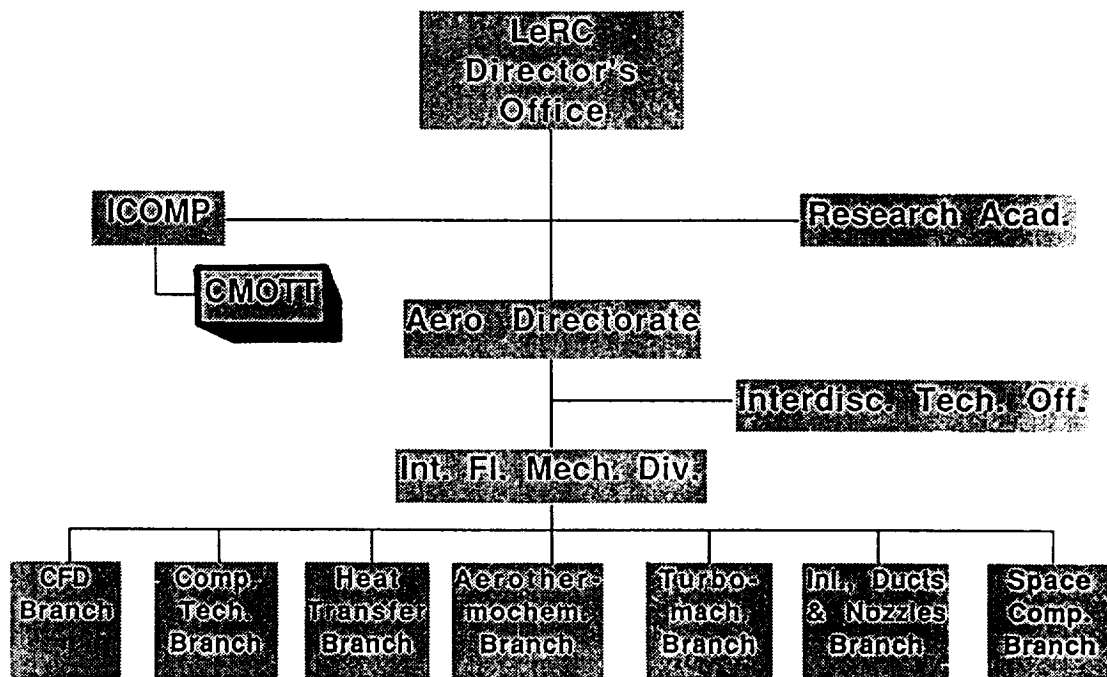
acceptable CPU cost. A fourth-order finite difference scheme on stretched and staggered grids, a fully implicit time-marching technique, a semi-coarsening multigrid based on the so-called approximate line-box relaxation, and a buffer domain for the outflow boundary conditions were all used high-order accuracy, good stability, and fast convergence. A new fine-coarse-fine grid mapping technique was developed to keep the code running after the laminar flow breaks down. A number of numerical simulations have been performed which show good agreement with linear stability theory, secondary instability theory and some experiments. This potentially provides a tool for direct numerical simulation of bypass transition. The cost for a typical case with  $162 \times 34 \times 34$  grid is around 2 CRAY-YMP CPU hours for 10 T-S periods.



## Appendix A

### Organization - 1993

#### Position Chart



**ICOMP Director**

Dr. Louis A. Povinelli  
Deputy Chief  
Internal Fluid Mechanics Division  
NASA Lewis Research Center

**Coordinator**

Dr. Meng-Sing Liou  
Senior Scientist  
Internal Fluid Mechanics Division  
NASA Lewis Research Center

**CMOTT Technical Leader**

Dr. Tsan-Hsing Shih  
Senior Research Associate  
ICOMP, NASA Lewis Research Center

### Current Listing of Members

<u>Names/Term</u>	<u>Affiliation</u>	<u>Research Areas</u>
Duncan, Beverly 7/1991 - present	Sverdrup Tech., Inc.	Multiple-Scale Turbulence Models
Hsu, Andrew T. 5/1990 - present	Sverdrup Tech., Inc.	PDF Turbulence Modeling, DNS
Liou, William W. 11/1990 - present	ICOMP	Compressible Flow Modeling, Weakly Nonlinear Wave Models
Norris, Andrew 4/1993 - present	ICOMP	PDF Turbulence Modeling, DNS
Rubinstein, Robert 7/1991 - present	ICOMP	Analytical Theories of Turbulence
Shabbir, Aamir 5/1990 - present	ICOMP	Buoyancy Effects on Turbulence, Turbulence Modeling
Shih, Tsan-Hsing 5/1990 - present	ICOMP	Turbulence Modeling
Steffen, Christopher J. Jr. 10/1990 - present	NASA LeRc	Upwind Algorithms Incompressible Flow Two-Equation Turbulence Models
Van der Vegt, Jacobus J. 10/1991 - 8/1993	ICOMP	DNS Compressible Flows High Order Shock Capturing Schemes
Yang, Zhigang 7/1990 - present	ICOMP	Modeling of Bypass Transition
Yu, Sheng-Tao 3/1991 - present	Sverdrup Tech., Inc.	Modeling of Chemical Reacting Flows, DNS
Zhu, Jiang 4/1992 - present	ICOMP	Application of Turbulence Models in Complex Flows





*Center for Modeling of Turbulence and Transition  
Research Briefs -1993*

## Appendix B

### CMOTT Biweekly Seminars

The purpose of these seminars is to exchange ideas and opinions on the latest developments and current state of turbulence and transition research. The speakers are invited from within and without of the NASA LeRC, including foreign speakers. The seminars were intended not only to keep the members informed of the latest development of local turbulence and transition modeling research but also to increase interactions between group members and other researchers at the NASA LeRC.

The following are the abstract of the seminars during the reporting period.



*CENTER FOR MODELING OF  
TURBULENCE AND TRANSITION*

Biweekly Meeting Series (1992-13)

**Analytical Theories of Turbulence Applied to  
Second Order Closures and Time-Dependent Modeling**

by

**Robert Rubinstein  
Sverdrup Tech. Inc.**

**Wed., August 19, 1992  
1:30-2:30 PM  
Room 228, SVR Building**

**ABSTRACT**

The general program of deriving turbulence models from analytical theories like renormalization group and direct interaction approximation will be described. Renormalization group analysis of the Reynolds stress transport equation leads to the Launder-Reece-Rodi as a lowest order approximate model with theoretically computed constants in good agreement with accepted values. However, the analysis shows that this model is not exact and justifies its replacement either with higher order non-linear models or with a generalization of the stress transport equation based on a decomposition of the Reynolds stress. Application of the direct interaction approximation to time-dependent turbulence models will be discussed.

CONTACT: William W. Liou, PABX 3-6682



*CENTER FOR MODELING OF  
TURBULENCE AND TRANSITION*

Biweekly Meeting Series (1992-14)

**Some Practical Turbulence Modeling Options for Full  
Reynolds Averaged Navier-Stokes Calculations of 3D Flows**

by

**Trong T. Bui**  
NASA Lewis Research Center

Wed., September 2, 1992  
1:30-2:30 PM  
Room 228, SVR Building

**ABSTRACT**

New turbulence modeling options currently under development for Proteus, a general purpose compressible full Reynolds averaged Navier-Stokes code, are discussed. The turbulence modeling capability in the 3-D version of Proteus in the current work consists of four turbulence models: the Baldwin-Lomax, the Baldwin-Barth, the Chien k-e, and the Launder-Sharma k-e models. Five compressibility corrections and one length scale correction are also available for the k-e models. Features of the Proteus turbulence modeling package include: well documented and easy to use turbulence modeling modules, uniform integration of turbulence models from different classes, automatic starting options for turbulence calculations using any turbulence model, and fully vectorized L-U solver for one- and two-equation models. Validation test cases include the incompressible and compressible flat plate turbulent boundary layers, turbulent developing S-duct flow, and glancing shock wave/turbulent boundary layer interaction. Sensitivity of the turbulence solutions with  $y^+$  computation and compressibility options are examined. The test cases show that the highly optimized one- and two-equation turbulence models can be used in routine 3-D Navier-Stokes computations with no significant increase in CPU time as compared with the algebraic Baldwin-Lomax model.

CONTACT: William W. Liou, PABX 3-6682



*CENTER FOR MODELING OF  
TURBULENCE AND TRANSITION*

Biweekly Meeting Series (1992-15)

**Calculation of Unsteady Turbulent Flow over  
Oscillating Airfoil**

by

**S.-W. Kim, K. Zaman and J. Panda**  
NASA Lewis Research Center

Wed., September 16, 1992  
1:30-2:30 PM  
Room 228, SVR Building

**ABSTRACT**

A numerical method to solve unsteady turbulent flows with moving boundaries and calculation of unsteady turbulent flow over an oscillating NACA 0012 airfoil at Reynolds number of 44,000 are presented. The Navier-Stokes equations defined on Lagrangian-Eulerian coordinates are solved by a time-accurate finite volume method that incorporates an incremental pressure equation for the conservation of mass. The turbulence field is described by a multiple-time-scale turbulence model. The numerical method successfully predicts the large dynamic stall vortex and the trailing edge vortex that are periodically generated by the oscillating airfoil. The calculated turbulence field show that the transition from laminar to turbulent state occurs widely along the airfoil. The calculated streaklines and the ensemble-average mean velocity profiles are in good agreement with the measured data.

CONTACT: William W. Liou, PABX 3-6682



## *CENTER FOR MODELING OF TURBULENCE AND TRANSITION*

Biweekly Meeting Series (1992-16)

### **Heat Transfer in Film-Cooled Turbine Blades**

by

**Vijay K. Garg**  
NRC Senior Research Associate

Wed., September 30, 1992  
1:30-2:30 PM  
Room 228, SVR Building

#### **ABSTRACT**

There is a growing tendency to use higher temperatures at the inlet to a gas turbine in an effort to improve the thermal efficiency and increase the specific power output. This calls for increasingly effective means of cooling the turbine blades. One cooling technique presently receiving wide application is film cooling. In order to study the effect of film cooling on the flow and heat transfer characteristics of actual turbine blades, Rod Chima's three-dimensional Navier-Stokes code has been modified. The effects of film cooling have been incorporated into the code in the form of appropriate boundary conditions at the hole locations on the blade surface. Each hole exit (generally an ellipse) is represented by several control volumes. This provides the code an ability to study the effect of hole shape on the film-cooling characteristics. Different velocity and temperature profiles for the injected gas can be specified at the hole exit. These include uniform, laminar or turbulent (1/7th power-law) profiles. The code can also handle either a specified heat flux or a variable temperature condition on the blade surface. A periodic C-grid with nearly half a million grid points is used. Comparison with experimental data is fair.

CONTACT: William W. Liou, PABX 3-6682



*CENTER FOR MODELING OF  
TURBULENCE AND TRANSITION*

**Biweekly Meeting Series (1992-17)**

**Unsteady Flows, Their Impact on  
Turbomachinery Blade Row Performance**

by

**John Adamczyk**

**NASA Lewis Research Center**

**Wed., October 14, 1992**

**1:30-2:30 PM**

**Room 228, SVR Building**



*CENTER FOR MODELING OF  
TURBULENCE AND TRANSITION*

Biweekly Meeting Series (1992-18)

**Experimental Investigation of Turbulent Supersonic  
Developing Pipe Flow**

by

**D.O. Davis**

NASA Lewis Research Center

Wed., October 28, 1992

1:30-2:30 PM

Room 228, SVR Building

**ABSTRACT**

Turbulent, supersonic, developing pipe flow is being investigated in the NASA Lewis 5"X5" Supersonic Wind Tunnel. The objective of the study is to establish a baseline dataset for the validation of turbulence measurement techniques. The resulting dataset should also be useful for turbulence model and CFD code validation. The mean flow and turbulence field is being measured with pressure probes and hot-wire anemometry. Preliminary results have been obtained for a Mach 3 inlet condition and a flow development length of  $x/D=32$  ( $D=2.0$  inches). These results, along with a discussion of the problems of hot-wire anemometry in a compressible boundary layer will be presented. Input from turbulence modelers and code developers regarding future testing with the supersonic pipe flow facility will be solicited.

CONTACT: William W. Liou, PABX 3-6682



*CENTER FOR MODELING OF  
TURBULENCE AND TRANSITION*

**Biweekly Meeting Series (1992-19)**

**Validation of a Two-Scale Turbulence Model for  
Incompressible Shear Flows**

by

**Beverly S. Duncan**  
Sverdrup Technology Inc.

**Wed., November 4, 1992  
1:30-2:30 PM  
Room 228, SVR Building**

**ABSTRACT**

**A two-scale eddy viscosity model has been developed which splits the energy spectrum into a high wavenumber regime and a low wavenumber regime. Dividing the energy spectrum into multiple regimes simplistically emulates the cascade of energy through the turbulence spectrum. This new model has been calibrated and tested for turbulent shear layers. Calculations of mean and turbulent properties show good agreement to experimental data for a plane jet, a round jet and two mixing layers. Preliminary results for boundary layers will also be presented.**

CONTACT: William W. Liou, PABX 3-6682





*CENTER FOR MODELING OF  
TURBULENCE AND TRANSITION*

Biweekly Meeting Series (1992-20)

**Extension of a Two-Scale Turbulence Model to  
Compressible Free Shear Flows**

by

William W. Liou  
ICOMP

Wed., November 18, 1992  
1:30-2:30 PM  
Room 228, SVR Building

**ABSTRACT**

A two-scale model for compressible turbulent flows is described. The model incorporates a notion that the effect of compressibility on turbulence is mainly on the energetic large eddies. The small eddies are affected through the increased spectral energy transfer from the large eddies due to the effect of compressibility. The turbulent eddy-viscosity is determined by the total turbulent kinetic energy and the energy transfer rate, which is different from the energy dissipation rate. The model is tested against high-speed mixing layers. The results agree satisfactorily with measured data.

CONTACT: William W. Liou, PABX 3-6682



*CENTER FOR MODELING OF  
TURBULENCE AND TRANSITION*

Biweekly Meeting Series (1992-21)

**Prediction of Surface Roughness Effects on  
Turbine Aerodynamic and Heat Transfer Performance**

by

**Robert J. Boyle**  
IFMD

Wed., December 2, 1992  
1:30-2:30 PM  
Room 228, SVR Building

**ABSTRACT**

Surface roughness has been shown to affect the aerodynamic performance of turbomachinery. Tests on the SSME fuel turbine showed a 20% increase in overall loss between smooth nearly a doubling of the blade profile loss. An approach to predicting the effects of blade surface roughness on the aerodynamic performance and heat transfer rates is discussed. An algebraic turbulence model, which includes the effect of surface roughness, was incorporated into a quasi three-dimensional Navier-Stokes analysis code (RVCQ3D). Comparisons are shown for both heat transfer and aerodynamic performance data.

CONTACT: William W. Liou, PABX 3-6682



## *CENTER FOR MODELING OF TURBULENCE AND TRANSITION*

Biweekly Meeting Series (1992-22)

### **Evaluation of the Turbulence Models in PARC**

by

**Nick Georgiadis**

Nozzle Technology Branch  
Propulsion System Division

Wed., December 16, 1992

1:30-2:30 PM

Room 228, SVR Building

#### **ABSTRACT**

The PARC2D/3D Navier-Stokes codes are used to analyze a variety of complex turbulent propulsion flows. Both algebraic and two-equation turbulence models are available in PARC. This presentation will compare the capabilities of PARC's turbulence models to predict several flows including benchmark turbulent test cases (flow over a flat plate and over a backward-facing step), the Sajben transonic diffuser flow, and other propulsion flow cases. The algebraic turbulence models that are investigated are the P.D. Thomas model (the standard turbulence model in PARC which was optimized for free shear layer flows but also calculates wall boundary layers), the Baldwin-Lomax model, and a new combination model which uses the Modified Mixing Length (MML) for wall boundary layers and the Thomas model for free shear layers. The two-equation model that is also investigated is the Chien k-epsilon model with modifications for compressibility added by Nichols. The presentation will show that there are significant differences among flow solutions obtained with these turbulence models for even the simplest of flows.

CONTACT: William W. Liou, PABX 3-6682



## *CENTER FOR MODELING OF TURBULENCE AND TRANSITION*

Biweekly Meeting Series (1993-1)

# **The Application of PDF Methods to the Modeling of Turbulent Diffusion Flames**

by

**A.T. Norris**

Sibley School of Mechanical and Aerospace Engineering  
Cornell University, Ithaca, New York 14853.

Wed., January 20, 1992

1:30-2:30 PM

Multipurpose Room, OAI Building

### **ABSTRACT**

The modeled transport equation for the joint probability density function (jpdf) of velocity and dissipation provides a closed set of equations for the modeling of turbulent flows. Features of this method include the presence of length and time scales, intermittency and the exact treatment of convection. This approach is extended to reactive flows by including composition, (i.e. Solving for the jpdf of velocity, dissipation and composition.) which has the feature that reaction is treated exactly.

A particle-based Monte Carlo scheme is used to solve the transport equation, for several different classes of flow of increasing complexity. The simplest flow considered is a variable density plane mixing layer while the most complex is a piloted CO/H<sub>2</sub>/N<sub>2</sub> - Air diffusion flame close to extinction. Details of the modeling, including molecular mixing models and reduced thermochemical mechanisms, are discussed for each applicable flow.

CONTACT: Aamir Shabbir, PABX 3-5927



*CENTER FOR MODELING OF  
TURBULENCE AND TRANSITION*

**Biweekly Seminar Series (1993-2)**

**A Realizable Reynolds Stress Algebraic Equation Model  
For Complex Flows**

by

**Jiang Zhu and Tsan-Hsing Shih**

**CMOTT, ICOMP**

**Wed., February 10, 1992**

**1:30-2:30 PM**

**Room 2B206, OAI Building**

**ABSTRACT**

The invariance theory in continuum mechanics is applied to analyze Reynolds stresses in high Reynolds number turbulent flows. The analysis leads to a turbulent constitutive relation that relates the Reynolds stresses to the mean velocity gradients in a more general form in which the classical isotropic eddy viscosity model is just the linear approximation of the general form. On the basis of realizability analysis, a set of model coefficients are obtained which are functions of the time scale ratios of the turbulence to the mean strain rate and the mean rotation rate. These coefficients will ensure the positivity of each component of the turbulent kinetic energy — realizability that most existing turbulence models fail to satisfy. Separated flows over backward-facing step configurations are taken as applications. The calculations are performed with a conservative finite-volume method. Grid-independent and numerical diffusion-free solutions are obtained by using differencing schemes of second-order accuracy on sufficiently fine grids. The calculated results are compared in detail with the experimental data for both mean and turbulent quantities. The comparison shows that the present proposal significantly improves the predictive capability of  $K - \epsilon$  based two equation models.

CONTACT: Aamir Shabbir, 962-3149



## *CENTER FOR MODELING OF TURBULENCE AND TRANSITION*

**Biweekly Seminar Series (1993-3)**

### **An Algebraic Turbulence Model for Three-Dimensional Viscous Flows**

by

**R.V. Chima, P.W. Giel and R.J. Boyle**

**Propulsion Systems Division**

**Wed., February 24, 1993**

**1:30-2:30 PM**

**Multipurpose Room, OAI Building**

#### **ABSTRACT**

An algebraic turbulence model is proposed for use with three dimensional Navier-Stokes analyses. It incorporates features of both the Baldwin-Lomax and Cebeci-Smith models. The Baldwin-Lomax model uses the maximum of function  $f(y)$  to determine length and velocity scales. An analysis of Baldwin-Lomax model shows that  $f(y)$  can have spurious maximum close to the wall, causing numerical problems and non-physical results. The proposed model uses the integral relations to determine  $\delta^+ u_e$  and  $\delta$  used in the Cebeci-Smith model. It eliminates a constant in the Baldwin-Lomax model and determines the two remaining constants by comparison to Cebeci-Smith formulation. Pressure gradient effects, a new wake model, and the implementation of these features in a three-dimensional Navier-Stokes code are also described. Results are shown for a flat plate boundary layer, an annular cascade, and endwall heat transfer in a linear turbine cascade. The heat transfer results agree well with experimental data which shows large variations in endwall Stanton number contours with Reynolds number.

CONTACT: Aamir Shabbir, 962-3149



*CENTER FOR MODELING OF  
TURBULENCE AND TRANSITION*

Biweekly Seminar Series (1993-4)

**Computations of Separated Aerodynamic Flows Using  
a Modified Near Wall  $k-\epsilon$  Model**

by

**Dr. Yuichi Matsuo**

National Aerospace Laboratory

Tokyo, Japan

Thursday, March 4, 1993

2:00-3:00 PM

Multipurpose Room, OAI Building

**ABSTRACT**

Complex aerodynamic flows with separation were computed by using a near wall  $k-\epsilon$  model. The model is modified so that the near wall damping functions do not include friction velocity and so that the predicted turbulence quantities are matched to the variations from DNS data. In order to apply the model to practical flows, an efficient and robust flow solver was developed. The code is based on a finite difference approach where a state-of-the-art upwind scheme is used for the convection terms and further source terms of the turbulence quantities are treated implicitly. Some representative computations were carried out for flows over backward facing step, a NACA0012 airfoil, a supersonic compression corner and the ONERA M6 wing. The last one is a 3D case. The results show that the present model provides satisfactory predictability even for the complex flows with separation.

CONTACT: Aamir Shabbir, 962-3149



## CENTER FOR MODELING OF TURBULENCE AND TRANSITION

Biweekly Seminar Series (1993-5)

# Direct Numerical Simulation of Boundary Layer Flow Over Surface Roughness

by

Russell G. De Anna

IFMD

Wednesday, March 10, 1993

1:30-2:30 PM

Multipurpose Room, OAI Building

### ABSTRACT

Results from a *direct numerical simulation* of transitional flow over a surface with spherical roughness elements of height  $k$  and a surface with random roughness of maximum height  $\pm k_{max}$  are presented. Periodic boundary conditions in the streamwise and spanwise directions simulate an infinite array of roughness elements, while a *body force*, designed to yield the streamwise Blasius velocity in the absence of roughness, maintains the flow. At  $k/\delta^* = 0.72$ , the mean velocity field in the spherical roughness domain contains secondary flow patterns within the region below  $2k$ , for Reynolds numbers,  $U_k k/\nu$ , between 90 and 225. The streamwise vorticity at these low Reynolds numbers is simply a result of the fluid's continuity and does not indicate rotating fluid or effects of inertia. The spheres distort the original Blasius profile into a mildly inflected layer containing low-momentum regions behind each sphere. These regions engender unsteady disturbances near the wall; however, the distribution of body force with vertical position above the wall is such that growth is suppressed in this region. Growth does occur in the unstable layer above the spheres where the body force is larger. The disturbance frequency is fixed by both the mean, streamwise velocity in the most unstable layer and the spacing between spheres; it is not the blunt-body vortex-shedding frequency expected for isolated bodies. When an oscillating component was added to the steady, Blasius body force, the response was independent of both forcing frequency and amplitude and, once again, depended on the mean velocity and the spacing between spheres.

CONTACT: Aamir Shabbir, 962-3149





*CENTER FOR MODELING OF  
TURBULENCE AND TRANSITION*

**Biweekly Seminar Series (1993-6)**

**Three-Dimensional Navier-Stokes Analysis and  
Redesign of an Imbedded Bellmouth Nozzle  
in a Turbine Cascade Inlet Section**

by

**P. W. Giel, J. R. Sirbaugh, I. Lopez, J. Van Fossen**

**Sverdrup Tech./ARMY/NASA**

**Wednesday, April 7, 1993**

**1:30-2:30 PM**

**Multipurpose Room, OAI Building**

**ABSTRACT**

A computational analysis of an imbedded bellmouth inlet was performed with the PARC code to identify and eliminate the source of measured pitchwise flow non-uniformity in the NASA LeRC Transonic Turbine Blade Cascade. The computational domain extended from the beginning of a constant span section to a plane just upstream of the cascade of turbine blades. Spanwise symmetry allowed modeling of just half of the span. The blockage and acceleration effects of the blades were accounted for by specifying a periodic static pressure exit condition interpolated from an RVC3D code isolated blade calculation. Calculations of the original geometry showed total pressure loss regions consistent in strength and in location to experimental measurements. An examination of the results shows that the distortions are caused by a pair of vortices that originate as a result of the interaction of the flow with the imbedded bellmouth. Computations were performed for an inlet geometry which eliminated the imbedded bellmouth by bridging the region between it and the upstream wall. This analysis indicated that eliminating the imbedded bellmouth eliminates the troublesome pair of vortices, resulting in a flow with much greater pitchwise uniformity.

CONTACT: Aamir Shabbir, 962-3149



*CENTER FOR MODELING OF  
TURBULENCE AND TRANSITION*

**Biweekly Seminar Series (1993-7)**

**A PDF Approach for Compressible Turbulent  
Reacting Flows**

by

**Andrew Hsu**

**Sverdrup Tech.**

**Wednesday, April 21, 1993**

**1:30-2:30 PM**

**Room 2B-204, OAI Building**

**ABSTRACT**

The objective of the present work is to develop a probability density function (pdf) turbulence model for compressible reacting flows for use with a CFD flow solver. The probability density function of the species mass fraction and enthalpy are obtained by solving a pdf evolution equation using a Monte-Carlo scheme. The pdf solution procedure is coupled with a compressible CFD flow solver which provides the velocity and pressure fields. A modeled pdf equation for compressible flows, capable of capturing shock waves and suitable to the present coupling scheme, is proposed and tested. Convergence of the combined finite-volume Monte-Carlo solution procedure is discussed, and an averaging procedure is developed to provide smooth Monte-Carlo solutions to ensure convergence. Two supersonic diffusion flames are studied using the proposed pdf model and the results are compared with experimental data; marked improvements over CFD solutions without pdf are observed. Preliminary applications of pdf to 3D flows are also reported.

CONTACT: Aamir Shabbir, 962-3149



*CENTER FOR MODELING OF  
TURBULENCE AND TRANSITION*

**Biweekly Seminar Series (1993-8)**

**On the linear stability of a trailing line vortex**

by

**Zhigang Yang**

**ICOMP**

**Wednesday, May 5, 1993**

**1:30-2:30 PM**

**Multipurpose Room, OAI Building**

**ABSTRACT**

The viscous linear stability of a trailing line vortex (Batchelor vortex) is studied. The flow is characterized by two parameters, the Reynolds number  $Re$  and the rotation rate  $q$ . The marginal stability curve which separates the stable domain from the unstable domain was searched over the  $(Re, q)$  plane. It is found that on the marginal stability curve,  $q$  increases with the Reynolds number and does not approach a constant even when the Reynolds number is as large as  $10^5$ . The values of  $q$  for large Reynolds numbers are higher than the inviscid counterpart. These findings suggest that modes giving rise to the marginal stability are viscous and do not approach the inviscid limit as the Reynolds number goes to infinity. These modes have an azimuthal wavenumber  $n = -1$  when the Reynolds number is larger than 200, in contrast to  $n = -2$  for smaller Reynolds numbers. As the Reynolds number is increased, the eigenfunctions of the marginal stability modes become more and more concentrated near the axis of the vortex, suggesting that these modes are viscous center modes in the limit of large Reynolds number.

CONTACT: Aamir Shabbir, 962-3149



*CENTER FOR MODELING OF  
TURBULENCE AND TRANSITION*

**Biweekly Seminar Series (1993-9)**

**Weakly Nonlinear Models for Turbulent Free Shear Flows (3)  
- Linear Instability of Curved Free Shear Layers**

by

**William Liou  
ICOMP**

**Wednesday, June 9, 1993  
1:30-2:30 PM  
Room 2B-204, OAI Building**

**ABSTRACT**

**Turbulence closure schemes based on a weakly nonlinear theory with a description of the dominant large-scale structures as instability wave have been applied successfully in the prediction of various plane and axisymmetric free shear flows. In order to extend the wave model to curved mixing layers, a linear stability analysis has been performed. Two mean velocity profiles that represent stably and unstably curved free mixing layers were considered. In this presentation, results of the linear instability study for five curvature Richardson number are described. The instability characteristics of the mixing layer were found to vary significantly with the introduction of the curvature effects. The results also indicate that, in a manner similar to the Görtler vortices observed in a boundary layer along a concave wall, instability modes of spatially developing streamwise vortices pairs may appear in unstably curved mixing layer.**

**CONTACT: Aamir Shabbir, 962-3149**



*CENTER FOR MODELING OF  
TURBULENCE AND TRANSITION*

Biweekly Seminar Series (1993-10)

## Development of Reduced Chemistry for CFD Applications

by

J.-Y. Chen

Department of Mechanical Engineering  
University of California at Berkeley  
Berkeley, California

Friday, June 11, 1993

1:30-2:30 PM

Multipurpose Room, OAI Building

### ABSTRACT

Simplified chemical reaction mechanisms are often required for simulation of reacting flows to reduce computational time. Recent development of simplified mechanisms for complex combustion processes is based on systematic reduction of the detailed chemical mechanism rather than curve fits to limited experimental observations. Consequently, these newly developed features are capable of capturing many salient features of the detailed chemical kinetics. More importantly, for CFD applications, these features of the detailed mechanism can be obtained by a small number of scalars. This presentation will be given from the point view of CFD developers and users. The concept of systematic reduction method will be introduced with a simple thermal *NO* reaction mechanism. A step by step reduction of the detailed mechanism will be illustrated for hydrogen and methane air combustion. Automation of the procedures for constructing reduced reaction mechanisms by a computer program is currently being developed. Results for hydrogen combustion with *NO<sub>x</sub>* formation will be presented.

CONTACT: Aamir Shabbir, 962-3149



*CENTER FOR MODELING OF  
TURBULENCE AND TRANSITION*

**Biweekly Seminar Series (1993-11)**

**Some Turbulence Modeling Issues Related to Heat Transfer  
in Turbomachinery**

by

**Ali Ameri**

**Turbomachinery Flow Physics Branch**

**Wednesday, June 16, 1993**

**1:30-2:30 PM**

**Multipurpose Room, OAI Building**

**ABSTRACT**

Navier-Stokes calculations were carried out in order to predict the heat transfer rates on surfaces of turbine blades. The code TRAF was modified to handle a variety of two-equation models in addition to the baseline Baldwin and Lomax model. The calculations were performed efficiently by utilizing a multigrid method. The results of the calculations generally agree with the experimental measurements in the laminar and the fully turbulent regimes. The transition process is however not well predicted. The two-equation model results also show a very distinct sensitivity to the assigned free stream length scale of turbulence. The accuracy level of the results obtained using the Baldwin-Lomax model was comparable to those obtained using the two-equation models. With that in mind a transition model was incorporated into the code which when used in conjunction with the B-L model produced very good results. The extension of the two-equation and the transition model to 3-d calculations will be addressed and some example cases will be considered.

CONTACT: Aamir Shabbir, 962-3149



Biweekly Seminar Series (1993-12)

## Modeling of Intercomponent Transfer In Reynolds Stress Closures Of Homogeneous Turbulence

by

Arne V. Johansson

Department of Mechanics  
Royal Institute of Technology  
Stockholm, Sweden

Monday, June 21, 1993

1:30-2:30 PM

Multipurpose Room, OAI Building

### ABSTRACT

In *classical* Reynolds stress closures of turbulent flows transport equations are formulated for the Reynolds stress tensor and dissipation rate. For homogeneous turbulence there is no spatial redistribution of energy and the modeling difficulties lie in the treatment of  $\epsilon$ -equation and the intercomponent transfer processes. The transport equations for  $\overline{u_i u_j}$  may be replaced by equations for the kinetic energy,  $k$ , and stress anisotropy tensor  $a_{ij}$  ( $\equiv \overline{u_i u_j} / k - 2\delta_{ij}/3$ ) to effectively separate the "amplitude" related issues involved in the prediction of  $k$  and  $\epsilon$  from the relative distribution among the components described by the normalized, traceless tensor  $a_{ij}$ .

Intercomponent transfer in the transport equations for  $a_{ij}$  (or  $\overline{u_i u_j}$ ) is represented by  $\Pi_{ij}^{(r)}$ ,  $\Pi_{ij}^{(s)}$  denoting the so called rapid and slow pressure strain rate terms, respectively, and a term related to the effects of anisotropic dissipation rate.

Detailed data for the individual terms obtained from direct numerical simulations and physical experiments are presented and used in the evaluation of the modeling ideas and other aspects of intercomponent transfer.

New experimental results will be presented where a pair of specially built hot-wire X-probes have been used to investigate the anisotropy of the dissipation rate in axisymmetric turbulence. The trends are to be well described by the model proposed by Hallback *et al.* (Phys. Fluids 1990) both for the simulation results and for the higher Reynolds number data obtained from the physical experiments.

For low turbulence Reynolds numbers the simulations have shown the slow part of the pressure-strain rate to be strongly suppressed. A simple model for the variation of Rotta constant has been shown to capture this Reynolds number variation.

Recently developed modeling ideas for the rapid pressure-strain rate will also be discussed. Strong realizability and kinematic constraints have been used to derive tensorially correct forms of the model, and the model constants have been calibrated by use of rapid distortion theory.



*CENTER FOR MODELING OF  
TURBULENCE AND TRANSITION*

Biweekly Seminar Series (1993-13)

**Computation of Confined Coflowing Jets with  
Three Turbulence Models**

by

**J. Zhu and T.-H. Shih**

**CMOTT/ICOMP**

**Wednesday, June 30, 1993**

**1:30-2:30 PM**

**Multipurpose Room, OAI Building**

**ABSTRACT**

A numerical study of confined jets in a cylindrical duct is carried out to examine the performance of two recently proposed turbulence models: an RNG-based  $K-\epsilon$  model and a realizable Reynolds stress algebraic equation model. The former is of the same form as the standard  $K-\epsilon$  model but has different model coefficients. The latter uses an explicit quadratic stress-strain relationship to model the turbulent stresses and is capable of ensuring the positivity of each turbulent normal stress. The flow considered involves recirculation with unfixed separation and reattachment points and severe adverse pressure gradients, thereby providing a valuable test of the predictive capability of the models for complex flows. Calculations are performed with a finite-volume procedure. Numerical credibility of the solutions is ensured by using second-order accurate differencing schemes and sufficiently fine grids. Calculations with the standard  $K-\epsilon$  model are also made for comparison. Detailed comparisons with experiments show that the realizable Reynolds stress algebraic equation model consistently works better than the standard  $K-\epsilon$  model in capturing the essential flow features, while the RNG-based  $K-\epsilon$  model does not seem to give improvements over the standard  $K-\epsilon$  model under the flow conditions considered.

CONTACT: Aamir Shabbir, 962-3149





## *CENTER FOR MODELING OF TURBULENCE AND TRANSITION*

**Biweekly Seminar Series (1993-14)**

# **Turbulence Modeling for Compressible Flows Part I - Modeling Mixing and Boundary Layer Flows**

by

**P.G. Huang**

Eloret Institute/  
Modeling and Experimental Validation Branch  
NASA-Ames, CA

Monday, July 12, 1993  
1:30-2:30 PM  
Room 2B-201, OAI Building

### **ABSTRACT**

The present seminar centers on the "dissipation-transport" equation and its role in predicting the compressible law of the wall. First, a skin friction and velocity profile family for compressible turbulent boundary layers is developed. The profile family has been compared with a range of high speed flow data with great success, including supersonic and hypersonic experiments and a recent compressible channel flow DNS.

Predictions of the velocity profiles using standard turbulence models have shown that the unmodified models have given rise to too small value of von Kármán constant,  $\kappa$ , in the log-law region. Thus, if the models are otherwise accurate, the "wake" component is over-predicted and the predicted skin friction is lower than the expected value. The magnitude of the errors that results from neglecting the dependence on density depends on the variables used to specify the length scale.

To agree with experimental values for  $\kappa$  in compressible boundary layer, the apparent eddy viscosity must be increased. This "compressible effect" – which is an artifact of conventional turbulence modeling rather than something real – is exactly opposite to that in mixing layers, where the growth rate, and by implication the eddy viscosity, decreases with increasing Mach number. As a consequence, recent compressibility modifications proposed for the mixing layer has increased the errors in predictions of flat-plate compressible boundary layer flows.

CONTACT: Aamir Shabbir, 962-3149



*CENTER FOR MODELING OF  
TURBULENCE AND TRANSITION*

**Biweekly Seminar Series (1993-15)**

**Turbulence Modeling for Compressible Flows  
Part II - Complex Flow Computations**

by

**P.G. Huang**

**Eloret Institute/  
Modeling and Experimental Validation Branch  
NASA-Ames, CA**

**Wednesday, July 14, 1993**

**1:30-2:30 PM**

**Room 2B-204, OAI Building**

**ABSTRACT**

Calculations of high Mach number turbulent flows have become a major challenge in CFD in recent years. In the present seminar, attention will be focused on some of the recent activities undergoing at NASA Ames on predictions of flows with complex shock-wave/boundary-layer interactions. Numerical methods to solve mean flow and turbulence equations, including Reynolds stress transport models, will be discussed. Comparison of low-Reynolds-number and wall-function techniques will also be made.

The seminar presents results of calculations for a range of 2-D and 3-D compressible turbulent flows using both two-equation and Reynolds stress transport models. Comparisons with the experimental data have shown that baseline models under-predict the extent of flow separation but over-predict the heat transfer near flow re-attachment. Modifications to the models are described which remove the above-mentioned deficiencies.

CONTACT: Aamir Shabbir, 962-3149



## *CENTER FOR MODELING OF TURBULENCE AND TRANSITION*

**Biweekly Seminar Series (1993-16)**

### **Towards the Simulation of a Full Turbofan Engine In the Meridional Plane**

by

**M. Stewart**

**Sverdrup Technology**

**Wednesday, July 28, 1993**

**1:30-2:30 PM**

**Room 2B-204, OAI Building**

#### **ABSTRACT**

The numerical simulation of the aerodynamics of a full jet engine is a problem of interest in engineering research and design. Existing analysis techniques deal with individual components and largely neglect inter-component effects. Yet the aerodynamic performance of a jet engine depends on these components working together efficiently.

In this simulation of a jet engine, the three-dimensional flow equations are averaged to axisymmetric flow equations, defined in the two-dimensional meridional plane of an engine. The engine's meridional plane is covered with a multiblock grid which resolves blades and other components. The meridional plane includes external flow outside the engine and the internal ducts. The turning effects of blades, combustion, blockage, losses and real gas effects are represented in the equations with terms and interior conditions.

Some numerical, modeling and physical issues in this simulation will be discussed including accounting for losses, imposing internal conditions and the numerical stability of large multistage compressors and turbine components.

The method will be demonstrated with two examples. Convergent numerical solutions will be shown for the 1.15 Pressure Ratio Fan Engine model. The applicability of these methods to commercial engines will be demonstrated with the Energy Efficient Engine.

(Refreshments will be provided)

CONTACT: Aamir Shabbir, 962-3149



*CENTER FOR MODELING OF  
TURBULENCE AND TRANSITION*

Biweekly Seminar Series (1993-17)

# Effect of the Coriolis Force on Compressible Turbulence

by

T.-H. Shih (ICOMP)

and

A.T. Hsu (Sverdrup Technology)

Wednesday, August 11, 1993

1:30-2:30 PM

Multipurpose Room, OAI Building

## ABSTRACT

Direct numerical simulation results and theoretical analysis are presented for the effect of the Coriolis force on compressible homogeneous isotropic turbulence. It is shown that the Coriolis force serves as a frequency modulator on turbulence. While the Coriolis force neither creates nor destroys turbulent kinetic energy, it redistributes energy by eliminating low frequency waves and transferring energy to waves with a frequency of  $2\Omega$ . The dissipation rate of turbulent kinetic energy can be either reduced or enhanced depending on whether or not the ratio between the rotation time scale and the Kolmogorov time scale is much greater than one. It has been demonstrated both theoretically and numerically that the Taylor-Proudman theorem is applicable to homogeneous turbulence only when the time scale of rotation, defined as the inverse of the frequency of the inertial waves, approaches the Kolmogorov time scale, and that two-dimensionalization occurs in this regime.

(Refreshments at 1:15)

CONTACT: Aamir Shabbir, 962-3149

## Appendix C

### List of Member's Publications

Barton, J. M., Rubinstein, R. and Kirtley, K. R. "Nonlinear Reynolds stress model for turbulent shear flows," AIAA Paper No. 91-0609, (Jan. 1991).

Barton, J. M. and Rubinstein, R., "Nonlinear algebraic Reynolds stress model for anisotropic turbulent flows," 11th U. S. National Congress of Applied Mechanics, Tucson, AZ (May 1990).

Barton, J. M. and Rubinstein, R., "Renormalization group theory and turbulence modeling," 2nd International Workshop on Chaos and Turbulence, Tsukuba, Japan (Jan. 1992).

Barton, J. M. and Rubinstein, R., "Renormalization group analysis of turbulence-driven secondary flows," 11th Australian Fluid Mechanics Conference, Hobart, Australia (Dec. 1992).

Brown, S., Leibovich, S. and Z. Yang, "On the linear instability of the Hall-Stewartson vortex," *Theoretical and Computational Fluid Dynamics*, **2**, 27-46, (1990).

Duncan, B. S., Liou, W. W. and Shih, T.-H., "A multiple-scale turbulence model for incompressible flow," AIAA 93-0086 (1993).

Duncan, B.S., Lumley, J.L., Shih, T.H. and To, W.M., "A new model for the turbulent dissipation" International Conference of Fluid Mechanics and Theoretical Physics, Beijing, China (1992).

Hsu, A.T. and Liou, M., "Computational analysis of underexpanded jets in the hypersonic regime," *Journal of Propulsion and Power*, **7**, No. 2, (1991).

Hsu, A.T., "Progress in the development of PDF turbulence models for combustion," 10th NASP Symposium, April 23-16, 1991, Monterey, California.

Hsu, A.T., "A study of hydrogen diffusion flames using PDF turbulence model," AIAA 91-1780, AIAA 22nd Fluid Dynamics Conference, June 24-26, 1991, Honolulu, Hawaii.

Hsu, A.T. and Chen, J.Y., "A continuous mixing Model for PDF simulations and its applications to combustng shear flows," 8th International Symposium on Turbulence Shear Flows, Sept. 9-11, 1991, Munich, Germany.

Lang, N.J. and Shih, T.-H., "A critical comparison of two-equation turbulence models," NASA TM 105237, (1991).

Liou, M. S. and Steffen, Jr., C. J., "A new flux splitting scheme," NASA TM 104404 (1991).

- Liou, W. W. and Shih, T.-H., "A two-scale model for compressible turbulent flows," NASA TM 106072 (1993).
- Liou, W. W. and Shih, T.-H., "Compressible turbulent boundary layer predictions using a multiple-scale model," NASA TM (to appear) (1993).
- Liou, W. W., "Linear instability of curved free shear layer," AIAA 93-3252 (1993).
- Liou, W. W. and Shih, T.-H., "On the basic equations for second-order modeling of compressible turbulence," NASA TM 105277 (1991).
- Liou, W. W. and Morris, P. J., "Weakly nonlinear models for turbulent mixing in a plane mixing layer," *Phy. Fluids*, 4, 2788-2808 (1992).
- Liou, W. W. and Morris, P. J., "The eigenvalue spectrum of the Rayleigh equation for a plane shear layer," *International Journal of Numerical Methods in Fluids*, 15, 1407-1415 (1992).
- Liou, W. W., "A new energy transfer model for turbulent free shear flow," NASA TM 105854 (1992).
- Mansour, N N. and Shih, T.-H. and Reynolds, W. C., "The effects of rotation on initially anisotropic homogeneous flows," *Physics of fluid A*, 3, 10, 2421-2425 (1991).
- Michelassi, V. and Shih, T.-H., "Low Reynolds number two-equation modeling of turbulent flows," NASA TM 104368, (1991).
- Michelassi, V. and Shih, T.-H., "Elliptic flow computation by low Reynolds number two-equation turbulence models," NASA TM 105376, (1991).
- Moin, P., Shih, T.-H., Driver, D. and Mansour, N., "Direct numerical simulation of a three-dimensional turbulent boundary layer," *Physics of Fluids A* 2, 10, 1846-1853 (1990).
- Norris, A.T., "The application of PDF methods to piloted diffusion flames," Ph.D. Thesis, Cornell University, 1993.
- Rubinstein, R. and Barton, J. M., "Renormalization group analysis of the Reynolds stress transport equations, nonlinear Reynolds stress models and the renormalization group," *Phys. Fluids A* 4, 1759-1766 (1992).
- Rubinstein, R. and Barton, J. M., "Nonlinear Reynolds stress models and the renormalization group," *Phys. Fluids A* 2, 1472 (1990).
- Rubinstein, R. and Barton, J. M., "Renormalization group analysis of anisotropic diffusion in turbulent shear flow," *Phys. Fluids A* 3, 415 (1991).
- Rubinstein, R. and Barton, J. M., "Renormalization group analysis of the Reynolds stress transport equation," to appear in *Physics of Fluids A*, (July 1992).

Shabbir, Munich. A., "Experimental balances for the second moments for a buoyant plume and their implication on turbulence modeling," Eighth Symposium on Turbulent Shear Flows, 27-1-1 to 27-1-6 (1991).

Shabbir, A. and Shih, T.-H., "Critical comparison of second order turbulence models in homogeneous flows," Submitted to AIAA Annual meeting in Reno, Jan. 1992.

Shih, T.-H., Liou, W.W., Shabbir, A., Yang, Z., and Zhu, J., "A vorticity dynamics based model for the turbulent dissipation," NASA TM 106177 (1993).

Shih, T.-H. and Lumley, J.L., "Remarks on turbulent constitutive relations," NASA TM 106116 (1993).

Shih, T.-H. and Lumley, J.L., "Kolmogorov behavior of near-wall turbulence and its application in turbulence modeling," NASA TM 105663 (1992)

Shih, T.-H., Chen, J.-Y. and Lumley, J. L., "Second order modeling of free turbulent shear flows," AIAA Journal, **30**, 6, 1553-1560 (1992).

Shih, T.-H. and Lumley, J.L., "A critical comparison of second order closures with direct numerical simulation of homogeneous turbulence," NASA TM 105351 (1991).

Shih, T.-H. and Hsu, A.-T., "An improved  $k - \epsilon$  model for near-wall turbulence," AIAA paper, 91-0611 (1991).

Shih, T.-H. Shih, Shabbir, A. and Lumley, J.L., "Advances in modeling the pressure correlation terms in the second moment equations," *The Lumley Symposium: Recent Developments in Turbulence*, November, 12-13, 1990, ICASE, NASA Langley Research Center, Edited by Gatski, T.B., Sarkar, S., Speziale, C.G.

Shih, T.-H., "An improved  $k - \epsilon$  model for near-wall turbulence and comparison with direct numerical simulation," NASA TM 103221 (1990).

Shih, T.-H. and Mansour, N. N., "Modeling of near-wall turbulence," *Engineering Turbulence Modeling and Experiments*, September 24-28, 1990, Dubrovnik, Yugoslavia, Editors: W.Rodi, E.N. Ganic.

Shih, T.-H. and Reynolds, W. C., "A spectrum model for weakly anisotropic turbulence," *Physics of Fluids A*, **2**, 8, (1990).

Steffen, Jr., C. J., "A critical comparison of several low Reynolds number k-epsilon turbulence models for flow over a backward-facing step," NASA TM 106173 (1993).

Steffen, Jr., C. J., "An investigation of DTNS2D for use as an incompressible turbulence modelling test-bed," NASA TM 105593 (1992).

Steffen, Jr., C. J. and Beard, L. M., "Incompressible Navier Stokes solutions using the pseudo compressibility technique," *Proceeding of the 23rd Annual Pittsburgh Conference on Modeling and Simulation*, in print (1992).

Van der Vegt, Jaap, "ENO-Osher schemes for Euler equations," AIAA Paper 93-0335 (1993)

Van der Vegt, J., "Assessment of flux splitting for viscous compressible flows," AIAA Paper 91-0243 (1991).

Van der Vegt, Jaap, "Overview of the Osher approximate Riemann solver for three-dimensional flows," NASA TM, in print (1992).

Yang, Z. and Leibovich, S., "On the linear marginal stability of the trailing line vortex," Submitted for publication.

Yang, Z. and Leibovich, S., "Unstable viscous wall modes in rotating pipe flow," AIAA Paper 91-1801, (1991). Also submitted to Physics Fluids A for publication.

Yang, Z. and Shih, T.H., "A  $k - \epsilon$  modeling of near wall turbulence," Proc. of 4th Intl. Sym. on CFD, Davis, CA, 1305-1310, (1991). Also available as NASA TM 105238.

Yang, Z. and Leibovich, S. "Nonlinear dynamics near the stability margin in rotating pipe flow," J. Fluid Mech. **233**, 329-347, (1991).

Yang, Z. and Shih, T.H., "A Galilean and tensorial invariant  $k - \epsilon$  model for near wall turbulence," AIAA Paper 93-3105 (1993).

Yang, Z. and Shih, T.H., "A  $k - \epsilon$  calculation of transitional boundary layers," *Proc. Near Wall Turbulent Flows*, Elsevier, 1993.

Yang, Z. and Shih, T.H., "On the wall functions for two equation turbulence models," prepared for publication.

Yang, Z. and Shih, T.H., "An invariant theory based model for the dissipation rate equation," In preparation.

Yang, Z. and Shih, T.H., "A  $k - \epsilon$  calculation of transitional boundary layers," *Transition and Turbulence*, Springer-Verlag, 1992.

Yang, Z. and Shih, T.H. "A new time scale based  $k - \epsilon$  model for near wall turbulence," AIAA J. **31**, 1191 (1993).

Yang, Z. and Shih, T. H., "A modeling of transitional boundary layers," In preparation.

Zhu, G., Lai, M.-C and Shih, T.-H., "Second-order closure modeling of turbulent buoyant wall plumes," NASA TM (in print) (1992).

Zhu, J., "FAST-2D: A computer program for numerical simulation of two dimensional incompressible flows with complex boundaries," Rept. No.690, Institute for Hydromechanics, University of Karlsruhe (1991).

Zhu, J. and Shih, T.H., "Calculations of turbulent separated flows, NASA TM 106154 (1993).

Zhu, J. and Shih, T.H., "A numerical study of confined turbulent jets," NASA TM 106197 (1993).

Zhu, J. and Shih, T.H., "Computation of confined coflow jets with three turbulence models," AIAA Paper 93-3120.



REPORT DOCUMENTATION PAGE			Form Approved OMB No. 0704-0188	
Public reporting burden for this collection of information is estimated to average 1 hour per response, including the time for reviewing instructions, searching existing data sources, gathering and maintaining the data needed, and completing and reviewing the collection of information. Send comments regarding this burden estimate or any other aspect of this collection of information, including suggestions for reducing this burden, to Washington Headquarters Services, Directorate for Information Operations and Reports, 1215 Jefferson Davis Highway, Suite 1204, Arlington, VA 22202-4302, and to the Office of Management and Budget, Paperwork Reduction Project (0704-0188), Washington, DC 20503.				
1. AGENCY USE ONLY (Leave blank)		2. REPORT DATE January 1994		3. REPORT TYPE AND DATES COVERED Technical Memorandum
4. TITLE AND SUBTITLE Center for Modeling of Turbulence and Transition: Research Briefs—1993			5. FUNDING NUMBERS  WU-505-90-5K	
6. AUTHOR(S) William W. Liou, editor				
7. PERFORMING ORGANIZATION NAME(S) AND ADDRESS(ES) National Aeronautics and Space Administration Lewis Research Center Cleveland, Ohio 44135-3191			8. PERFORMING ORGANIZATION REPORT NUMBER  E-8202	
9. SPONSORING/MONITORING AGENCY NAME(S) AND ADDRESS(ES) National Aeronautics and Space Administration Washington, D.C. 20546-0001			10. SPONSORING/MONITORING AGENCY REPORT NUMBER NASA TM-106383 ICOMP-93-44; CMOTT-93-16	
11. SUPPLEMENTARY NOTES William W. Liou, Institute for Computational Mechanics in Propulsion and Center for Modeling of Turbulence and Transition, NASA Lewis Research Center (work funded under NASA Cooperative Agreement NCC3-233). ICOMP Program Director, Louis A. Povinelli, (216) 433-5818.				
12a. DISTRIBUTION/AVAILABILITY STATEMENT  Unclassified - Unlimited Subject Category 34			12b. DISTRIBUTION CODE	
13. ABSTRACT (Maximum 200 words)  This research brief contains the progress reports of the research staff of the Center for Modeling of Turbulence and Transition (CMOTT) from June 1992 to July 1993. It is also an annual report to the Institute for Computational Mechanics in Propulsion located at Ohio Aerospace Institute and NASA Lewis Research Center. The main objectives of the research activities at CMOTT are to develop, validate and implement turbulence and transition models for flows of interest in propulsion systems. Currently, our research covers eddy viscosity one- and two-equation models, Reynolds-stress algebraic equation models, Reynolds-stress transport equation models, nonequilibrium multiple-scale models, bypass transition models, joint scalar probability density function models and Renormalization Group Theory and Direct Interaction Approximation methods. Some numerical simulations (LES and DNS) have also been carried out to support the development of turbulence modeling. Last year was CMOTT's third year in operation. During this period, in addition to the above mentioned research, CMOTT has also hosted the following programs: an eighteen-hour short course on "Turbulence—Fundamentals and Computational Modeling (Part I)" given by CMOTT at the NASA Lewis Research Center; a productive summer visitor research program that has generated many encouraging results; collaborative programs with industry customers (e.g. P&W. and RocketDyne) to help improve their turbulent flow calculations for propulsion system designs; a biweekly CMOTT seminar series with speakers from within and without the NASA Lewis Research Center, including foreign speakers. In addition, CMOTT members have been actively involved in the national and international turbulence research activities. The current CMOTT roster and organization are listed in Appendix A. Listed in Appendix B are the abstracts of the biweekly CMOTT seminar. Appendix C lists the papers contributed by CMOTT members.				
14. SUBJECT TERMS Turbulence modeling; Transition			15. NUMBER OF PAGES 255	
			16. PRICE CODE A12	
17. SECURITY CLASSIFICATION OF REPORT Unclassified	18. SECURITY CLASSIFICATION OF THIS PAGE Unclassified	19. SECURITY CLASSIFICATION OF ABSTRACT Unclassified	20. LIMITATION OF ABSTRACT	



**National Aeronautics and  
Space Administration  
Lewis Research Center  
21000 Brookpark Rd.  
Cleveland, OH 44135-3191**

**Official Business  
Penalty for Private Use \$300**

**POSTMASTER: If Undeliverable — Do Not Return**

